The Effects of Porosity on The Out-of-Plane Tensile Strength of Laminated Composites

by

Alfred P. Tomasino

thesis submitted to the Faculty of the

Virginia Polytechnic Institute and State University

in partial fulfillment of the requirements for the degree of

Master of Science

in

Engineering Mechanics

APPROVED:

Zafer Gürdal, Chairman

O. Hayden Griffin

Eric R. Johnson

October, 1988

Blacksburg, Virginia

The Effects of Porosity on The Out-of-Plane Tensile Strength of Laminated Composites

by

Alfred P. Tomasino

Zafer Gurdal, Chairman

Engineering Mechanics

(ABSTRACT)

The objective of this study was to investigate the out-of-plane tensile strength of graphite/epoxy laminates as a function of porosity. An experimental test program was designed to apply tension to the faces of circular graphite/epoxy specimens in a direction perpendicular to the laminate mid-plane. The specimens were removed from the webs of angle sections fabricated by Lockheed Georgia Company using AS4/1806 and AS4/3501-6 graphite/epoxy material systems with a stacking sequence of $(\pm 45/90_2/\pm 45/0_2)_S$ or $(\pm 45/0_2/\mp 45/90_2)_S$. The specimen porosities were the result of four distinct processing methods: a baseline hand lay-up, low pressure cure-cycle, a solvent wipe of pre-preg to remove resin, and the addition of water between pre-pregs. The experimental results have shown a significant reduction in the out-of-plane tensile strength as a function of increasing void content.

The volume fraction of pores, pore geometry, size, and orientation were determined for a representative number of specimens by metallography and optical analysis methods. This data was combined with the out-of-plane tensile data and used in the theoretical model, prepared by Brown et al, to predict the out-of-plane strength as a function of porosity. The predicted strength values compared very well with the experimental data when the pores were found to be uniformly distributed throughout the laminate.

Acknowledgements

The author wishes to thank his graduate advisor, Dr. Zafer Gurdal, for the opportunity and experience provided in this research project. His suggestions, advice and guidance during the course of this work is immensely appreciated. The author is indebted to Professors O. Hayden Griffin and Eric R. Johnson for graciously serving on his committee.

The author would like to acknowledge the monetary support of Lockheed Aeronautical Systems Company and the valuable assistance of , the project's technical monitor.

Special thanks to for her time and assistance at various stages of this work.

One-thousand thanks for

and a host of friends who have lent a helping hand at many a time.

The author is sincerely thankful to his mother and father, brothers and sister, their wives and husband, and his wife's family. Their love and support has sustained both the author and his family.

Finally, the author would like to dedicate this work to his wife and daughter for their love and patience. This work could never have been completed without them.

Table of Contents

List of Illustrations

List of Tables

1.0 Introduction

Fiber reinforced composite materials have found increased usage in the last decade. Their applications range from snow skis to satellites. Their high strength-to-weight and stiffness-to-weight ratios make them an ideal material for a large array of structural components, both military and commercial. In addition to the substantial weight savings achieved by the incorporation of composite materials in an advanced structure, composites possess good thermal and corrosion properties, are resistant to fatigue, and can be cost effective in many applications. The unique feature of directional dependent material properties make it possible to tailor a a fiber reinforced material to meet the service requirements of both primary and secondary structural components. Graphite/epoxy material systems are commonly used in both commercial and military aircraft applications. One such usage is in the construction of graphite/epoxy angle spars for wing and empennage structure. Figure 1 shows the location of an angle spar in a typical wing structure. The wing skin is fastened to the spar flanges, forming a box beam. Torsional loading of the box beam will result in forces applied transverse to the plane of the web. Several analytic studies have shown that external loads on a curved laminated structure of this sort, result in the occurance of interlaminar tensile stresses in the bend [1,2]. Though graphite/epoxy materials possess excellent load bearing capabilities in the plane of the laminate, they are also known to be poor in the transverse direction. To further

compound this problem, graphite/epoxy laminates will contain voids whenever volatile polymerization by-products (such as water) are unable to escape from the laminate during the cure process. In addition, the effects of cure cycle parameters (such as temperature and pressure) have been found to affect the void content of graphite/epoxy laminates [3]. The inclusion of defects during the manufacture and processing of graphite/epoxy will have an immediate impact on the mechanical properties of that material system. This is of primary concern to the design engineer interested in the practical application of graphite/epoxy materials in structural components.

A number of theoretical and experimental investigations have examined the effects of porosity on mechanical properties. However most of the theoretical analyses have been devoted to spherical voids, and the experiments have concentrated on polycrystalline refractory solids. In 1953, Ryshkewitch and Duckworth [4,5] related the strength of a ceramic material to the porosity by the following empirical relation:

$$\sigma = \sigma_{max} e^{-bP}$$

where σ_{max} is the strength at zero porosity, b is an empirical constant and P is the volume fraction of open-cell porosity. This relation was used repeatedly over the next ten years in the the investigation of porosity on the strength and mechanical properties of ceramic materials [6-12]. In 1964 S.D. Brown et al [13] related the empirical constant b to pore size, geometry, and orientation to calculate theoretical strength as a function of porosity. Brassel, Horak, and Butler [14] successfully used the theoretical model prepared by Brown et al for predicting the transverse tensile strength of filament wound carbon-carbon composites [14].

The objective of this investigation was to experimentally determine the effects of porosity on the transverse modulus and tensile strength of AS4/3501-6 and AS4/1806 graphite/epoxy laminates. The $(\pm 45/0_2/\mp 45/90_2)_S$ and $(\pm 45/90_2/\mp 45/0_2)_S$ quasi-isotropic laminates with void contents ranging between 0.5 and 7% were tested in out-of-plane tension. The theoretical

model prepared by Brown et al was used to predict the transverse tensile strength as a function of specimen porosity. The parameters necessary for the strength prediction model were obtained by optical analyses of the laminates.

2.0 Experimental Methods

2.1 Flatwise Tensile Testing

The experimental program was directed toward the determination of interlaminar normal tensile strength as a function of porosity for two graphite/epoxy laminates. The strength testing was performed by applying tension to the faces of circular specimens in a direction perpendicular to the midplane of the laminate. The circular specimens employed in this study were machined from 16 ply quasi-isotropic angle sections in 2.5-, 2.0- and 1.5-inch diameters. The angles were 30-inches long with an 'L-shaped' cross section comprised of a 3.0-inch long leg and a 1.5-inch short leg, Figure 2. The twenty angle sections were manufactured at Lockheed Georgia Company using both AS4/3501-6 and AS4/1806 material systems with $(\pm 45/0_2/\mp 45/90_2)_S$ or $(\pm 45/90_2/\mp 45/0_2)_S$ stacking sequences. The 0° plies were oriented parallel to the angle length. Four processing methods were used in an attempt to induce uniform porosities throughout the test parts. The first, or baseline, processing method was a standard lay-up, and cure to produce an angle with minimal porosity. The remaining processes included a solvent wipe during layup for removal of resin, the introduction of moisture between plies during layup and a low pressure cure. Each angle was C-scanned at Lockheed

to evaluate the effects of processing and the extent of voids in the laminate. Based on this evaluation the angles were qualitatively grouped into four defect levels: (0) baseline, (1) solvent wipe, (2) moisture introduction and (3) low pressure cure. The resulting ten combinations of test specimen parameters are listed in Table 1. The angle sections were then cut into 66 2.75-, 2.5- or 1.75-inch wide coupons and sent to Virginia Tech for machining and testing. The sectioning of the large angles and their corresponding part numbers are summarized in Figure 2.

2.1.1 Test Fixtures

To apply a uniformly distributed out-of-plane tensile loading across a flat laminated plate, test specimens were adhesively bonded to the test fixture assembly pictured in Figure 3. Finite element analyses were used to aide in both the selection of a suitable fixture material and geometry, and to examine the stresses applied to the laminate during testing. As a result of those analyses the fixture was designed with a tapered conical geometry to achieve minimal bending effects at the bond interface and thereby insuring a relatively uniform stress field across the laminate. The circular geometry would also eliminate stress concentrations occurring at specimen corners. The tensile stress distribution applied to the laminate by some of the preliminary fixture designs, obtained from finite element studies, is summarized in Figure 4. The finite element results are discussed at greater length in a later section.

Stainless steel was selected because of its high stiffness and good bonding characteristics, and alsodue to the elimination of oxidation and corrosion at the bond surfaces. One fixture was fabricated of 416 stainless steel hardened to a 0.2% yield strength of 150 ksi. This fixture was designed for the testing of both large diameter and low porosity specimens. Two additional fixtures were fabricated with lower strength 303 stainless steel bond plates threaded to

hardened A2 steel shanks with a 0.2% yield strength of 150 ksi. Both fixture types are pictured in Figure 3.

A removable pin assembly was included in the fixture design to insure centering of the test specimen and the two parts of the fixture (A and B) during bonding. A 3/16-inch diameter pin was machined to fit to a centering hole on part A of the test fixture. The centering hole was bored through the entire length of the shank to facilitate the removal of the pin after bonding. The test specimen, also with 3/16-inch diameter center hole, was then slipped over the alignment pin and bonded to part A. The centered hole on part B was next fitted over the pin and also bonded to the specimen. Once the adhesive was cured the pin could be driven out of the bored hole of part A to prevent interference of the pin during testing. Figure 5 illustrates the alignment assembly described above. During machining the fixture centering holes were indicated to within 0.002 of an inch. The maximum combined eccentricity resulting from the off-centering of both the laminate and fixture was determined to produce negligibile bending effects. The effects of the centering hole on the test results are more closely examined in section 4.0.

2.1.2 Specimen Machining

The 66 angle coupons received from Lockheed were first lightly sand blasted with medium grit aluminum oxide beads at 80-psi to remove peel-ply and mold release residues from the laminate surface [15]. To ascertain the effects of geometry the specimens were machined with 1.5-, 2.0-, and 2.5-inch diameters. The specimens were cut from the 3.0-inch legs of the angle sections using a diamond impregnated core drill. The use of the core drill required a 3/16-inch diameter hole to first be drilled as a centering guide. This hole was later used for the fixture alignment assembley mentioned in the prior section. The centering of all holes were indicated to within 0.001 of an inch. The 1.5-inch leg of each angle section and the scrap

pieces following machining were retained for use in ASTM D 2734 void content experiments and optical analyses. All specimen machining was done in the Engineering Science and Mechanics Department machine shop.

2.1.3 Specimen Bonding

Prior to tensile testing the machined specimens were desiccated in a vacuum oven at 100°F until an equilibrium weight was attained. The surfaces were then sanded with 400 grit emery cloth and wiped with a thinned adhesive solvent in preparation for bonding. The specimen dimensions were measured for use in the analysis of test data.

The bond surfaces of the test fixtures were grit blasted with alumimum oxide beads at 80-psi to produce a rough surface finish suitable for bonding. The fixtures were then vapor degreased in an isopropyl alcohol bath for 15 minutes. The alignment pin was coated with mold release and inserted into the center hole of fixture part A (Figure 5).

The specimens were bonded to the fixture using Hysol EA 9309 NA two-part adhesive. Five mil glass beads were added to the adhesive to insure a relatively uniform bond thickness. A glass bead quantity measuring 0.10% of the weight of the two-part adhesive was added to the resin and hardener prior to mixing. The adhesive was cured at room temperature for twelve hours then oven cured for one hour at 150° F.

2.1.4 Test Set-up

To select an appropriate system for the out-of-plane tension test program it was necessary to first estimate the maximum stresses and displacements that could occur while testing. As a

result of both a survey of transverse tensile strength data available in the literature [2] and preliminary analyses using classical laminated plate theory to determine displacements for a 20-kip out-of-plane loading, an ultimate stress of approximately 6500 psi with displacements less than 0.001-inches to failure were anticipated for a low porosity material system. Based on this information the experiments were performed on a load controlled Instron Series 2150 servohydraulic closed loop test system with 20.0 kip capacity. The data acquisiton system consisted of a Solatron 3530 data logger. A data translation board was used for data aquisition in conjunction with an IBM-AT and the software package MATPACO developed at Virginia Tech [17]. It was possible to achieve a data aquisition rate of approximately 2 data sweeps per second while plotting stress-displacement response on the CRT in real time. This plot was used to follow the progress of the test. Displacements were measured during the test using a 1.0-inch MTS extensometer and two crack-opening displacement gages. A Tripp Lite Line Stabilizer/Conditioner voltage regulator was used for suppression of isolated noise and surging of electronic power supplies. The test set-up is pictured in Figure 6.

2.1.5 Test Procedure

The three displacement gages were mounted at 120° intervals along the laminate circumference, as shown in Figure 7. The number and location of the gages were selected to provide accurate data necessary to determine any bending effects or nonuniform displacements occuring during testing. The specimens were tested in load control at a rate of approximately 13 kips per minute until failure. Load and displacement data were collected during the test and stored on computer. The raw test data was then post-processed using MATPACO. This information was then used in determining both the average interlaminar tensile strength and the combined elastic modulus, $\bar{E}_z$, of the adhesive and laminate.

2.2 Adhesive Tests

Tensile and torsional adhesion tests were performed on Hysol EA 9309 NA, the epoxy used to bond the flatwise tensile test specimens. The purpose of these experiments was to verify manufacturer supplied material properties, determine the effects of geometric constraints on those properties and to characterize the mechanical response of the adhesive under conditions similar to the test configuration. This information, in turn, was used for the anlaysis of the test specimen to make a more accurate assesment of the laminate response. Hysol EA 9309 NA is a two part paste adhesive that forms a flexible bond with high peel strength. The manufacturer's bulk resin properties were experimentally determined using 0.125-inch castings per ASTM D 638. Bulk resin testing tends to yield lower properties due to the absence of constraining effects present when two materials are bonded and, therefore, the properties obtained from these experiments were expected to yield much higher values.

Six adhesive experiments were performed on the Instron Series 2150 (Biaxial) servohydraulic test set-up with 20.0-kip tension/compression and 10 kip-inch torsional capacity. Four specimens were loaded in tension and two in torsion. The test specimens consisted of two 1.0-inch diameter, 3.0-inch long, A2 steel shafts hardened to an 0.2% offset yield strength of 150 ksi. The shaft ends were grit blasted with aluminum oxide shot at 80-psi to produce a good bond surface. The surfaces were vapor degreased in an isopropyl alcohol bath for 15 minutes and bonded with EA 9309 NA. A special test jig was used to maintain an 0.001-inch bond thicknes and shaft aligment. The bonded shafts were cured at room temperature for 12 hours then oven cured at 150° F. The bonded specimens were allowed to cool to room temperature prior to testing. Torsional angular twist was measured using the Instron's rotary stroke feedback. Care was taken to insure similar specimen preparation, bonding, test set-up and procedure for direct comparison of results.

2.3 Material Characterization Tests

It was necessary to obtain the in-plane and out-of-plane material properties of AS4/1806 and AS4/3501-6 quasi-isotropic laminates as input for the finite element analyses. The normal modulus, E_z, was determined from flatwise tensile test data. The in-plane properties, E_x, E_y, and ν_{xy} were obtained by in-plane compression testing. Twenty-one 1.0x1.5-inch specimens were cut from the ends of the angle sections, specimens numbered 14 in Figure 2. A diamond impregnated circular saw blade was used to machine the required specimen sizes. The edges of the specimens were milled to an 0.001-inch tolerance to insure a smooth surface finish and specimen alignment in the test fixture. A staff research associate employed by the Department of Engineering Science and Mechanics performed the experiments using a displacement controlled screw driven United Testing Systems 20.0 kip capacity tension/compression machine (Model FM-20-A-E). The cross-head motion of the test machine was controlled with an IBM-XT. The data aquisition system consisted of Measurement Group's Vishay 2100 system amplifier. A data translation board was used for data acquisition in conjunction with the IBM-XT and the software package MATPACO. It was possible to achieve a data acquisition rate of approximately three data sweeps per second. Displacements were monitored through the use of a single Texas Measurement type FRA-2-11 rossette located at the center of the specimen. The special compression fixture pictured in Figure 8 was used to support the specimen while testing. The specimens were loaded in compression to failure.

2.4 Porosity Determination

The porosities of the test laminates were determined by the optical analysis of twenty specimens, representative of the 66 laminates tested in out-of-plane tension. These tests were performed at Virginia Tech using a Zeiss image processing system and standard metallography techniques. The void content of each out-of-plane tensile specimen was concurrently determined by Lockheed Georgia Company using ASTM test method D 2734. The results of both methods were then compared and the data was used in the theoretical prediction of the out-of-plane tensile strength as a function of specimen porosity. In this section the void content data provided by Lockheed using ASTM D 2734 will be discussed. Later, section 5.0 will examine the porosities determined by optical analyses and the data from the two methods will be compared.

The specimen porosities were determined by Lockheed in accordance with the ASTM D 2734 standard test method for the void content of reinforced plastics. The densities of the composites were determined from their weights in air and water, while the density of the fibers and resin were supplied by the pre-preg manufacturer (Hercules, Inc.). The precision of the test method is dependent on the size and distribution of voids in the composite. It has been reported that small, evenly dispersed voids will give specimens in which the void content determinations will agree to within ± 0.1 % [18]. Large voids with nonuniform distribution may cause considerable variation and, in general, increased void contents call for increased specimen sizes. C-scan data of the angle sections, from which flatwise tensile test specimens were removed, indicate both a nonuniform distribution of pores and the existence of large voids. The resin and void contents of the specimens tested by Lockheed are listed in Tables 2-4. The resin content, fiber density, and resin density are also reported.

3.0 Experimental Results

3.1 Flatwise Tensile Test Results

Interlaminar tensile strength allowables for AS4/3501-6 and AS4/1806 specimens, having different porosity levels were determined by out-of- plane tension testing. In addition to obtaining strength, the tensile response data (σ_z vs. displacement) was used to determine the combined out-of-plane elastic modulus, $\bar{E}_z$, of the laminate for later use as input for finite element analyses. The effects of both specimen geometry and stacking sequence were also investigated. A total of 66 specimens were tested with 54 failures occurring through the laminate thickness, five through the adhesive and seven during gripping of the fixture. Gripping failures occured unintentionally when the Instron was transferred from stroke control to load control for tensile testing. The Instron servo controller has an inherent accuracy of $\pm$ 1 % of the indicated load range. That means load cell feedback smaller than $\pm$ 1 % of the indicated load range was not detected by the Instron signal conditioner, so the servo valve controller regulating actuator movement was allowed to drift until a control signal in excess of $\pm$ 1 % occured and then corrective action was taken. The inability of the Instron to correct actuator drift less than $\pm$ 1% often resulted in a compressive overloading of the test specimen

when transferring to load control prior to running a tension test. This random drift proved critical for many 1.5-inch diameter specimens. Specimen overloading during transfer was monitored on both a digital voltmeter and an external oscilloscope and recorded. No observed overload exceeded 5.0 $\pm$1.0% of the maximum load range. The compressive overloading resulted in damage to some of the specimens often indicated by audible cracking noises while gripping and very low strength to failure data.

Representative normal tensile response data is shown in Figure 9 for a 2-inch diameter AS4/3501-6 $(\pm 45/90_2/\mp 45/0_2)_S$ laminate with a defect level of 0. Three curves in Figure 9 are the displacements of the three gages mounted at 120° intervals around the specimen. Note the slight sinusoidal response of the two C.O.D. gages. This noise in the test data, attributed to the effects of actuator-drift, was detected by high sensitivity C.O.D. gages and can be observed in the data from several flatwise tension tests. In post-processing the data the $\pm$ 1% actuator noise not detected by the Instron electronics was smoothed using a cubic spline fit that minimizes a linear combination of the sum of the squares of the residuals of fit and the integral of the square of the second derivative [19]. The smoothed signal from each of the three displacement transducers was then averaged to obtain a characteristic normal stress versus displacement plot. This is the curve designated 'gages averaged' in Figure 9 and represents the displacement of the middle of the specimen. Also note the difference in displacements and the nonlinear response of the material near failure. Since the transducers monitor the combined displacements of both the laminate and the adhesive, it is necessary to examine the mechanical response of the adhesive to determine whether this apparent nonlinearity in displacements is the result of material nonlinearity, bending effects or a combination of the two. The flatwise tensile test data for all specimens are included in Appendix A. The average tensile response (σ_z versus z-displacement in the z-direction) for specimen groups of similar material, stacking sequence, defect level and geometry are included in Appendix B. The average response of 2.0-inch diameter AS4/3501-6 $(\pm 45/90_2/\mp 45/0_2)_S$ laminate group with defect level 0 is shown in Figure 10.

The strength allowables, combined elastic moduli and failure locations for all specimens tested are summarized in Tables 5-11. Specimens were categorized according to material, laminate, and geometry then further grouped by defect levels 0-3. There were either three or six specimens per defect level grouping. Tables 5-7 summarize the test results for AS4/3501-6 specimens with $(\pm 45/0_2/\mp 45/90_2)_S$ stacking sequence and 1.5-, 2.0- and 2.5-inch diameters. In Tables 8-10 AS4/3501-6 specimens with a $(\pm 45/90_2/\mp 45/0_2)_S$ stacking sequence are similarly presented. Table 11 summarizes the test results for AS4/1806 specimens with a stacking sequence of $(\pm 45/0_2/\mp 45/90_2)_S$. The flatwise tensile strength was obtained directly from the test data. The combined normal modulus, $\bar{E}_z$, which included the displacement of both laminate and adhesive was calculated from the initial slopes of the respective data using a least squares fit. The primary interest in the out-of-plane modulus was to provide material data necessary as input for finite element studies examining the laminate stresses during testing. An iterative finite element technique accounting for the influence of adhesive displacement and transverse effects on the out-of-plane laminate modulus was then used to determine the actual laminate properties. This is discussed in a later section. It is important to remember that the modulus reported in Tables 5 through 11 and discussed in the following sections is a combined modulus reflecting the load-displacement response of the laminate and adhesive.

3.1.1 Average Interlaminar Normal Strength

The effects of stacking sequence, specimen size, and porosity on the experimentally determined interlaminar normal strength are investigated in the three subsequent sections.

3.1.1.1 The Effects of Stacking Sequence

AS4/3501-6 angles were fabricated with either $(\pm 45/0_2/\mp 45/90_2)_S$ or $(\pm 45/90_2/\mp 45/0_2)_S$ quasi-isotropic stacking sequences. Because both laminates are quasi-isotropic stacking sequences, the in-plane tensile strengths should be the same. The out-of-plane tensile strength is primarily a function of the 1806 or 3501-6 matrix material and, therefore, also independent of stacking sequence. The angles were fabricated in lengths of 30 inches, with the 0° fibers oriented parallel to this length. The 90° fibers are oriented perpendicularly and extend the combined length of the angle web and flange, 3.0- and 1.5-inches, respectively. It was suspected that entrapped residuals (water, solvent, air) would bleed in a direction parallel to the fibers. The 0° plies bei ng directed along the largest angle dimension would, therefore, retain the highest number of voids. This void concentration could be most significant in the stacking sequence with four 0° at the laminate mid-plane and could possibly result in a decreased strength of $(\pm 45/90_2/\mp 45/0_2)_s$ specimens. To determine the effects of a quasi-isotropic stacking sequence on the normal strength, specimens having the same defect level and geometry were compared in Figures 11 and 12. The 2.0-inch diameter specimens machined from angle 2 had a stacking sequence of $(\pm 45/0_2/\mp 45/90_2)_S$ and 2.0-inch diameter specimens from angle 15 had a $(\pm 45/90_2/\mp 45/0_2)_S$ sequence. Both angles were categorized as defect level 1. The average strengths of specimens from either group, 3.822 and 3.571 ksi respectively, differ by no more than 7.0%. Defect level 3 specimens having the same material and geometry as above were removed from angles 18 and 20, with a stacking sequence of $(\pm 45/90_2/\mp 45/0_2)_S$, and angles 17 and 19 with a $(\pm 45/0_2/\mp 45/90_2)_S$ sequence. The average strength for these two groups, 1.977 and 1.711 ksi respectively, differed by 15.5%. Considering the nonuniformity of the void content throughout a single angle section, as indicated by both C-scan and porosity data, these percent differences are not considered to be significant. The experimental data indicates that the average normal strength does not differ for the two quasi-isotropic laminates investigated.

3.1.1.2 Effects of Specimen Geometry

Test specimens were machined in 1.5-, 2.0- and 2.5-inch diameter sizes to determine any effects related to specimen geometry. Because strength was found to be independent of the stacking sequences examined, 1.5-, 2.0- and 2.5-inch diameter AS4/3501-6 $(\pm 45/0_2/\mp 45/90_2)_S$ or $(\pm 45/90_2/\mp 45/0_2)_S$ specimens with the same defect level were compared.

Defect level 0, AS4/3501-6 speicmens with 1.5-, 2.0- and 2.5-inch diameters are compared in Figure 13. The specimen geometries and laminates are clearly designated in the figure's legend. The 2.5-inch diameter specimens have an average strength of 3.881 ksi with a standard deviation of 0.249 compared to an average strength of 4.078 ksi with a standard deviation of 0.443 for 2.0-inch diameter specimens. The average interlaminar normal strength for the two sizes differ by only 5.0%. The average normal strength for 1.5-inch diameter specimens is 3.434 ksi differing from the 2.0-inch diameter specimens by 13.0%. The comparisons show a decrease in average strength for 1.5-inch specimens. The standard deviation for the 1.5-inch diameter specimens is 0.872. There is an increase in the deviation of strength data as the specimen diameter decreases.

Defect level 1 specimens are compared in Figure 14. The average strength of 2.5-inch diameter $(\pm 45/90_2/\mp 45/0_2)_S$ and $(\pm 45/0_2/\mp 45/90_2)_S$ specimens are 3.663 and 4.030 ksi respectively. The corresponding standard deviations are 0.919 and 0.240. The 2.0-inch diameter specimen strengths are 3.822 and 3.571 ksi with standard deviations of 0.840 and 0.238 respectively. There is a maximum difference of 12.8% in average normal strength for the specimens from these two geometry groups. The single normal strength of 2.705 ksi for the $(\pm 45/90_2/\mp 45/0_2)_S$ 1.5-inch specimen differs from the 2.0-inch diameter specimens by as much as 41.3%. There is no apparent trend in the standard deviations of average strength. For both defect level 0 and 1 specimens, the normal strength of the smallest diameter speci-

mens are low, but it seems to increase as the specimen diameter increases and levels-off after a specimen diameter of 2.0-inches.

The effects of specimen size on the strength of defect level 2 AS4/3501-6 specimens are examined in Figure 15. The average strength of 2.5-inch defect level 2 $(\pm 45/0_2/\mp 45/90_2)_S$ specimens is 2.889 ksi with a standard deviation of 0.352. The average strength of the 2.0-inch $(\pm 45/90_2/\mp 45/0_2)_S$ specimens is 2.030 ksi with a standard deviation of 0.338. The 1.5-inch diameter specimens with a $(\pm 45/0_2/\mp 45/90_2)_S$ stacking sequence have an average strength of 1.034 ksi and a standard deviation of 0.199. The average strength of the 2.5-inch diameter specimens differs from the 2.0-inch specimens by 29.7% and the average strength of the 1.5-inch diameter specimens differ from the 2.0-inch specimens by 96.3%. The data shows a substantial decrease in strength with decreasing specimen diameter. The standard deviations do not tend to increase with decreasing specimen geometry.

The comparison of average normal strength data for specimens of the same material, defect level and either quasi-isotropic stacking sequence discloses a dependence of strength on specimen geometry. For defect levels 0 and 1 there is a significant reduction in strength for specimen diameters smaller than 2.0-inches. At defect level 2 there is a reduction in strength for specimen diameters below 2.5-inches. The dependence of strength on specimen diameter is thought to be related to the size and distribution of voids in the laminate. The size of the test specimen will be a function of the size and distribution of voids in the part from which the specimen is removed. A lamainate with large, nonuniformly distributed voids, will require a large specimen size to accurately represent the distribution of voids in the laminate. The change in strength as a function of specimen diameter occured when the specimen size became too small to accurately represent the void distribution in the test part.

3.1.1.3 Effects of Porosity

As mentioned earlier, angle sections were manufactured using four processing techniques in an attempt to introduce varying porosity levels. The void contents of the test specimens using ASTM test method D 2734 are used in this section. The test values have been reported in Tables 2-4. The AS4/3501-6 test results indicate the void content of defect level 0, baseline laminates, to range between 1.50 and 2.85 percent by volume independent of laminate. Solvent wiping of plies during lay-up (defect level 1) resulted in void contents ranging between 1.52 and 2.78%. The addition of moisture to plies for defect level 2 specimens resulted in void contents of 2.89 to 5.88%. Defect level 3 specimens utilizing a low pressure cure to create voids ranged between 2.82 and 6.77%. AS4/1806 defect level 0 specimens varied between 0.85 and 2.31%, defect level 2 specimens varied between 0.84 and 1.89%.

Strength as a function of porosity for all specimens tested is plotted in Figures 16 through 18. A linear regression is used to fit the data. The strength data for AS4/3501-6 $(\pm 45/0_2/\mp 45/90_2)_S$ specimens in Figure 16 clearly shows a decrease in strength with increasing porosity. The decrease in the strength of 1.5-inch diameter specimens is much more significant in comparison to the 2.0- and 2.5-inch diameter specimens because of the dependence of specimen size on pore distribution, as discussed in the prior section. Much of the scatter in the experimentally determined normal strengths for specimens of similar porosity can be attributed to the dependence of the void content test method on the size and distribution of voids in the composite. The nonuniform distribution of voids throughout each angle was verified by C-scan data. The data for AS4/3501-6 $(\pm 45/90_2/\mp 45/0_2)_S$ specimens in Figure 17 shows a similar trend. Note that there were only two flatwise tensile tests for 2.5-inch diameter specimens in this category and one successful test of a 1.5-inch diameter specimen. These tests are plotted in Figure 17 as data points only. The linear regression is used to fit the 2.0-inch specimens only.

The strength of AS4/1806 ($\pm 45/0_2/\mp 45/90_2)_S$ specimens as a function of porosity are plotted in Figure 18. The data in Figure 18 has an excessive amount of scatter and, therefore, no attempt was made to relate the strength to the specimen void content. The data scatter could be the result of erroneous void content values from ASTM D 2734 tests. The averaged void contents of defect level 0 specimens was 1.542% compared to 1.262% for defect level 2 specimens. Because of the addition of water to the composite during lay-up, defect level 2 specimens were expected to have a higher average void content than the baseline defect level 0 specimens. The average strength of defect level 0 specimens from Table 11 was 4445 psi compared to an average strength of 3090 psi for defect level 2 specimens and was thought to be related to an increase in the porosity of the defect level 2 test specimens. C-scan data shows a lower percent transmission of defect level 2 angles (angles 3 and 16, Table 1) compared to defect level 0 angles indicating defect level 2 should have a higher void content. The void contents determined for AS4/1806 defect level 2 specimens by ASTM D 2734 may be in error and therefore the effects of porosity on the strength were not determined. The source of scatter in the strength data will later be reviewed in the optical investigation of the AS4/1806 specimens.

3.1.2 Combined Out-of-Plane Modulus

The effects of stacking sequence, specimen size, and porosity on the experimentally determined combined modulus are investigated in the the three subsequent sections. The displacement transducers mounted to the test fixture measured the combined displacements of the adhesive and laminate during out-of-plane testing. The combined out-of-plane modulus, calculated from the slope of the load-displacement data, is designated as $\bar{\bar{E}}_z$

3.1.2.1 Effects of Stacking Sequence

To determine the effects of stacking sequence on the combined normal modulus, specimens having the same material, defect level, and geometry were compared in Figures 19 and 20. The 2.0-inch diameter AS4/3501-6 specimens in Figure 19, with a stacking sequence of $(\pm 45/0_2/\mp 45/90_2)_S$ and a defect level of 1, had an average modulus of 3.526 million psi compared to $(\pm 45/90_2/\mp 45/0_2)_S$ specimens with an average modulus of 3.998 million psi. The average moduli for the two quasi-isotropic 2.0-inch specimens in Figure 20 differ by 11.8%. A comparison of the 2.5-inch diameter specimens shows the $(\pm 45/0_2/\mp 45/90_2)_S$ specimens, with an average modulus of 3.156 million psi, to differ from the $(\pm 45/90_2/\mp 45/0_2)_S$ specimens, with an average modulus of 3.902 million psi, by 23.6%. Figure 20 compares 2.0-inch diameter AS4/3501-6 $(\pm 45/90_2/\mp 45/0_2)_S$ and $(\pm 45/0_2/\mp 45/90_2)_S$ laminates with a defect level of 3. The average moduli for the two specimens are 3.124 and 2.785 million psi respectively differ by 10.8% The moduli of the $(\pm 45/0_2/\mp 45/90_2)_S$ specimens appear to be consistently lower than the $(\pm 45/90_2/\mp 45/0_2)_S$ specimens. However, at this point, the dependency of the modulus on stacking sequence cannot be conclusively determined.

3.1.2.2 Effects of Specimen Geometry

As mentioned in section 3.1.1.2 the test specimens were machined in 1.5-, 2.0- and 2.5-inch diameter sizes to determine any effects related to specimen geometry. The effects of specimen diameter on the combined normal modulus of AS4/3501-6 specimens with the same defect level and stacking sequence are presented in Figures 21, 22 and 23. The average modulus of the 2.5-inch diameter defect level 0 specimens is 3.705 million psi compared to an average modulus of 3.180 million psi for the 1.5-inch diameter specimens. The average normal modulus of the 1.5-inch diameter specimens is 16.5% lower.

Defect level 1 AS4/3501-6 $(\pm 45/90_2/\mp 45/0_2)_S$ specimens are compared in Figure 22. The average modulus of 2.5-inch specimens is 3.902 million psi and the average modulus of the 2.0-inch diameter specimens is 3.998. The two moduli differ by only 2.5%. The average modulus from the single test of a 1.5-inch diameter $(\pm 45/90_2/\mp 45/0_2)_S$ specimen with a defect level of 1 is 2.325 million psi, 67.8% lower than the average modulus of the 2.0-inch specimens.

Defect level 2, AS4/3501-6 specimens with a stacking sequence of $(\pm 45/0_2/\mp 45/90_2)_S$ are shown in Figure 23. The average modulus for the 2.5-inch diameter specimens is 3.453 million psi while the average modulus for the 1.5-inch diameter specimens is 3.007 million psi. The moduli differ by 14.8%.

Similar to the normal strength data, the investigation of test data has shown the experimentally determined normal modulus to be affected by specimen geometry. In section 3.1.1.2, examining the effects of specimen geometry on normal strength, there is a reduction in strength for specimen diameters smaller than 2.0-inches and a reduction of strength in defect level 2 specimens with diameters below 2.5-inches. This trend is also present with the experimentally determined moduli for defect level 1 specimens. There is a substantial drop in modulus for specimens with diameters smaller than 2-inches.

3.1.2.3 Effects of Porosity

The scatter in the experimentally determined combined modulus, $\bar{E}_z$, could be the result of specimen porosity. The out-of-plane stiffness as a function of specimen porosity is plotted in Figures 24 through 26 for specimens of the same material and defect level. A linear regression is used to fit the data points in these plots. As with the effects of porosity on strength, there is a decrease in stiffness with increasing porosity for AS4/3501-6 laminates. There is

still a significant amount of scatter but this again could be attributed to the nonuniform distribution of voids in specimens from the same angle. The effects porosity on AS4/1806 laminates could not be determined because of the large amount of scatter in the test data.

3.2 Adhesive Test Results

Simple tension and torsion tests were performed on bonded A2 steel shafts to verify manufacturer supplied material properties and to characterize the mechanical response of the adhesive under conditions similar to the out-of-plane tension test configuration. As mentioned earlier, the tensile moduli determined from these tests were expected to be much higher than the values provided by Dexter Hysol due to the constraining effects of the bonded steel on the adhesive. The tensile and shear moduli determined from bulk resin tests were 345 ksi and 130 ksi respectively with a tensile strength of 5600 psi. The tensile modulus was calculated graphically by using a least squares fit through the experimental data. A typical stress-displacement curve used in the calculations is shown in Figure 27. The average slopes of the respective stress-displacement curves were used in calculating the modulus. Since the displacement transducers mounted on the bonded steel shanks measured the combined deformation of both the adhesive and steel, a two spring stiffness model was used to more accurately determine the stiffness of the adhesive. The steel and adhesive are modeled as three springs in series. The central spring representing the adhesive and the two outer springs attached to either end of the central spring, the steel shanks. The stiffness matrix is assembled knowing the cross-sectional area and length of each spring element and the stiffness of the steel. There is a known force applied to the model, determined from experimental data, and a known combined displacement. The system of equations is then solved to determine the unknown modulus of the adhesive. The resulting tensile modulus for EA 9309 NA was determined to be 604 ksi. The average tensile strength at failure, 5557 psi, was taken

directly from the tensile response data. The remaining test data are included in Appendix C. An average shear modulus of 68 ksi was similarly calculated from the torsion-twist data in Appendix C. The low shear modulus determined from these experiments was expected to be the result of using a solid circular shaft in torsion instead of the ASTM E 229 recommended hollow shaft with a more uniform shear stress distribution.

In addition to property verification, the adhesive tests provided valuable information into the mechanical response of the adhesive under conditions similar to the flatwise tensile test configuration. Since the transducers monitored the combined displacements of both the laminate and the adhesive during the out-of-plane tension tests, it was uncertain as to whether the difference in displacements was due to bending effects related to the misalignment of the Instron crosshead (with alignment accurate to $\pm$ 0.002 inches) or localized plastic flow of the adhesive at different regions within the bond. If bending due to misalignment was occurring then the gages should measure differing displacements from the start of the test. The typical mechanical response data in Figure 27 shows the adhesive to behave linear elastically to approximately 3000 psi after which the load-deflection response becomes nonlinear. By combining the tensile response data of the adhesive with the finite element adjusted out-of-plane laminate modulus (discussed in section 4.3.3), the stress- deflection data determined from out-of-plane tensile testing can be can be reproduced. The out-of-plane tensile response of a 2.0-inch diameter AS4/3501-6 $(\pm 45/90_2/\mp 45/0_2)_2$ specimen with a defect level of 0 is plotted in Figure 28 using the above method and the experimental data from specimen 7-5. The difference in slopes is related to the different values of $\bar{E}_z$ for the two methods. More importantly, the characteristic response of these two curves is the same. This shows the nonlinearity near failure, observed in the flatwise tensile test data, to be the effect of adhesive material response. The laminate response remains linear and the difference of displacements is the result of the adhesive.

3.3 Material Characterization Test Results

The objective of the material characterization testing was to determine the in-plane properties of AS4/1806 and AS4/3501-6 quasi-isotropic laminates as a function of porosity. The in-plane modulus E_x, and Poisson's ratio ν_{xy}, were determined from the compression testing of the 21 specimens summarized in Table 12. Three specimens from each defect level were tested for both material systems. The only category of specimens not included in the compression test program were AS4/3501-6 $(\pm 45/90_2/\mp 45/0_2)_S$ laminates with defect level 1. The in-plane E_x modulus and Poisson's ratio, ν_{xy}, for the three $(\pm 45/0_2/\mp 45/90_2)_S$ defect level 1 laminates not tested should be the same as the $(\pm 45/90_2/\mp 45/0_2)_S$ laminates tested according to classical lamination theory, provided that the void contents are the same. The modulus and Poisson's ratio listed in Table 12 were calculated graphically by using a least squares fit through the experimental data. Typical stress-strain and strain-strain data plots are shown in Figures 29 and 30. The principal slopes of the respective curves were used in calculating the Young's Modulus E_x and Poisson's ratio ν_{xy}. The vertical lines seen in the stress strain diagrams are due to an erroneous strain limit setting of 1.0%. No strain data was collected beyond that value. This, however did not affect the data necessary to determine modulus and Poisson's ratio.

The average in-plane modulus versus defect level is plotted in Figure 31 for AS4/1806 and AS4/3501-6 specimens having the same stacking sequence and defect level. The two quasi-isotropic stacking sequences are designated by separate plot symbols though in theory the in-plane extensional modulus should be the same for either laminate. A linear regression is used to fit a plot line through the test data. This fit shows the modulus of the AS4/3501-6 material to remain constant for increasing defect level. The linear fit to the AS4/1806 data shows a decrease in slope by a mere 8.3%. It has been shown in an experimental study of AS4/3502 [20] that porosity primarily effects matrix dominated properties while having little

effect on fiber dominated properties such as E_x. In the case of two different quasi-isotropic laminates, one would not expect, therefore, a significant change of in-plane properties for increasing porosity. Figure 32 is a plot of Poisson's ratio, ν_{xy}, versus defect level. Again the linear fit to the data shows little effect of porosity on Poisson's ratio. Because the experimentally determined in-plane material properties, E_x and ν_{xy}, for AS4/3501-6 and AS4/1806 show little dependence on void content, the data is averaged independent of defect level for use as laminate input properties in the finite element analyses.

4.0 Finite Element Analysis

To apply a uniformly distributed out-of-plane tensile loading across a flat laminated plate the test specimens would be bonded to a specially designed test fixture. A linear three-dimensional finite element analysis was used to aide in the design of this fixture and to examine the stress field applied to the laminate. The analysis was accomplished by using EISI-EAL System Level 2091, a high-order finite element language developed by Engineering Informations Systems, Incorporated. Particular interest was given to the influence of the fixture on the deformations transverse to the applied load direction, due to the Poisson's effect occurring at the bond interface of two dissimilar materials, and the effects of introducing a center hole in the laminate for alignment purposes. The finite element analysis was also used to modify the combined out-of-plane modulus obtained from experiment to account for the effects of adhesive deformation and specimen geometry on the measured displacements.

4.1 Finite Element Mesh

The finite element analysis was to be used in the design of the test fixture and to understand the stresses applied to the specimen during testing as a function of both the fixture and specimen geometry. Through-the-thickness stresses and strains were not intended to be studied and, therefore, the sixteen ply laminates were modeled as an orthotropic material with a single layer of elements. The in-plane laminate material properties were obtained directly from the compression test experiments (Table 12). The out-of-plane properties used in the preliminary fixture design were obtained by assuming transverse isotropy and using the transverse properties of AS4/3501-6 and AS4/1806 available in the literature. In later analyses the out-of-plane properties were determined from the flatwise tensile test data (Tables 5-11). By modeling the laminate using smeared properties it was possible to take advantage of circular symmetry and model the bonded fixture using a 24° axisymmetric wedge. In addition, through the thickness mid-plane symmetry was also used to model the upper half of the fixture set-up. The finite element code utilized eight node hexahedral and six node pentahedral elements. A course mesh of 41, 43, and 46 elements was used to model 1.5-, 2.0-, 2.5-inch specimen configurations, respectively. The finite element mesh used for 2.5-inch configuration is illustrated in Figure 33. The 2.0-inch configuration is modeled by the removal of the outermost laminate element along edge FG. Similarly, the 1.5-inch configuration is modeled by eliminating the two outermost elements along edge FG.

4.2 Boundary Conditions

The loading of the specimen is specified as a constant displacement of the nodes along the edge AB in the y-direction. By symmetry considerations, all the nodes along FG, the laminate

mid-plane, are constrained from displacement in the y-direction. Also by axisymmetry, all nodes on the ABCDEFG face are assigned to have zero displacements in the circumferential (z) direction. Nodes along the edge AB, where the fixture is gripped by the Instron, are constrained from displacing in the x-direction. To gain a general understanding into the effects of including a center hole in the laminate the nodes along edge AG were constrained from displacement in the x-direction. The constraint of these elements would simulate the boundary conditions present for a specimen and fixture with no center hole. The joints along edge AG in Figure 33 would then be modeled using rollers, similar to edge FG.

4.3 Results

Finite element runs were made individually for specimens of the same material, geometry, defect level, and stacking sequence.

4.3.1 Test Fixture

Several combinations of materials and geometry were examined in the design of the fixture for use in the out-of-plane tension testing. The primary criterion was to apply a uniform stress field to the laminate while testing. This would require the selection of a material and geometry that would minimize the bending effects in the x-z plane, edge FG in Figure 33. An additional constraint on the design was the selection of a material with good bonding characteristics. Based on the finite element analyses of different fixture configurations, a tapered conical cross section using hardened stainless steel was selected. The fixture is pictured in Figure 3. In the

preliminary design of the fixture, laminate properties were obtained by assuming transverse isotropy and using AS4/3501-6 and AS4/1806 data available in the literature. Once the data was available from the compression and the out-of-plane tension tests, the finite element analyses were re-run using these experimentally determined properties. The tensile stresses in the steel fixture are plotted in Figure 34, as a function of the radial distance from the center, for 2.5-, 2.0- and 1.5-inch diameter defect level 0 specimens. As mentioned previously, 0.0005 inch uniform displacements are applied for each run. The tensile stresses in the fixture varied from 1263 psi at the outer edge to 2327 psi at the fixture center hole for the 2.5-inch diameter specimen. The 2.0-inch specimens stresses varied from 1301 psi to 2707 psi at the same locations. The stress field across the 1.5-inch specimens ranged from 1442 psi to 3035 psi.

4.3.2 Modification of Out-of-Plane Tension Data

An iterative finite element method was used to modify experimentally determined out-of-plane stiffness to obtain more accurate properties for later use as input in finite element runs examining the stresses on the laminate during testing. The displacements monitored during the out-of-plane tensile tests included the combined deformations of both the laminate and the adhesive. As a result of bonding the laminate to the test fixture a restraint is imposed on the transverse deformation of the laminate and shear stresses are introduced to the laminate due to the Poisson mismatch of the two materials. The transverse effects are further complicated by the influence of the specimen geometry. The iterative finite element approach uses the known values of the material properties for the fixture, adhesive, and the in-plane specimen properties obtained from the compression test program. A guess value of the through-the-thickness elastic modulus of the specimen material is used. A finite element analysis of this test configuration is then performed. The slope of the numerically determined load-deflection curve is determined from the finite element data, at the joints where the displacement gages

would be mounted on the fixture, and compared to the input value of the through-the-thickness modulus. The ratio of the finite element determined combined modulus to the input modulus reflects the increase in the numerically determined modulus resulting from the combined influence of adhesive effects, transverse restraint, and specimen geometry. The ratio is then used to factor the experimental data to obtain a more accurate value of the out-of-plane modulus. Since the numerically calculated value of the slope is a non-linear function of the material property itself this procedure had to be repeated until factor convergence was achieved. The factors determined from this iterative study and the modified test data are listed in Tables 13-15 and compared to the combined out-of-plane experimental modulus. Comparison of the combined out-of-plane moduli with the laminate moduli found by this method shows the experimental values to be greater. The restraint imposed on the transverse laminate displacement, at the bond interface, would inhibit out-of-plane laminate deformations and result in a combined stress-state. This would cause the experimentally determined combined modulus to be greater than the laminate modulus. The modified out-of-plane data was then used as material property input for the investigation into the effects of the center hole and the determination of stresses during flatwise tensile testing.

4.3.3 Effects of Laminate Center Hole

To determine the effects of a center hole in the flatwise tensile test specimens, the 24° wedge was modeled with the nodes along edge AG fixed from displacements in the x-direction. This constraint imposed on the model would simulate the symmetry condition present in a specimen with no center hole. The stresses in the laminate as a function of radial distance from the specimen center are plotted in Figures 35 and 36 for AS4/3501-6 ($\pm 45/90_2/\mp 45/0_2)_S$ defect level 0 specimens. A comparison of finite element results for the two models show the inclusion of the center hole to result in slightly higher tensile stresses at the hole boundary.

The tensile stress at the center of the 2.5-inch diameter specimen with no hole is 1872 psi compared to a stress of 2078 psi at the laminate mid-plane along the holes edge. The 2.0-inch diameter specimen with center hole has a mid-plane laminate tensile stress of 2584 psi at the hole's edge compared to 2562 psi for the 2.0-inch specimen with no center hole. The tensile stresses arising at the specimen center for a 1.5-inch diameter laminate with no hole is 3052 psi compared to the 3120 psi at the node bordering the center hole of the same specimen. The maximum difference between stresses at the laminate center of a solid circular specimen and the inside radius of a specimen with a hole was 9.9%, occuring in the 2.5-inch diameter laminates. The finite element analyses indicate that the use of a center hole would not significantly affect the tensile stress distribution across the laminate.

4.3.4 Tensile Stresses on Laminate

To determine the tensile loading on the laminate during out-of-plane tensile testing, linear finite element analyses were run using the numerically modified out-of-plane laminate properties, the experimentally determined in-plane properties, and manufacturer supplied resin properties. Analyses were conducted on specimen configurations of the same material, stacking sequence, geometry, and defect level. Tables 16 through 18 summarize the laminate stresses obtained from those analyses using a uniform displacement field of 0.0005-inches. The tensile stresses on the laminate increased as the radial distance approached the specimen's outer edge. The maximum and minimum tensile stresses, occurring at the outside and inside diameters, respectively, differed from the averaged uniform tensile stress field on the laminate by as much as 4%. A maximum difference of 4% was not considered a significant deviation from an assumed uniform out-of-plane tensile stress distribution.

5.0 Optical Analysis

The pore size, shape, and orientation were characterized using standard optical metallography techniques. These measurements were necessary to provide input for strength/porosity prediction modeling. Prior to machining the circular specimens for tensile testing the edges parallel with the 90° fiber direction of all angle sections were microscopically examined to determine the size and distribution of voids in the laminate. The angles were examined at a magnification of 16X using a Neophot 21 large incident-light camera microscope. Based on these preliminary examinations a total of twenty samples, representative of the pore size and distribution of each defect level, were selected for a more detailed optical investigation. The specimens were removed in approximately 1.00-inch lengths from one edge parallel with the 90° fiber axis following machining of circular test specimens. The samples were bonded between graphite/vinyl-ester mounting blocks and subjected to rough polishing using dry silicon carbide, beginning with 240 grit and gradually advancing down to 600 grit. The samples were then subjected to fine polishing beginning with 5 μ alumina powder and advancing down to 0.05 μ. The optical specimens were then washed in an Ultramet II Sonic Cleaner for 5 minutes and dessicated in a vaccum oven at 100° F. The specimen identification numbers of the optical analysis samples are summarzied in Tables 19-21.

The pore characterization studies were conducted using a Zeiss IBAS/SEM-IPS image processing system equipped with a Zeiss ICM 405 inverted camera microscope, Figure 37. The microscopic image is digitized to a 10 bit (1024) gray level resolution, and subsequently reduced to an 8 bit (256) gray level resolution, and displayed as a standard gray level image. All subsequent image enhancement and processing steps are performed on the 256 gray level image. Objects of interest (those to be measured or counted) are separated from the background of the image. The segmenting or discriminating is achieved by a gray level thresholding step in which pixels with grey values within a range determined by the operator have their gray values converted to a binary 1. All other pixels in the image are converted to binary 0. The resulting binary image is now a black-and-white picture of the objects of interest. This binary image is used to make measurements of either field- or object-specific type. Object-specific parameters refer to measurements related to a single objects in a field, such as voids. The image processor enabled automatic scanning, storage, and statistical evaluation of multiple binary image frames. The binary frame of one image processing step, displayed on a high resolution RGB monitor, is pictured in Figure 38.

The image processor was programmed to scan and evaluate data from six adjacent frames for a single optical specimen. At a magnification of 5X each frame measured an average of 2450x1800 μ (0.096x0.07 inches). Data from as many as 500 voids per specimen was collected and evaluated. The object- specific parameters of interest included the maximum and minimum pore diameter, the orientation of the pore with respect to the laminate out-of-plane axis, the pore perimeter, the diameter of the area equivalent circle, elliptical shape factor, and feret. Statistical histogram data from the six frame scan of each specimen provided the minimum, maximum, mean, standard deviation, and median class of each object-specific parameter. This data was used in combination with photomicrographs to provide the data necessary for strength/porosity modeling. The only field-specific parameter of interest was the void content computed as a percent area of the combined six frame scan.

Virtually all images contain irregularities in gray values due to a variety of sources. In some cases these irregularities present themselves as spots or regions of shadowing which interfere with proper image segmentation. Irregularities related to surface polishing, such as the scratches on the specimen surface shown in Figure 39, can be filtered using image processing techniques available on the IPS system. Grains of silica carbide or alumina powder are often forced into soft epoxy matrix material creating tiny black spots resembling pores. In addition large grains are often lodged in the laminate and carried to the next stage of polishing where they are loosened and scratch the laminate surface. Shade correction filters were used to eliminate surface irregularities possibly related to polishing. This enabled proper image segmentation of voids outside the filter range but may have eliminated many smaller voids.

5.1 Average Pore Size

The pore characterization studies of $(\pm 45/90_2/\mp 45/0_2)_S$ and $(\pm 45/0_2/\mp 45/90_2)_S$ AS4/3501-6 laminates and the AS4/1806 $(\pm 45/0_2/\mp 45/90_2)_S$ laminates were conducted using a combination of photomicrographs and image-analysis data. The photomicrographs reveal the average pore geometry to be cylindrical. The pores are generally oriented with the cylinder lengths parallel to the fiber direction. The 0° fiber orientation is always perpendicular to the plane of the photomicrograph. In Figure 40 the 90° plies located at the center of the AS4/3501-6 $(\pm 45/0_2/\mp 45/90_2)_S$ defect level 2 laminate clearly show the cylindrical length parallel to the fiber and the circular diameters in the 0° layers. The average pore diameter and length were determined from the maximum and minimum pore diameter IBS parameters obtained from image analysis histogram data. The average histogram parameters determined from the optical specimens examined are listed in Tables 19-21. The average cylinder length was obtained from the maximum diameter measurements of pores in the 90° layers only. The cylinder diameters were determined from the minimum diameter measurements. The cylin-

drical pores occurring in the AS4/3501-6 ($\pm 45/90_2/\mp 45/0_2)_S$ specimens had an average length of 456.1μ and an average diameter of 24.56μ with an average pore orientation of 60.8° with respect to the out- of-plane load axis. The pores in the AS4/3501-6 ($\pm 45/0_2/\mp 45/90_2)_S$ specimens had an average length of 538.0μ and an average diameter of 24.38μ oriented at 56.23°. The AS4/1806 specimen pores had an average length measuring 402.4μ with a diameter of 18.98μ orientated at 57.8° with respect to the load axis.

5.2 Pore Distribution

The percent area of voids was determined by the automated segmenting of pores and computation of the cumulative pore area over an adjacent six frame scan. The percent areas are summarized in Table 19-21. It was noted earlier that gray level filtering omitted many of the smaller objects shown in these photomicrographs. The void contents determined by optical analysis were therefore lower than those determined by ASTM test method D 2734 for defect levels 0 and 1. As the void content increased the size and number of larger pores increased. This resulted in better correlation of void contents for the two methods used with defect level 2 and 3 specimens. Comparison of the void contents determined by these two methods, for specimens from the same angle and location, show the AS4/3501-6 defect level 0 and 1 specimen void contents to differ by 43-90% while defect level 2 and 3 specimens differ by 3-54%. Only four AS4/1806 specimens (2 defect level 0 and 2 defect level 2) were used for the optical investigation. The void contents of the two defect level 0 specimens used in the two test methods differed by 59 and 83%. The defect level 2 specimens differed by 21 and 50%. Much of this difference in test method results could be related to the nonuniform distribution of pores in the angle section and the presence of large voids or delaminations not common to the two specimens. The photomicrographs taken of the specimens at a magnification of 5X are shown in Appendix D. The specimen photomicrographs show the general increase in

the size and number of voids with increasing defect level. There does not appear to be a significant increase in porosity for the AS4/1806 specimens from the two defect levels. This may indicate that the ASTM method D 2734 void content data, discussed in section 3.1.1.3, is correct and the scatter in strength data may be related to the presence of large voids or delaminations in the specimens. The occurrence of delaminations would explain the low percent transmission of the defect level 2 C-scans compared to defect level 0 and yet the similar void contents determined ASTM D 2734 for the same defect levels. A comparison of the photomicrographs for AS4/3501-6 specimens shows the $(\pm 45/90_2/\mp 45/0_2)_S$ laminates to contain a greater number of large voids concentrated in the 0° plies. The $(\pm 45/0_2/\mp 45/90_2)_S$ laminates have a more general distribution of large voids . This information would not be reflected in the image-analysis data.

6.0 Strength Prediction Model

The strength of a ceramic material as a function of porosity was empirically determined by Ryshkewitch and Duckworth to be

$$\sigma = \sigma_{max} e^{-bP} \tag{1}$$

where σ_{max} is the strength at zero porosity, b is an empirical constant and P is the volume fraction of open-cell porosity [4,5]. Eleven years later, S.D. Brown related the empirical constant b to pore size, geometry, and orientation to calculate theoretical strength as a function of porosity [13]. To retrace the derivation of the equation of Brown et al, define A_{solid} as the total effective solid area that lies in a plane normal to the stress in a tensile specimen of total porosity P, Figure 41. Thus, A_{Solid} is equal to A_{total} minus the sum of the projected maximum cross-sectional areas of all pores intersected by the fracture surface onto a plane normal to the applied stress. A_{total} is defined as the cross-sectional area of the specimen normal to the applied stress. The approximate strength can now be given as

$$\sigma = \sigma_{max}(A_{Solid}/A_{total}). \tag{2}$$

The next step makes an allowance for the multiple existence of i kinds of pores in a single specimen. Assuming these pores are uniformly distributed throughout the specimen,

$$A_{Solid}/A_{total} = 1 - \Sigma_i(A_i/A_{total}) \tag{3}$$

and

$$\sigma = \sigma_{max}[1 - \Sigma_i(A_i/A_{total})] \tag{4}$$

where A_i is the total effective void area due to porosity of kind i in the plane normal to the applied tensile stress. A_i can be written in terms of the volume of a single pore of the *ith* kind, v_i, and N_i the number of pores of the *ith* kind intersected by the plane in which A_i lies, by the simple relation

$$A_i = a_i N_i \tag{5}$$

where a_i is the projected maximum cross-sectional of an intersected pore of the *ith* kind by the plane normal to the applied stress. The number of pores of the *ith* kind within the total volume is given by

$$Z_i = P_i V_{total}/v_i \tag{6}$$

where P_i is the contribution made by the pores of the *ith* kind to the total porosity. By using a dimensionless constant γ_i whose value depends on pore geometry and orientation, and can be used to relate projected pore area to pore volume, equation (5) can be written as

$$A_i = \gamma_i v_i^{2/3} N_i \tag{7}$$

where $\gamma_i = a_i/v_i^{2/3}$, N_i may then be related to Z_i for a straight specimen of constant cross section normal to the applied stress as follows:

$$N_i = (\beta_i v_i^{1/3} A_{total}/V_{total})Z_i \tag{8}$$

where $\beta_i = x_i/v_i^{1/3}$ is a dimensionless constant whose value depends on pore geometry and orientation. The variable, x_i , is a characteristic length of the *ith* pores and is always parallel to the applied tensile stress. By combining equations (6), (7), and (8)

$$A_i/A_{total} = \beta_i \gamma_i P_i \tag{9}$$

and equation (4) becomes

$$\sigma = \sigma_{max}[1 - \Sigma_i(\alpha_i P_i)] \tag{10}$$

where $\alpha_i = \beta_i \gamma_i$ of equatin (9). From the definitions of α_i, β_i, and γ_i

$$\alpha_i = x_i a_i/v_i \tag{11}$$

so that equation (10) becomes

$$\sigma = \sigma_{max}[1 - \Sigma_i\{(x_i a_i/v_i)P_i\}] \tag{12}$$

σ_{max} is the strength at zero porosity obtained when the σ vs. P curve is extrapolated to $P = 0$. $x_i a_i$ and v_i are determined from the microscopic study of specimen pores. The *ith* kinds

of pores were assumed to be uniformly distributed through out the specimen so that any nonuniformity in pore distribution will result in deviations of equation (12).

By writing either equation (10) or equation (12) in logarithmic form and expanding the part corresponding to ln $(1 - \Sigma_i \alpha_i P_i)$ as an infinite series, a first order approximation of equation (1) can be derived. At small values of total porosity $\Sigma_i \alpha_i P_i$ is sufficiently small so that

$$\ln(\sigma/\sigma_{max}) = -\Sigma_i \alpha_i P_i \tag{13}$$

or

$$\sigma = \sigma_{max} e^{-\Sigma_i \alpha_i P_i} \tag{14}$$

The constant b in equation (1) can be related to α_i in equation (14) by the relation

$$b = \Sigma_i \frac{\alpha_i P_i}{P} \tag{15}$$

To account for the random orientation of pores in a specimen the average pore orientation $\bar{\alpha}_i$ may be computed as follows:

$$\bar{\alpha}_i = \frac{\int_{\theta_1}^{\theta_2} \alpha_i d\theta}{\int_{\theta_1}^{\theta_2} d\theta} \tag{16}$$

The micrographic and optical investigations have shown the average pore shape to be close to that of a cylinder oriented between 60° and 90° with respect to the transverse load axis. The b constant for a pore of this shape was calculated using equation (14) to be

$$b = \Sigma_i \bar{\alpha}_i = 0.304L/d + 0.239d/L + 1.2496 \quad (17)$$

where L is length of the cylinder and d the diameter. The extrapolated tensile strength of a specimen with porosity of 0 was graphically determined by using a linear regression curve fit to the out-of-plane tensile data. The AS4/3501-6 $(\pm 45/0_2/\mp 45/90_2)_S$ laminates were found to have an average pore length of 538.0μ and a diameter of 24.3 μ. The extrapolated value of σ_{max} was 4415 psi. The strength versus porosity data for these specimens is plotted in Figure 42 along with the linear regression fit of the data point and the predicted strengths using equation (12). The predicted strength matches the experimentally determined data very well.

AS4/3501-6 $(\pm 45/90_2/\mp 45/0_2)_S$ laminates had an average pore length of 456.1 μ with an average diameter of 24.5 μ. The extrapolated value of σ_{max} was found to be 4862 psi. The out-of-plane tensile data is plotted as a function of porosity in Figure 43. Again, the linear regression fit of the experimental plot is shown in the figure along with the predicted strength form equation (12). The theoretically determined strengths are greater than the experimental values. The theoretical model assumed a uniform distribution of pores in the tensile specimen. In section 5.2, where the pore distribution in the AS4/3501-6 $(\pm 45/90_2/\mp 45/0_2)_S$ were discussed, we noted a particularly high concentration of large voids in the central 0° plies in defect level 2 and 3 specimens, Figures 54-56. This nonuniformity of void distribution with increasing porosity would explain the deviation from theoretical behavior.

The theoretical strength prediction of AS4/1806 specimens was not attempted because of the high large amount of scatter in the experimental data.

7.0 Concluding Remarks

Out-of-plane tensile strength and deformation characteristics of AS4/3501-6 and AS4/1806 graphite/epoxy laminates were investigated as a function of porosity. The tensile specimens were removed from the 3.0-inch webs of angle sections fabricated at Lockheed Georgia Company. The AS4/3501-6 and AS4/1806 angles were fabricated with two quasi- isotropic stacking sequences, $(\pm 45/0_2/\mp 45/90_2)_S$ and $(\pm 45/90_2/\mp 45/0_2)_S$, and measured 30-inches in length. Four processing methods were used in the fabrication of these angles resulting in different levels of porosity: a baseline lay-up, a moisture wipe and solvent wipe of pre-preg prior to lay-up, and a low pressure cure cycle. The strength testing was performed by applying tension to the faces of circular specimens in a direction perpendicular to the laminate mid-plane. Circular specimens were removed in 1.5-, 2.0-, and 2.5-inch diameter sizes and bonded to a test fixture by using a high strength adhesive. In addition to the strength data, elastic response of the specimens were monitored through load-deformation measurements.

The displacements measured during testing included the combined deflections of both the bonded laminate and adhesive. As a result of bonding, the fixture imposed a restraint on the transverse deformation of the laminate which was expected to result in a combined loading of test specimens. An iterative finite element technique was used to determine the increase in the experimental modulus resulting from the combined influence of adhesive effects,

transverse restraint, and specimen geometry. The results were used to factor the experimental data to obtain a more accurate value of out-of-plane modulus.

The modified out-of-plane modulus was then used in a 3-dimensional finite element program to determine the tensile loading applied to the laminates during testing. The results of the analyses have shown the external loading of the laminate, during testing, to be an approximate uniform tensile distribution.

The combination of two material systems, four processing methods, two stacking-sequences, and three different specimen geometries resulted in several parameters influencing out-of-plane tension. The primary interest of this investigation was the effects of porosity on transverse strength. The specimen porosities were determined by optical analysis techniques and compared to the void contents obtained by Lockheed based on ASTM test method D 2734. ASTM tests were conducted on all out-of-plane tensile specimens and optical analyses were done on twenty representative specimens. Void contents determined by optical techniques were suspected of being low on account of grey level filtering used to eliminate irregularities thought to be the result of surface pretreatment. AS4/3501-6 specimens fabricated using the baseline process, had porosities that ranged between 1.50 and 2.82%. The void content of laminates with pre-preg that was solvent wiped varied between 1.50 and 2.58%. Pre-preg that was moisture wiped had porosities ranging between 2.89 and 4.82%. The low pressure cure cycle resulted in laminates with void contents between 2.82 and 6.77%.

The experimental strength decreased as a function of increasing porosity. In addition, both strength and stiffness were observed to be dependent on specimen geometry. For specimens in the void content range of 1.50 to 2.82% (baseline or solvent wiped) there was a significant reduction in strength and stiffness for specimens with diameters smaller than 2.0-inches. Specimens fabricated by the two remaining processing methods were found to have a reduction in strenth for diameters smaller than 2.5-inches. Optical investigations of the characteristic pore size and distribution have shown there to be an increase in both the size and

distribution of voids for high porosity specimens. Specimens containing large, unevenly distributed, voids require a larger geometry to eliminate the influence of specimen size on strength.

AS4/1806 specimens fabricated using the baseline process had void contents ranging from 0.74 to 2.31%. Specimens that were moisture wiped ranged between 0.85 to 1.98%. There was too much scatter in experimental tensile data to deduce the effects of porosity. Much of this scatter was found to be related to the nonuniform distribution of voids and the presence of delaminations in some angles.

Pore size, shape, and orientation were characterized by metallography and optical analysis techniques. The data from these analyses have revealed the average pore geometry to be cylindrical. The pores in the AS4/3501-6 $(\pm 45/90_2/\mp 45/0_2)_S$ specimens had an average length of 456.1 μ and diameter of 24.56μ oriented at 60.8° with respect to the out-of-plane load axis. Pores in the AS4/3501-6 $(\pm 45/0_2/\mp 45/90_2)_S$ specimens had an average length of 538.0μ and diameter of 24.38μ oriented at 56.2°. This data was used in an empirical stength/porosity model, developed by Brown et al [13], for isotropic polycrystalline materials [13]. The model was used for the prediction of out-of-plane tensile strength as a function of reduction in cross-sectional area due to porosity. The theoretically determined strength as a function of porosity was found to be in good agreement with experimental values. The predicted strength exceeded the experimenatal data for AS4/3501-6 $(\pm 45/90_2/\mp 45/0_2)_S$ specimens with high porosities. The deviation of predicted values was the result of the nonuniform concentration of large voids in the 0° plies. The extensive scatter in the experimental strength of AS4/1806 specimens prevented the use of the Bown et al model.

8.0 Figures and Tables

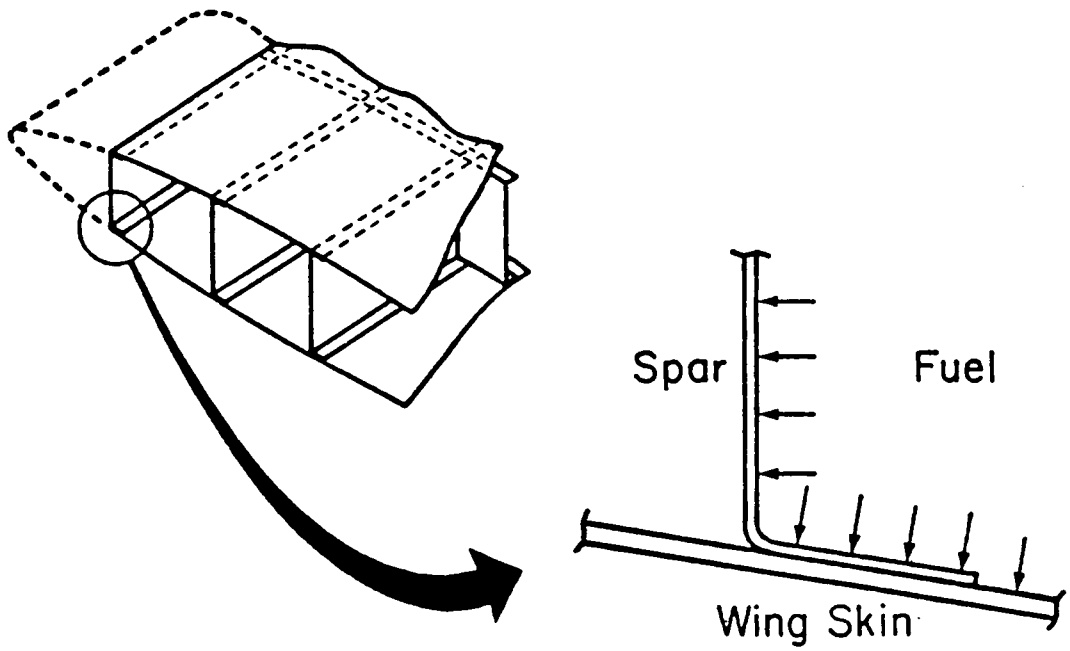

Figure 1. Stiffened Wing Structure using Graphite/Epoxy Angles.

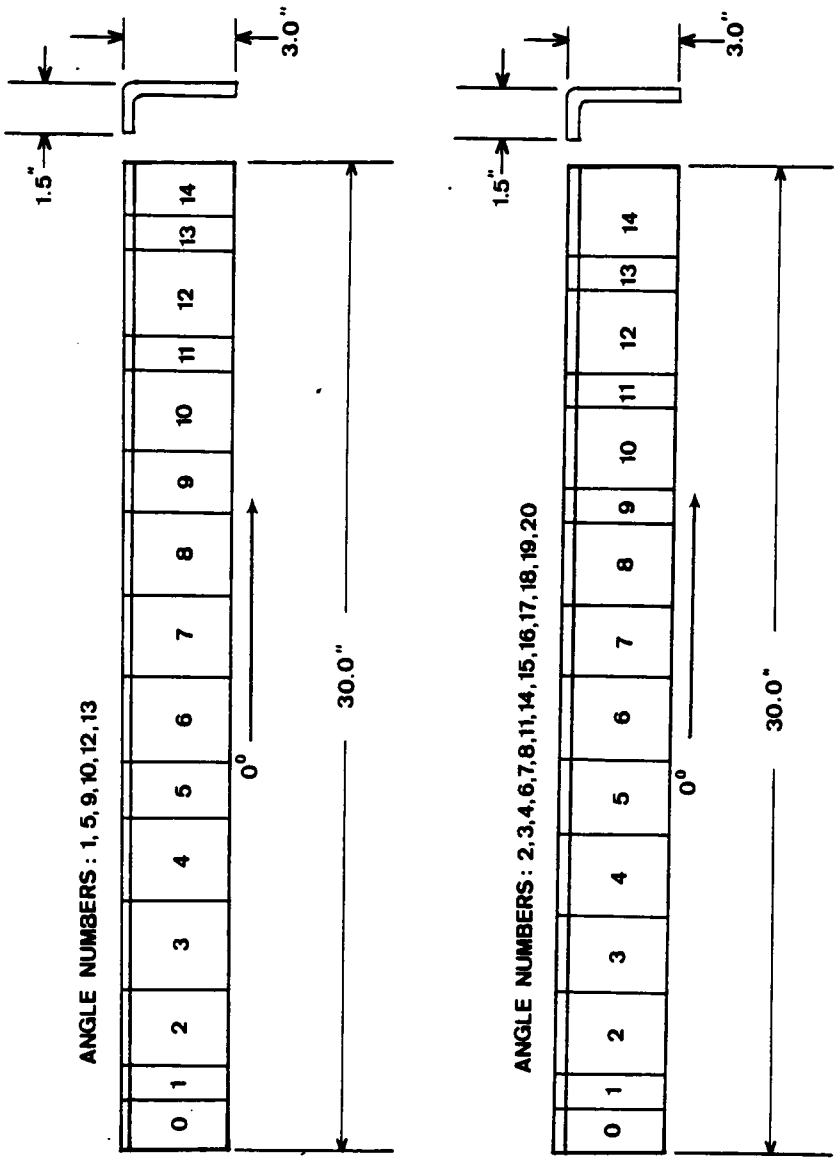

Figure 1. Stiffened Wing Structure using Graphite/Epoxy Angles.

Table 1. AS4/3501-6 and AS4/1806 Test Specimen Parameters.

Defect Level	AS4/3501-6 $(\pm 45/90_2/\mp 45/0_2)s$	AS4/3501-6 $(\pm 45/0_2/\mp 45/90_2)s$	AS4/1806 $(\pm 45/90_2/\mp 45/0_2)s$
0 (Baseline)	4-3[1] 4-5 4-7 6-3 6-5 6-7	1-3 1-5 1-7 1-9 5-3 5-5 5-7 5-9	7-3 7-5 7-7 8-3 8-5 8-7
1 (Solvent Wipe)	9-3 9-5 9-7 9-9 15-3 15-5 15-7	2-3 2-5 2-7 10-3 10-5 10-7 10-9	
2 (Moisture Add)	11-3 11-5 11-7 14-3 14-5 14-7	12-3 12-5 12-7 12-9 13-3 13-5 13-7 13-9	3-3 3-5 3-7 16-3 16-5 16-7
3 (Low Pressure)	18-3 18-5 18-7 20-3 20-5 20-7	17-3 17-5 17-7 19-3 19-5 19-7	

Note: (1) The first digit of the specimen I.D. number identifies the angle.

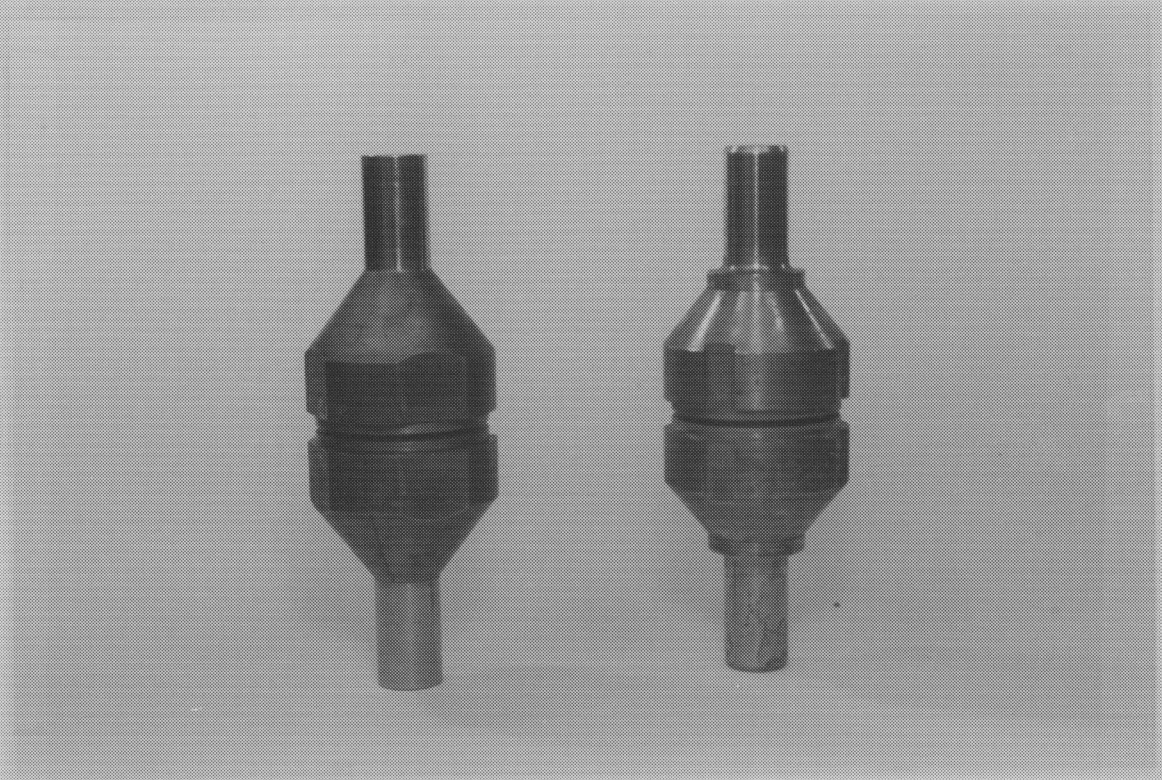

Figure 3. Stainless Steel Test Fixtures.

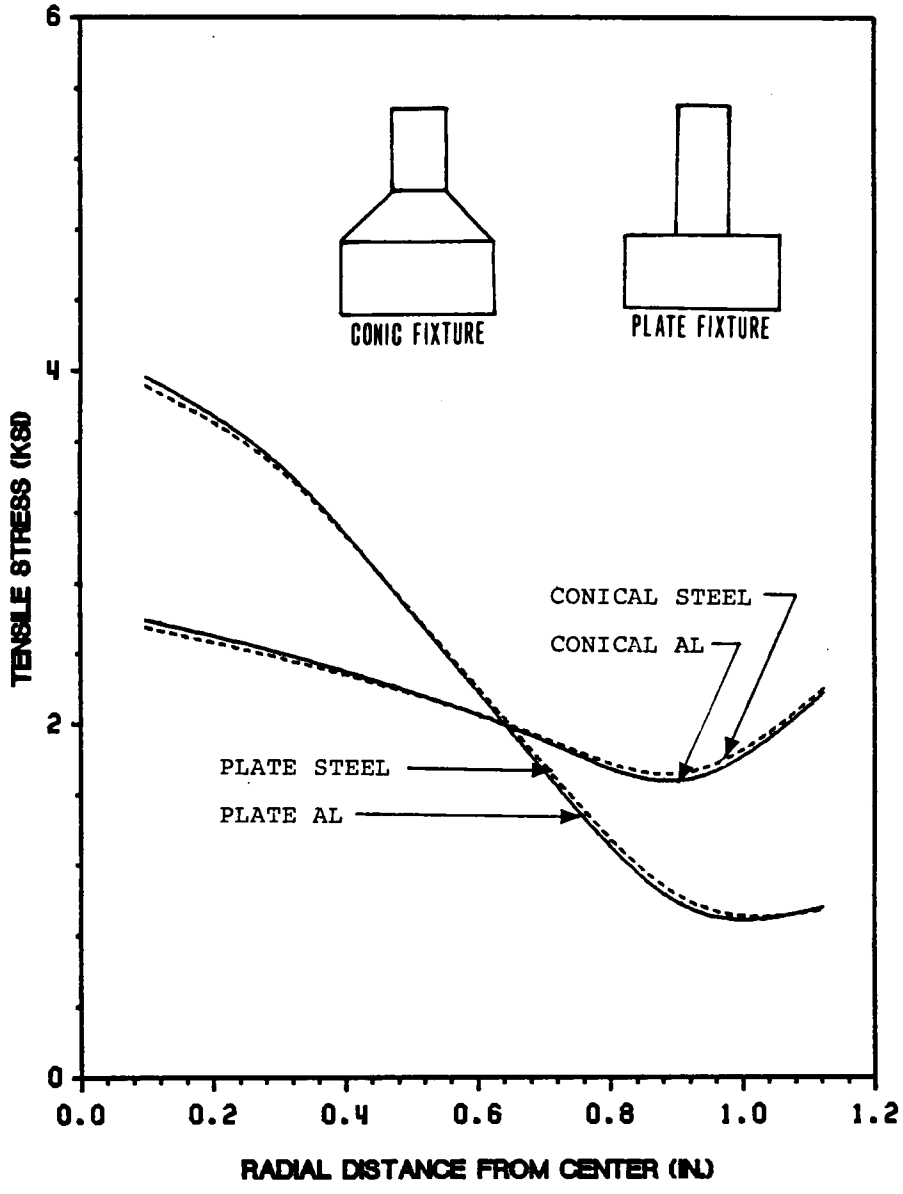

Figure 4. Tensile Stress Distribution in Test Fixture.

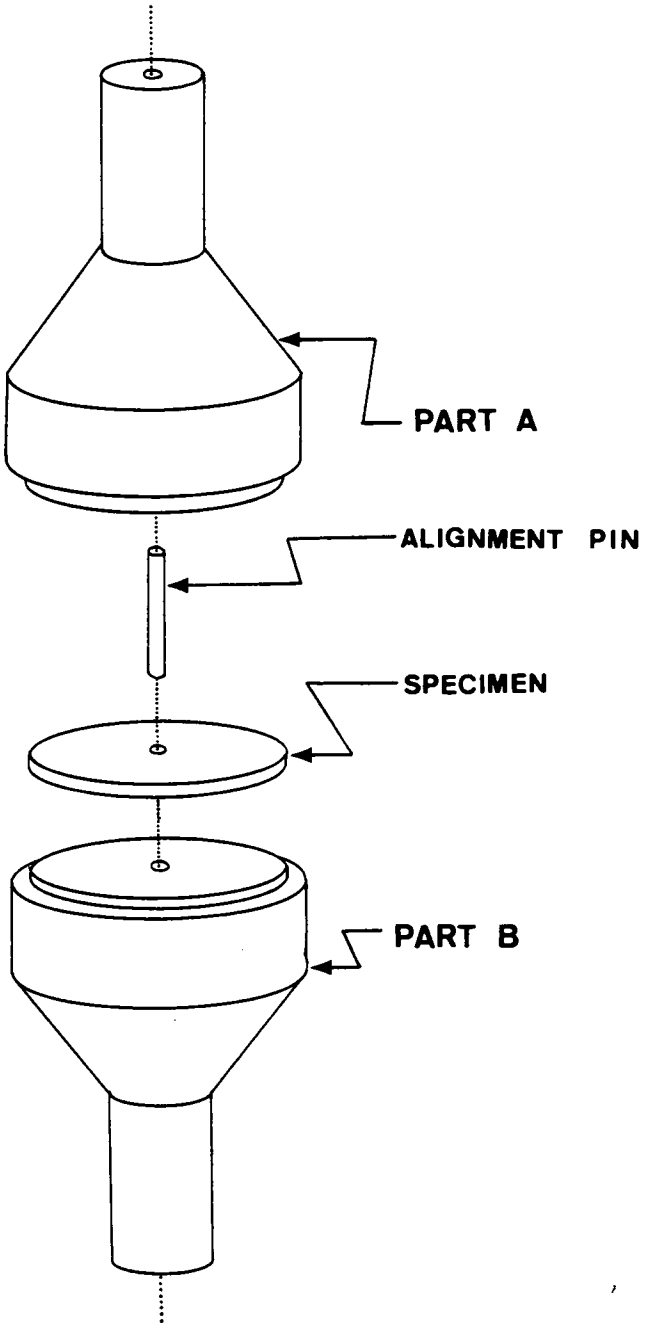

Figure 5. Test Fixture Assembly Drawing.

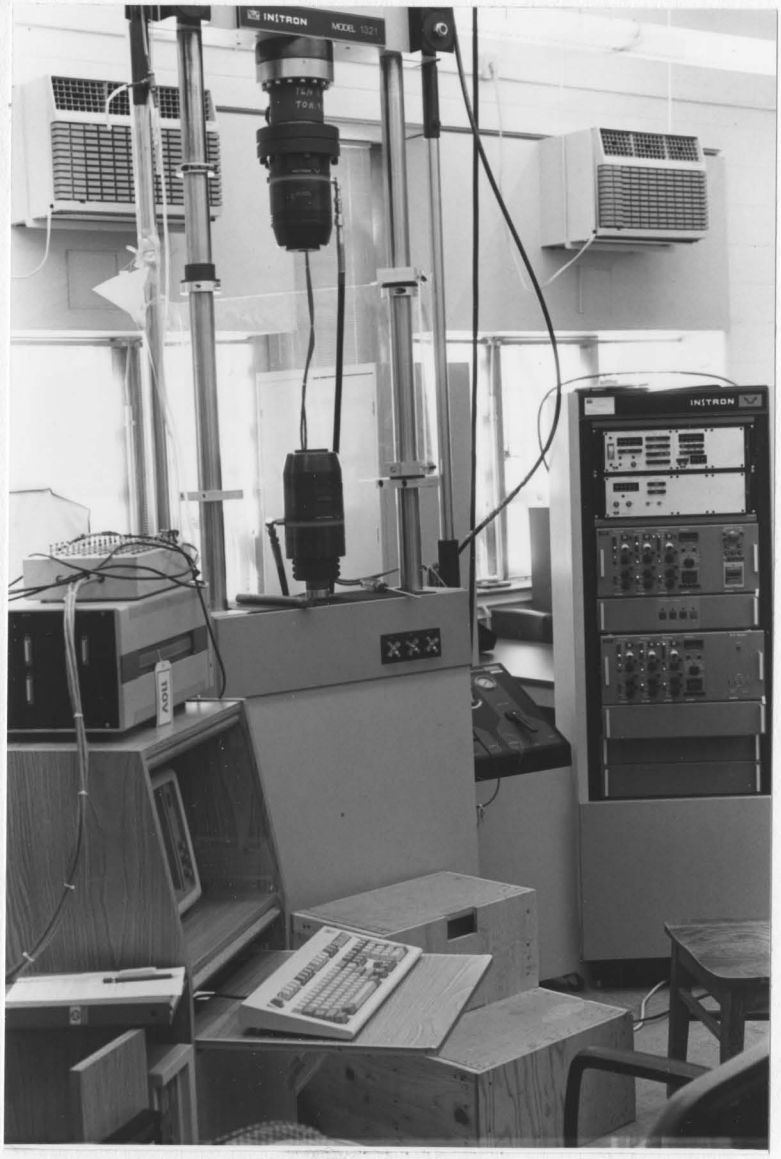

Figure 6. Test-System Used for Out-of-Plane Tensile Experiments.

Figure 7. Arrangement of Displacement Transducers on Test Fixture.

Figure 8. Compression Test Fixture.

Table 2. ASTM D 2734 Void Contents.

Void Contents Determined by ASTM Test Method D 2734
$(\pm 45/90_2/\mp 45/0_2)s$ AS4/3501-6

	Specimen I.D. No.	Resin Content (%)	Void Content (%)	Specimen Diameter (in.)
Defect Level 0	4-3	35.0	1.82	2.0
	4-5	35.6	1.81	2.0
	4-7	34.7	1.50	2.0
	6-3	35.5	1.95	2.0
	6-5	36.1	1.43	2.0
	6-7	34.7	1.99	2.0
Defect Level 1	9-3	29.3	2.01	2.5
	9-7	30.2	1.52	2.5
	15-3	30.9	2.13	2.0
	15-5	29.1	2.70	2.0
	15-7	27.9	2.57	2.0
	9-5	29.4	1.60	1.5
	9-9	30.0	1.76	1.5
Defect Level 2	11-3	30.5	4.26	2.0
	11-5	29.5	4.01	2.0
	11-7	30.0	4.03	2.0
	14-3	31.3	3.45	2.0
	14-5	30.1	4.64	2.0
	14-7	30.3	4.38	2.0
Defect Level 3	18-3	35.2	3.86	2.0
	18-5	35.0	4.70	2.0
	18-7	34.7	5.12	2.0
	20-3	35.5	5.90	2.0
	20-5	35.8	5.54	2.0
	20-7	35.5	6.77	2.0

Note: 1)Resin Density 1.265 g/cm^3
Graphite Fiber Density 1.78 g/cm^3
2)ASTM D 2734 tests were performed by Lockheed.

Table 3. ASTM D 2734 Void Contents.

Void Contents Determined by ASTM Test Method D 2734
$(\pm 45/0_2/\mp 45/90_2)s$ AS4/3501-6

	Specimen I.D. No.	Resin Content (%)	Void Content (%)	Specimen Diameter (in.)
Defect Level 0	1-3	35.0	1.53	2.5
	1-7	32.6	1.97	2.5
	5-3	34.2	2.11	2.5
	5-7	31.4	2.82	2.5
	1-5	34.5	2.85	1.5
	5-5	32.4	1.67	1.5
	5-9	31.9	2.29	1.5
Defect Level 1	10-3	36.2	2.22	2.5
	10-7	36.0	2.03	2.5
	2-3	36.7	1.67	2.0
	2-5	36.1	1.79	2.0
	2-7	34.9	2.78	2.0
	10-5	35.4	2.07	1.5
	10-9	34.4	2.34	1.5
Defect Level 2	12-3	30.5	2.89	2.5
	12-7	29.9	3.73	2.5
	13-3	28.0	5.88	2.5
	13-7	28.0	4.63	2.5
	12-5	29.6	3.86	1.5
	12-9	31.3	3.22	1.5
	13-5	28.4	3.89	1.5
	13-9	27.1	4.82	1.5
Defect Level 3	17-3	36.8	4.40	2.0
	17-5	36.0	2.82	2.0
	17-7	35.9	5.55	2.0
	19-3	34.9	3.60	2.0
	19-5	35.5	4.30	2.0
	19-7	36.6	3.23	2.0

Note: 1)Resin Density 1.265 g/cm^3
Graphite Fiber Density 1.78 g/cm^3
2)ASTM D 2734 tests were performed by Lockheed.

Table 4. ASTM D 2734 Void Contents.

Void Contents Determined by ASTM Test Method D 2734
$(\pm 45/0_2/\mp 45/90_2)s$ AS4/1806

	Specimen I.D. No.	Resin Content (%)	Void Content (%)	Specimen Diameter (in.)
Defect Level 0	7-3	35.6	0.74	2.0
	7-5	36.0	1.95	2.0
	7-7	36.7	2.31	2.0
	8-3	35.9	1.73	2.0
	8-5	35.2	1.67	2.0
	8-7	35.5	0.85	2.0
Defect Level 2	3-3	36.1	0.84	2.0
	3-5	36.6	1.98	2.0
	3-7	36.8	1.09	2.0
	16-3	36.0	1.07	2.0
	16-5	36.3	1.14	2.0
	16-7	36.1	1.45	2.0

Note: 1)Resin Density 1.265 g/cm^3
Graphite Fiber Density 1.78 g/cm^3
2)ASTM D 2734 tests were performed by Lockheed.

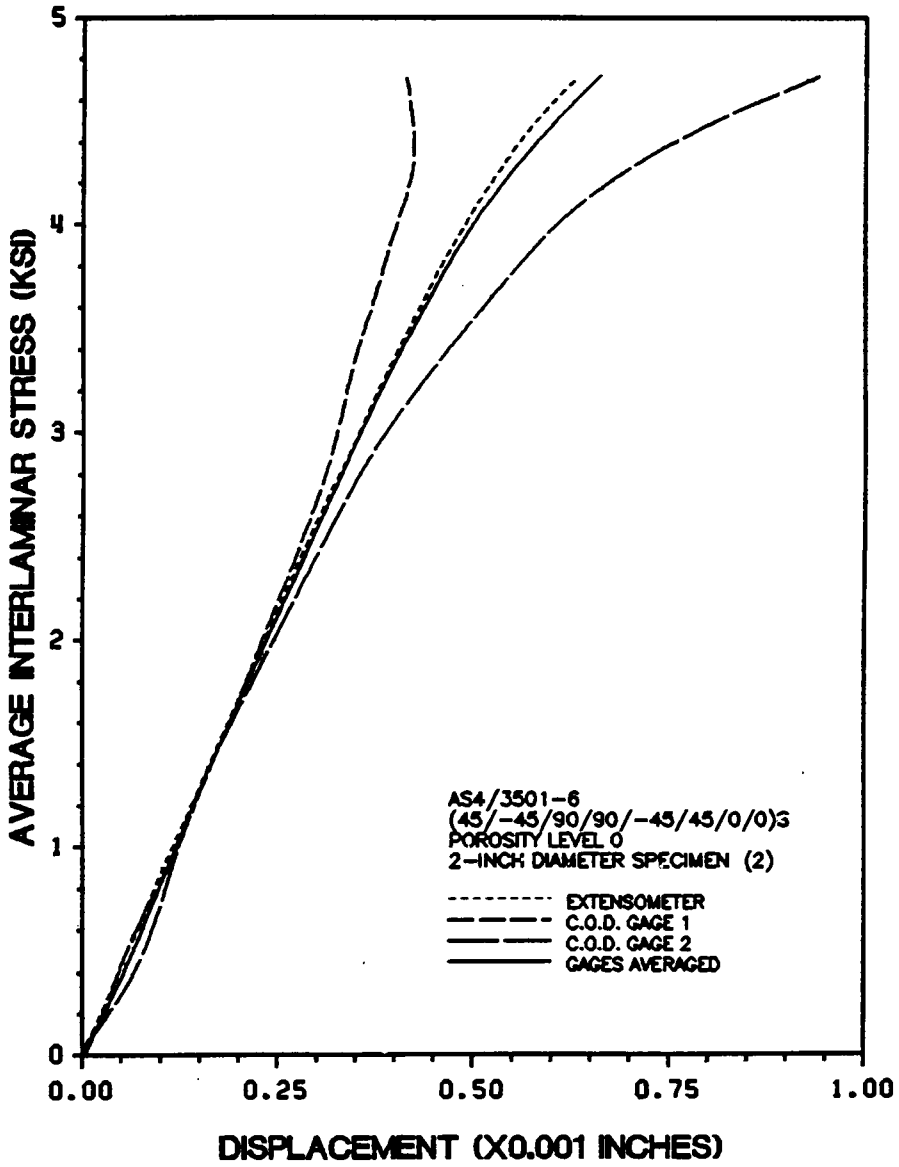

Figure 9. Sample of Out-of-Plane Tensile Test Data.

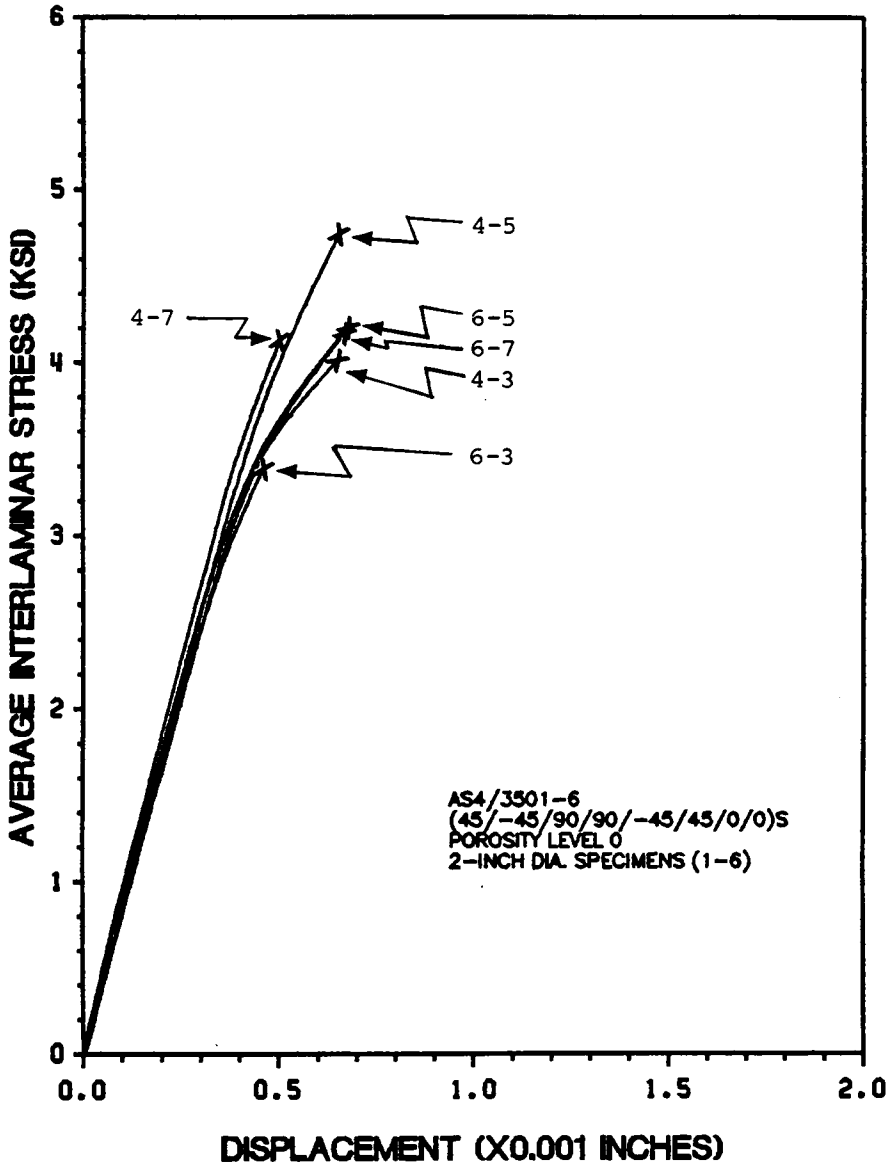

Figure 10. Average Response of 2.0-inch Diameter AS4/3501-6 Specimens.

Table 5. Summary of Out-of-Plane Tensile Test Data.

$(\pm 45/0_2/\mp 45/90_2)s$ AS4/3501-6 2.5-inch Diameter

	Specimen I.D. No.	Strength, σ_z (ksi)	Modulus, $\bar{E}_z$ ($x10^6$ psi)	Failure Locations
Defect Level 0	1-3	3.850	3.753	Laminate
	1-7	3.678	3.940	Laminate
	5-3	4.240	3.876	Laminate
	5-7	3.757	3.252	Laminate
	Average	3.881	3.705	
	Std Dev	0.249	0.312	
Defect Level 1	10-3	3.860	3.437	Laminate
	10-7	4.199	2.875	Laminate
	Average	4.030	3.156	
	Std Dev	0.240	0.397	
Defect Level 2	12-3	3.259	3.388	Laminate
	12-7	3.105	3.057	Laminate
	13-3	2.502	3.423	Laminate
	13-7	2.691	3.444	Laminate
	Average	2.889	3.453	
	Std Dev	0.352	0.340	

Table 6. Summary of Out-of-Plane Tensile Test Data.

$(\pm 45/0_2/\mp 45/90_2)s$ AS4/3501-6 2.0-inch Diameter

	Specimen I.D. No.	Strength, σ_z (ksi)	Modulus, $\bar{E}_z$ ($x10^6$ psi)	Failure Locations
Defect Level 1	2-3	3.228	3.308	Laminate
	2-5	--	--	Adhesive
	2-7	4.416	3.745	Laminate
	Average	3.822	3.526	
	Std Dev	0.840	0.309	
Defect Level 3	17-3	2.509	2.461	Laminate
	17-5	2.978	2.985	Laminate
	17-7	3.069	3.452	Laminate
	19-3	0.822	2.437	Laminate
	19-5	--	--	Grip
	19-7	0.542	2.592	Laminate
	Average	1.711	2.785	
	Std Dev	1.211	0.432	

Table 7. Summary of Out-of-Plane Tensile Test Data.

$(\pm 45/0_2/\mp 45/90_2)s$ AS4/3501-6 1.5-inch Diameter

	Specimen I.D. No.	Strength, σ_z (ksi)	Modulus, $\bar{E}_z$ ($x10^6$ psi)	Failure Locations
Defect Level 0	1-5	2.236	3.240	Laminate
	1-9	4.416	3.016	Laminate
	5-5	4.011	3.011	Laminate
	5-9	3.344	3.452	Laminate
	Average	3.434	3.180	
	Std Dev	0.872	0.211	
Defect Level 1	10-5	--	--	Adhesive
	10-9	--	--	Grip
Defect Level 2	12-5	--	--	Grip
	12-9	1.175	3.281	Laminate
	13-5	--	--	Grip
	13-9	0.893	2.773	Laminate
	Average	1.034	3.007	
	Std Dev	0.199	0.387	

Table 8. Summary of Out-of-Plane Tensile Test Data.

$(\pm 45/90_2/\mp 45/0_2)s$ AS4/3501-6 2.5-inch Diameter

	Specimen I.D. No.	Strength, σ_z (ksi)	Modulus, $\bar{E}_z$ ($x10^6$ psi)	Failure Locations
Defect Level 1	9-3	3.013	3.784	Laminate
	9-7	4.313	4.019	Laminate
	Average	3.663	3.902	
	Std Dev	0.919	0.166	

Table 9. Summary of Out-of-Plane Tensile Test Data.

$(\pm 45/90_2/\mp 45/0_2)s$ AS4/3501-6 2.0-inch Diameter

	Specimen I.D. No.	Strength, σ_z (ksi)	Modulus, $\bar{E}_z$ ($x10^6$ psi)	Failure Locations
Defect Level 0	4-3	3.944	4.074	Laminate
	4-5	4.746	4.197	Laminate
	4-7	4.094	4.416	Laminate
	6-3	3.370	3.865	Laminate
	6-5	4.201	4.122	Laminate
	6-7	4.111	3.736	Laminate
	Average	4.078	4.068	
	Std Dev	0.443	0.242	
Defect Level 1	15-3	3.688	4.096	Laminate
	15-5	3.729	4.272	Laminate
	15-7	3.297	3.625	Laminate
	Average	3.571	3.998	
	Std Dev	0.238	0.334	
Defect Level 2	11-3	2.461	2.854	Laminate
	11-5	--	--	Grip
	11-7	1.818	2.969	Laminate
	14-3	2.129	2.980	Laminate
	14-5	--	--	Grip
	14-7	1.711	2.830	Laminate
	Average	2.030	2.908	
	Std Dev	0.338	0.0772	
Defect Level 3	18-3	3.086	3.781	Laminate
	18-5	2.314	3.548	Laminate
	18-7	2.094	2.906	Laminate
	20-3	0.711	2.704	Laminate
	20-5	--	--	Grip
	20-7	1.681	2.679	Laminate
	Average	1.977	3.124	
	Std Dev	0.873	0.508	

Table 10. Summary of Out-of-Plane Tensile Test Data.

$(\pm 45/90_2/\mp 45/0_2)s$ AS4/3501-6 1.5-inch Diameter

	Specimen I.D. No.	Strength, σ_z (ksi)	Modulus, $\bar{E}_z$ ($x10^6$ psi)	Failure Locations
Defect Level 1	9-5	2.705	2.325	Laminate
	9-9	–	–	Adhesive

Table 11. Summary of Out-of-Plane Tensile Test Data.

$(\pm 45/0_2/\mp 45/90_2)s$ AS4/1806 2.0-inch Diameter

	Specimen I.D. No.	Strength, σ_z (ksi)	Modulus, $\bar{E}_z$ ($\times 10^6$ psi)	Failure Locations
Defect Level 0	7-3	4.119	2.679	Adhesive
	7-5	4.017	3.422	Laminate
	7-7	4.832	3.590	Laminate
	8-3	4.897	3.332	Laminate
	8-5	4.120	3.753	Laminate
	8-7	4.686	3.814	Laminate
	Average	4.445	3.432	
	Std Dev	0.402	0.412	
Defect Level 2	3-3	3.710	3.220	Laminate
	3-5	2.401	2.647	Laminate
	3-7	3.114	2.921	Laminate
	16-3	3.319	2.850	Laminate
	16-5	2.188	2.303	Adhesive
	16-7	3.813	3.696	Laminate
	Average	3.090	2.939	
	Std Dev	0.671	0.480	

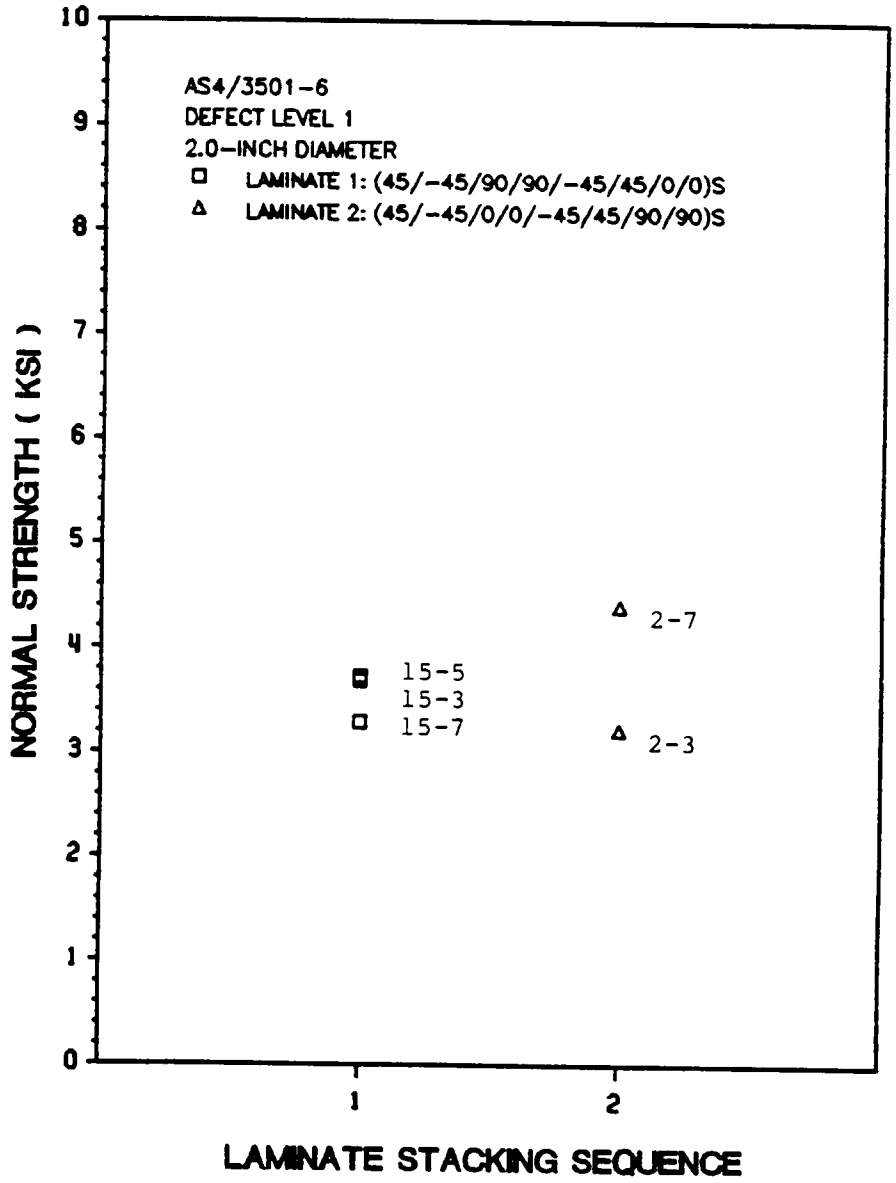

Figure 11. The Effects of Laminate Stacking Sequence on Normal Strength.

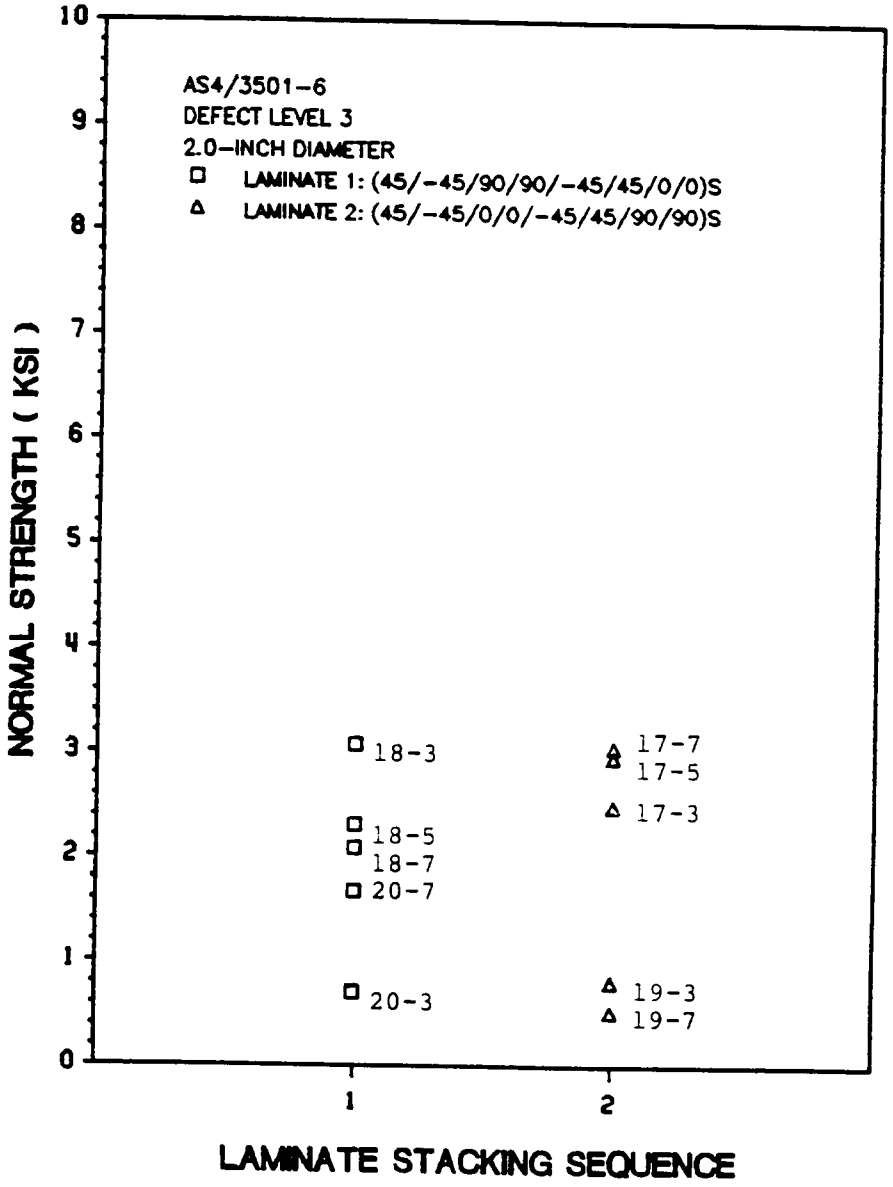

Figure 12. The Effects of Laminate Stacking Sequence on Normal Strength.

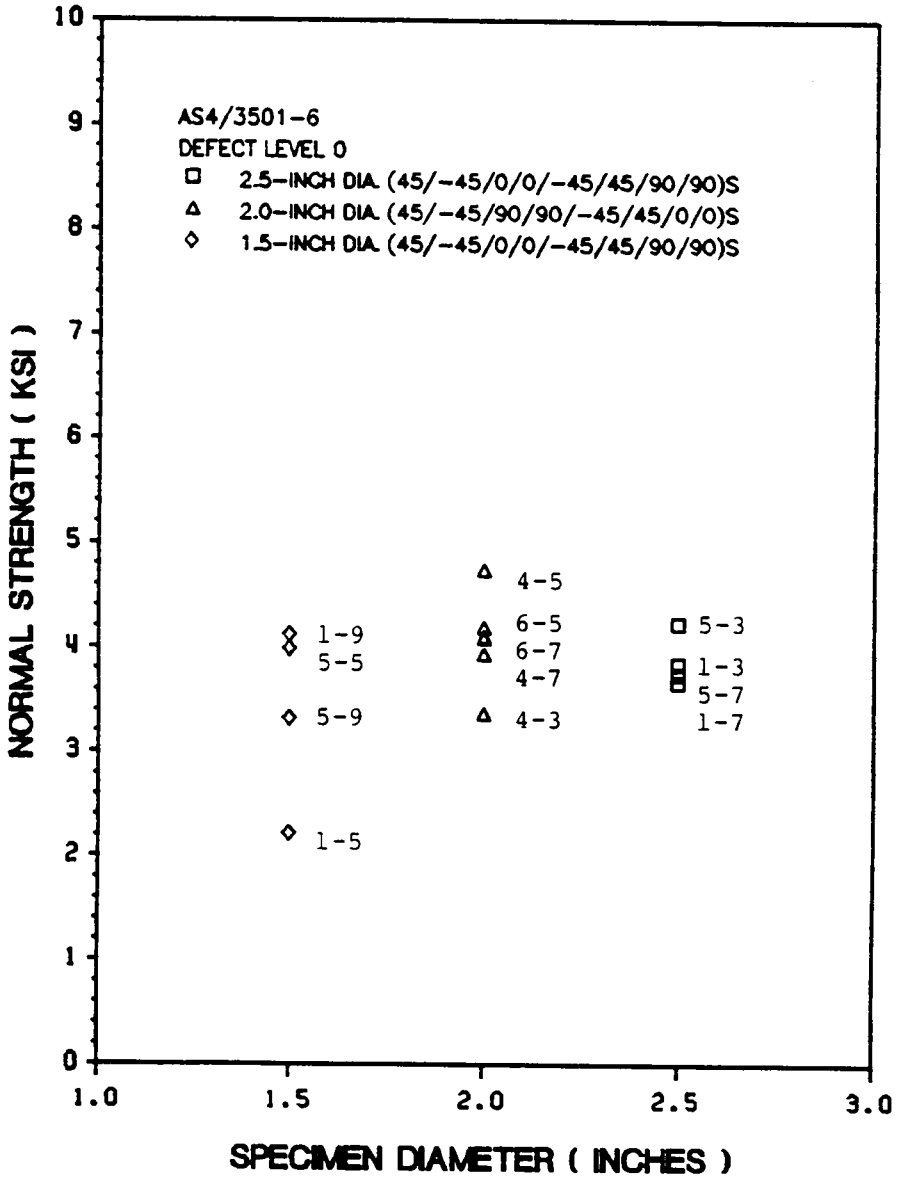

Figure 13. The Effects of Specimen Geometry on Normal Strength.

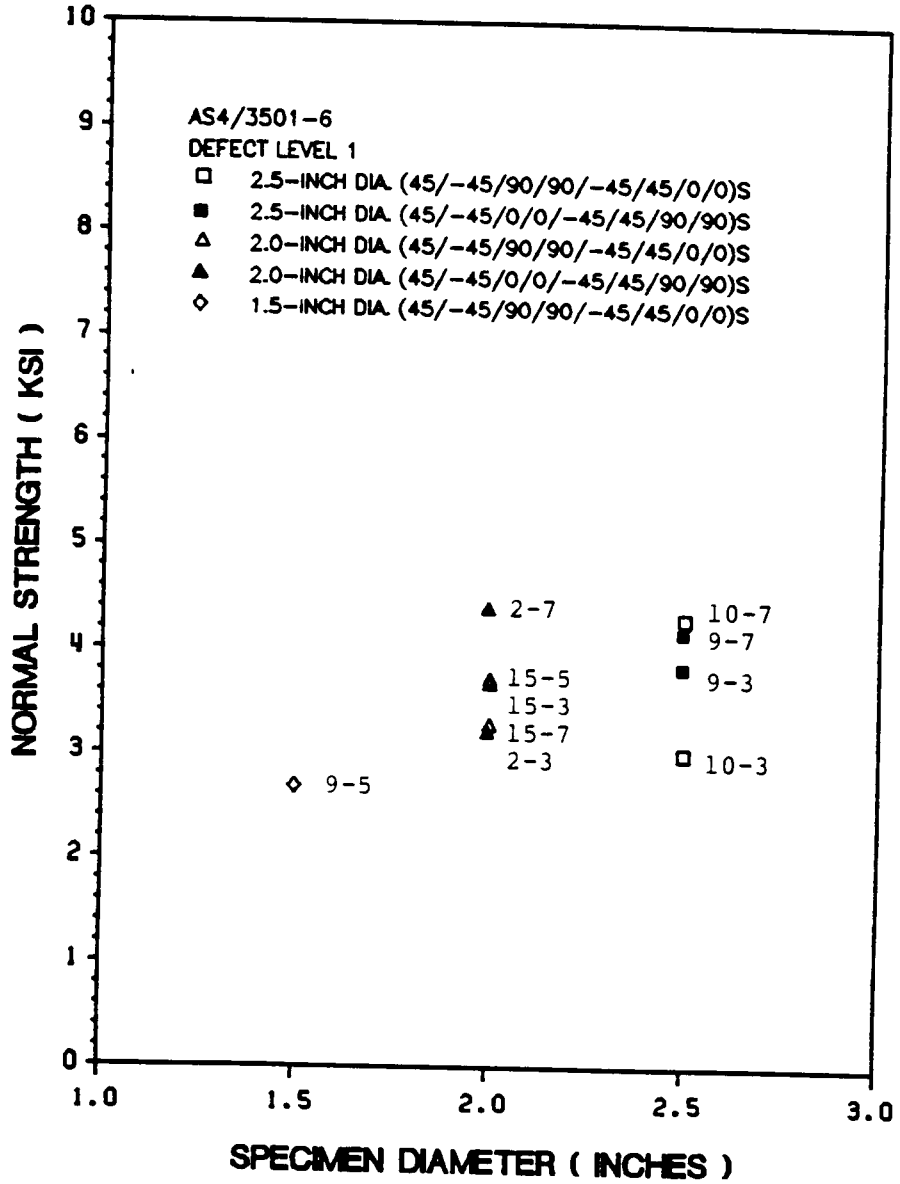

Figure 14. The Effects of Specimen Geometry on Normal Strength.

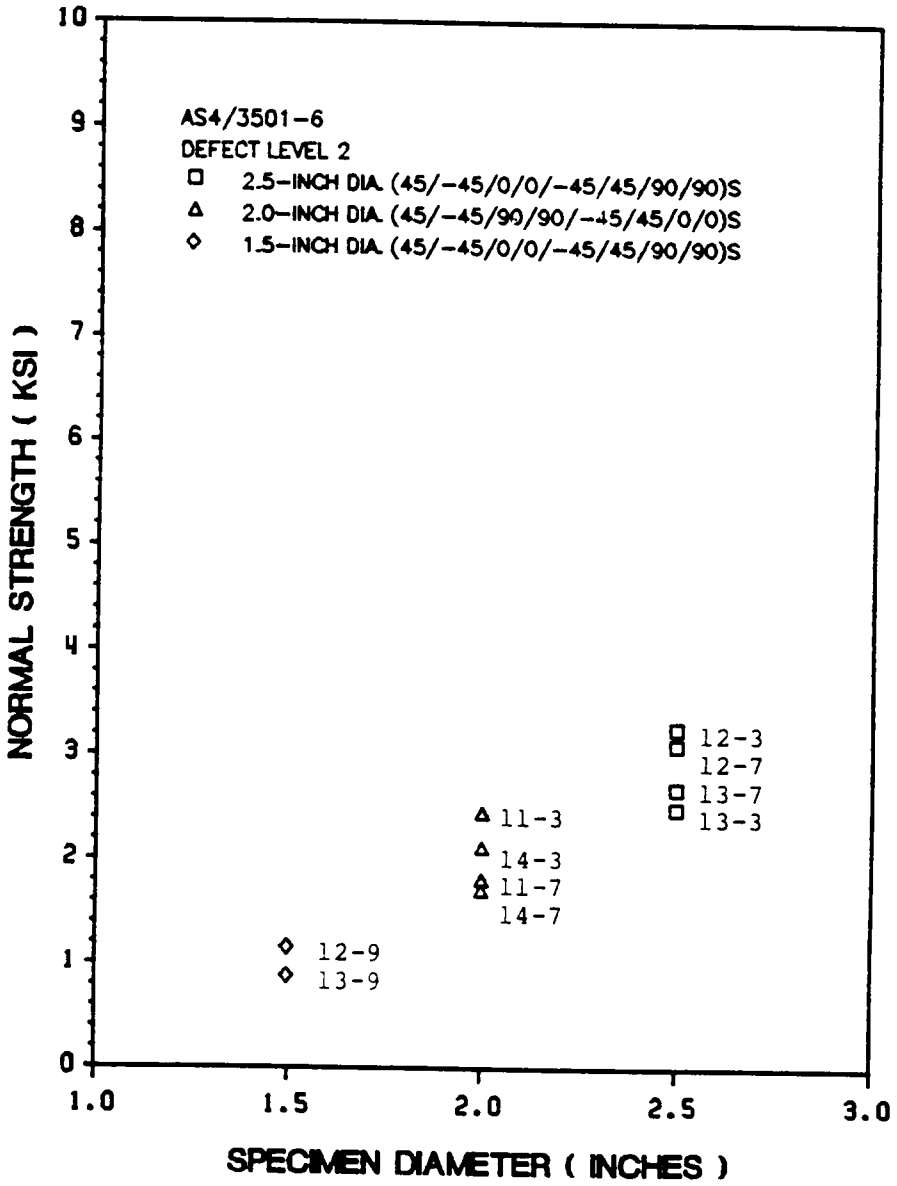

Figure 15. The Effects of Specimen Geometry on Normal Strength.

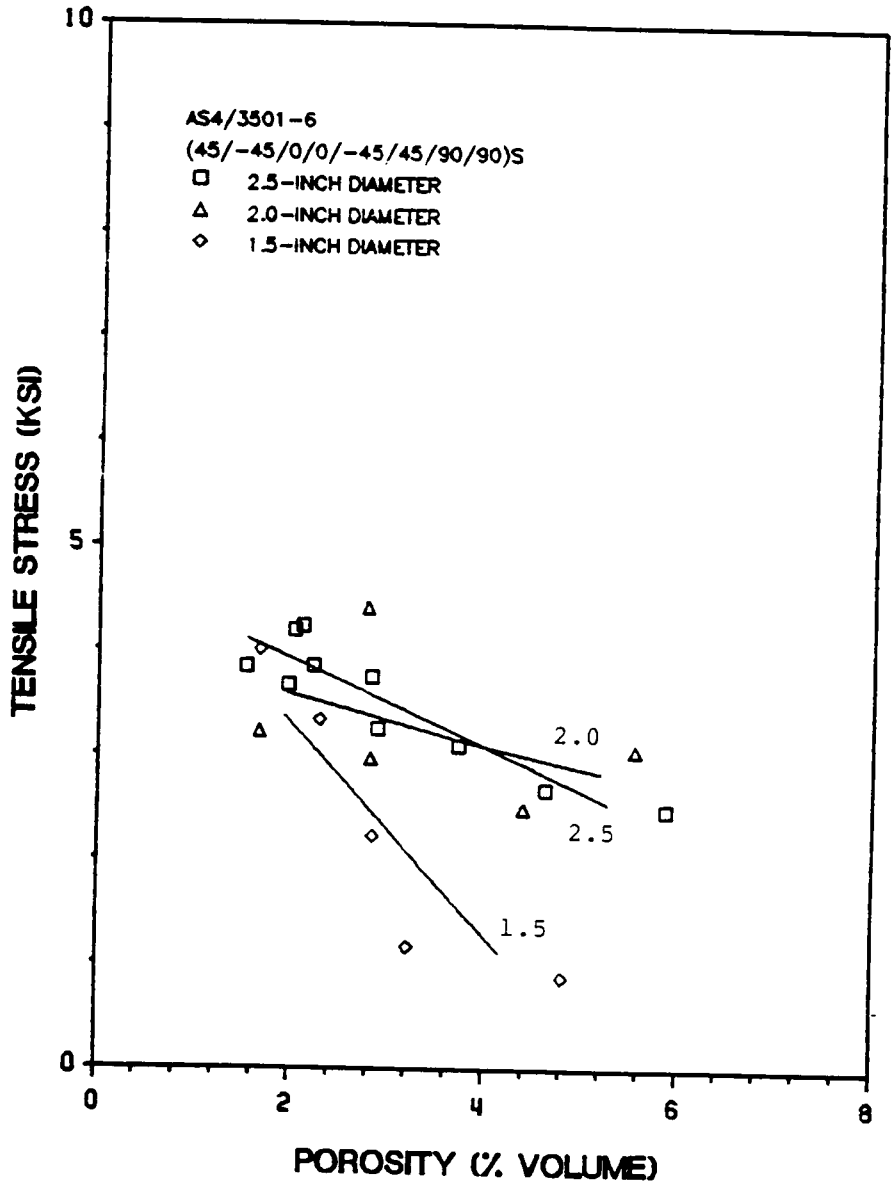

Figure 16. Specimen Strength as a Function of Porosity.

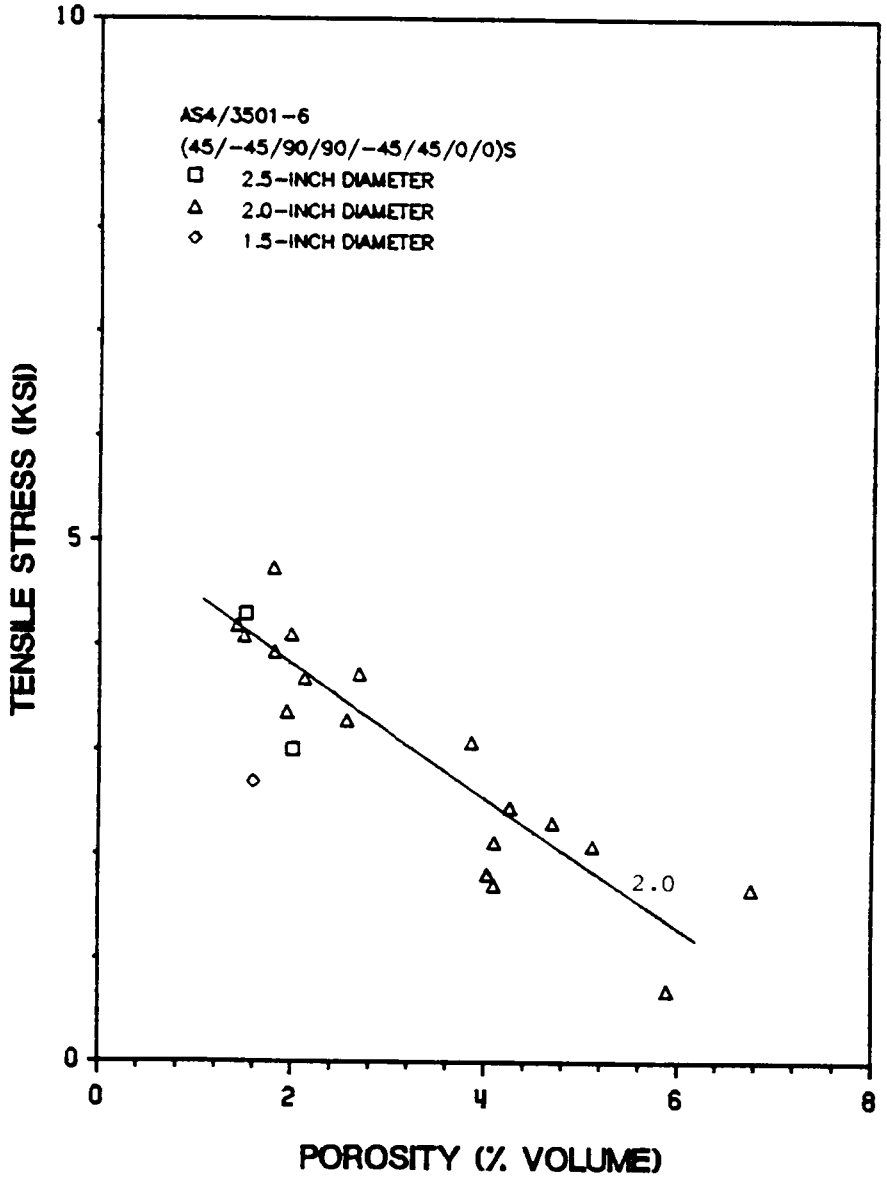

Figure 17. Specimen Strength as a Function of Porosity.

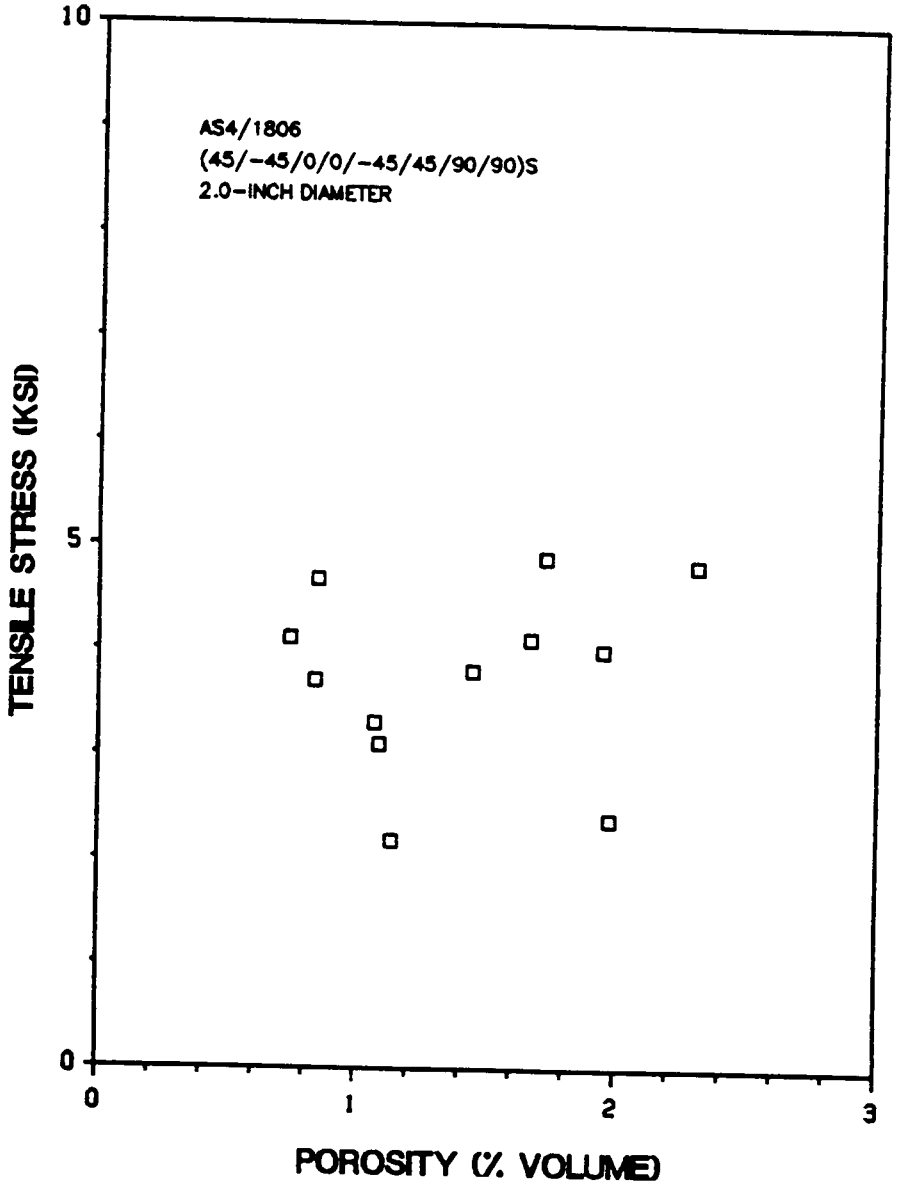

Figure 18. Specimen Strength as a Function of Porosity.

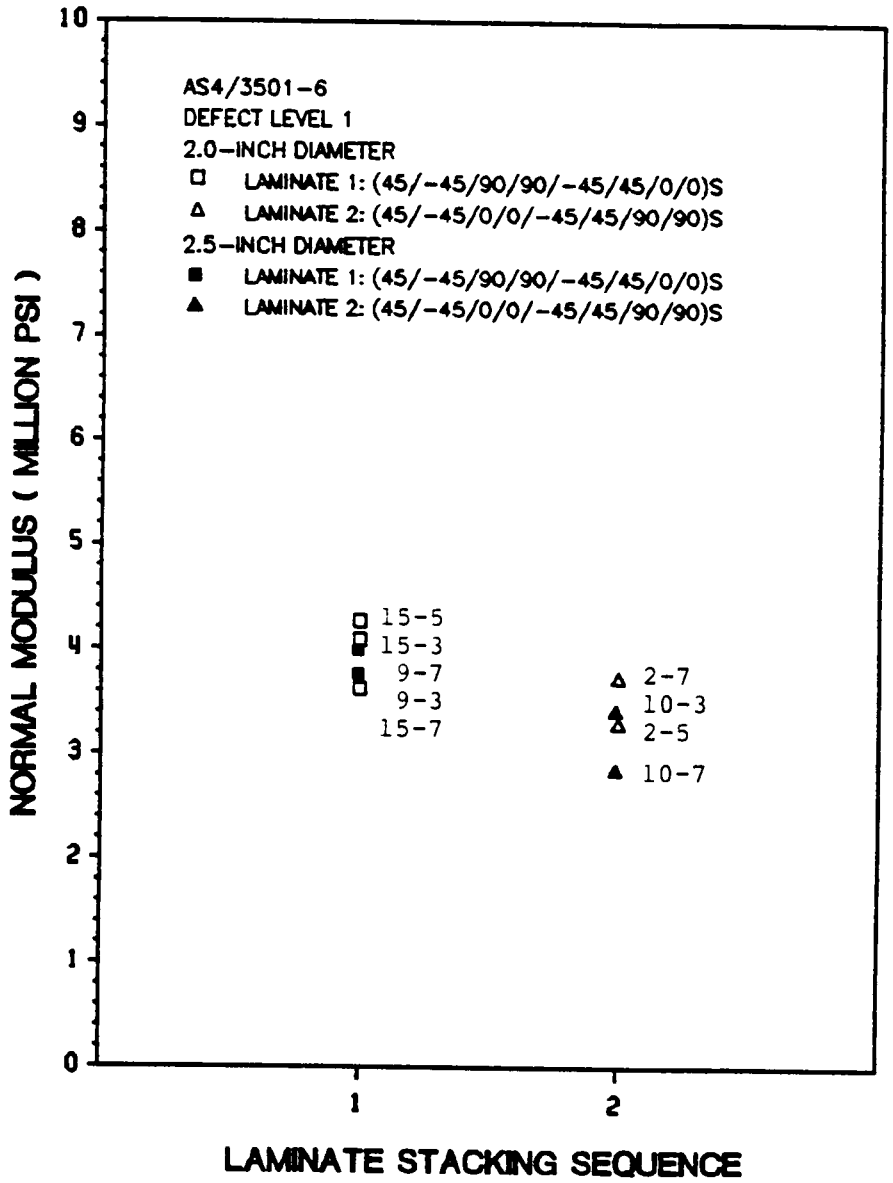

Figure 19. Effects of Stacking Sequence on Combined Out-of-Plane Modulus.

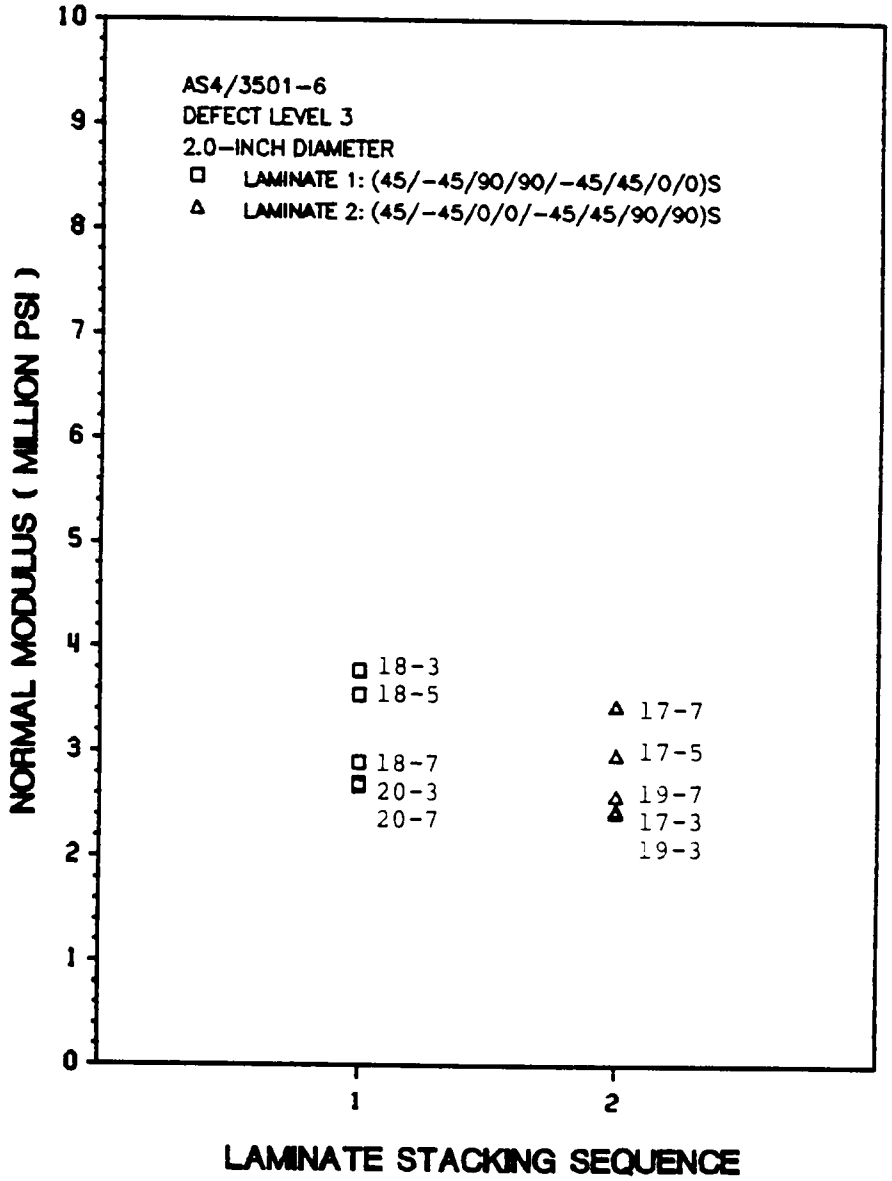

Figure 20. Effects of Stacking Sequence on Combined Out-of-Plane Modulus.

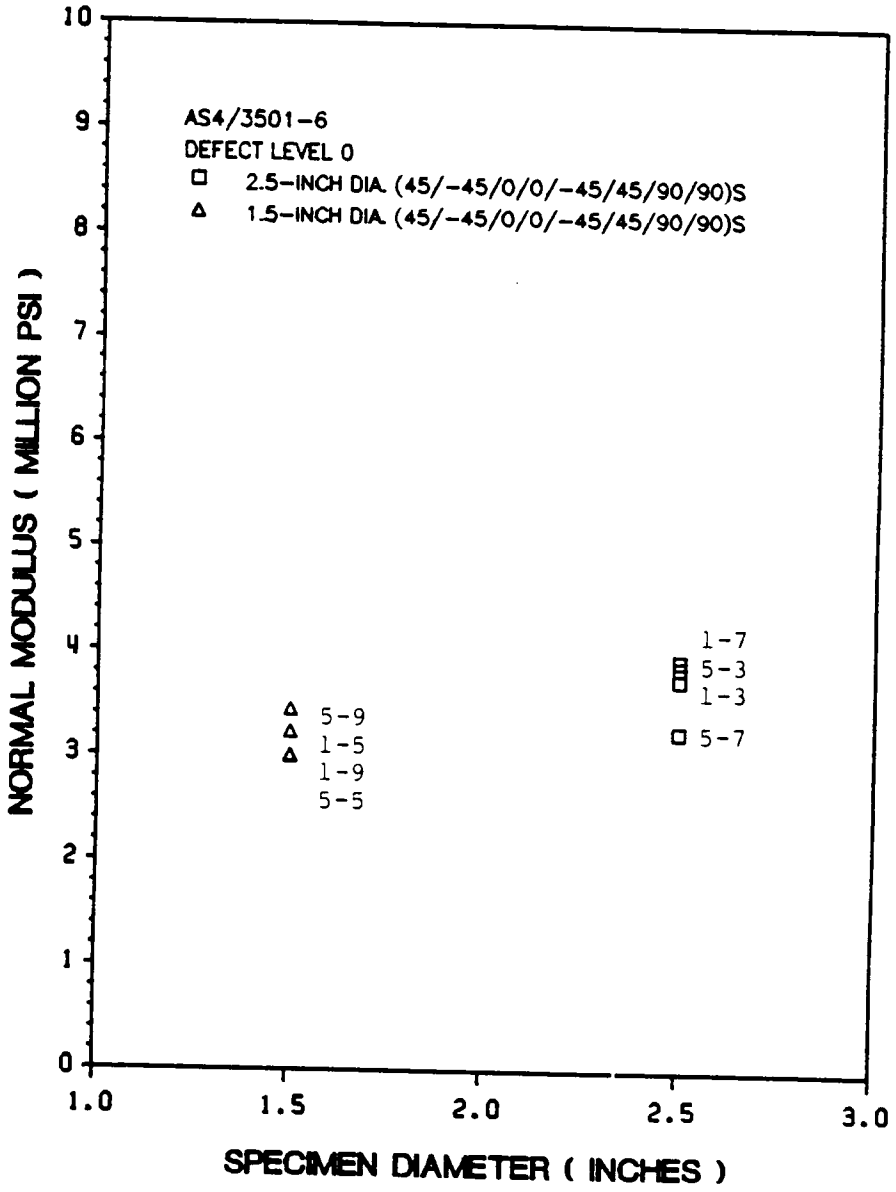

Figure 21. Effects of Specimen Diameter on Combined Out-of-Plane Modulus.

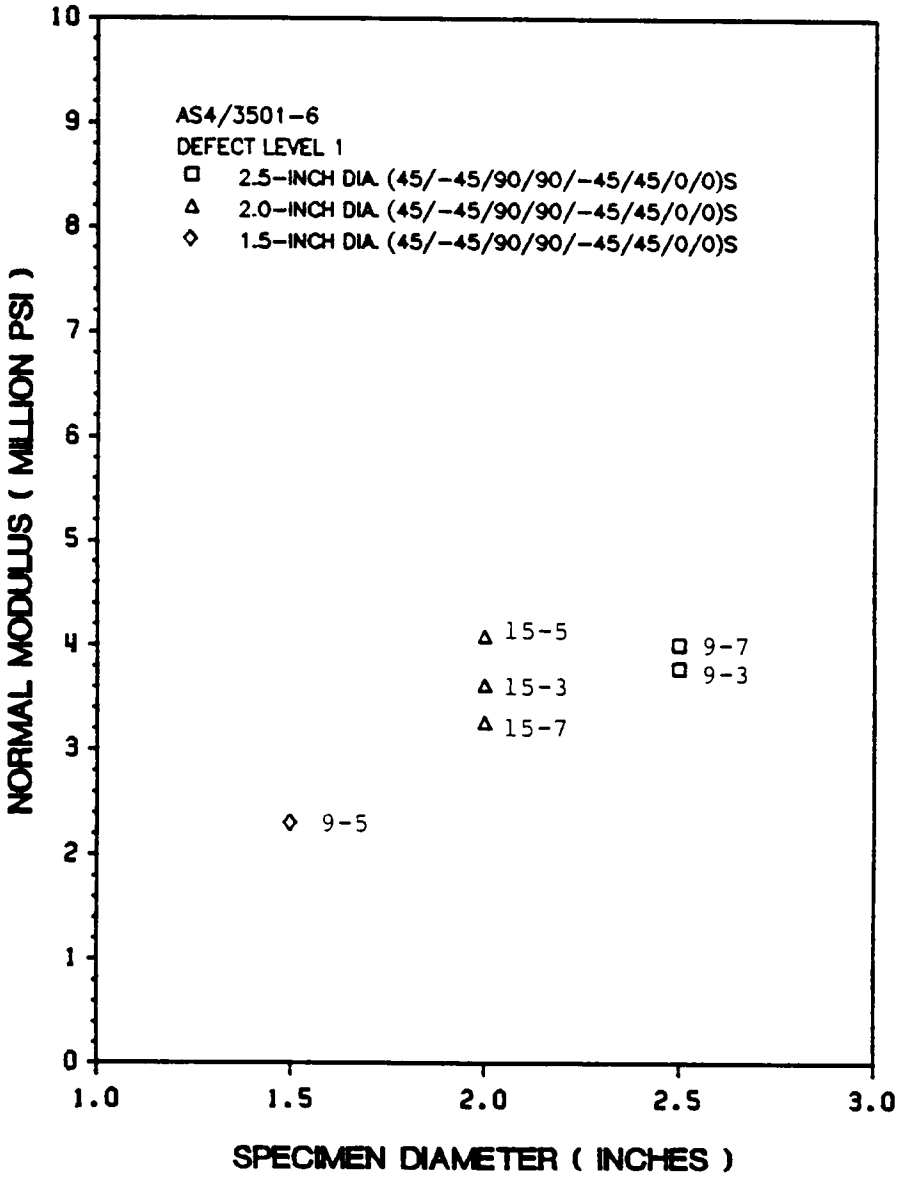

Figure 22. **The Effect of Specimen Diameter on Combined Out-of-Plane** Modulus.

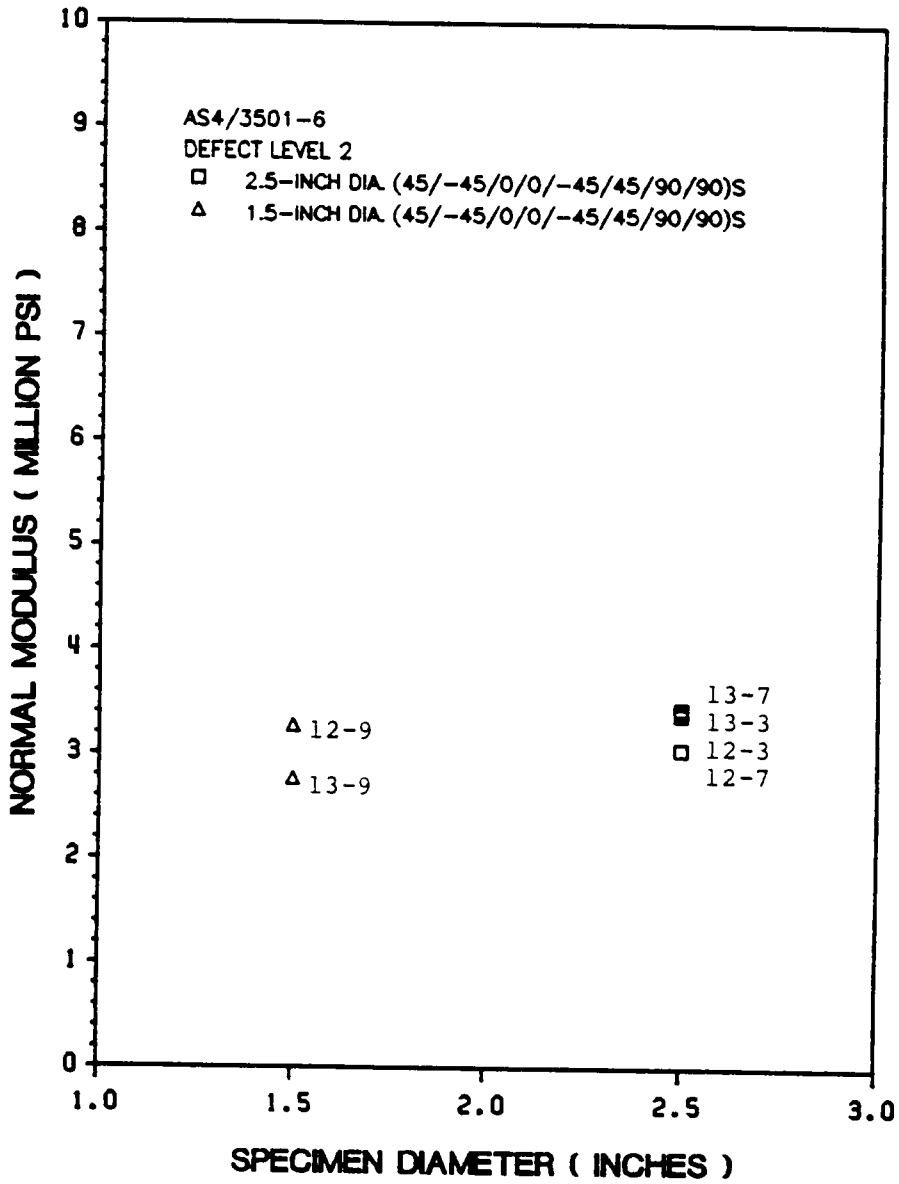

Figure 23. The Effect of Specimen Diameter on Combined Out-of-Plane Modulus.

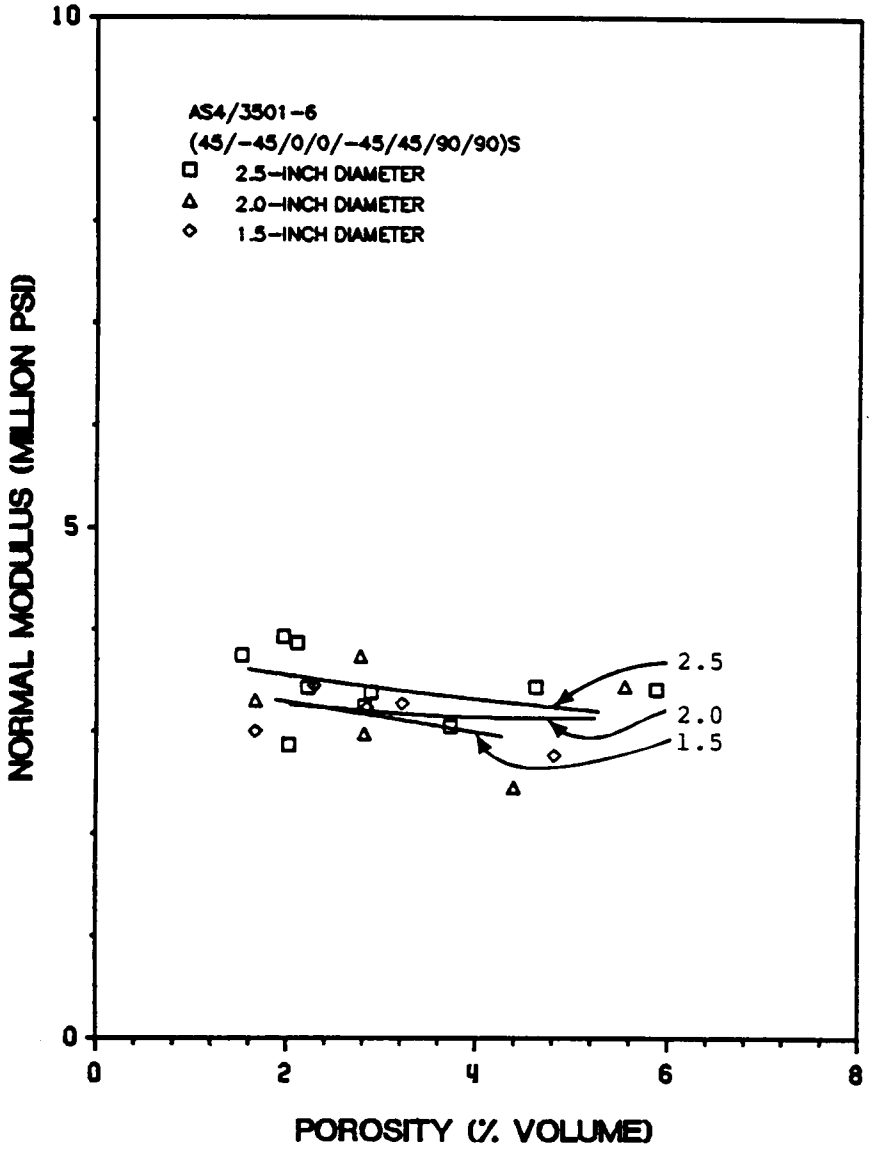

Figure 24. The Effect of Specimen Porosity on Combined Out-of-Plane Modulus.

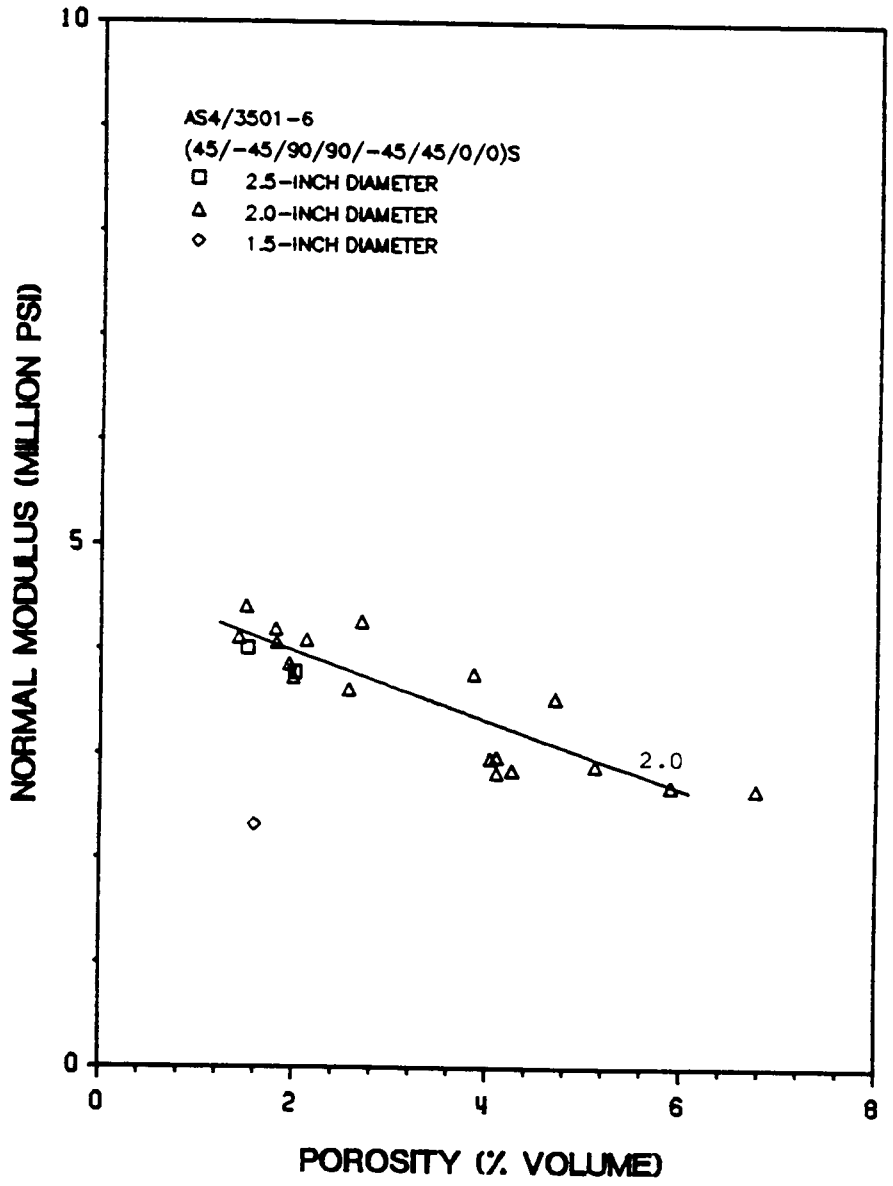

Figure 25. The Effect of Specimen Porosity on Combined Out-of-Plane Modulus.

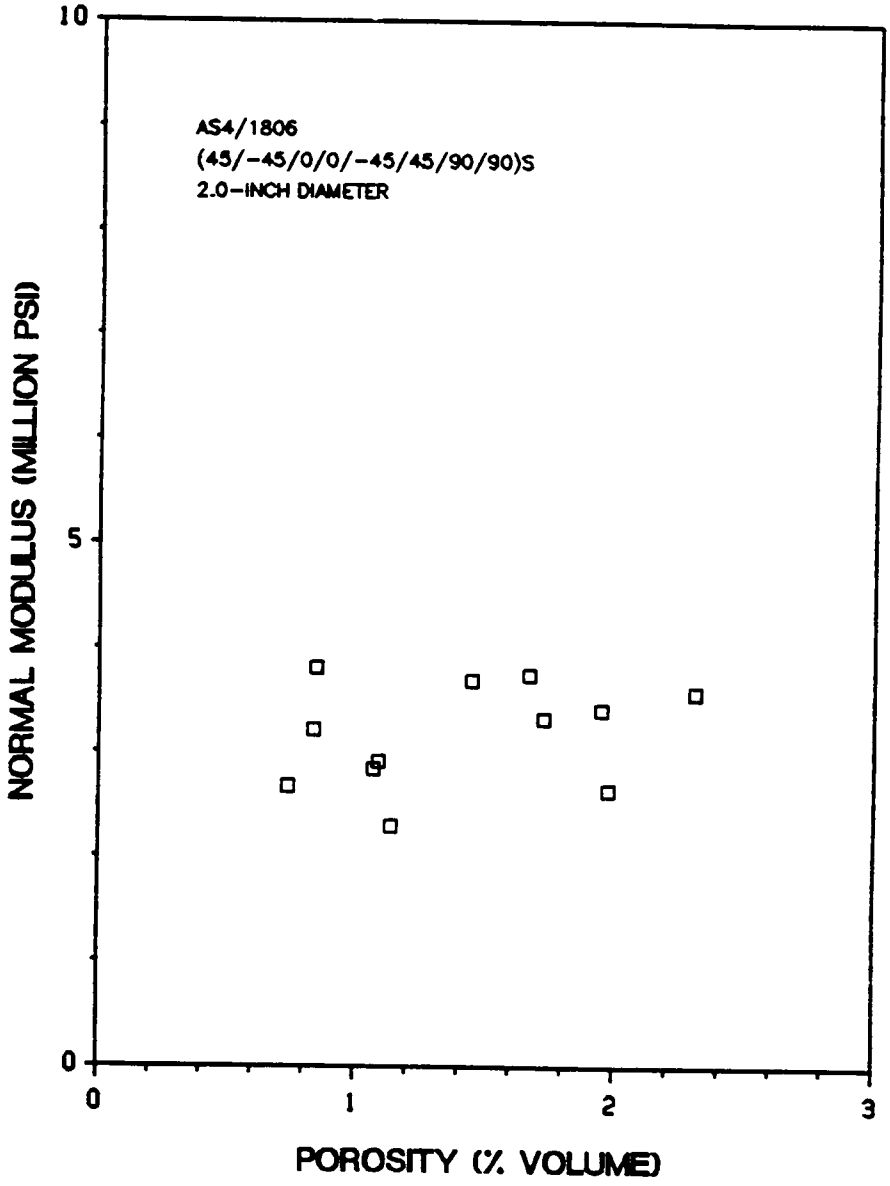

Figure 26. The Effect of Specimen Porosity on Combined Out-of-Plane Modulus.

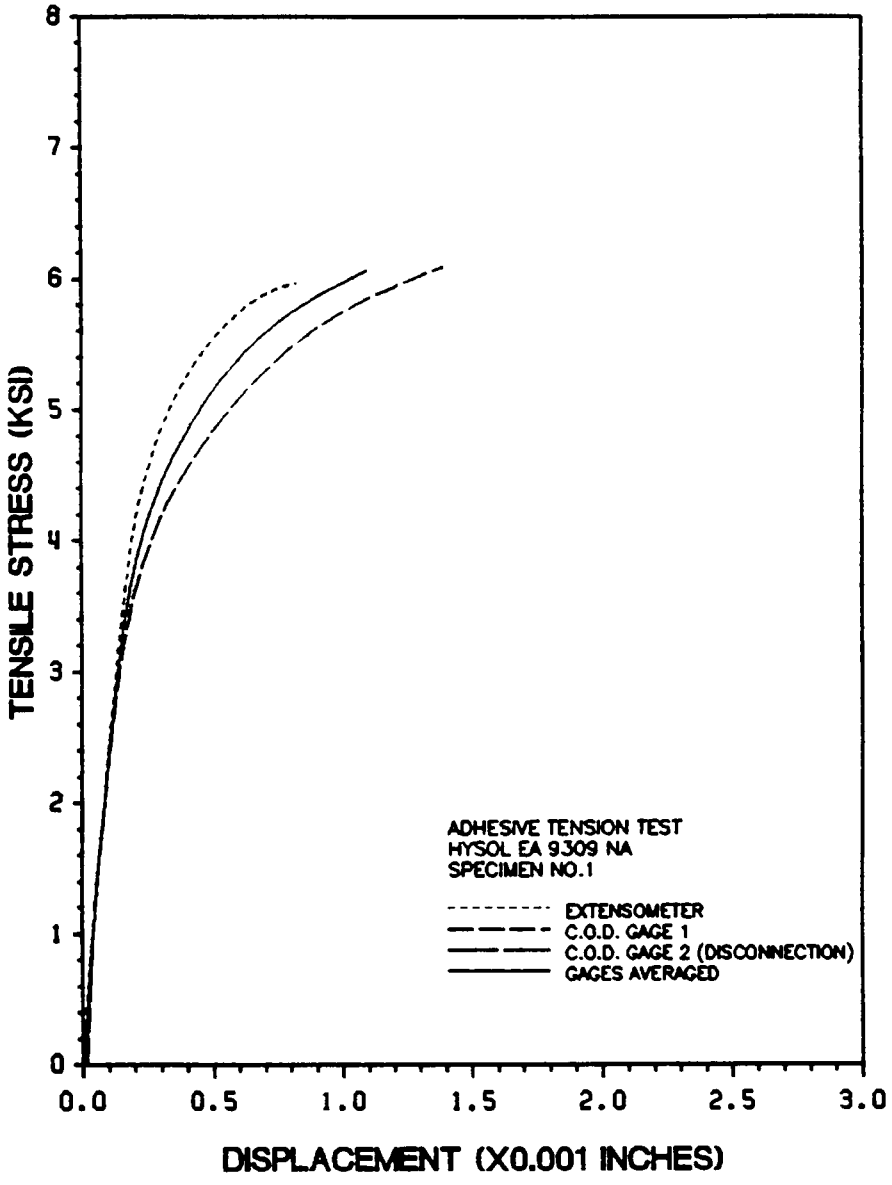

Figure 27. Adhesion Tensile Response.

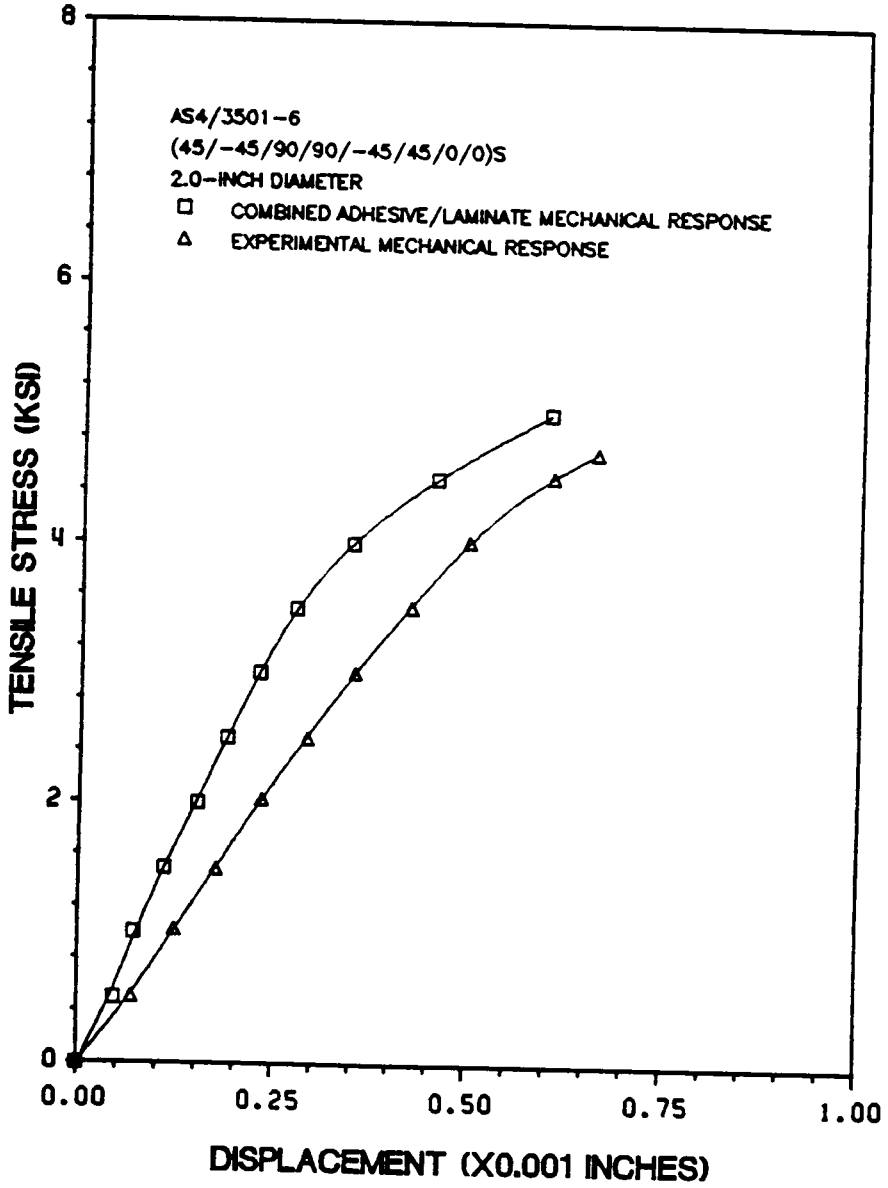

Figure 28. Comparison of Combined Tensile Response.

Table 12. Summary of Laminate Properties Determined by Compression Tests.

Specimen	E_x (Msi)	ν_{xy}
AS4/1806 (Angle 8)	6.4	0.30
$(\pm 45/90_2/\mp 45/0_2)_s$	6.8	0.33
Defect Level 0	6.5	0.31
average	6.5	0.31
AS4/3501-6 (Angle 4)	6.7	0.36
$(\pm 45/90_2/\mp 45/0_2)_s$	6.9	0.29
Defect Level 0	7.0	0.30
average	6.9	0.31
AS4/3501-6 (Angle 2)	6.8[1]	0.36
$(\pm 45/0_2/\mp 45/90_2)_s$	6.9[1]	0.29
Defect Level 1	6.3[1]	0.26
average	6.7	0.30
AS4/3501-6 (Angle 14)	5.9	0.26
$(\pm 45/90_2/\mp 45/0_2)_s$	7.0	0.25
Defect Level 2	7.2	0.28
average	6.7	0.26
AS4/1806 (Angle 16)	6.3	0.34
$(\pm 45/90_2/\mp 45/0_2)_s$	5.8	0.28
Defect Level 2	6.0	0.33
average	6.0	0.32
AS4/3501-6 (Angle 17)	6.9	0.33
$(\pm 45/0_2/\mp 45/90_2)_s$	—[2]	-
Defect Level 3	7.2	0.36
average	7.1	0.34
AS4/3501-6 (Angle 18)	6.9	0.31
$(\pm 45/90_2/\mp 45/0_2)_s$	6.8	0.31
Defect Level 3	6.9	0.29
average	6.9	0.31

[1] Specimen not tightly constrained at ends during testing.
[2] Specimen had a wire in it.

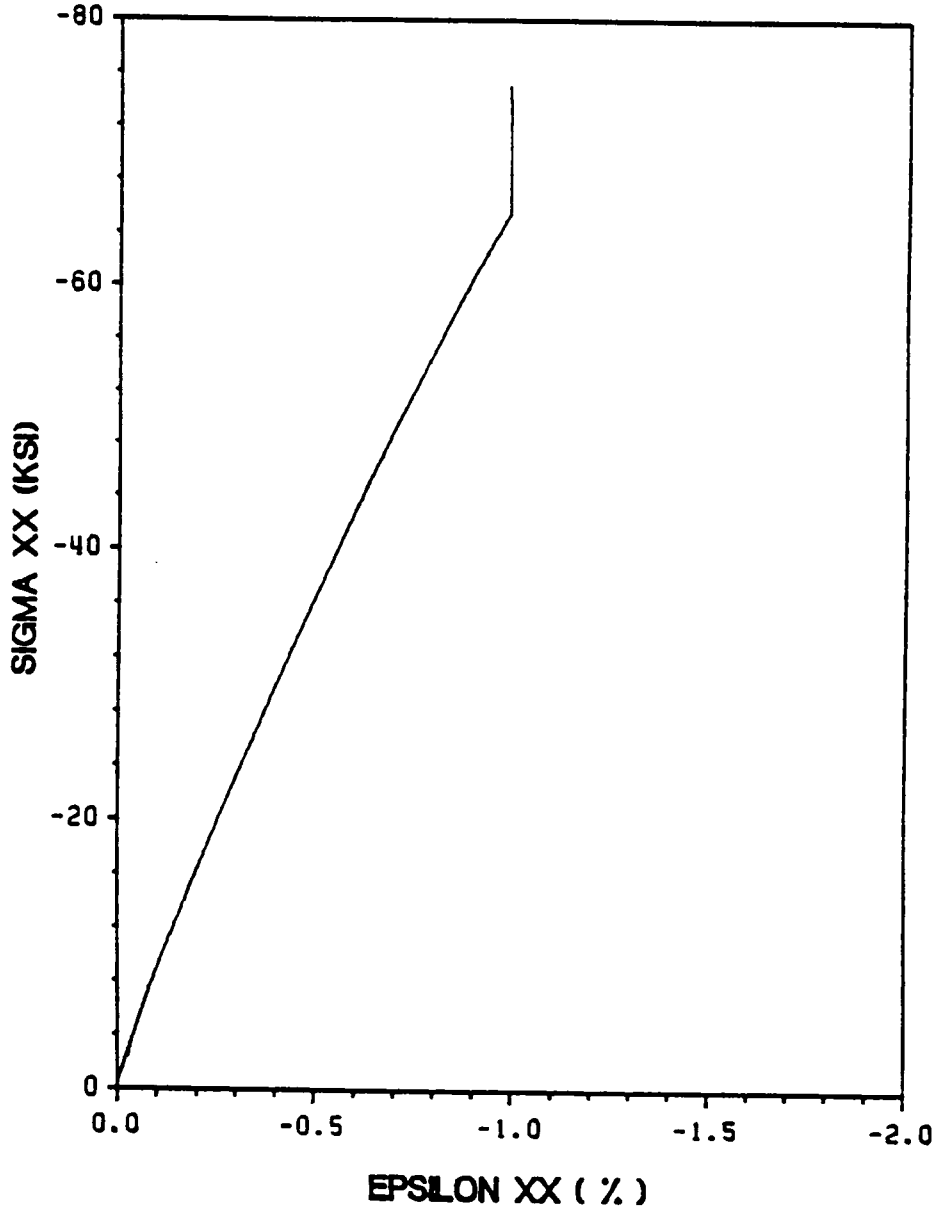

Figure 29. Stress-Strain Compressive Response.

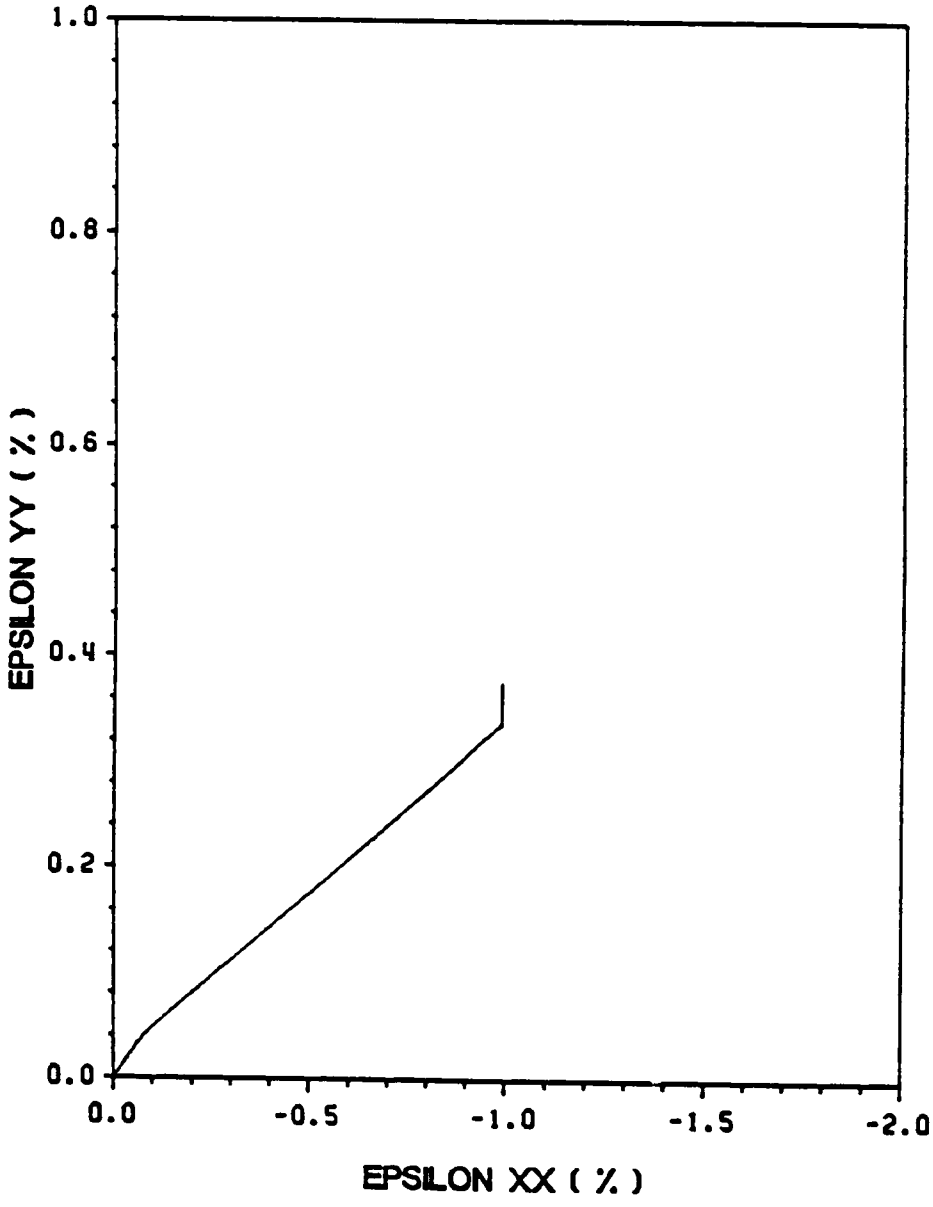

Figure 30. Strain-Strain Compressive Response.

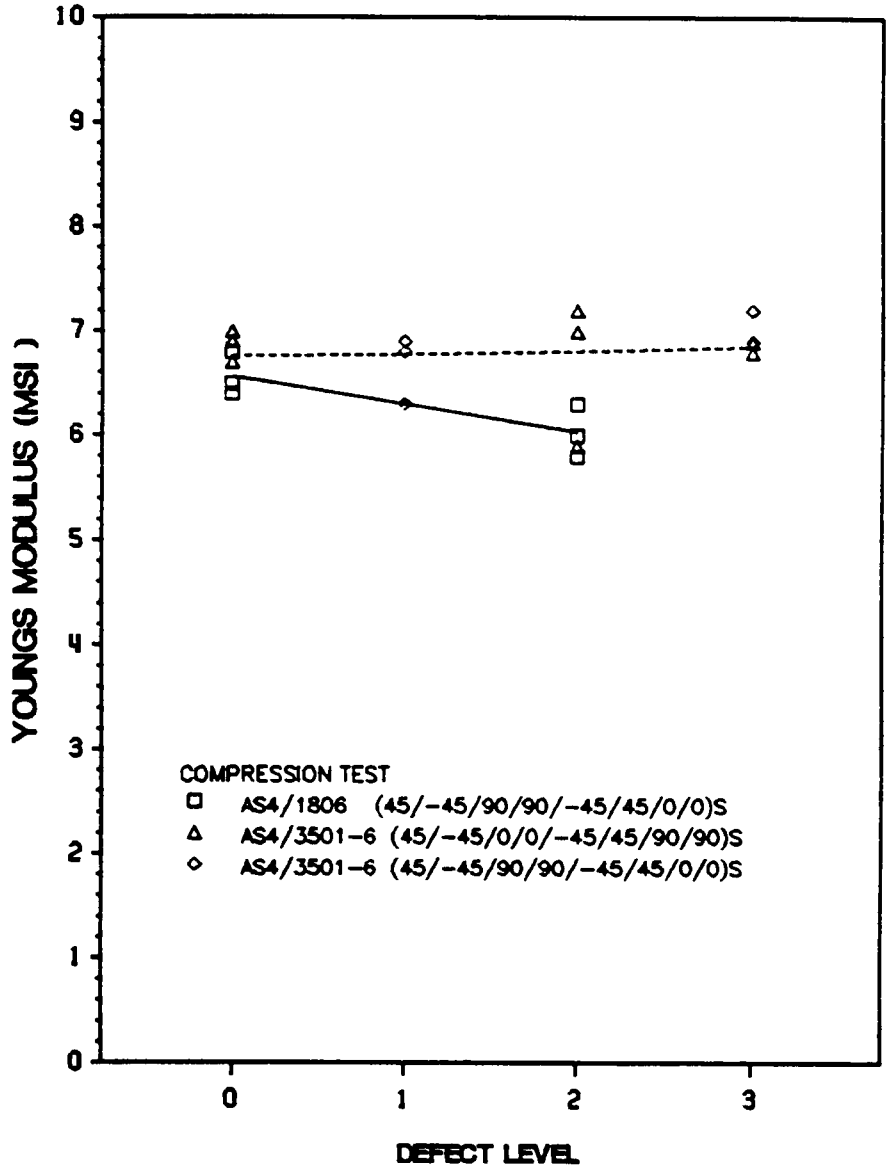

Figure 31. In-Plane Modulus as a Function of Defect Level.

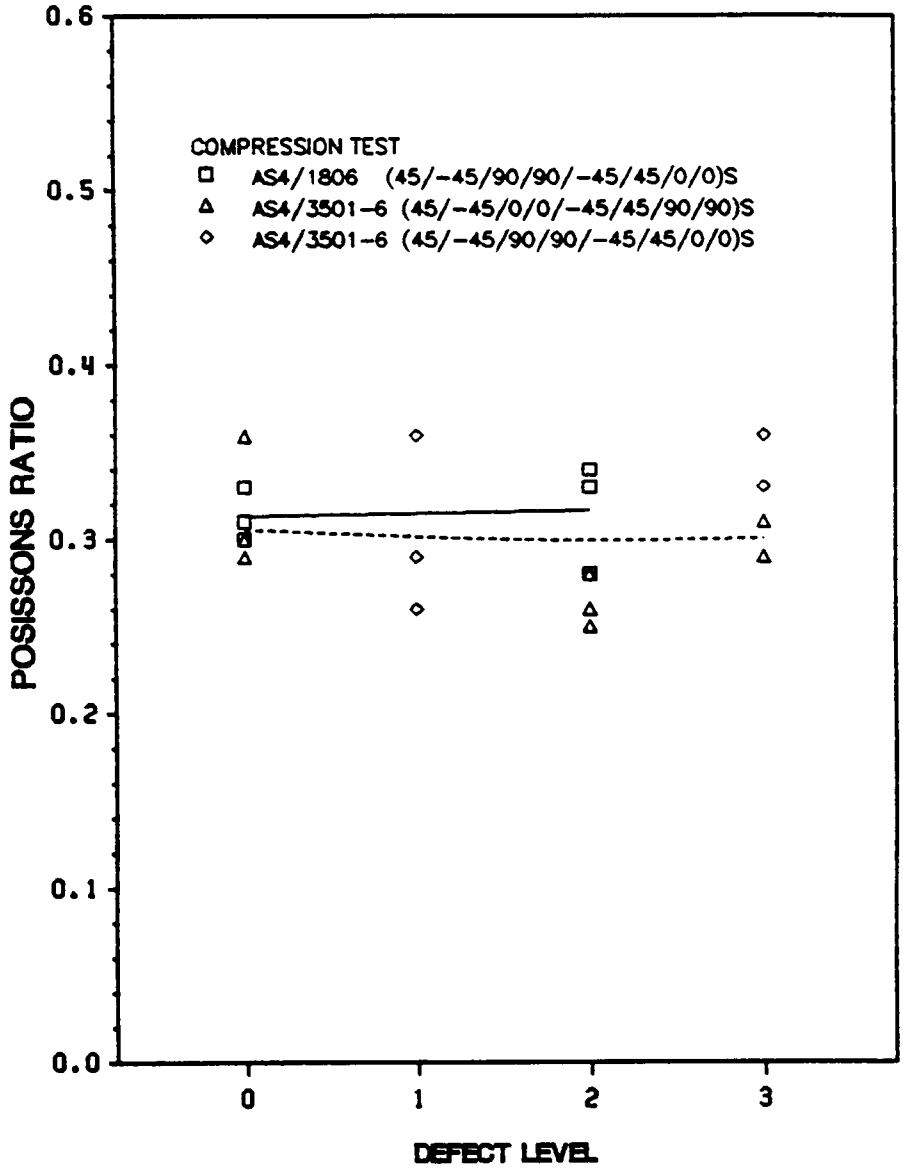

Figure 32. In-Plane Poisson's Ratio as a Function of Defect Level.

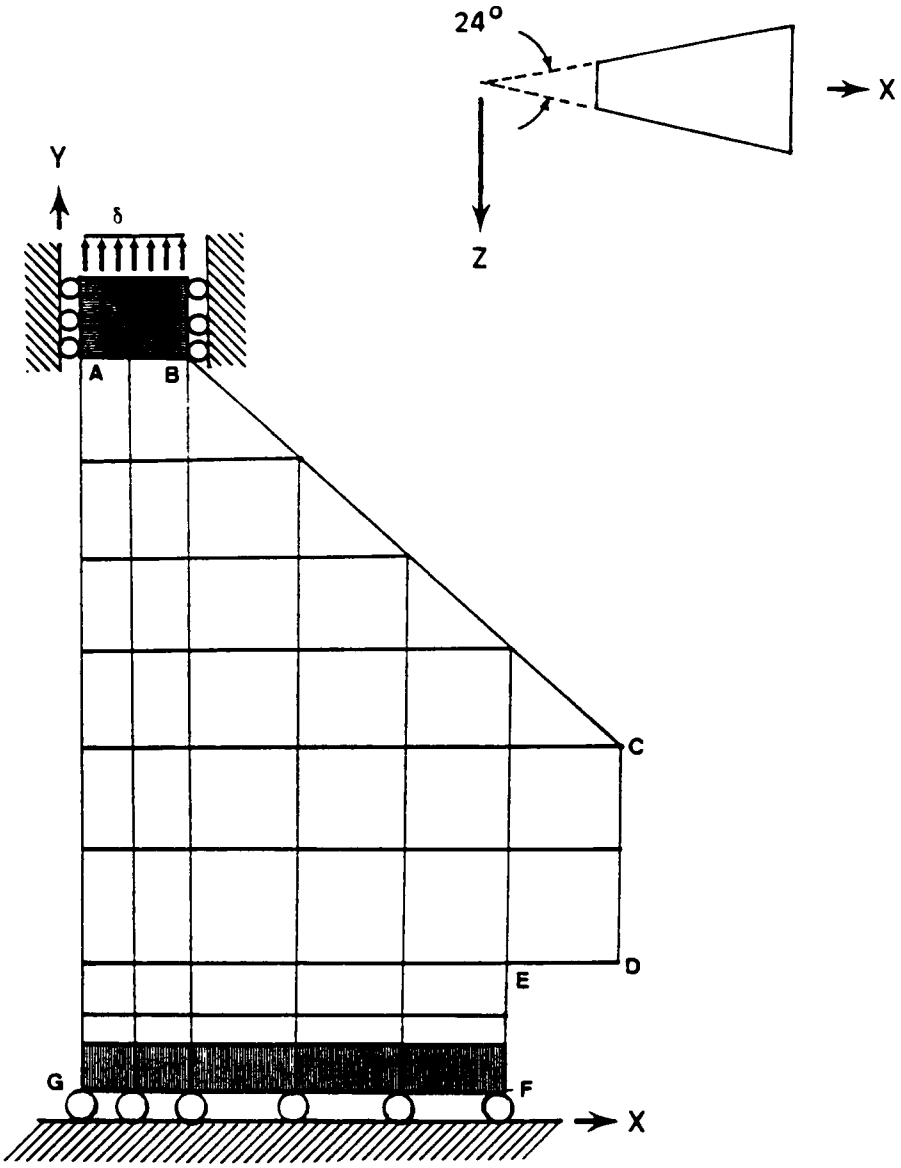

Figure 33. Finite Element Mesh.

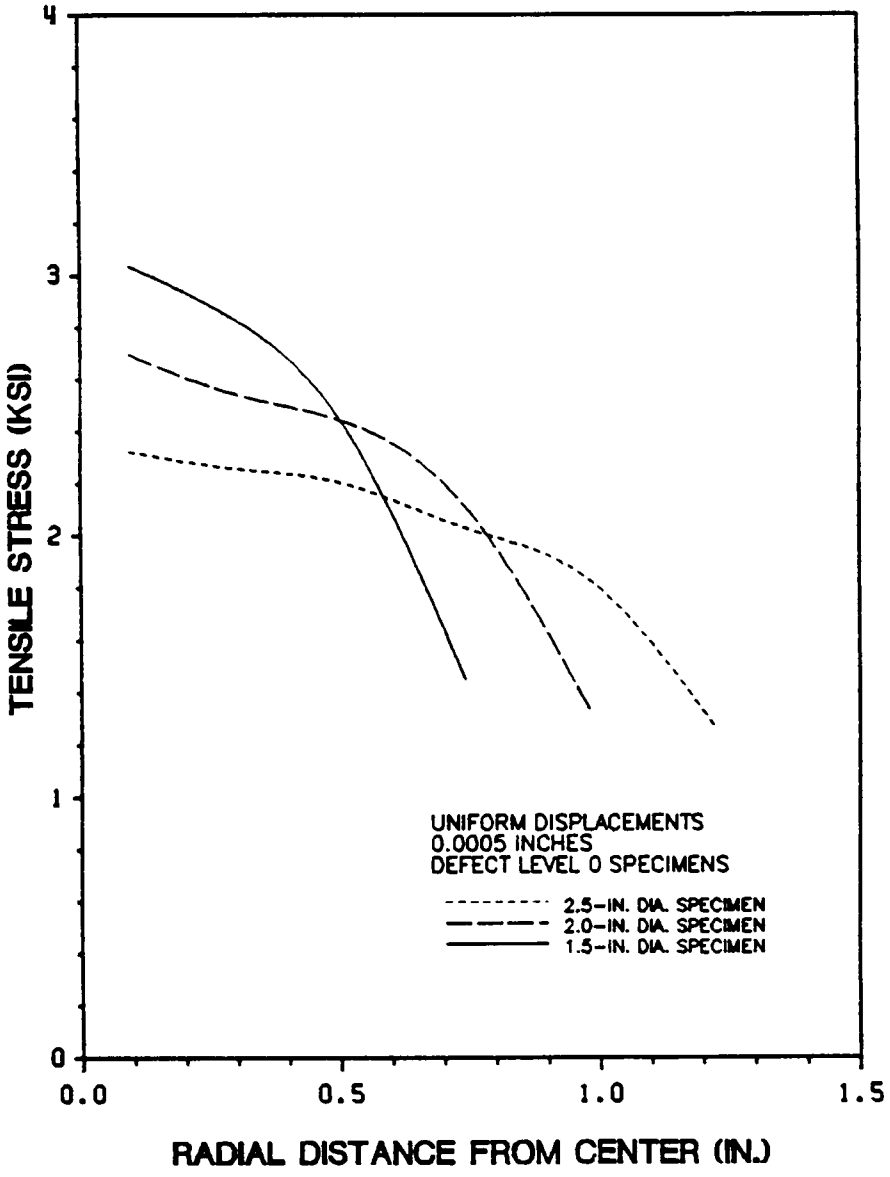

Figure 34. Tensile Stresses in Steel Fixture Near Bond Surface.

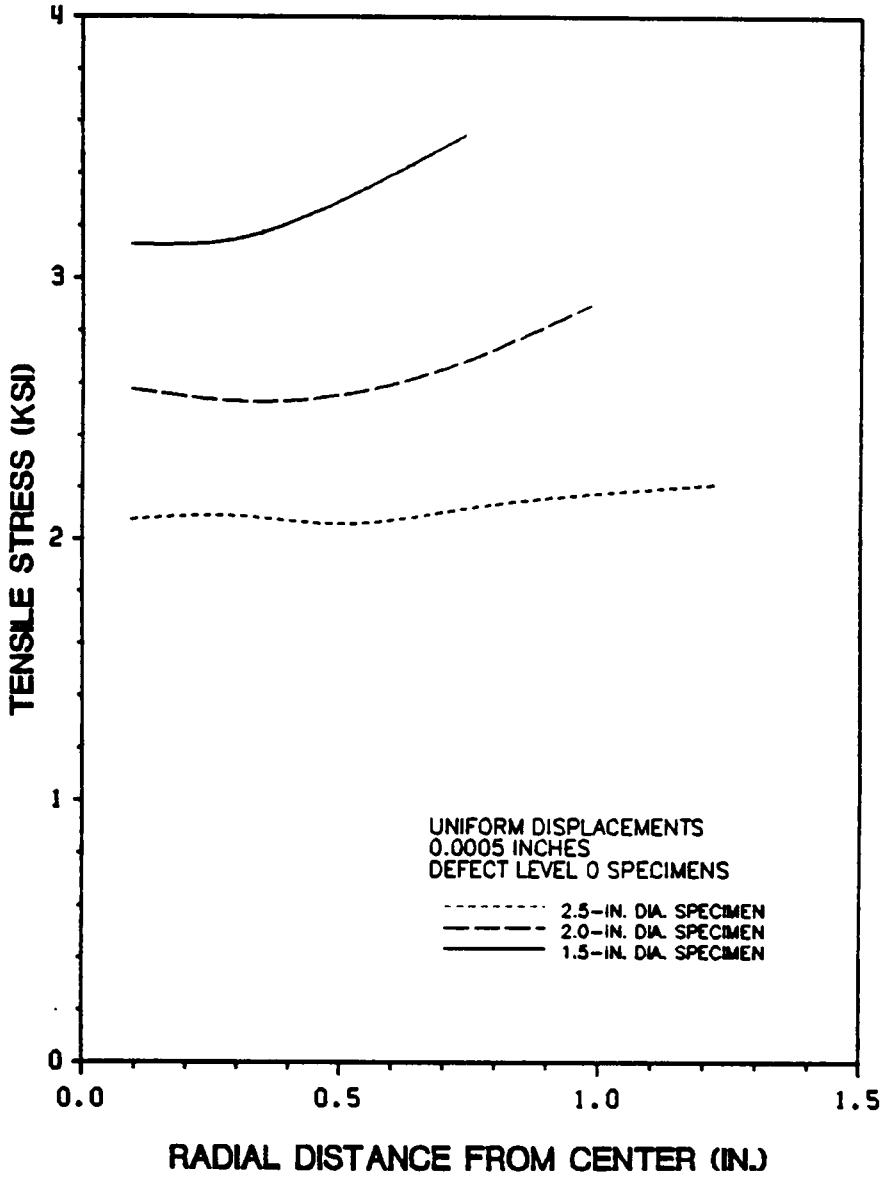

Figure 35. Tensile Stresses in a Laminate with a Center-Hole.

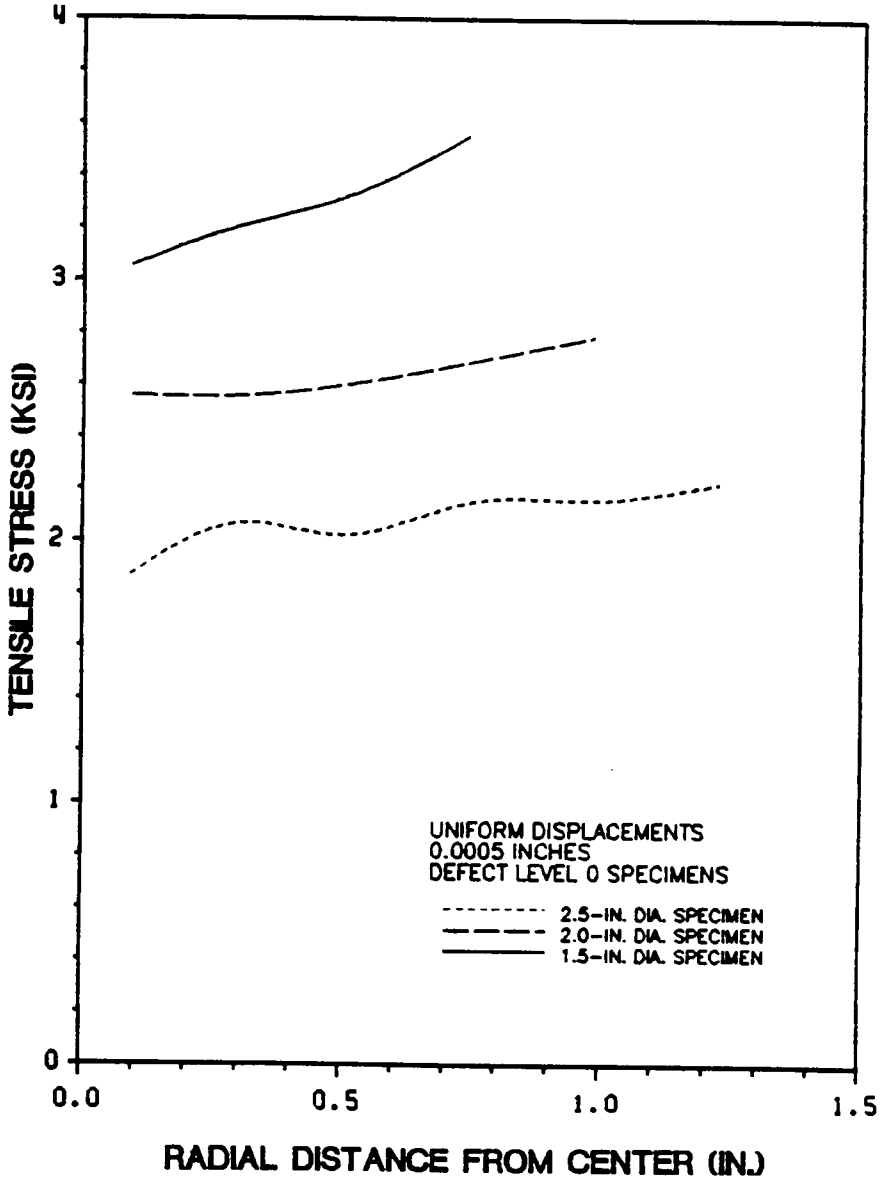

Figure 36. Tensile Stresses in a Laminate with No Center-Hole.

Table 13. Modified Out-of-Plane Modulus for AS4/3501-6 Specimens (1).

$(\pm 45/0_2/\mp 45/90_2)s$ AS4/3501-6

Defect Level	Specimen Diameter (in.)	Average Exper. E_z (x 10^6 psi)	Factor	Modified E_z (x 10^6psi)
0	2.5	3.705	1.027	3.695
1	2.5	3.156	1.008	3.131
2	2.5	3.453	1.141	3.026
1	2.0	3.526	1.035	3.407
3	2.0	2.785	1.558	1.788
0	1.5	3.180	1.037	2.997
1	1.5	-	-	-
2	1.5	3.007	1.165	2.581

Table 14. Modified Out-of-Plane Modulus for AS4/3501-6 Specimens (2).

$(\pm 45/90_2/\mp 45/0_2)s$ AS4/3501-6

Defect Level	Specimen Diameter (in.)	Average Exper. E_z (x 10^6 psi)	Factor	Modified E_z (x 10^6psi)
1	2.5	3.902	1.008	3.871
0	2.0	4.068	1.041	3.908
1	2.0	3.998	1.035	3.863
2	2.0	2.908	1.041	2.793
3	2.0	3.124	1.558	2.005
1	1.5	-	-	-

Table 15. Modified Out-of-Plane Modulus for AS4/1806 Specimens.

$(\pm 45/0_2/\mp 45/90_2)S$ AS4/1806

Defect Level	Specimen Diameter (in.)	Average Exper. E_z (x 10^6 psi)	Factor	Modified E_z (x 10^6psi)
0	2.0	3.432	1.055	3.253
2	2.0	2.939	1.526	1.926

Table 16. Stresses on the Laminate During Out-of-Plane Testing.

$(\pm 45/0_2/\mp 45/90_2)s$ AS4/3501-6

Defect Level	Specimen Diameter (in.)	Radial Distance (in.)	σ_y (psi)	τ_{xy} (psi)
0	2.5	0.195	2364.0	-22.771
		0.398	2432.6	18.151
		0.621	2448.7	-60.854
		0.862	2557.8	102.19
		1.103	2528.3	-7.619
1	2.5	0.195	2062.3	-44.678
		0.398	2098.1	23.604
		0.621	2107.5	-46.873
		0.862	2167.3	90.333
		1.103	2153.3	-24.394
2	2.5	0.195	2061.9	-4.998
		0.398	2097.7	23.221
		0.621	2107.4	-47.160
		0.862	2167.1	90.109
		1.103	2153.7	-24.625
1	2.0	0.195	2511.2	50.322
		0.398	2567.9	-63.944
		0.621	2660.4	96.586
		0.862	2739.5	-15.541
3	2.0	0.195	2501.5	37.613
		0.398	2563.0	-73.560
		0.621	2657.1	89.633
		0.862	2747.5	-22.225
0	1.5	0.195	3129.5	5.1768
		0.398	3290.3	101.80
		0.621	3366.4	-17.972
2	1.5	0.195	3123.2	1.2416
		0.398	3281.3	99.340
		0.621	3365.1	-20.718

Note: σ_y and τ_{xy} are the averaged axial and shear stresses at the element center.

Table 17. Stresses on the Laminate During Out-of-Plane Testing.

$(\pm 45/90_2/\mp 45/0_2)s$ AS4/3501-6

Defect Level	Specimen Diameter (in.)	Radial Distance (in.)	σ_y (psi)	τ_{xy} (psi)
1	2.5	0.195	2065.2	-9.913
		0.398	2100.5	26.149
		0.621	2108.7	-44.890
		0.862	2168.9	91.929
		1.103	2151.2	-22.782
0	2.0	0.195	2515.0	51.699
		0.398	2572.8	-60.983
		0.621	2665.2	97.7663
		0.862	2739.6	-13.557
1	2.0	0.195	2513.5	52.787
		0.398	2569.7	-61.642
		0.621	2662.1	98.102
		0.862	2738.0	-13.889
2	2.0	0.195	2507.7	46.670
		0.398	2565.4	-67.243
		0.621	2658.2	94.429
		0.862	2741.6	-17.853
3	2.0	0.195	2504.0	40.149
		0.398	2564.6	-71.410
		0.621	2658.3	91.007
		0.862	2746.3	-20.801

Note: σ_y and τ_{xy} are the averaged axial and shear stresses at the element center.

Table 18. Stresses on the Laminate During Out-of-Plane Testing.

$(\pm 45/0_2/\mp 45/90_2)s$ AS4/1806

Defect Level	Specimen Diameter (in.)	Radial Distance (in.)	σ_y (psi)	τ_{xy} (psi)
0	2.0	0.195	2508.3	47.933
		0.398	2567.1	-66.318
		0.621	2660.2	96.268
		0.862	2734.6	-14.315
2	2.0	0.195	2495.4	37.695
		0.398	2559.8	-76.576
		0.621	2654.1	92.086
		0.862	2726.3	-15.004

Note: σ_y and τ_{xy} are the averaged axial and shear stresses at the element center.

Figure 37. Zeiss IBAS/SEM-IPS Image Processing System.

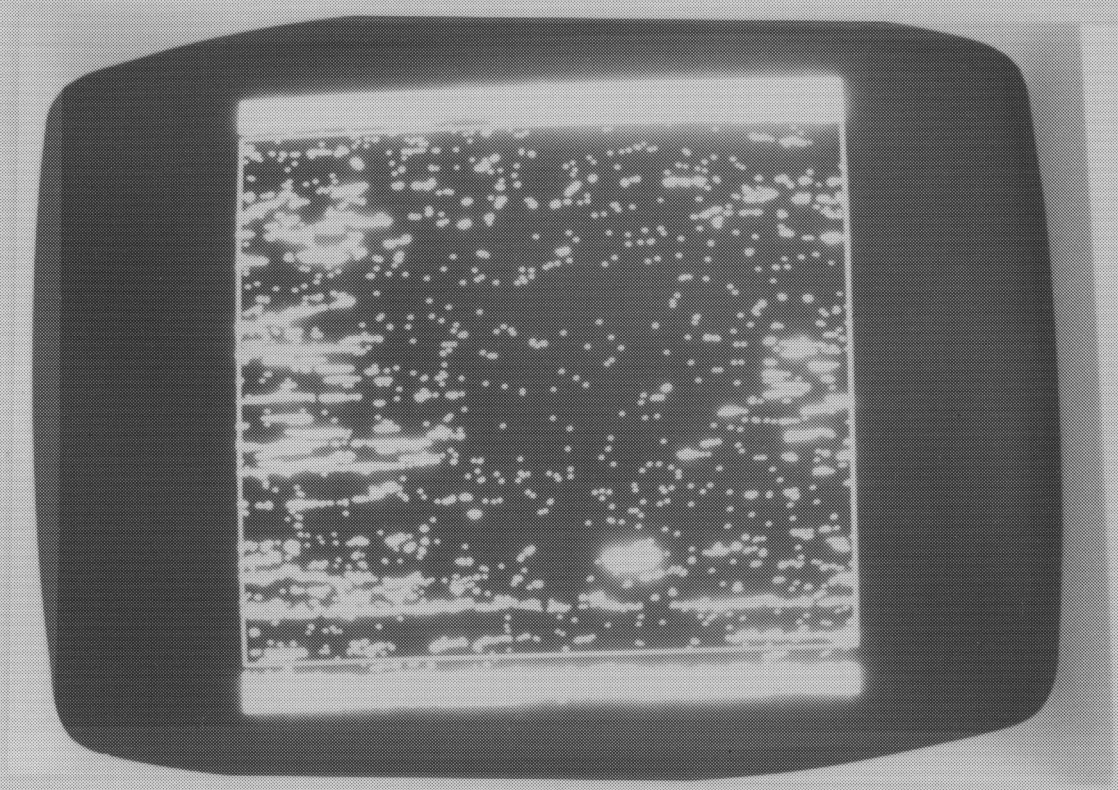

Figure 38. Image Processing Binary Frame.

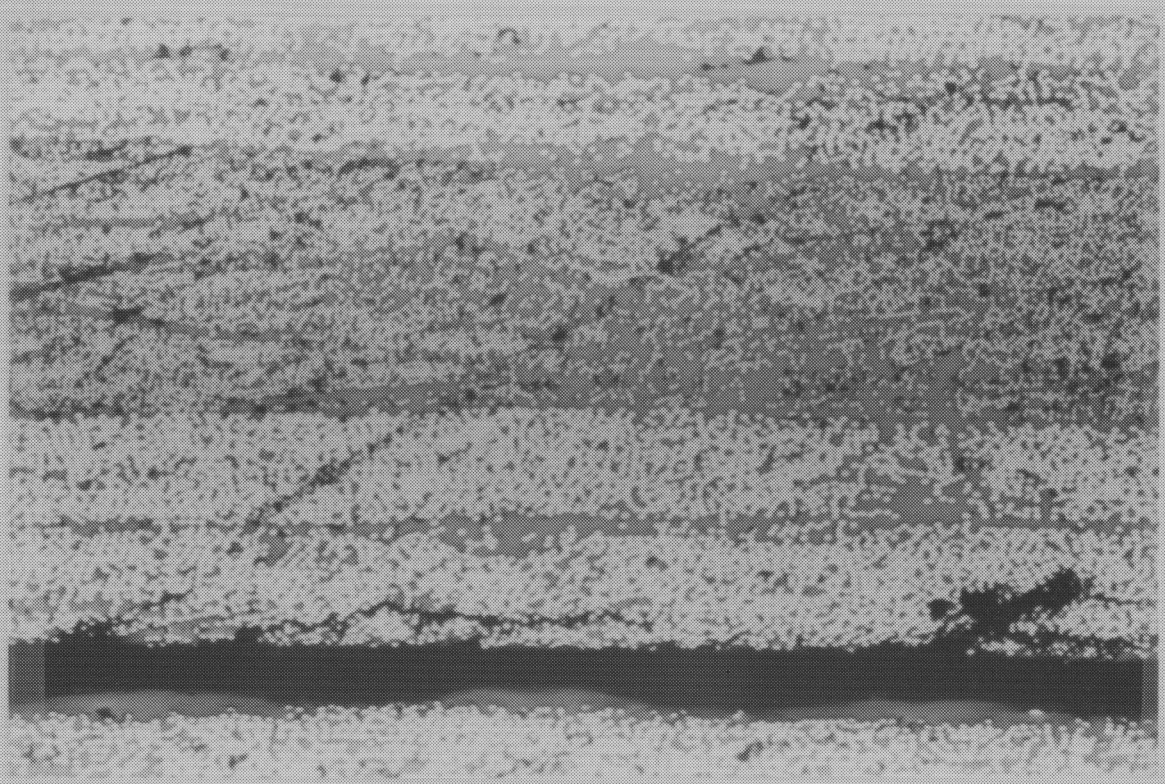

Figure 39. Surface Irregularities Related to Polishing.

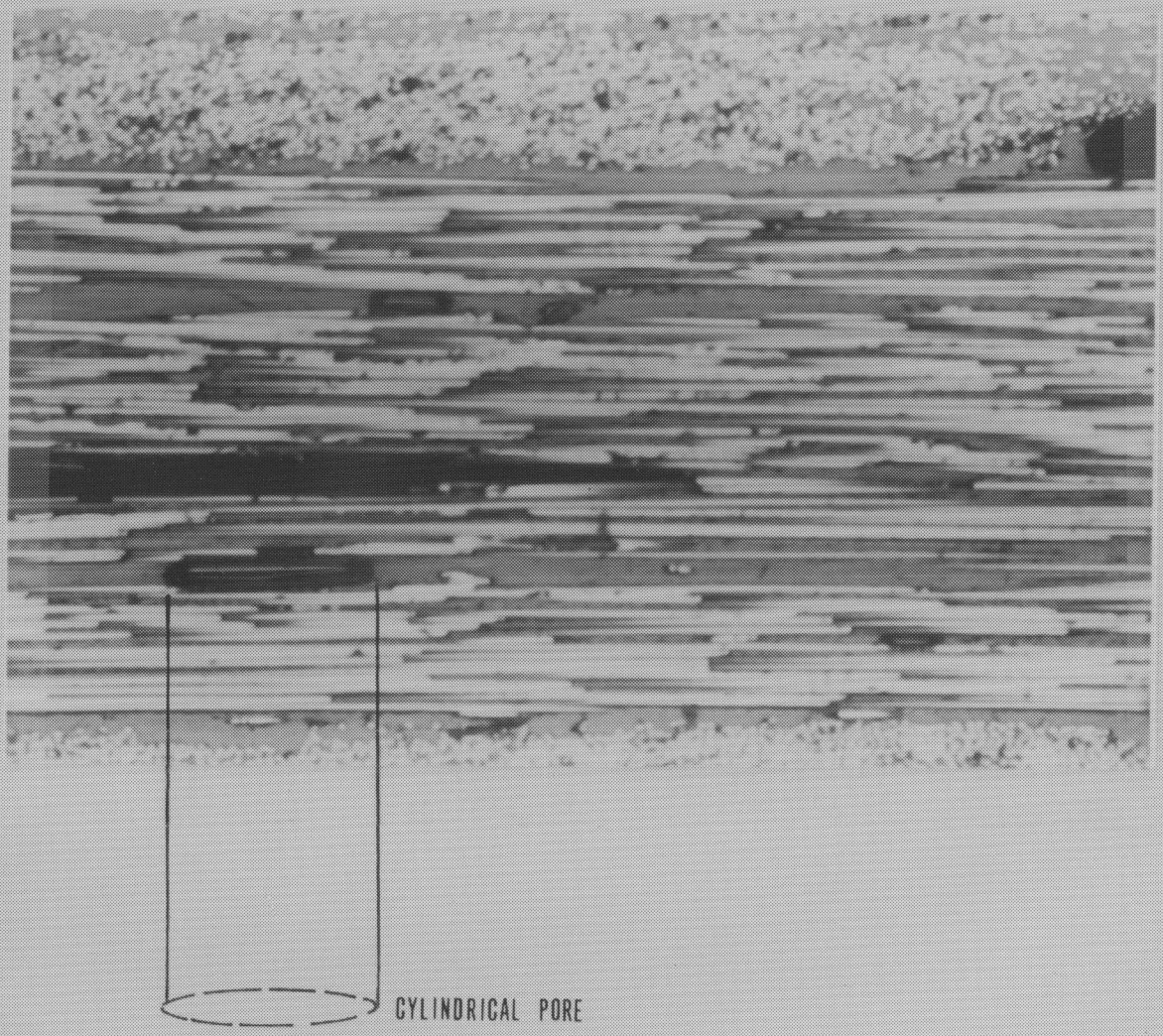

Figure 40. Cylindrical Pores Oriented Parallel with Fiber Direction.

Table 19. Image Processing Data Parameters for AS4/3501-6 Specimens (1).

$(\pm 45/0_2/\mp 45/90_2)s$ AS4/3501-6

Specimen I.D.No.	Average Length (in.)	Average Diameter (in.)	Angle	Void Content (%)
5-3	285.7	14.93	55.49	0.2133
1-3	309.5	20.32	57.70	0.3680
10-3	557.0	20.77	63.08	1.267
12-3	371.4	21.56	54.54	1.318
13-7	799.9	25.83	50.10	3.105
17-5	699.9	38.44	58.28	5.526
19-3	742.7	28.53	60.47	2.908
	538.0	24.34	56.23	

Table 20. Image Processing Data Parameters for AS4/3501-6 Specimens (2).

$(\pm 45/90_2/\mp 45/0_2)s$ AS4/3501-6

Specimen I.D.No.	Average Length (in.)	Average Diameter (in.)	Angle	Void Content (%)
4-7	159.7	17.16	67.78	0.2049
6-3	157.1	20.15	57.45	0.4296
15-7	304.7	24.14	65.59	0.7534
11-3	692.5	31.15	65.61	3.432
14-5	1118.0	28.95	64.97	4.800
18-7	767.7	31.89	50.15	5.576
20-3	566.6	30.35	65.03	6.956
9-7	147.7	19.09	56.57	0.5289
9-5	190.8	18.17	53.91	0.4182
	456.1	24.56	60.8	

Table 21. Image Processing Data Parameters for AS4/1806 Specimens.

$(\pm 45/0_2/\mp 45/90_2)s$ AS4/1806

Specimen I.D.No.	Average Length (in.)	Average Diameter (in.)	Angle	Void Content (%)
7-3	402.4	18.98	46.23	0.2924
8-3	204.1	18.24	58.03	0.3002
3-7	790.3	21.62	65.43	2.178
16-7	348.5	19.74	60.63	1.759
	---	---	---	
	402.4	18.98	57.58	

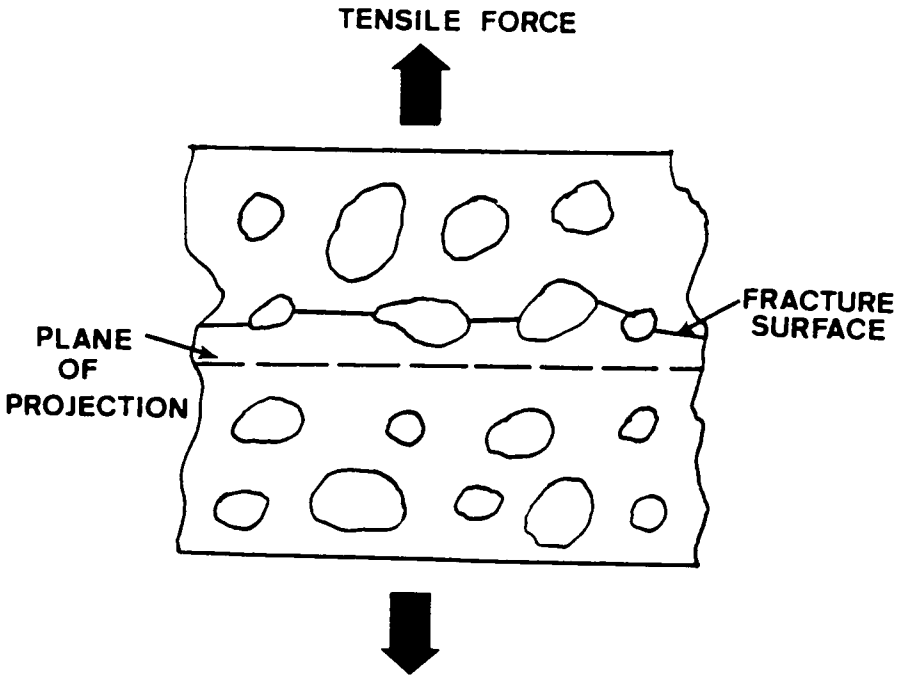

Figure 41. Section of Porous Specimen Projected Area of Fracture Surface.

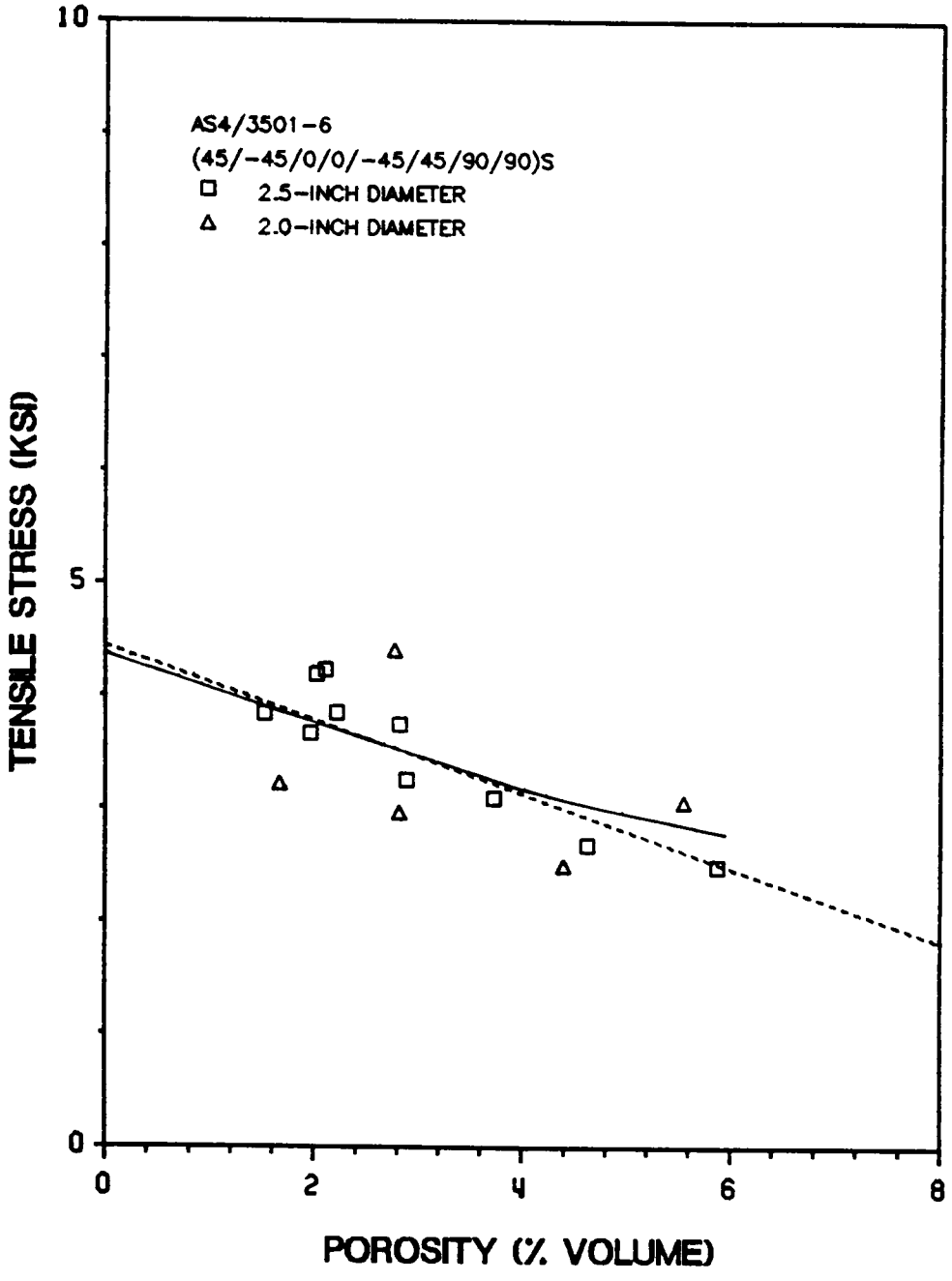

Figure 42. Predicted Strength of AS4/3501-6 $(\pm 45/0_2/\mp 45/90_2)_S$

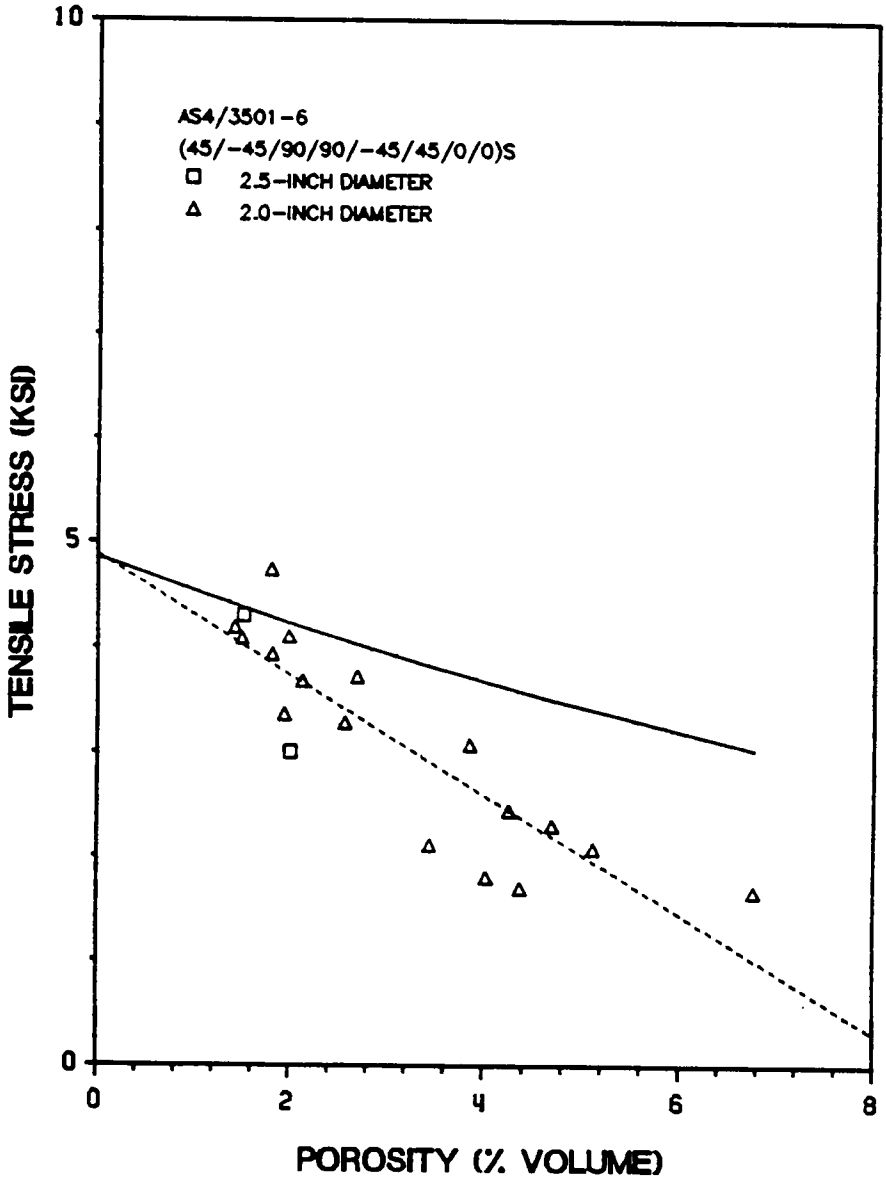

Figure 43. Predicted Strength of AS4/3501-6 ($\pm 45/90_2/\mp 45/0_2)_S$

9.0 References

1. Sun, C.T., and Kelly, S.R. "Failure Analysis of Composite Angle Structures," Developments in the Science and Technology of Composite Materials; Proceedings of the First European Conference on Composite Materials and Exhibition, Bordeaux France, September 1985, pp. 24-27.

2. Chang, F.K, and Springer, G.S. "The Strengths of Fiber Reinforced Composite Bends," Journal of Composite Materials, Vol. 20, January 1986, pp. 30-45.

3. Yokota, M.J. " In-Process Controlled Curing of Resin Matrix Composites," SAMPE Journal, Vol. 14, July/August 1978, pp. 11-17.

4. Ryshkewitch, E. "Compression Strength of Porous Sintered Alumina and Zirconia," Journal of the American Ceramic Society, Vol. 36, February 1953, pp. 65-68.

5. Duckworth, W. "Discussion of Ryshkewitch Papers," Journal of the American

Ceramic Society, Vol. 36, February 1953, p. 68.

6. Knudsen, F.P. "Dependence of Mechanical Strength of Brittle Polycrystalline Specimens on Porosity and Grain Size," Journal of the American Ceramic Society, Vol. 42, August 1959, pp. 376-387.

7. Spriggs, R.M. "Expression for Effect of Porosity on Elastic Modulus of Polycrystalline Refractory Materials, Particulrly Aluminum Oxide," Journal of the American Ceramic Society, Vol. 44, December 1961, pp. 628-629.

8. Hasselman, D.P.H. "On the Dependence of the Elastic Moduli of Polycrystalline Refractory Materials," Journal of the American Ceramic Society, Vol. 45, September 1962, pp. 452-453.

9. Knudsen, F.P. "Effect of Porosity on Young's Modulus of Alumina," Journal of the American Ceramic Society, Vol. 45, February 1962, pp. 94-95.

10. Spriggs, R.M. and Brissette, L.A. "Expressions for Shear Modulus and Poisson's Ratio of Porous Refractory Oxides," Journal of the American Ceramic Society, Vol. 45, April 1962, pp. 198-199.

11. Spriggs, R.M., Brissette, L.A. and Vasilos, T. "Effect of Porosity on Elastic and Shear Modulus of Polycrystalline Magnesium Oxide," Journal of the American Ceramic Society, Vol 45, August 1962.

12. Spriggs, R.M. "Effect of Open and Closed Pores on Elastic Moduli of

Polycrystalline Alumina," Journal of the American Ceramic Society, Vol. 45, September 1962, p. 454.

13. Brown, S.D., Biddulph, R.B. and Wilcox, P.D. "A Strength-Porosity Relation Involving Different Pore Geometry and Orientation," Journal of the American Ceramic Society, Vol. 47, 1964, pp. 320-322.

14. Brassel, G.W., Horak, J.A and Butler, B.L. "Effects of Porosity on Strength of Carbon-Carbon Composites," Journal of Composite Materials, Vol. 9, July 1975, pp. 288-296.

15. Parker, B.M, and Waghorne, R.M.,"Surface Pretreatment of Carbon Fibre-Reinforced Composites for Adhesive Bonding", Composites, July 1982 pp. 280-287.

16. "Composites and Laminates, Edition 1", D.A.T.A. Inc., 1987.

17. Hidde, J.S.,"A User's Guide for the Materials Testing Package (Matpac2)", Composite Mechanics Group, Department of Engineering Science and Mechanics, Virginia Polytechnic Institute and State University, July 1987.

18. "Test Method for Void Content of Reinforced Plastics" 1987 Annual Book of ASTM Standards, Section 8.02 - Plastics, pp. 520-523.

19. SAS/GRAPH - User's Guide, Version 5 Edition, 1985, p. 70.

20. Harper, B.D.,Staab, G.H., and Chen, R.S.,"A Note on the Effects of Voids upon the Hygral and Mechanical Properties of AS4/3502 Graphite/Epoxy",

Journal of Composite Materials, Vol. 21, March 1987, pp. 280-298.

Appendix A. Out-Of-Plane Tensile Data

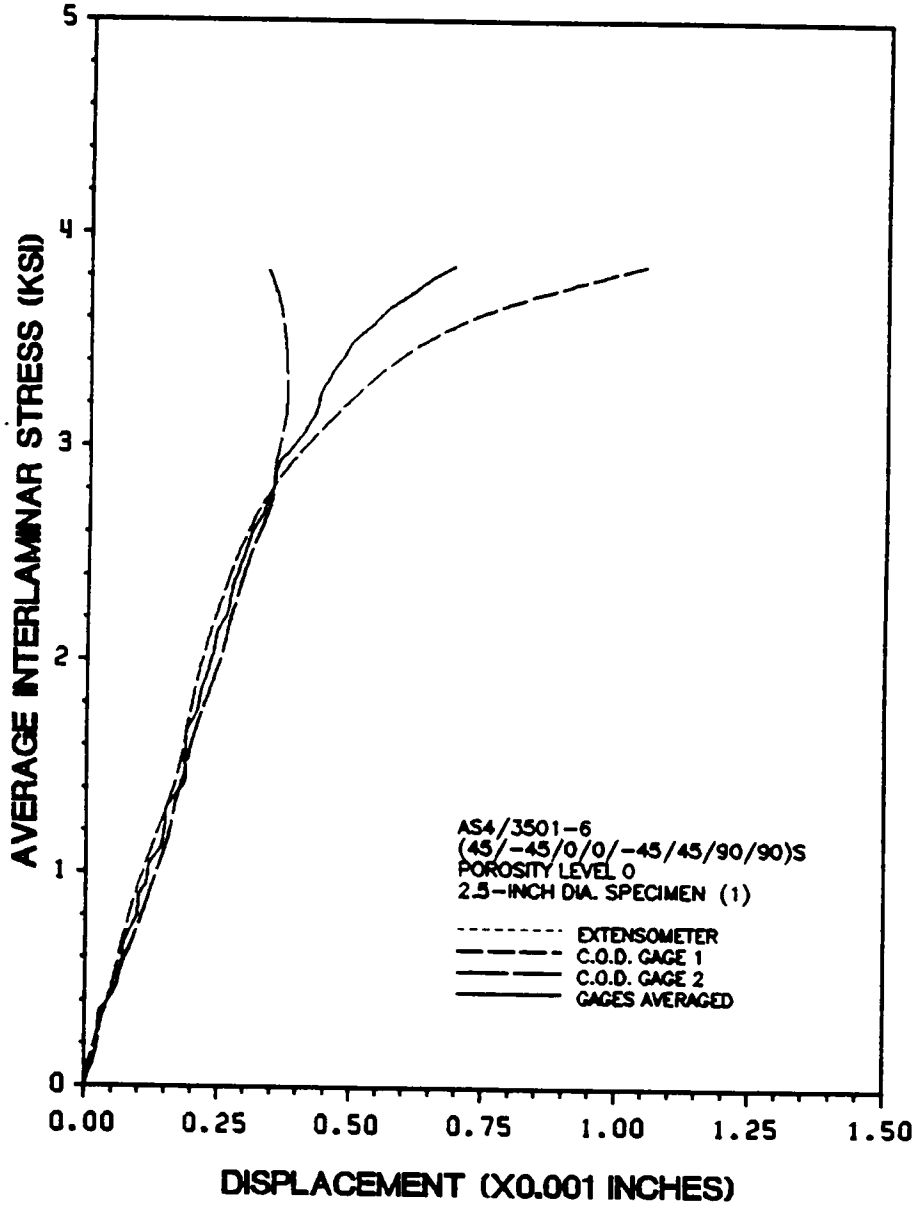

Figure 44. Flatwise Tensile Specimen Number 1-3.

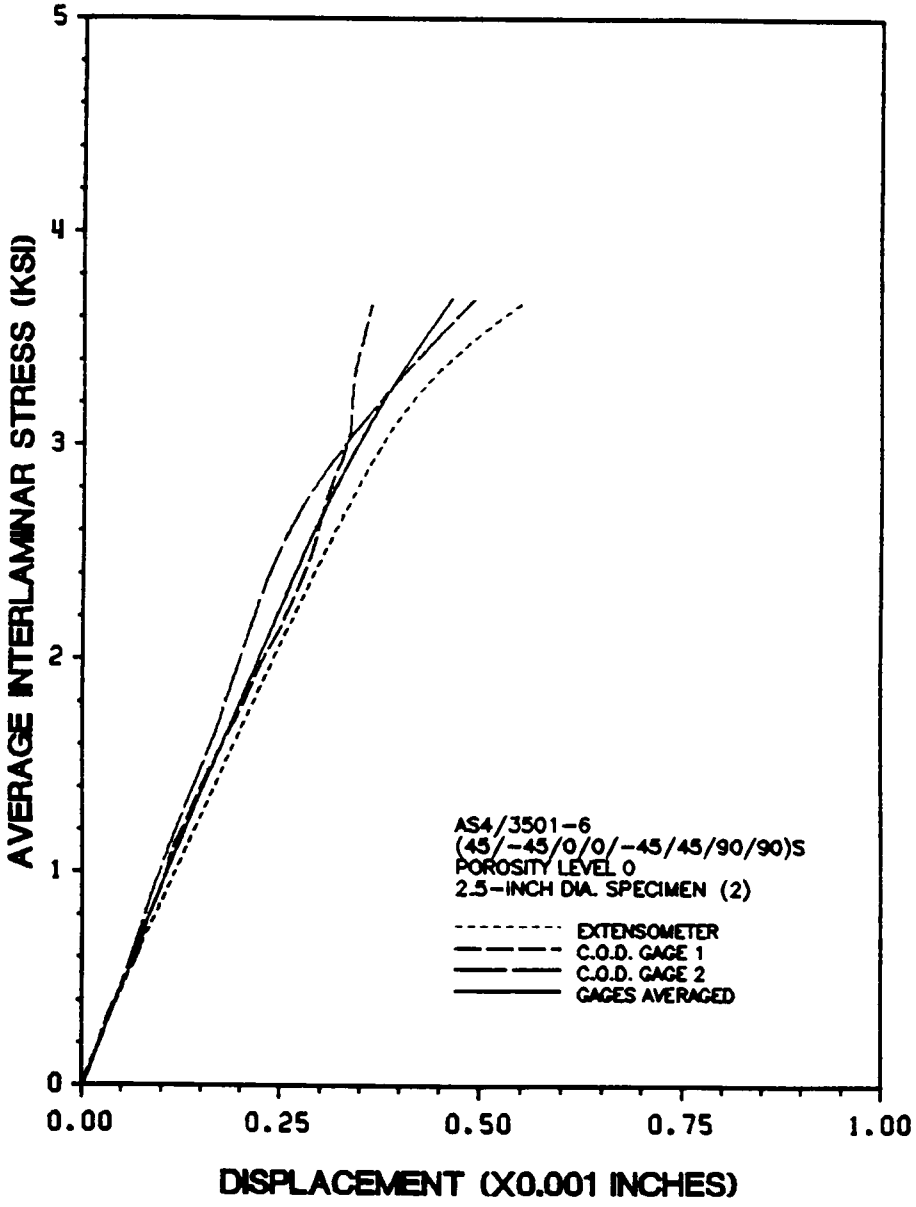

Figure 45. Flatwise Tensile Specimen Number 1-7.

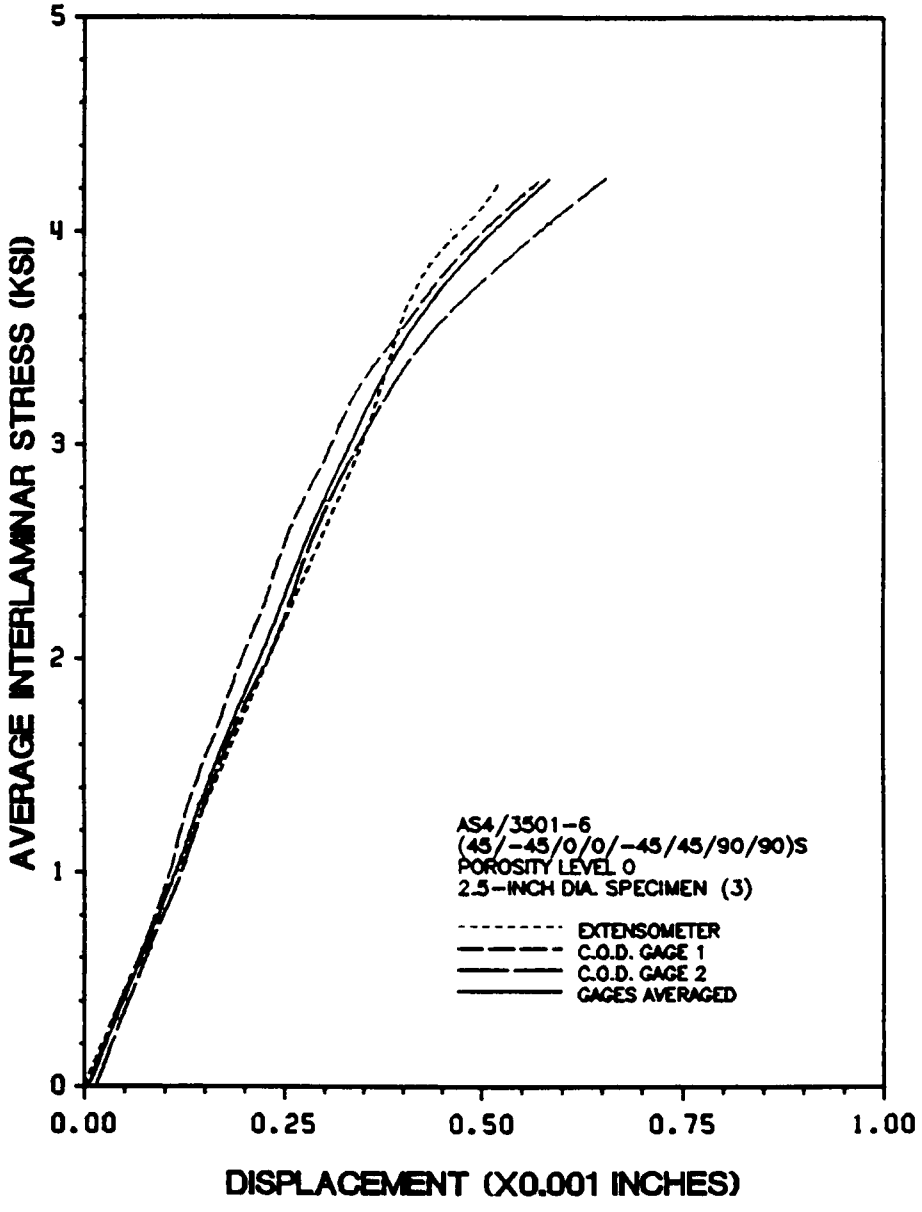

Figure 46. Flatwise Tensile Specimen Number 5-3.

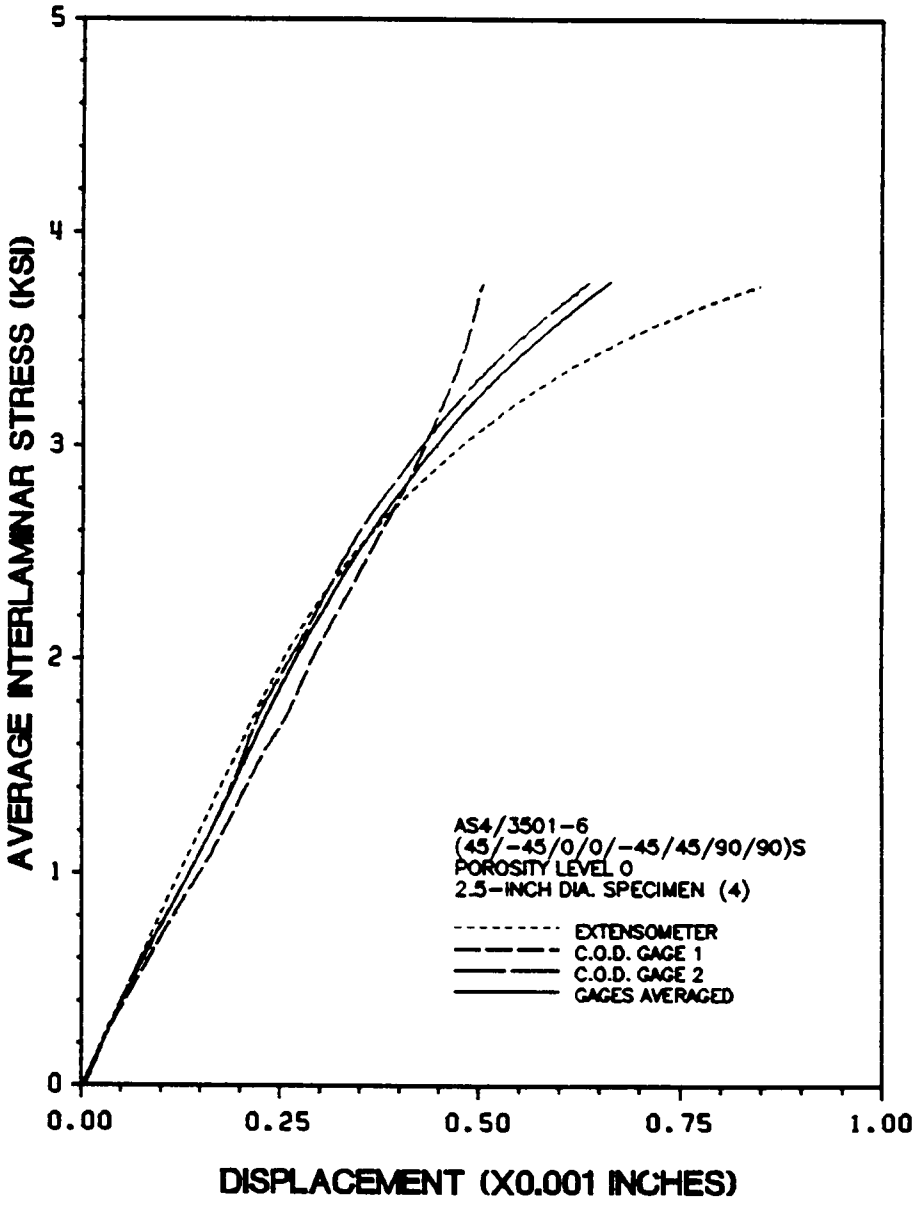

Figure 47. Flatwise Tensile Specimen Number 5-7.

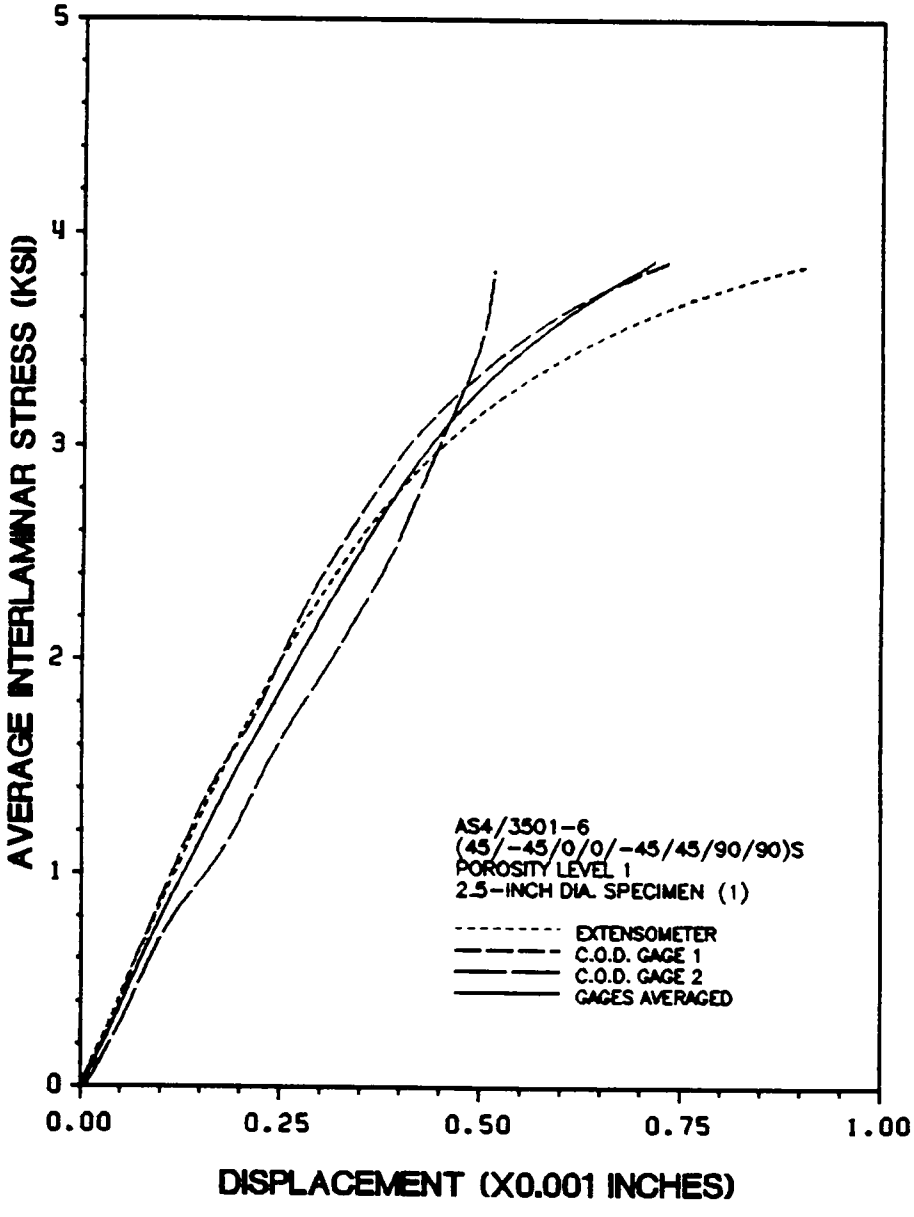

Figure 48. Flatwise Tensile Specimen Number 10-3.

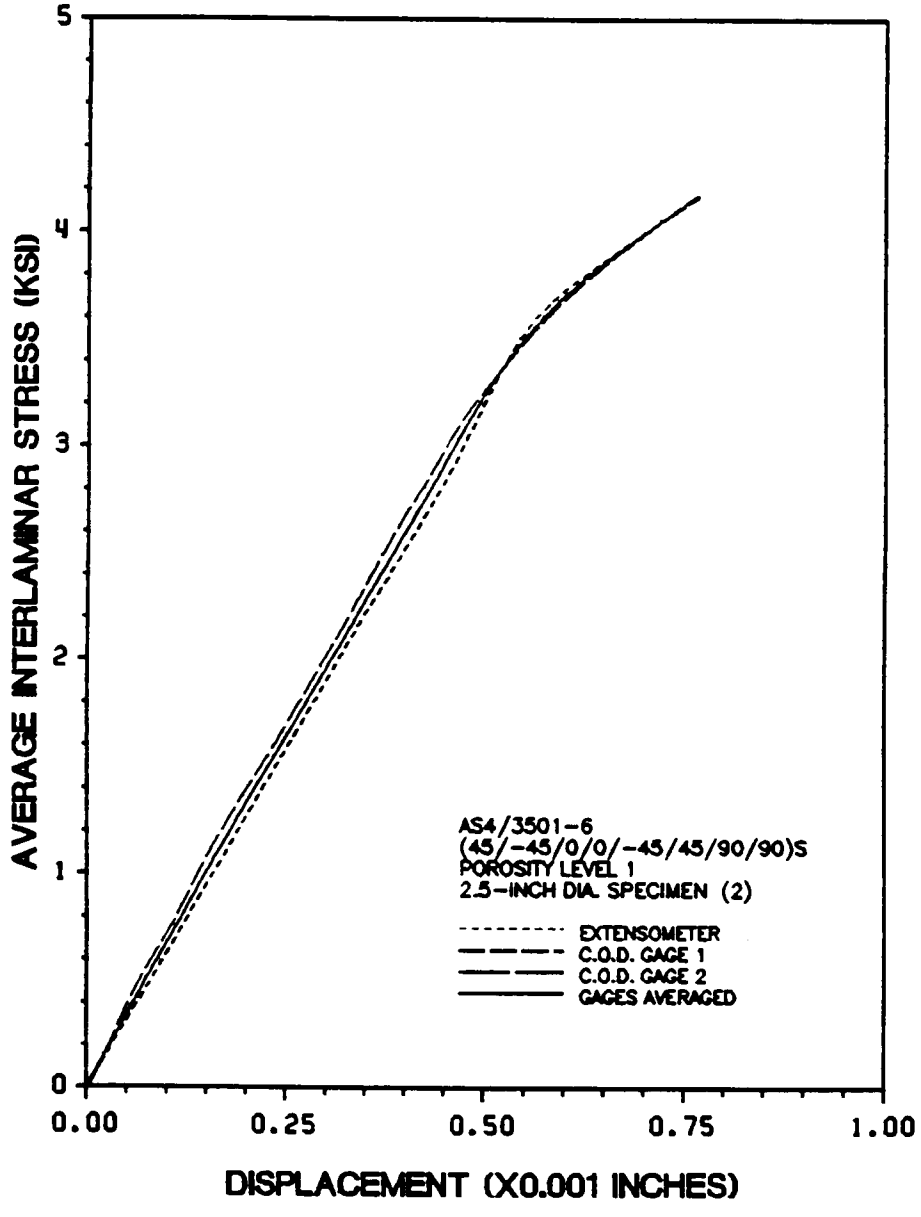

Figure 49. Flatwise Tensile Specimen Number 10-7.

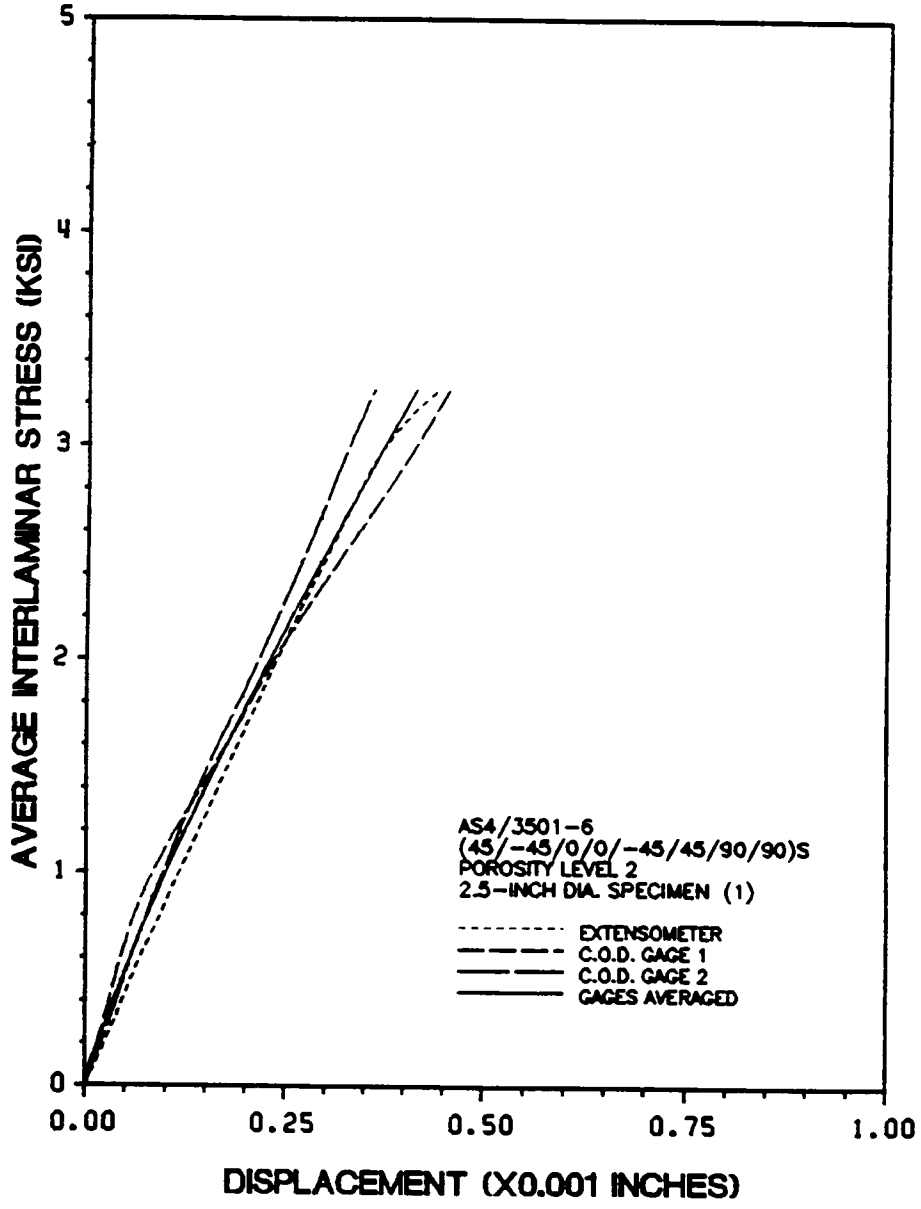

Figure 50. Flatwise Tensile Specimen Number 12-3.

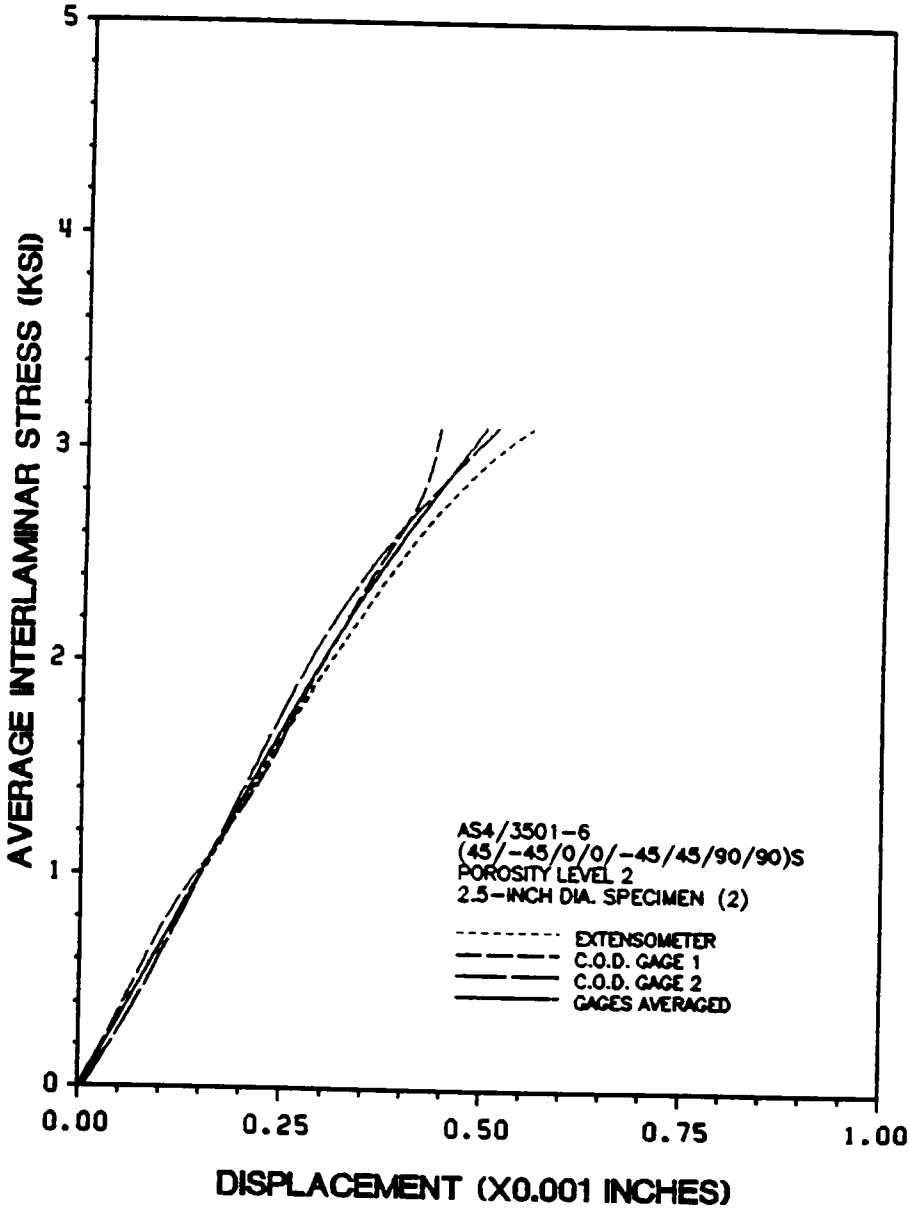

Figure 51. Flatwise Tensile Specimen Number 12-7.

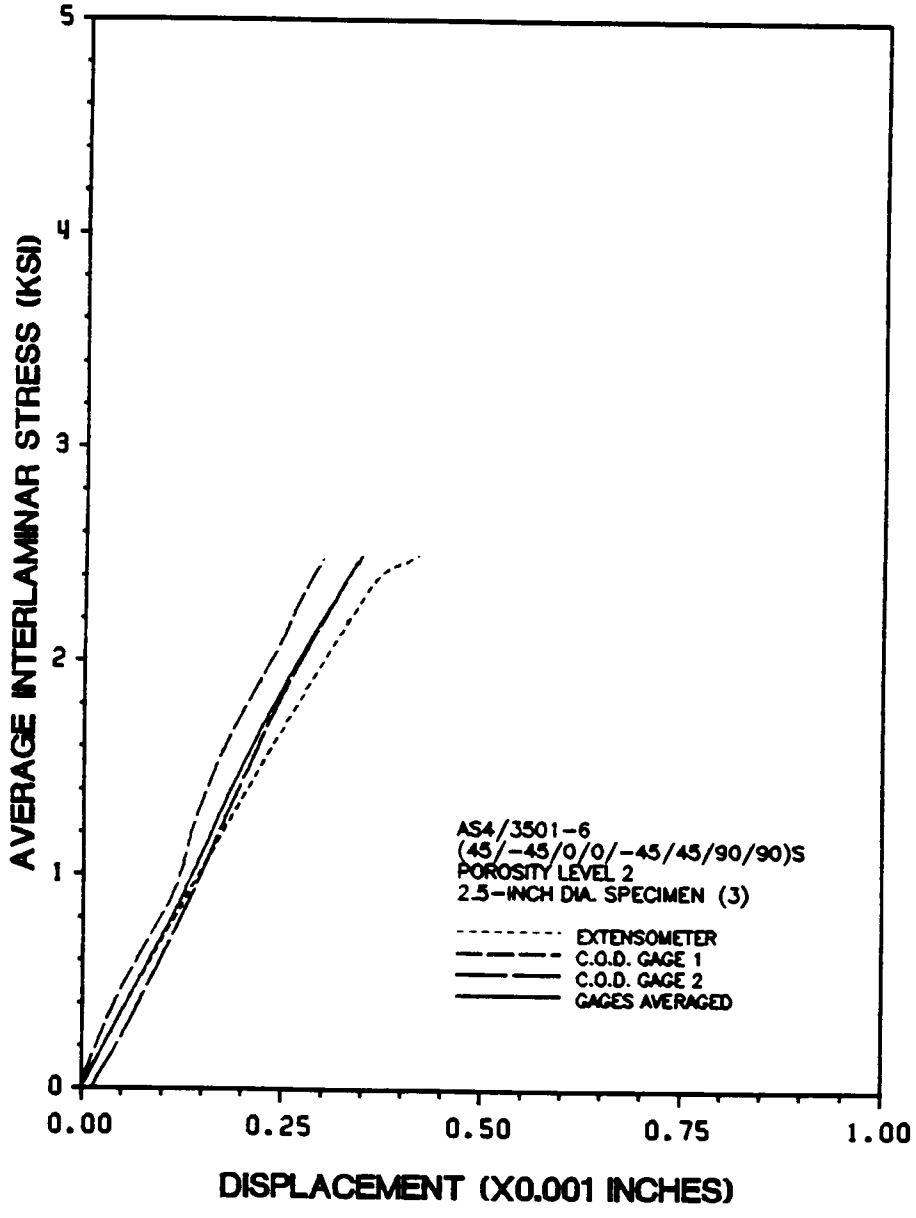

Figure 52. Flatwise Tensile Specimen Number 13-3.

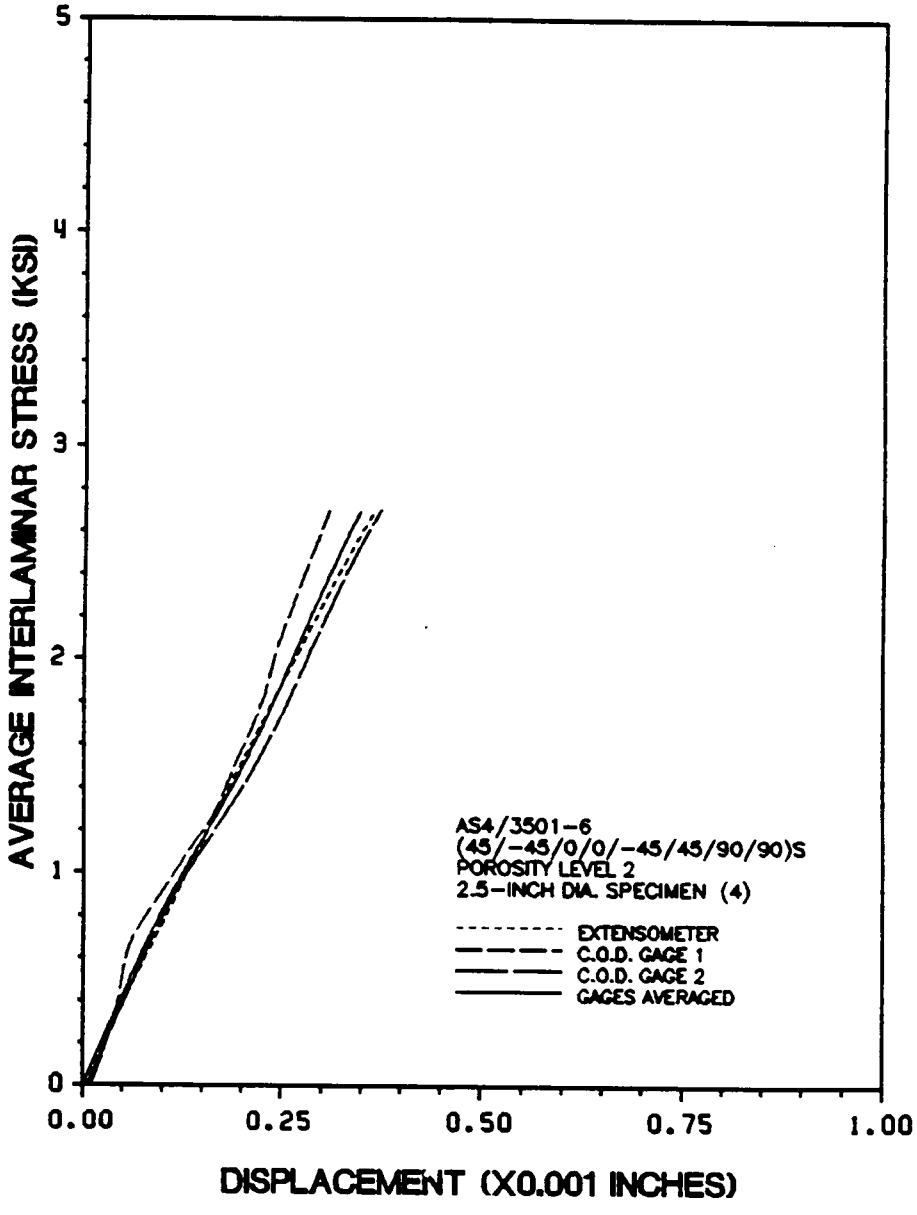

Figure 53. Flatwise Tensile Specimen Number 13-7.

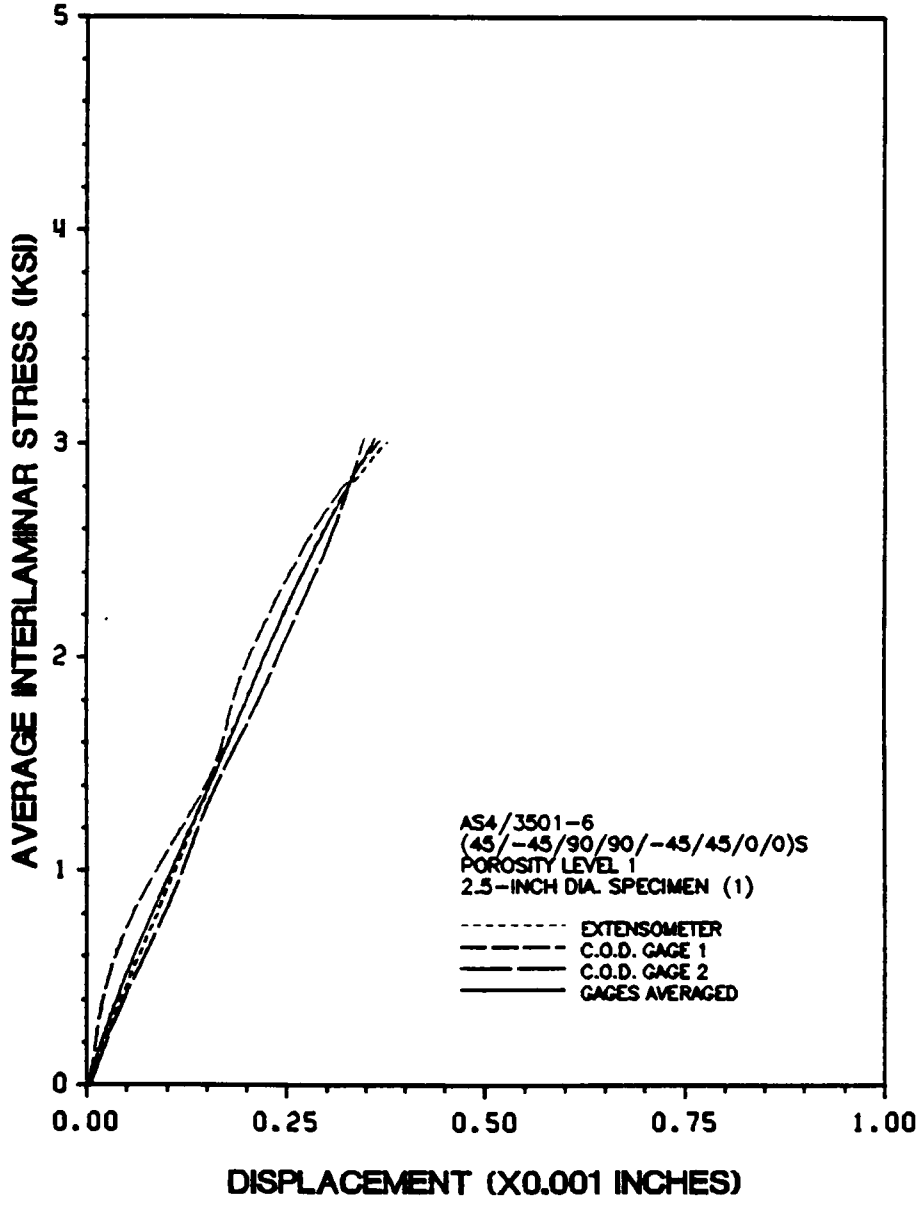

Figure 54. Flatwise Tensile Specimen Number 9-3.

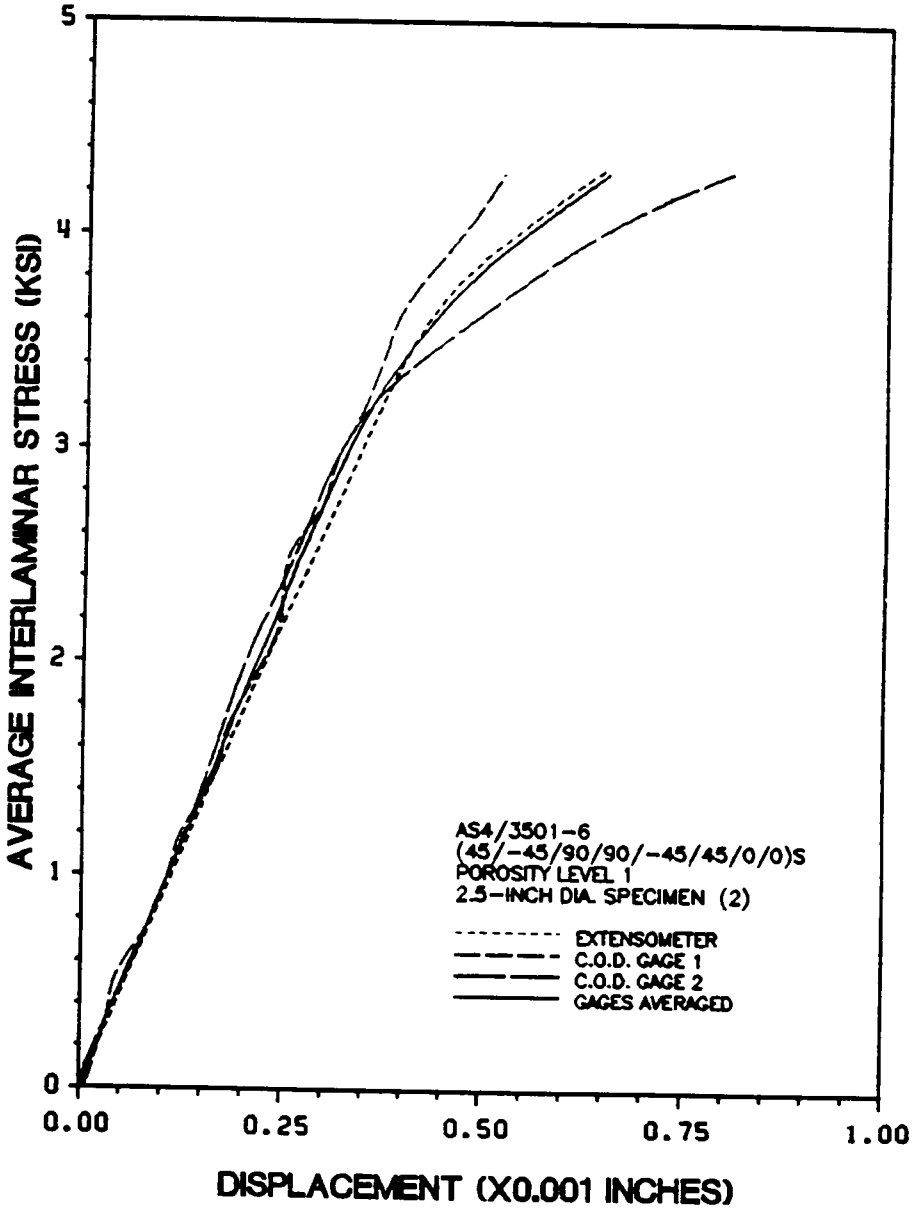

Figure 55. Flatwise Tensile Specimen Number 9-7.

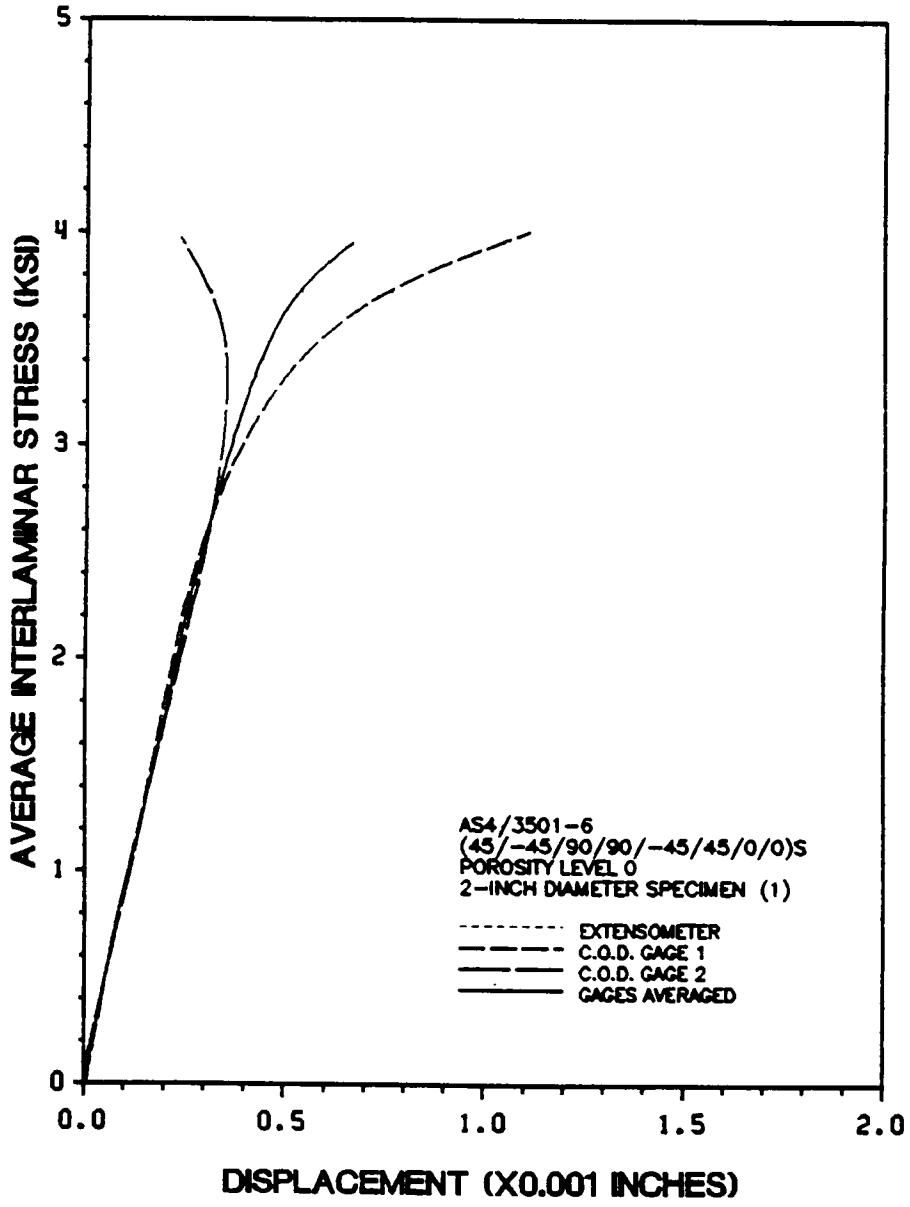

Figure 56. Flatwise Tensile Specimen Number 4-3.

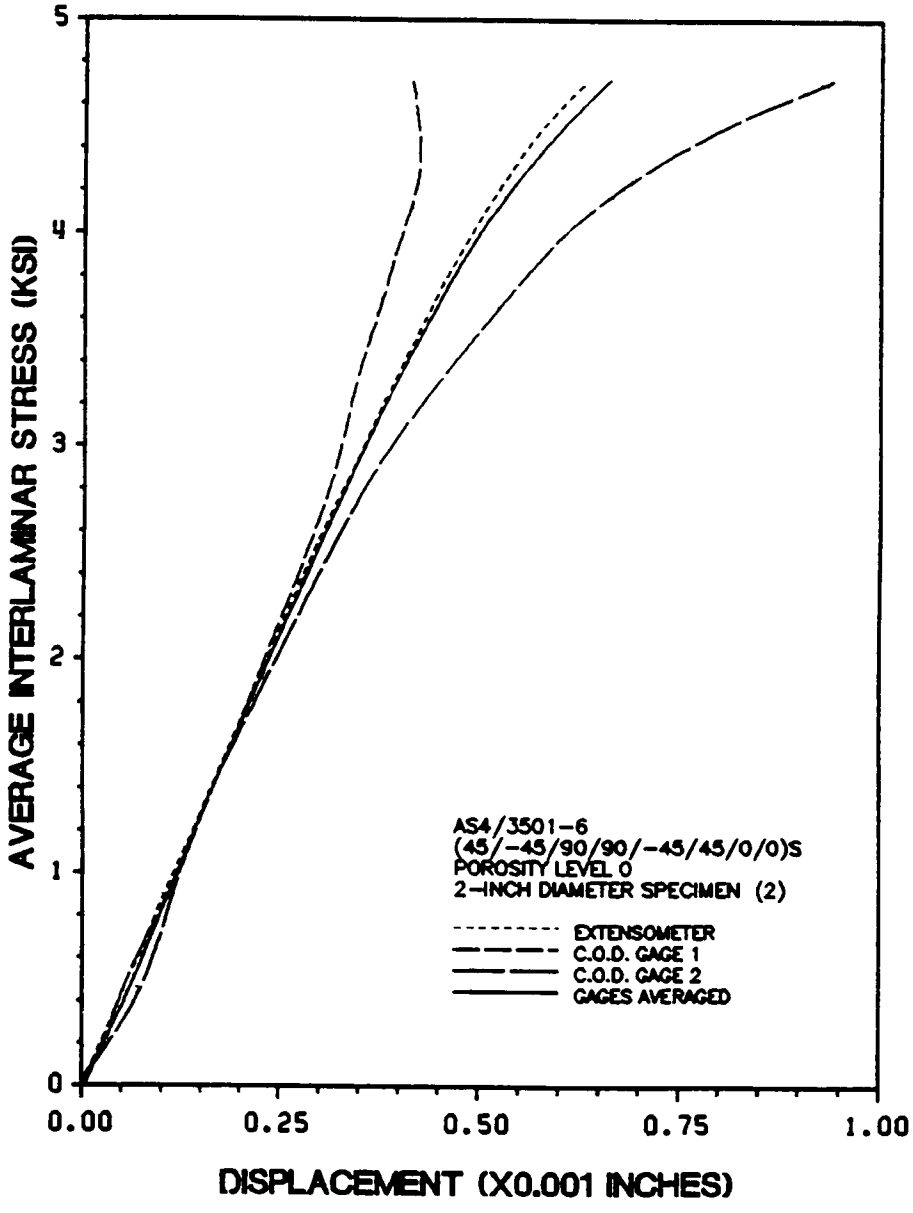

Figure 57. Flatwise Tensile Specimen Number 4-5.

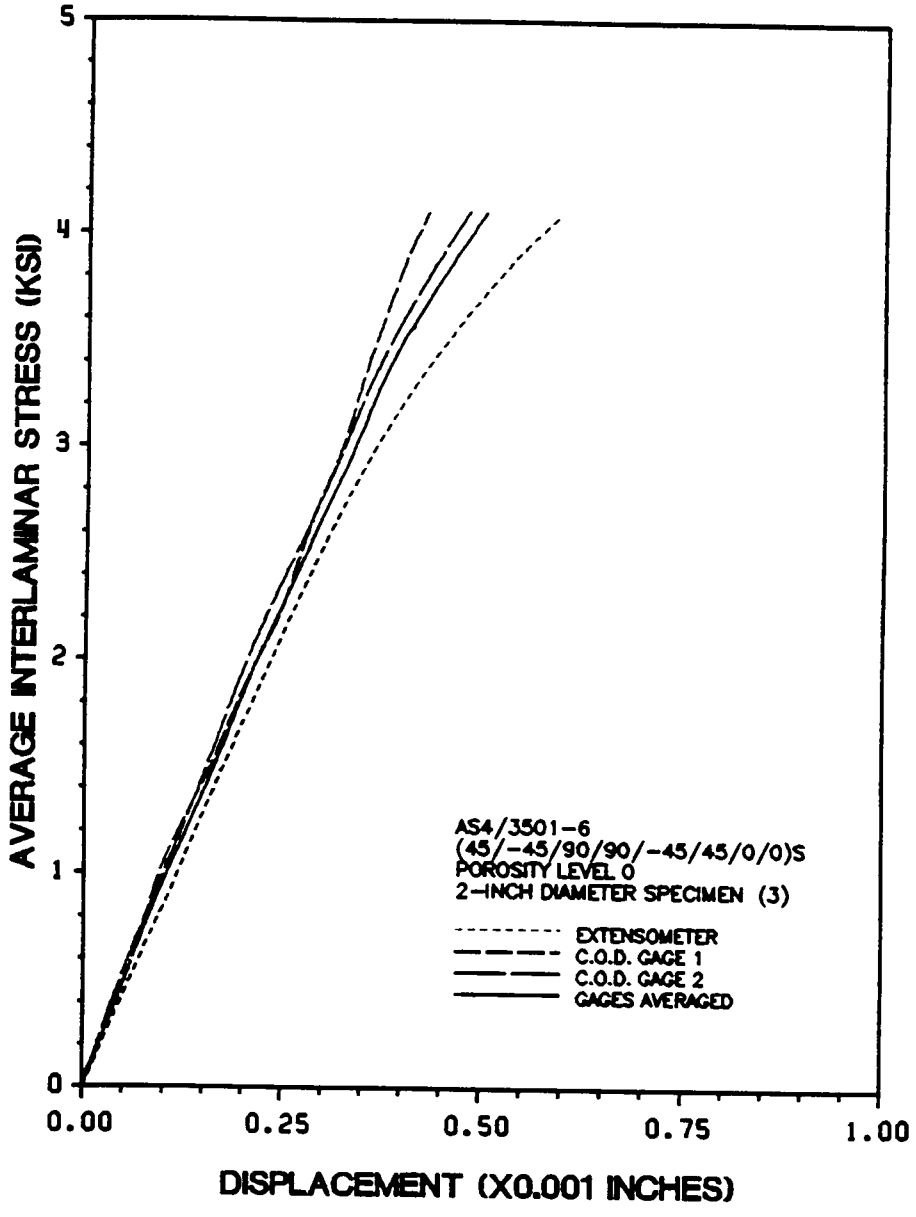

Figure 58. Flatwise Tensile Specimen Number 4-7.

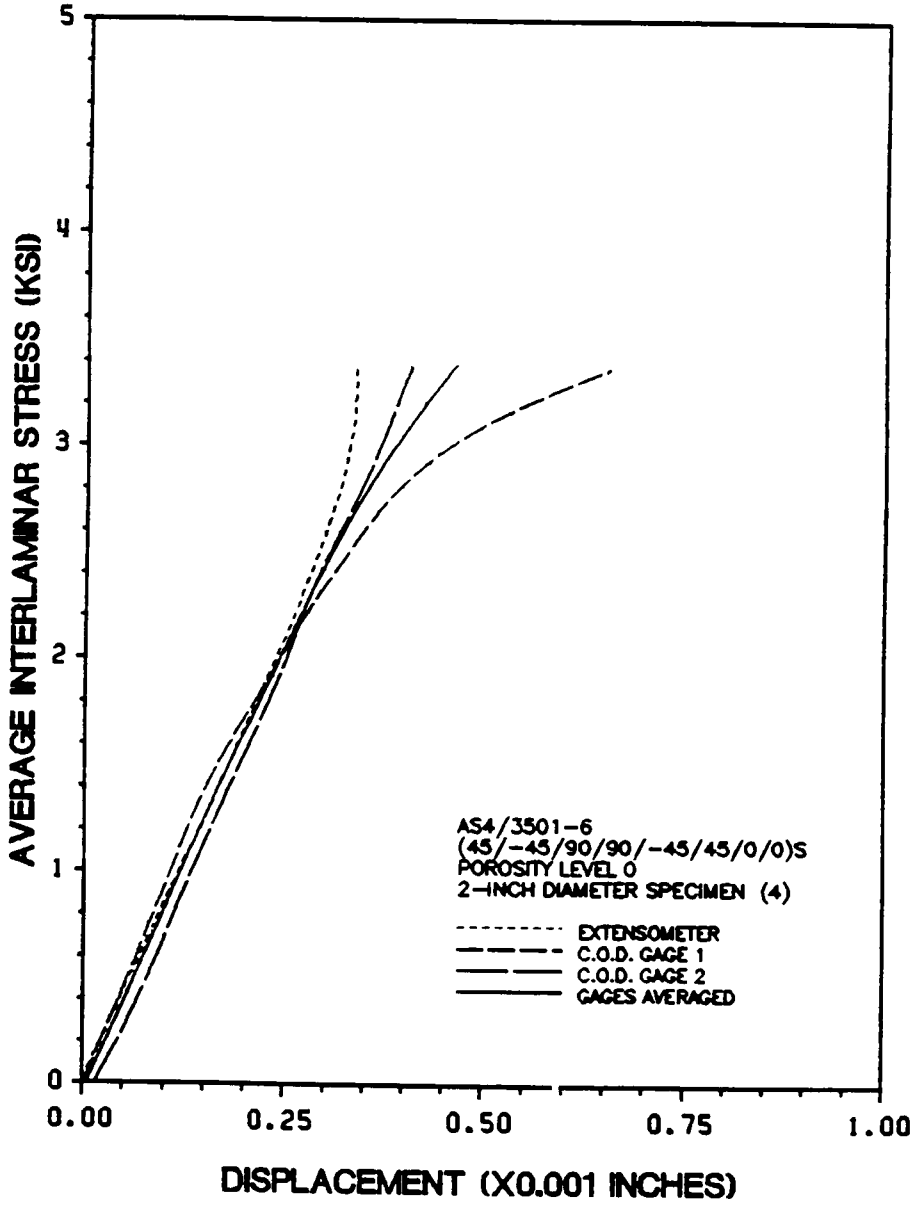

Figure 59. Flatwise Tensile Specimen Number 6-3.

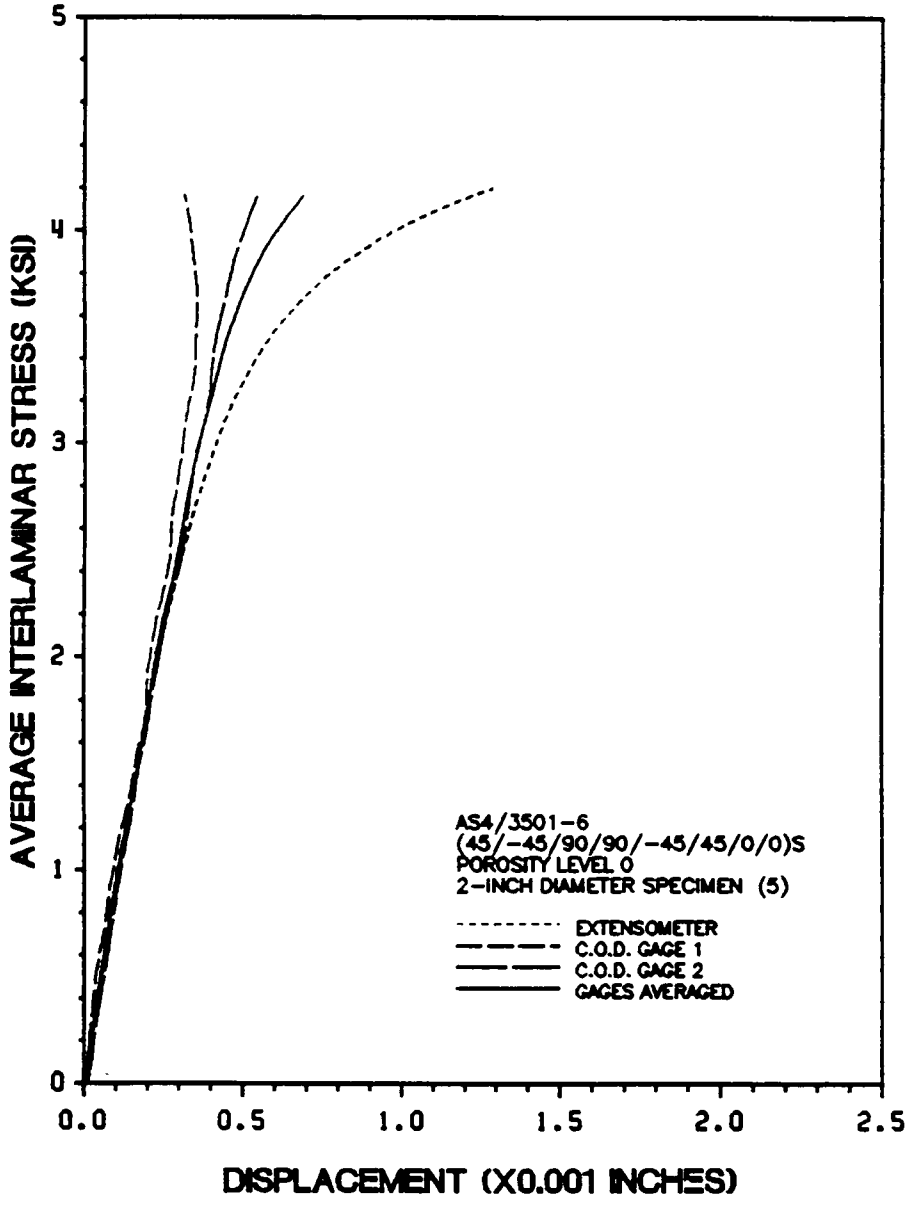

Figure 60. Flatwise Tensile Specimen Number 6-5.

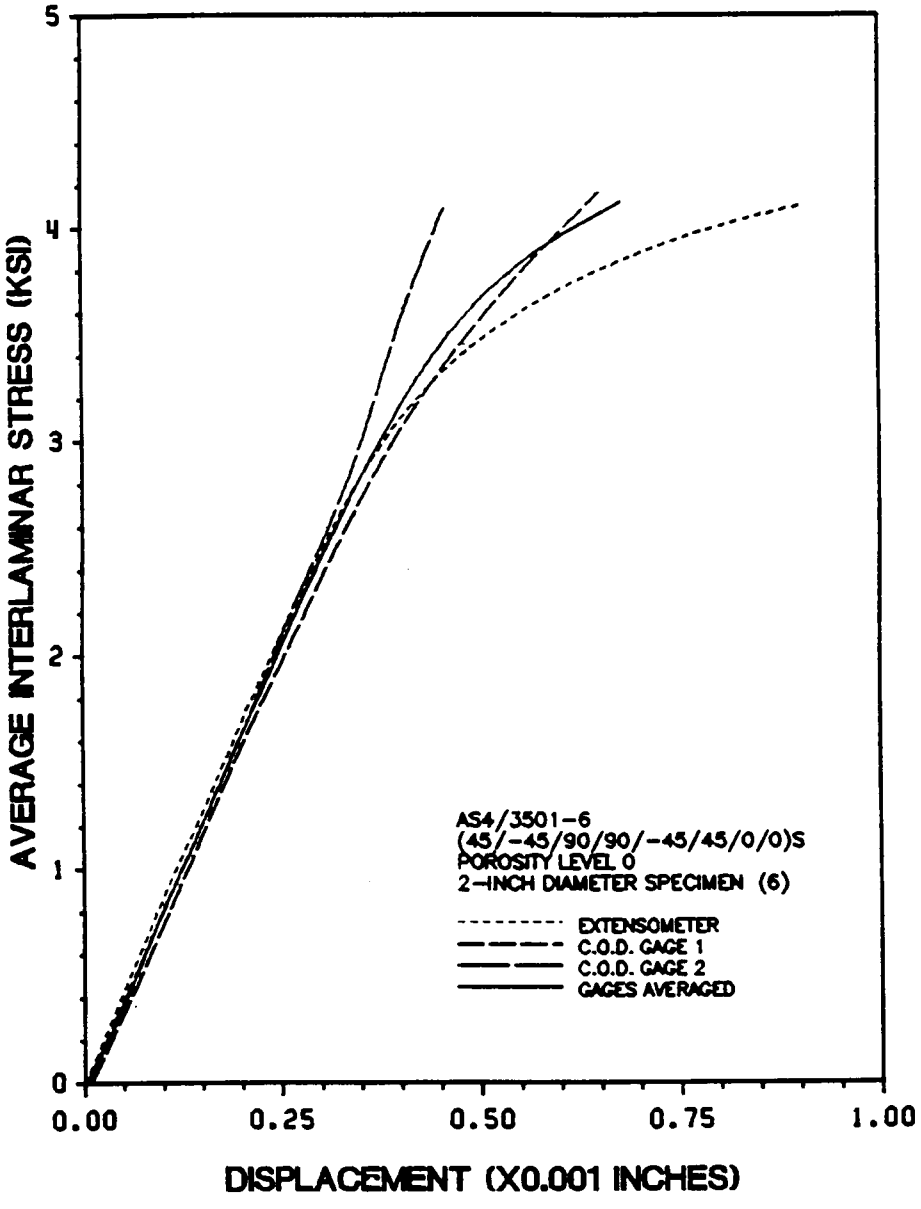

Figure 61. Flatwise Tensile Specimen Number 6-7.

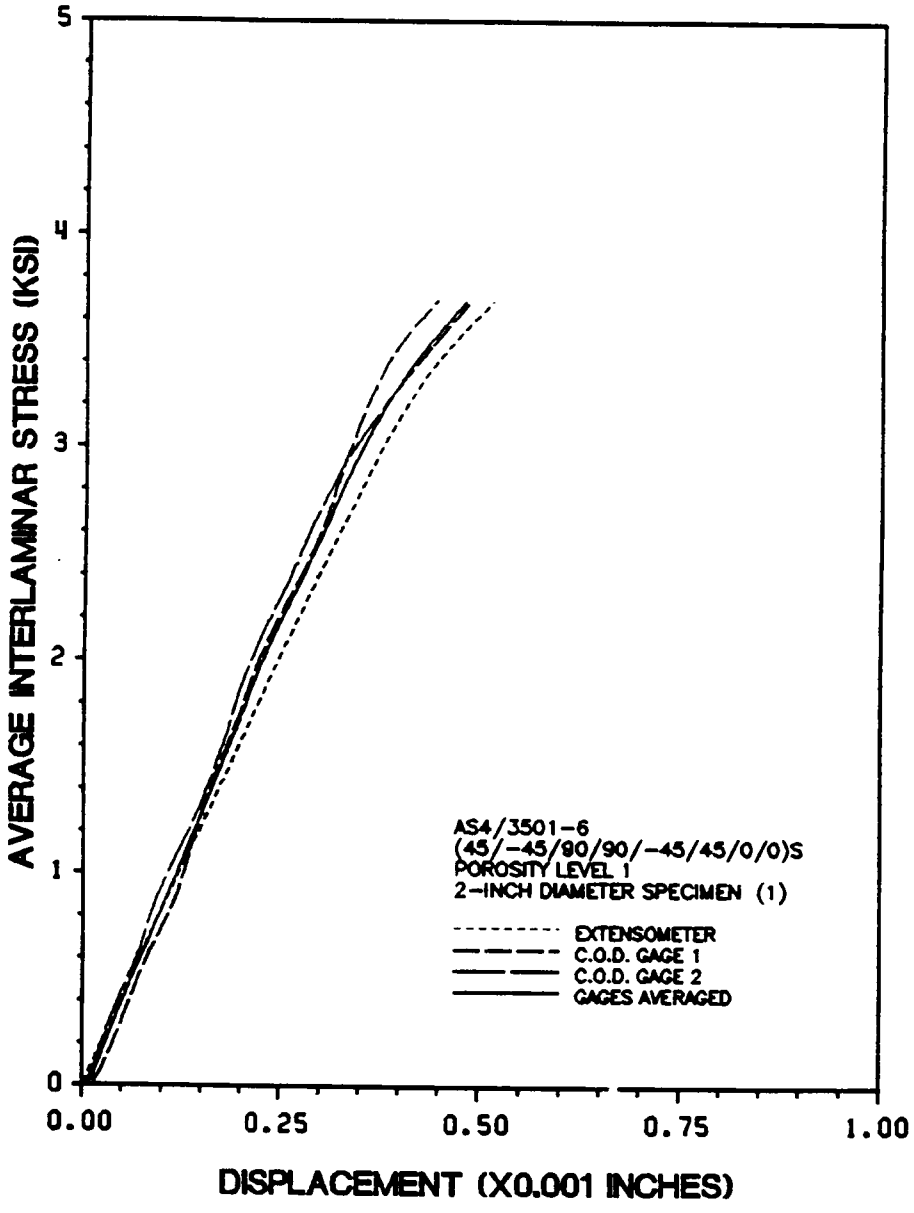

Figure 62. Flatwise Tensile Specimen Number 15-3.

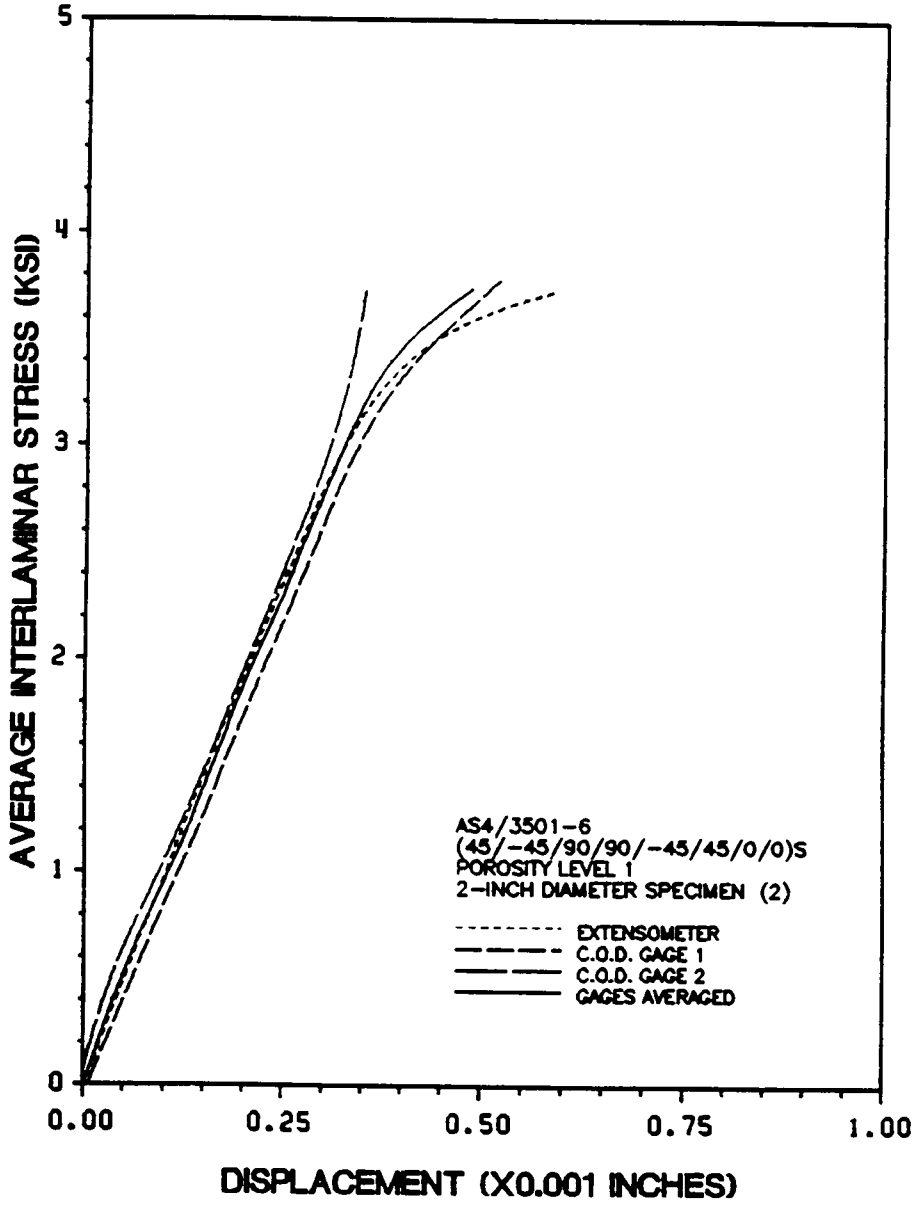

Figure 63. Flatwise Tensile Specimen Number 15-5.

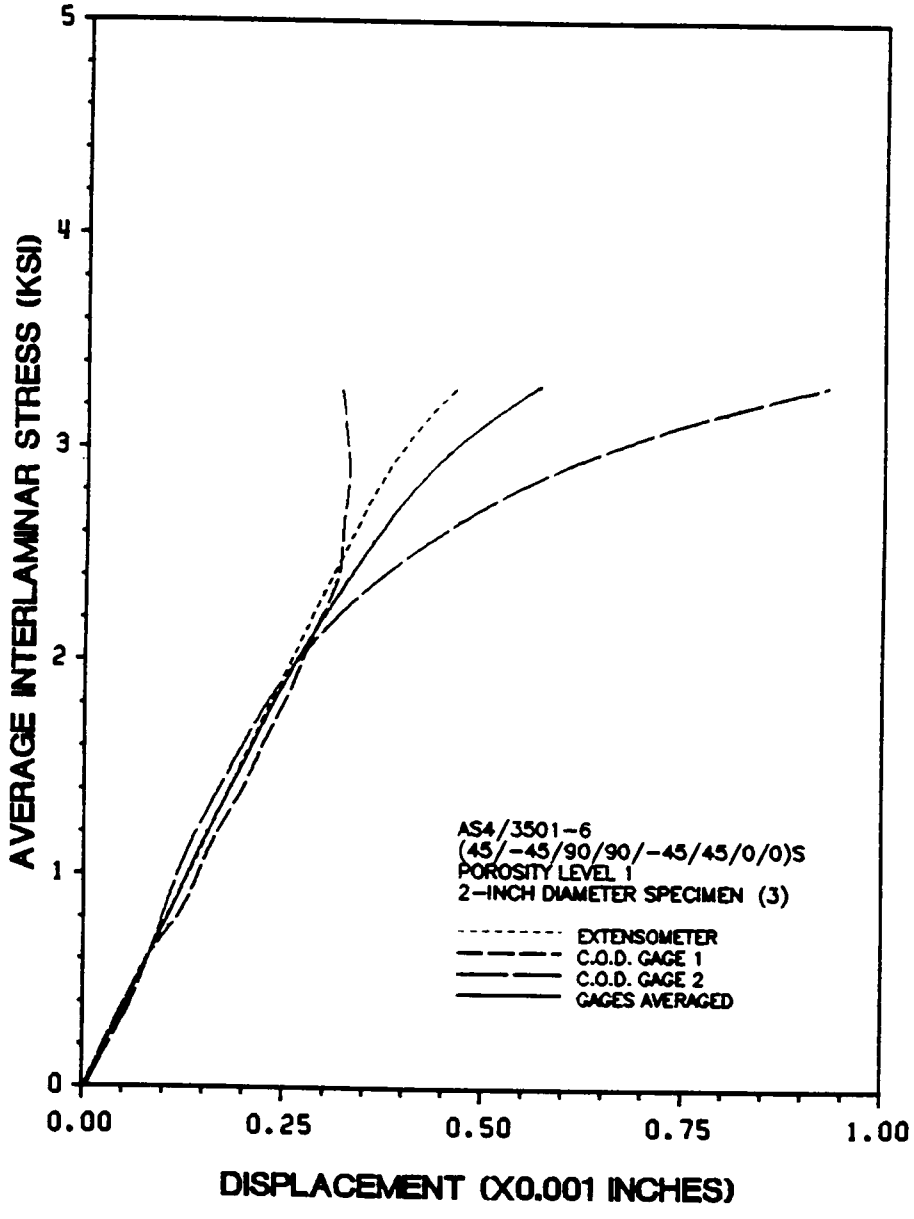

Figure 64. Flatwise Tensile Specimen Number 15-7.

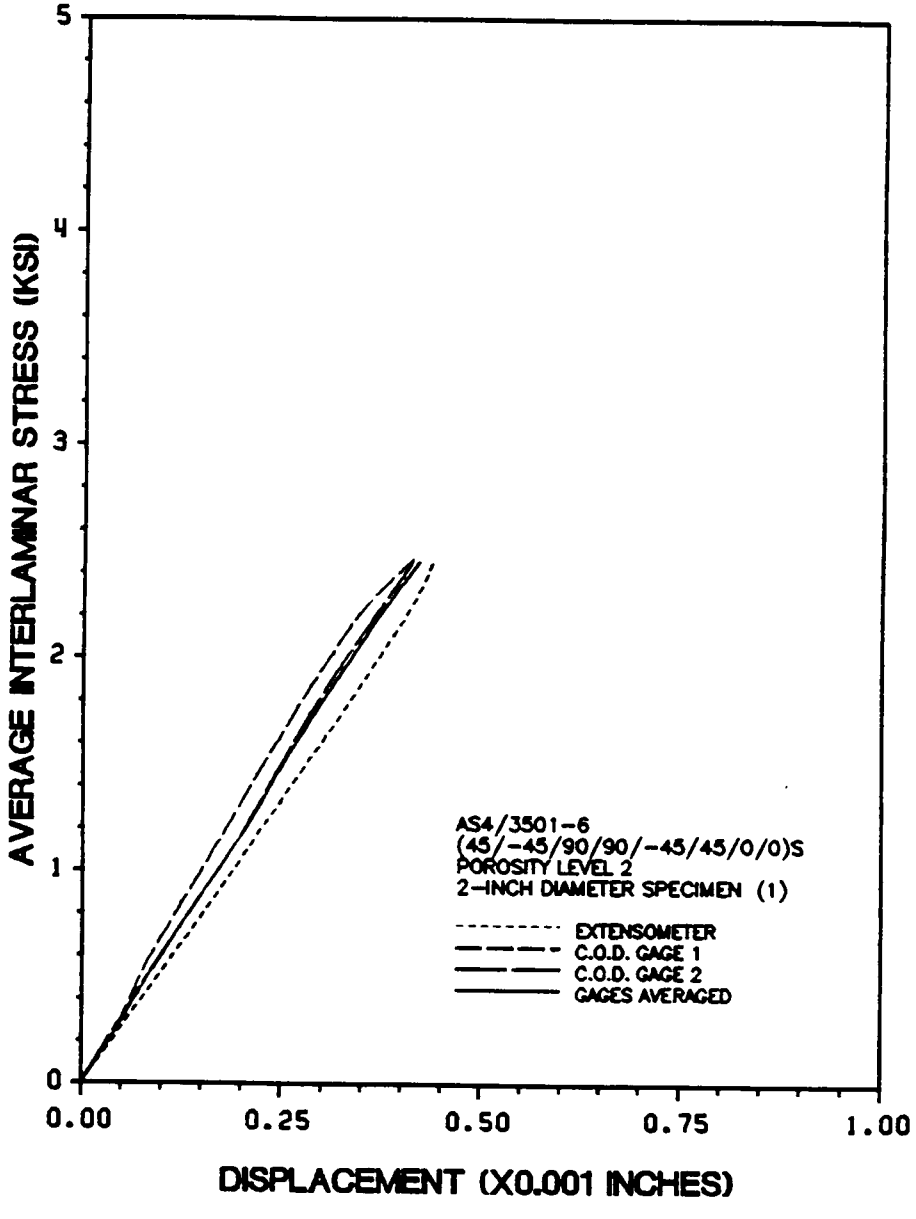

Figure 65. Flatwise Tensile Specimen Number 11-3.

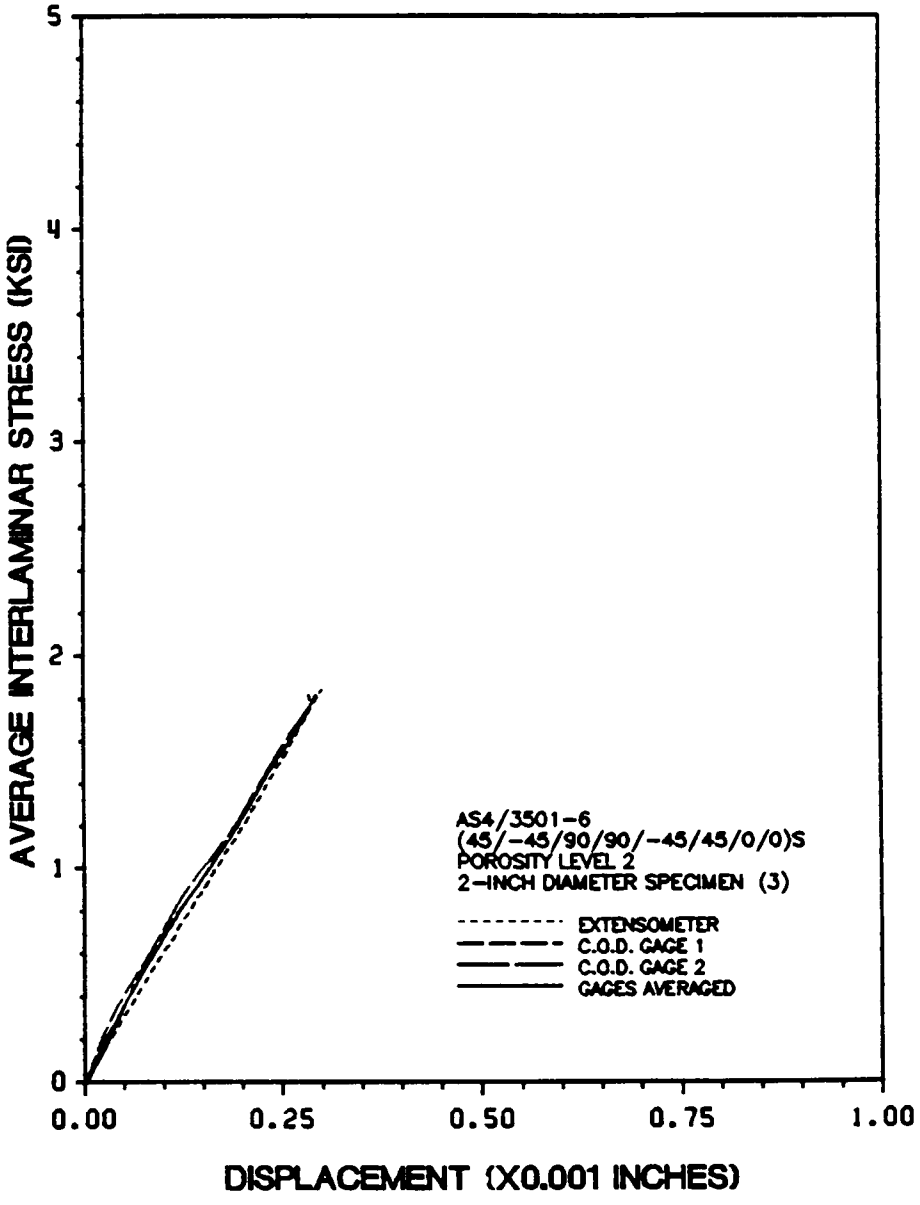

Figure 66. Flatwise Tensile Specimen Number 11-7.

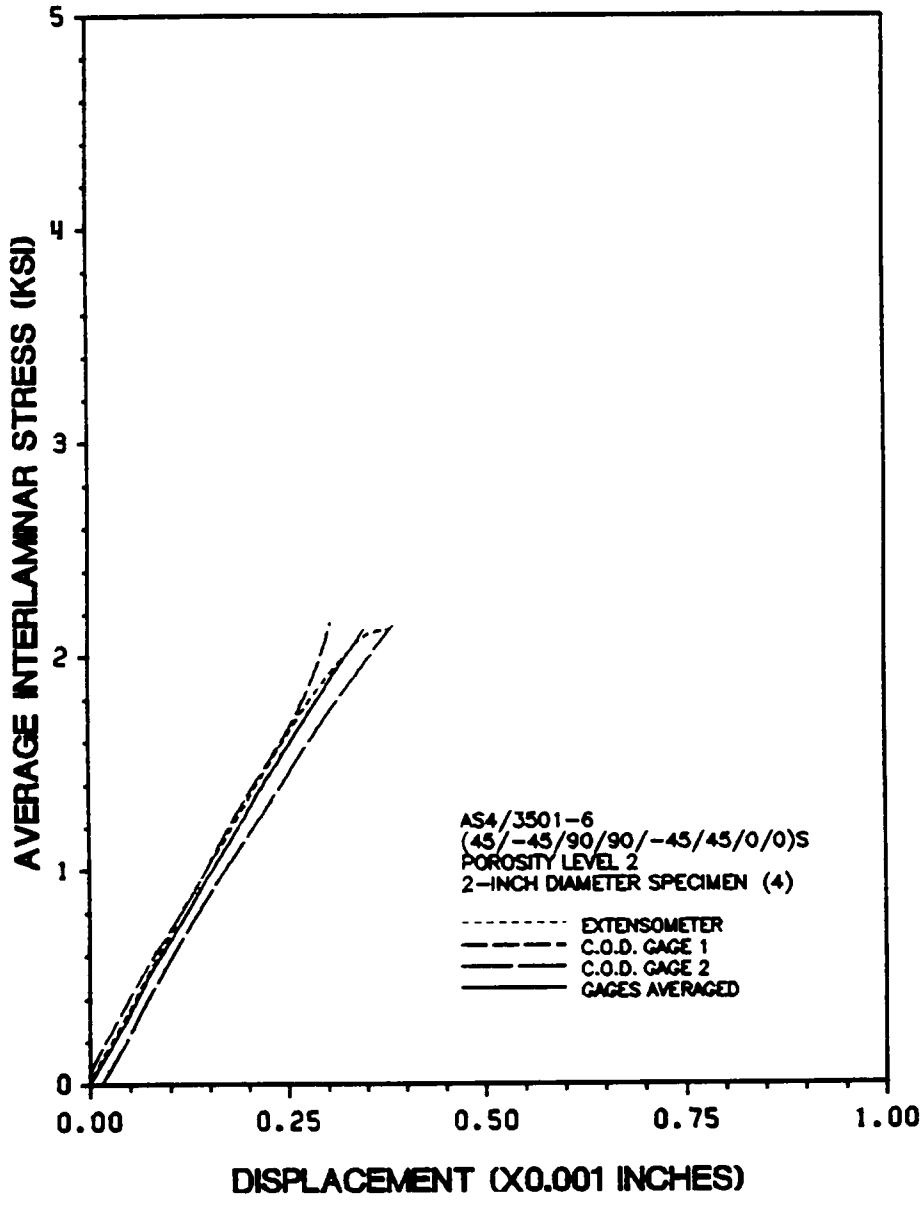

Figure 67. Flatwise Tensile Specimen Number 14-3.

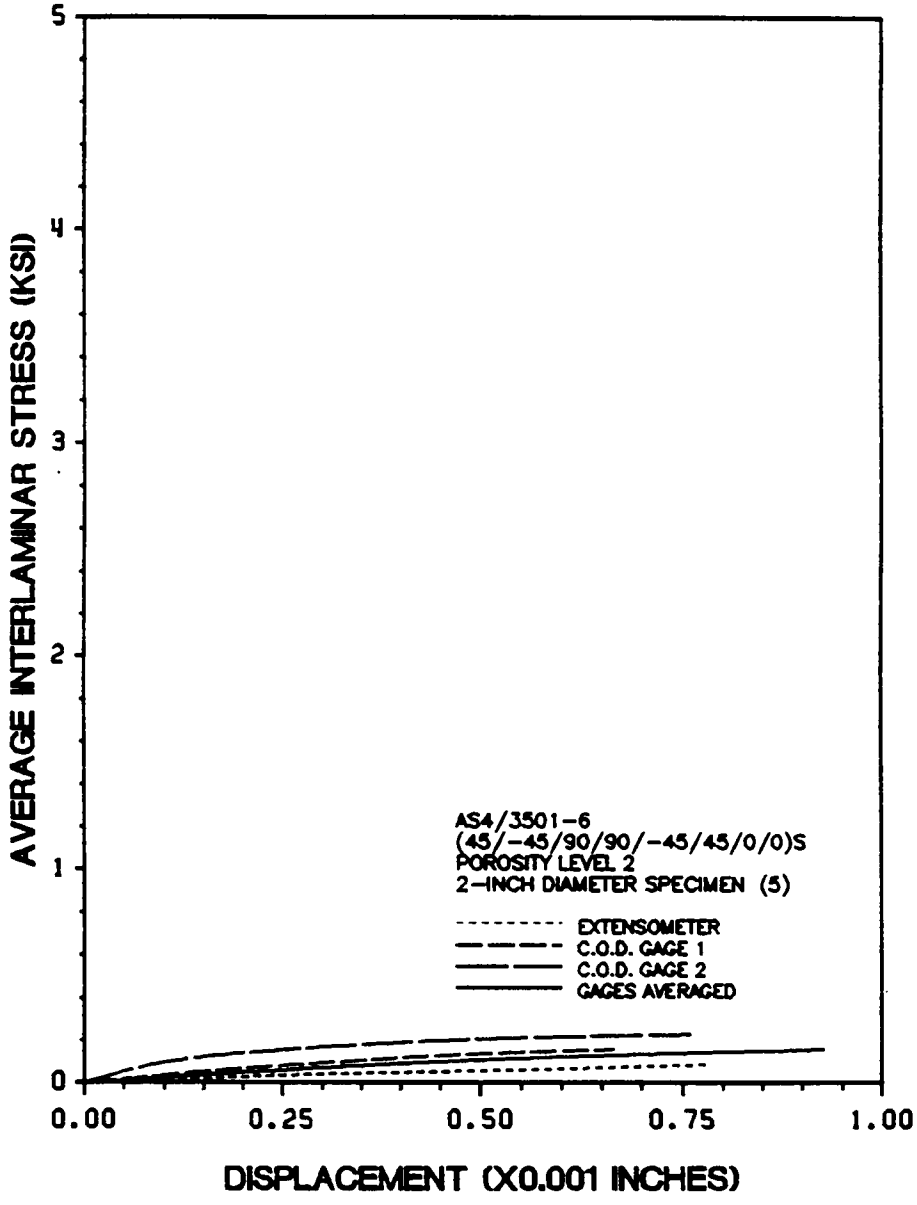

Figure 68. Flatwise Tensile Specimen Number 14-5.

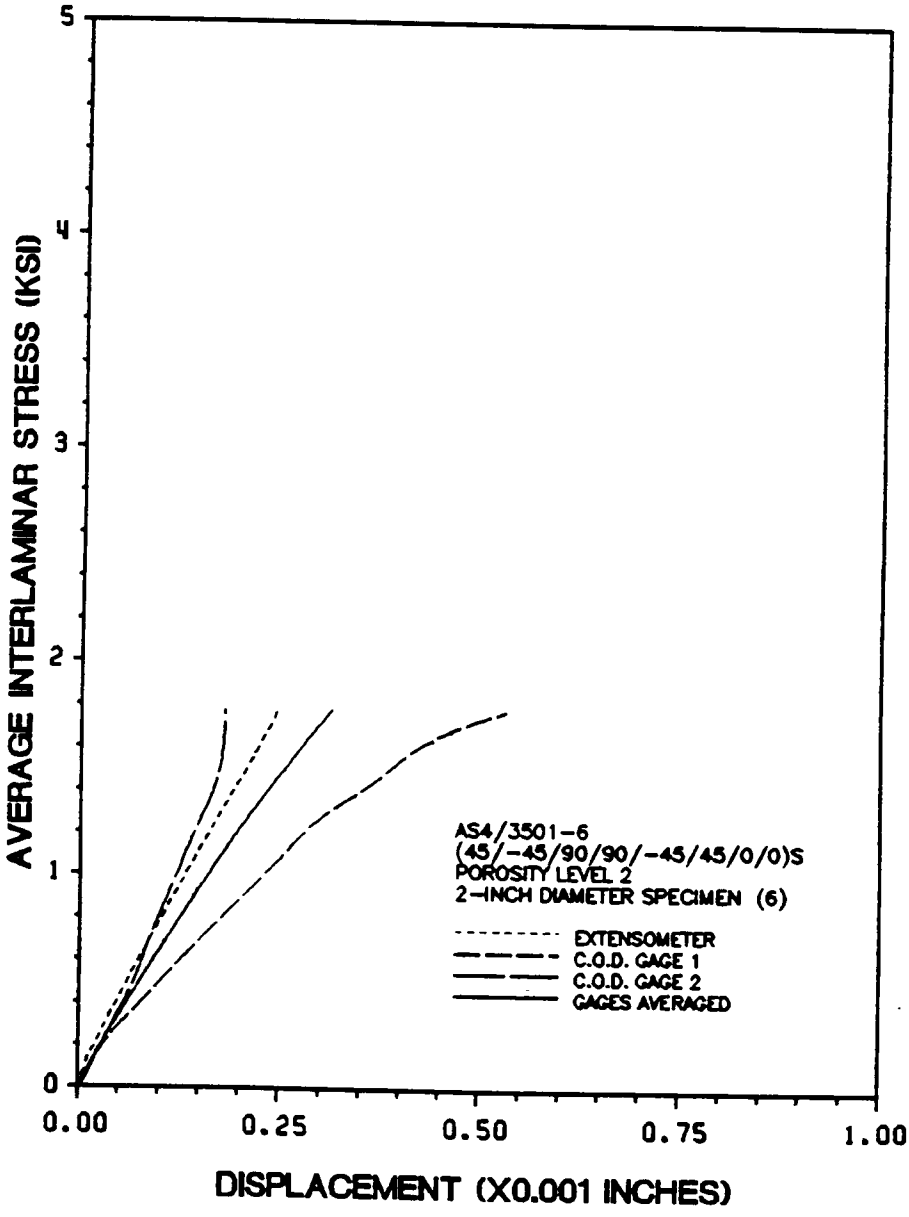

Figure 69. Flatwise Tensile Specimen Number 14-7.

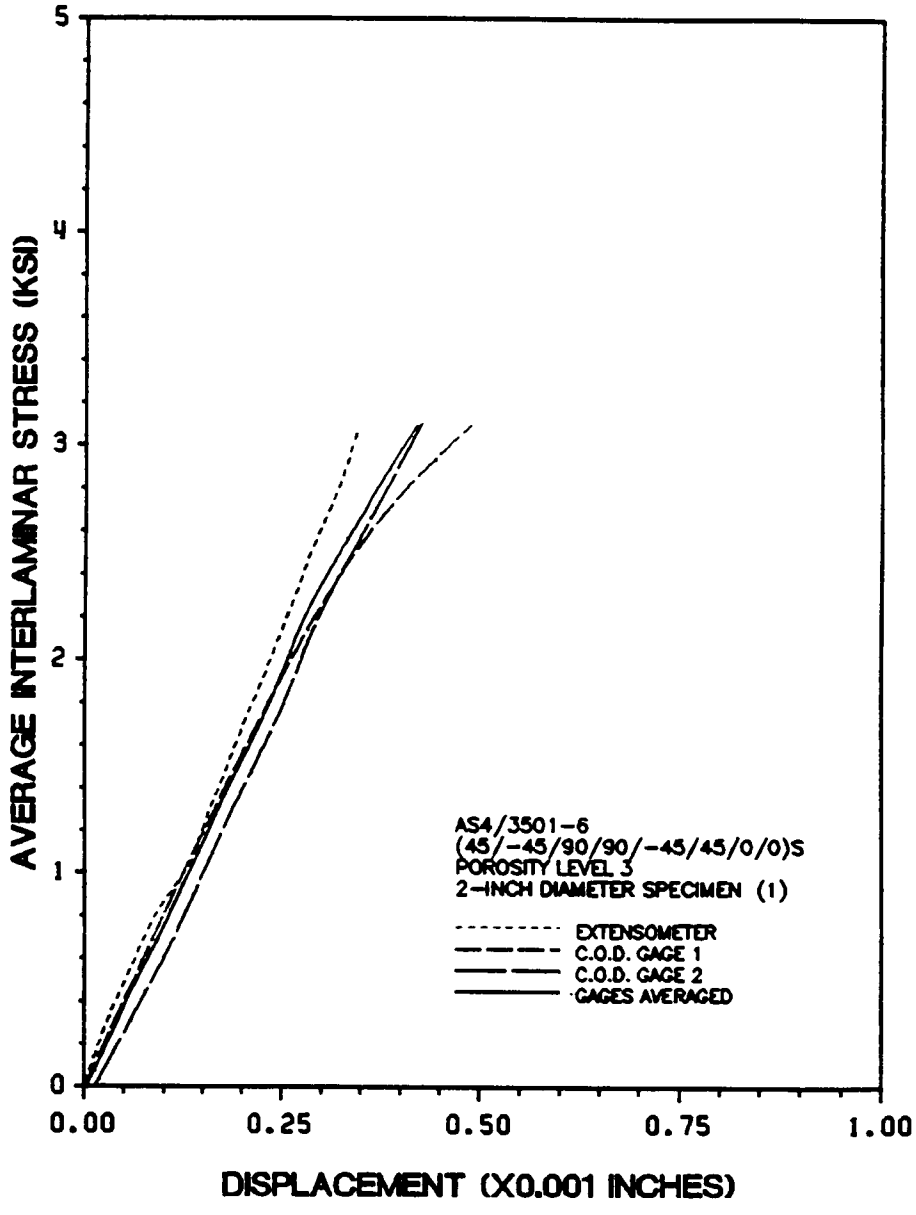

Figure 70. Flatwise Tensile Specimen Number 18-3.

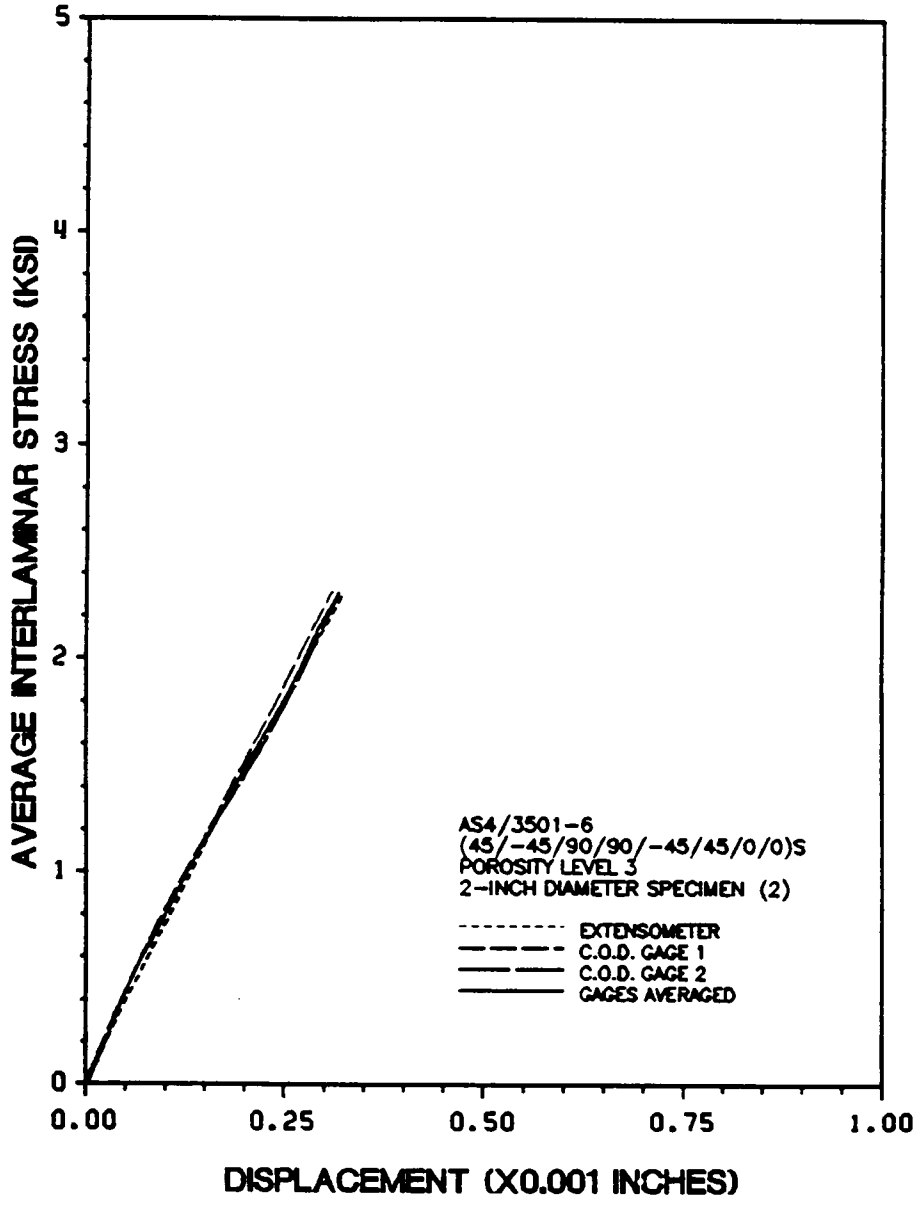

Figure 71. Flatwise Tensile Specimen Number 18-5.

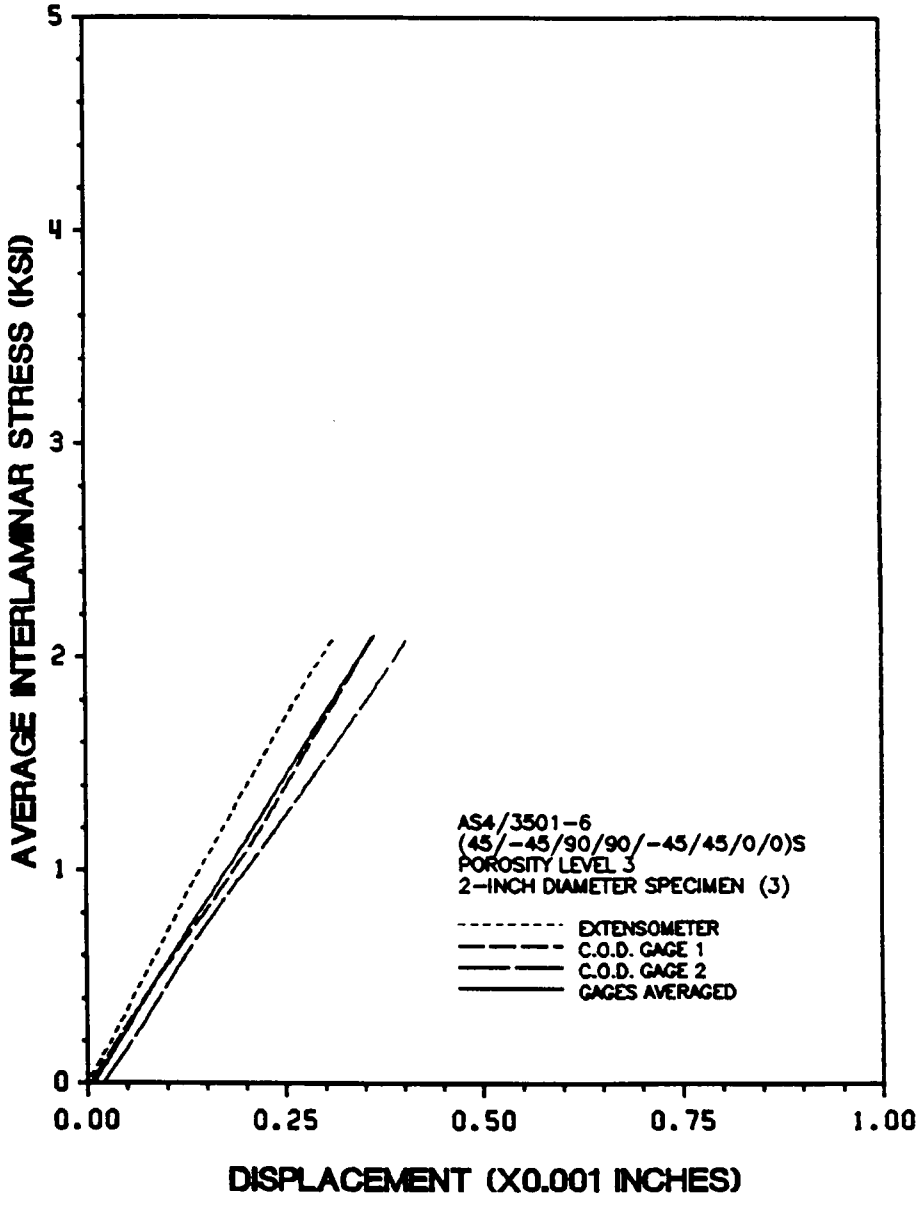

Figure 72. Flatwise Tensile Specimen Number 18-7.

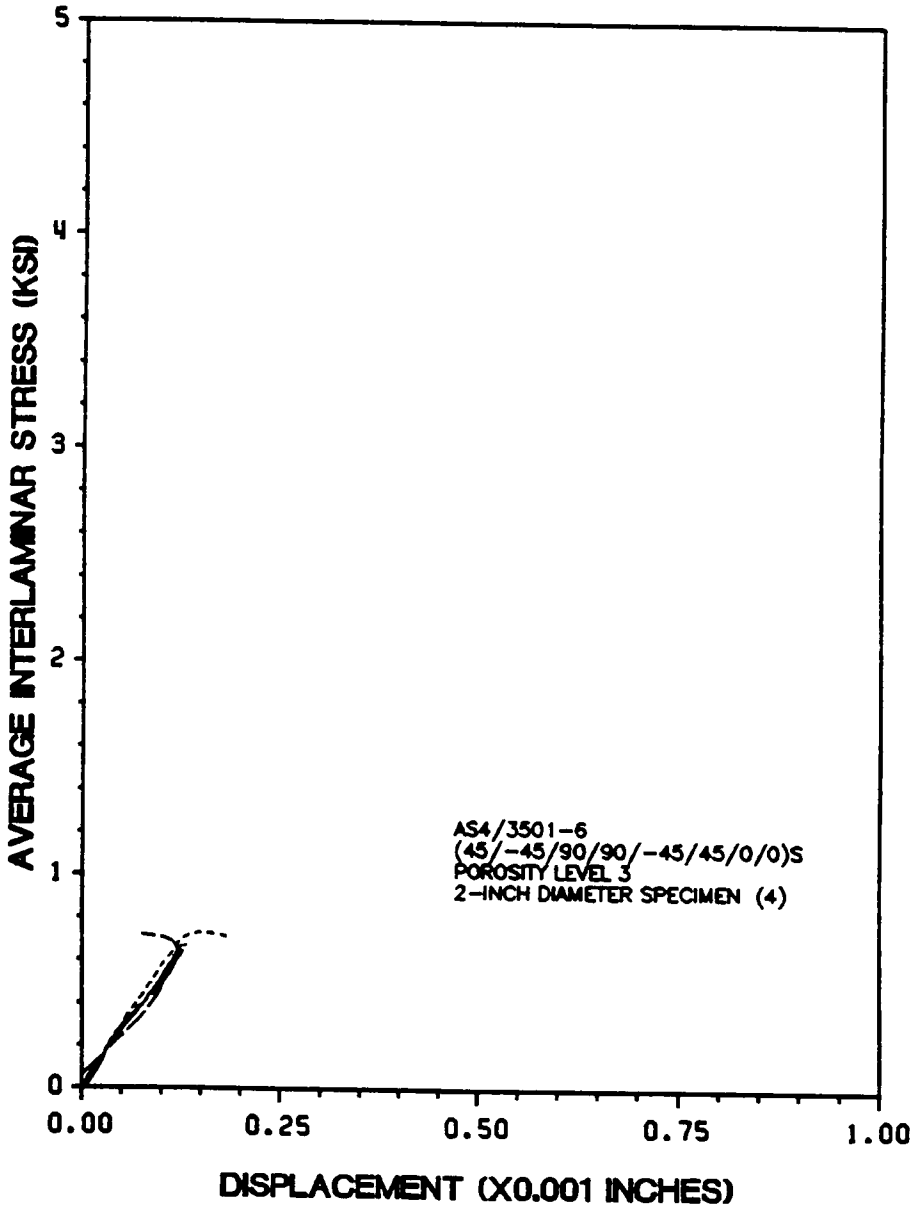

Figure 73. Flatwise Tensile Specimen Number 20-3.

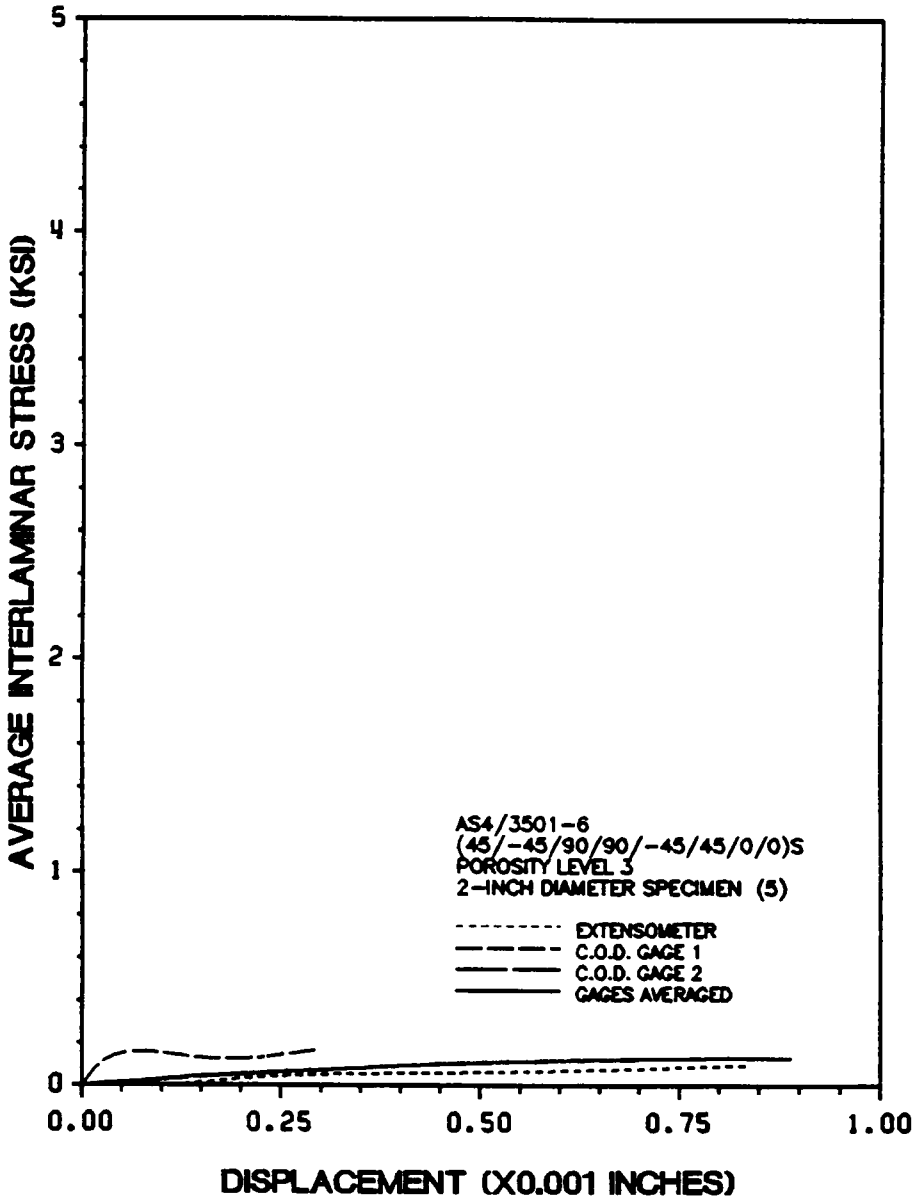

Figure 74. Flatwise Tensile Specimen Number 20-5.

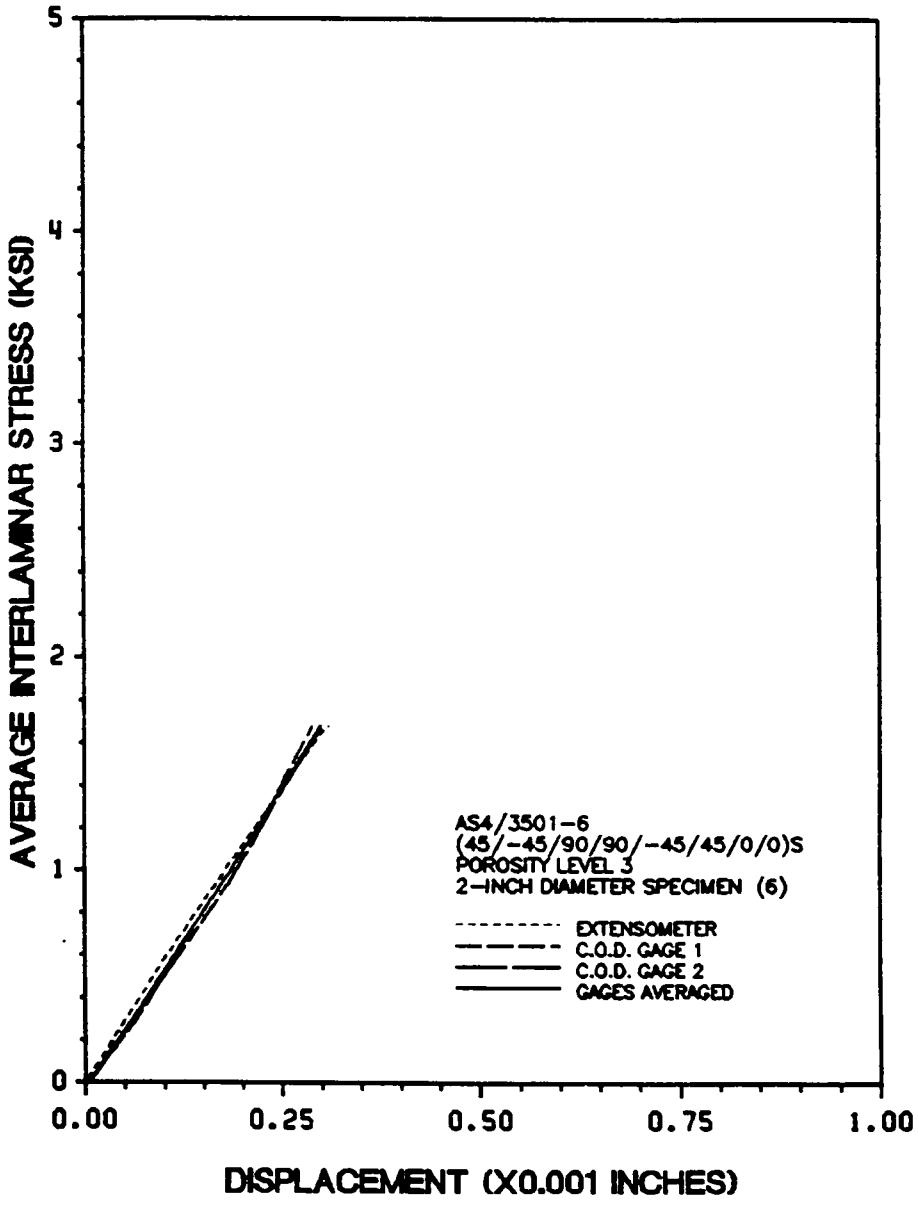

Figure 75. Flatwise Tensile Specimen Number 20-7.

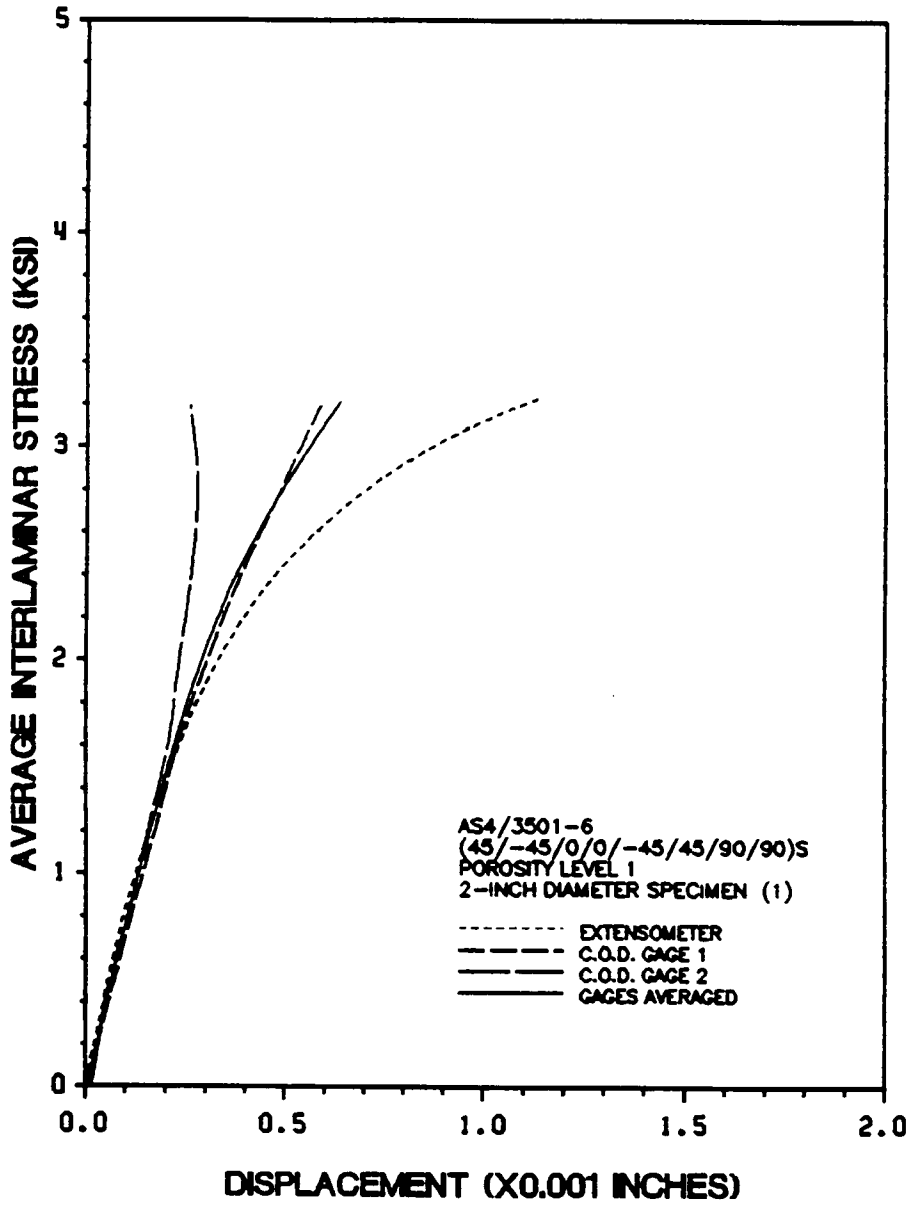

Figure 76. Flatwise Tensile Specimen Number 2-3.

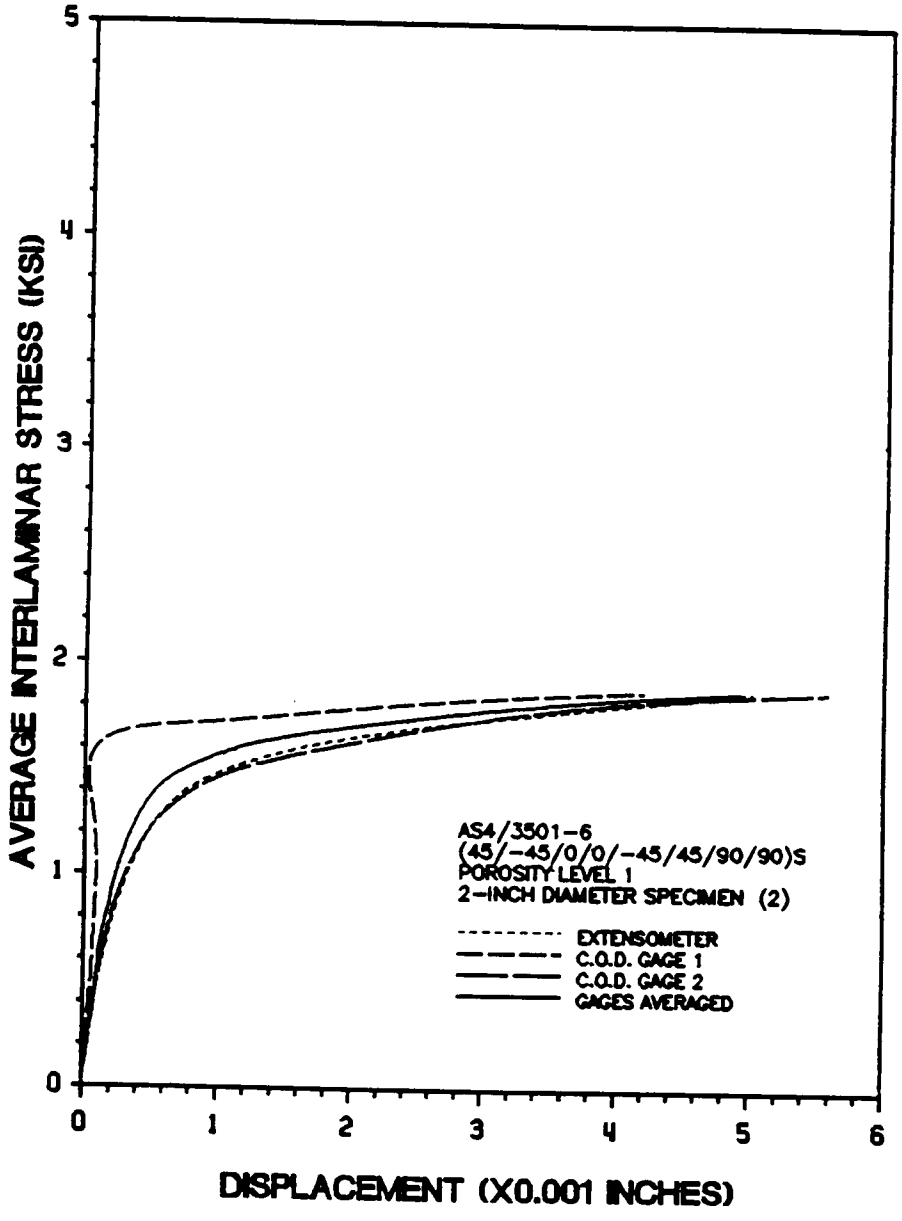

Figure 77. Flatwise Tensile Specimen Number 2-5.

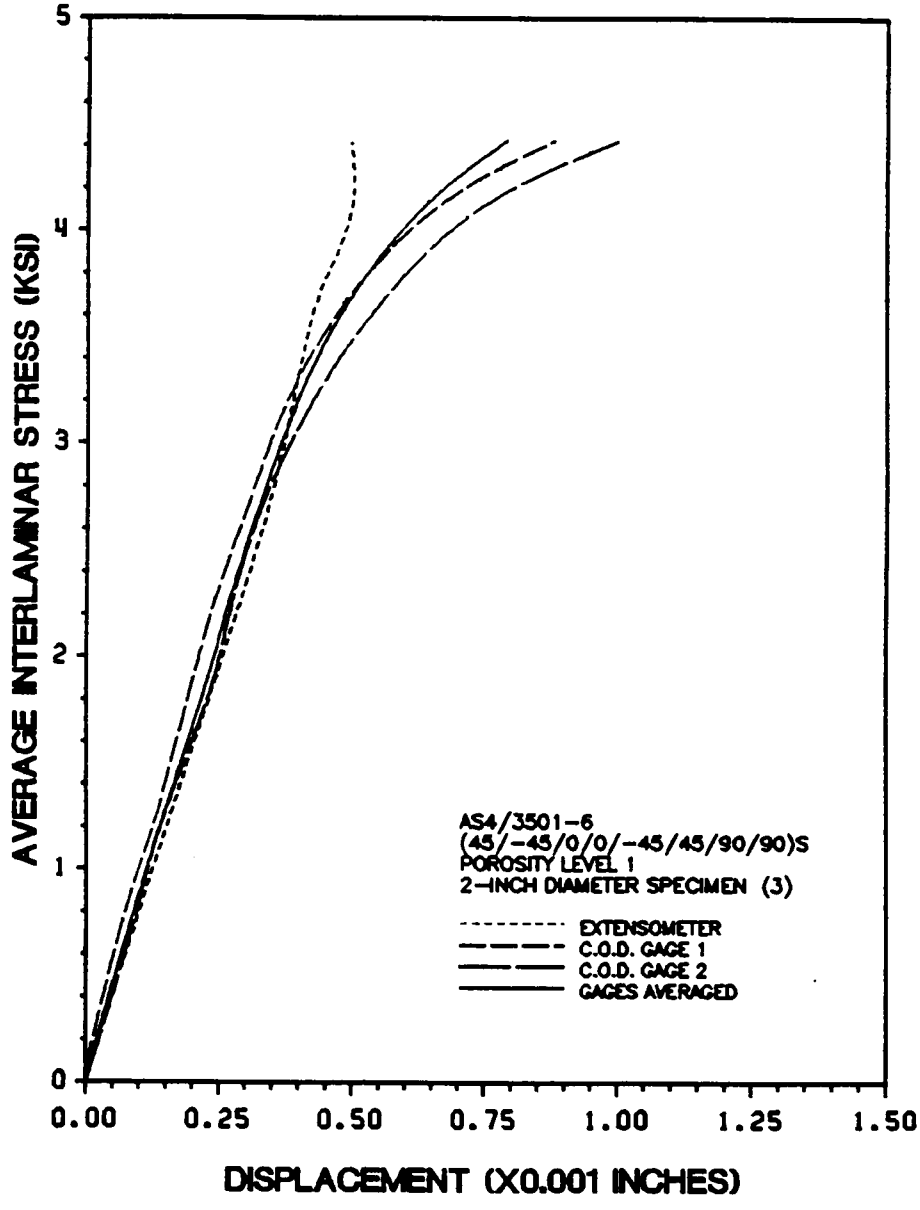

Figure 78. Flatwise Tensile Specimen Number 2-7.

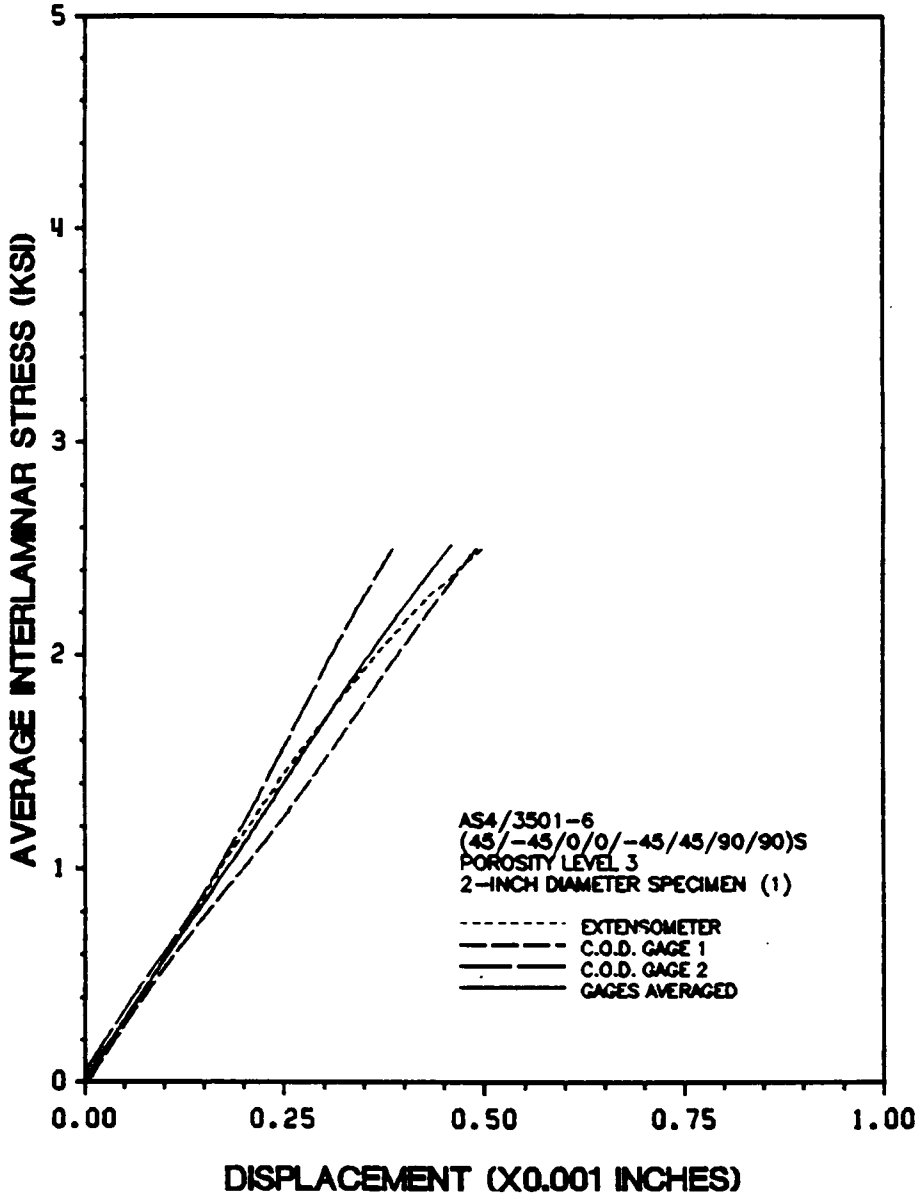

Figure 79. Flatwise Tensile Specimen Number 17-3.

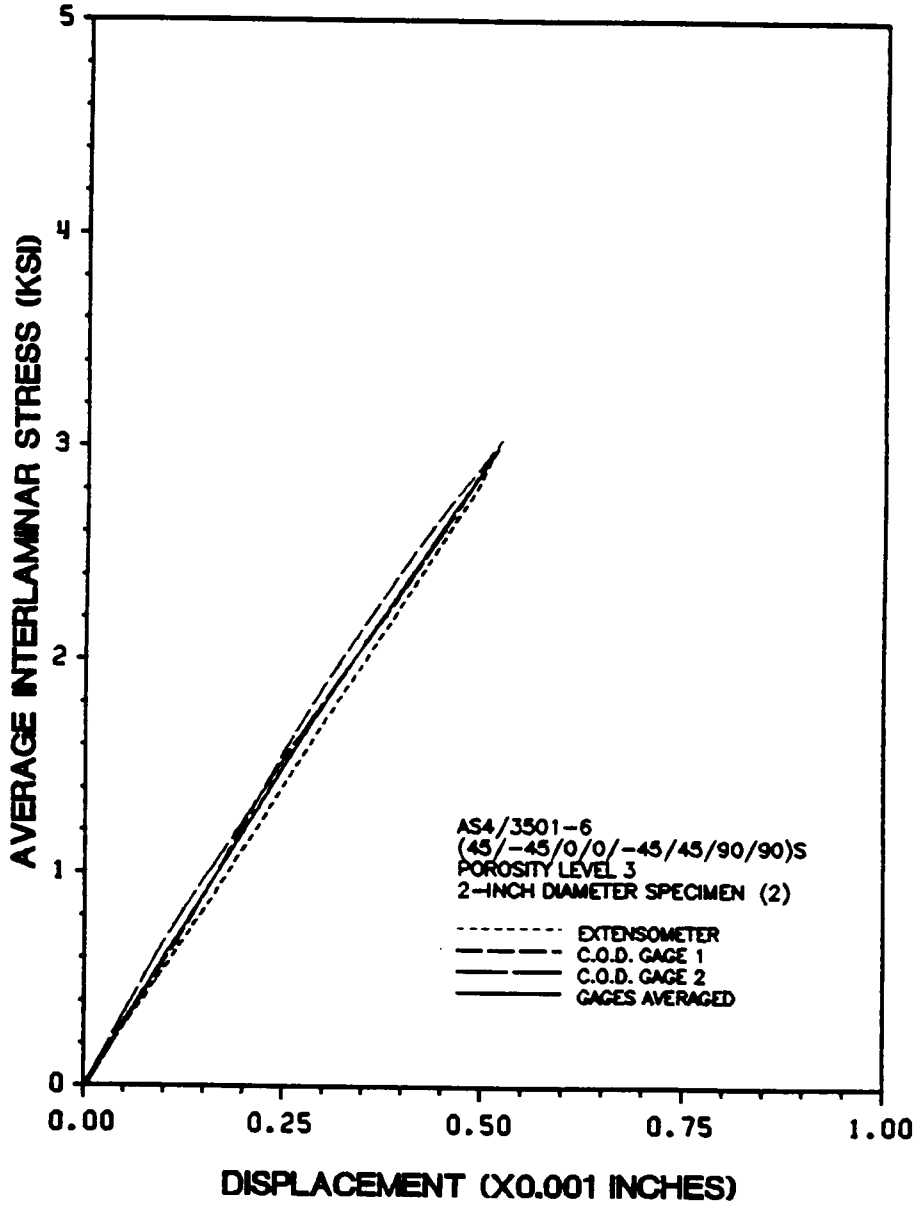

Figure 80. Flatwise Tensile Specimen Number 17-5.

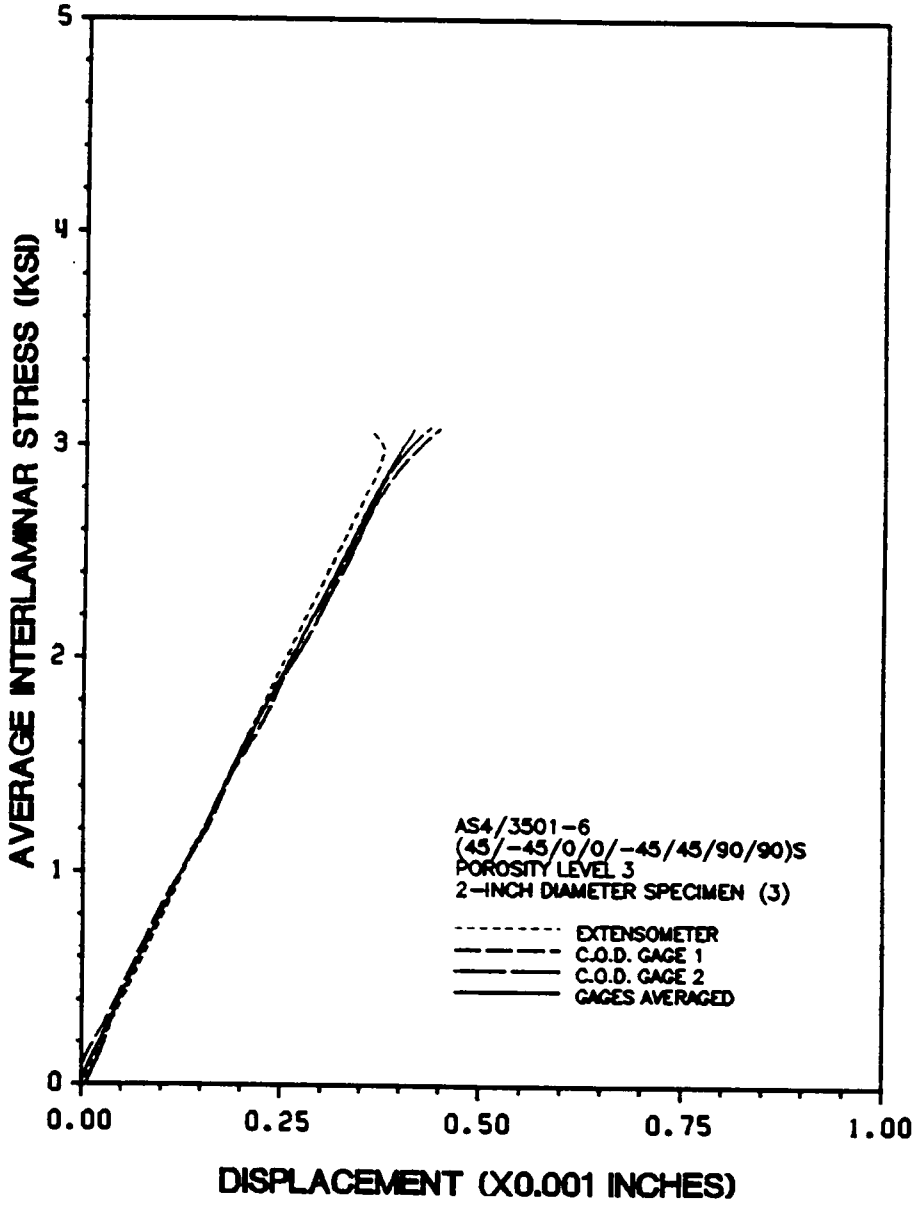

Figure 81. Flatwise Tensile Specimen Number 17-7.

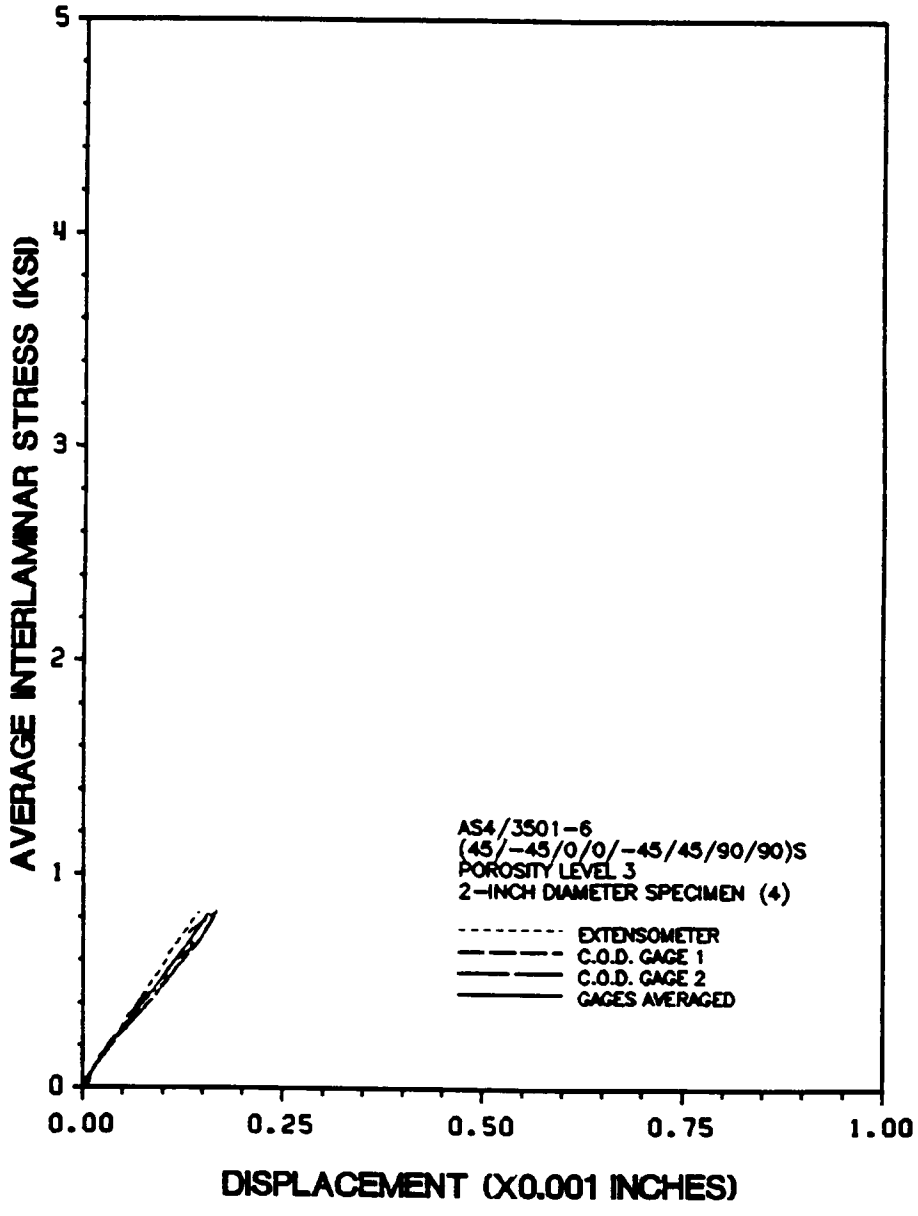

Figure 82. Flatwise Tensile Specimen Number 19-3.

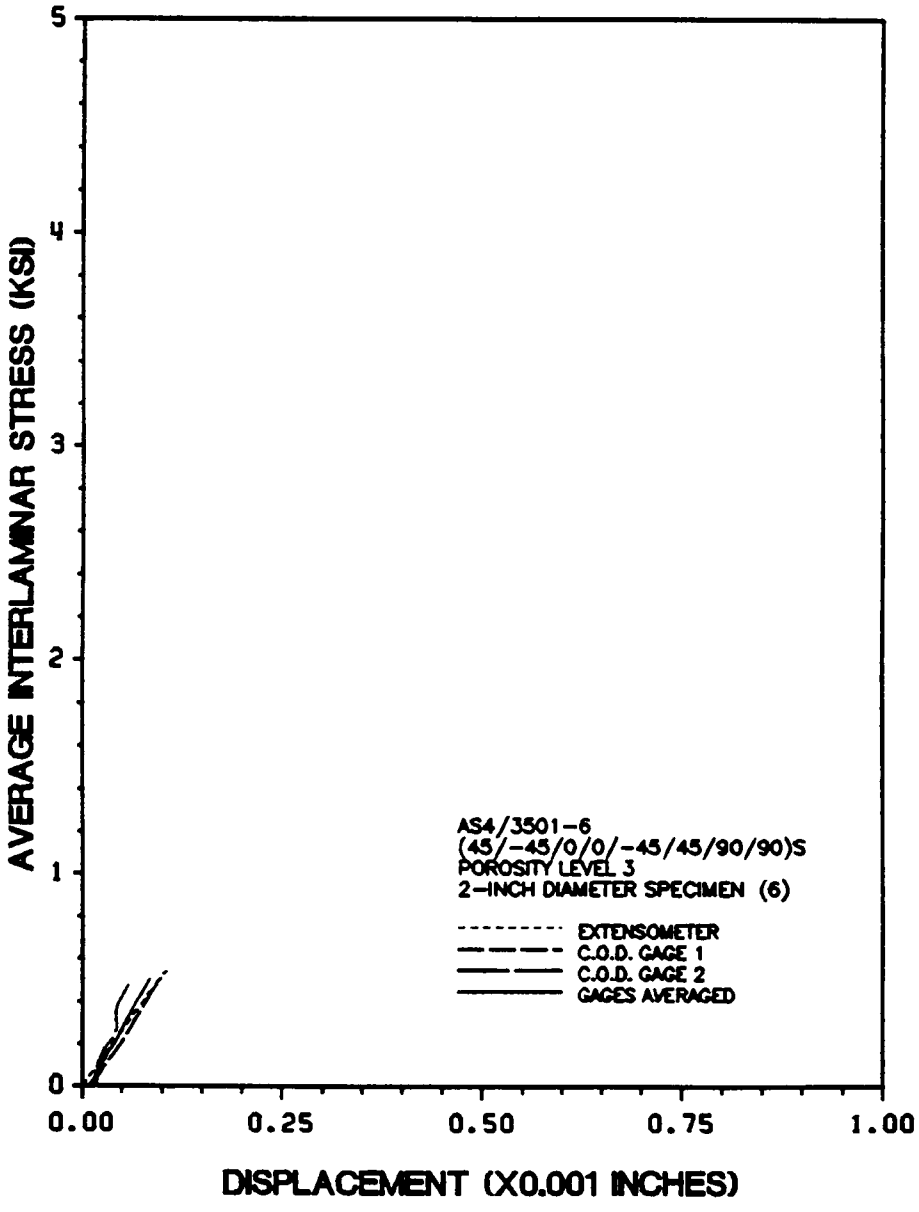

Figure 83. Flatwise Tensile Specimen Number 19-7.

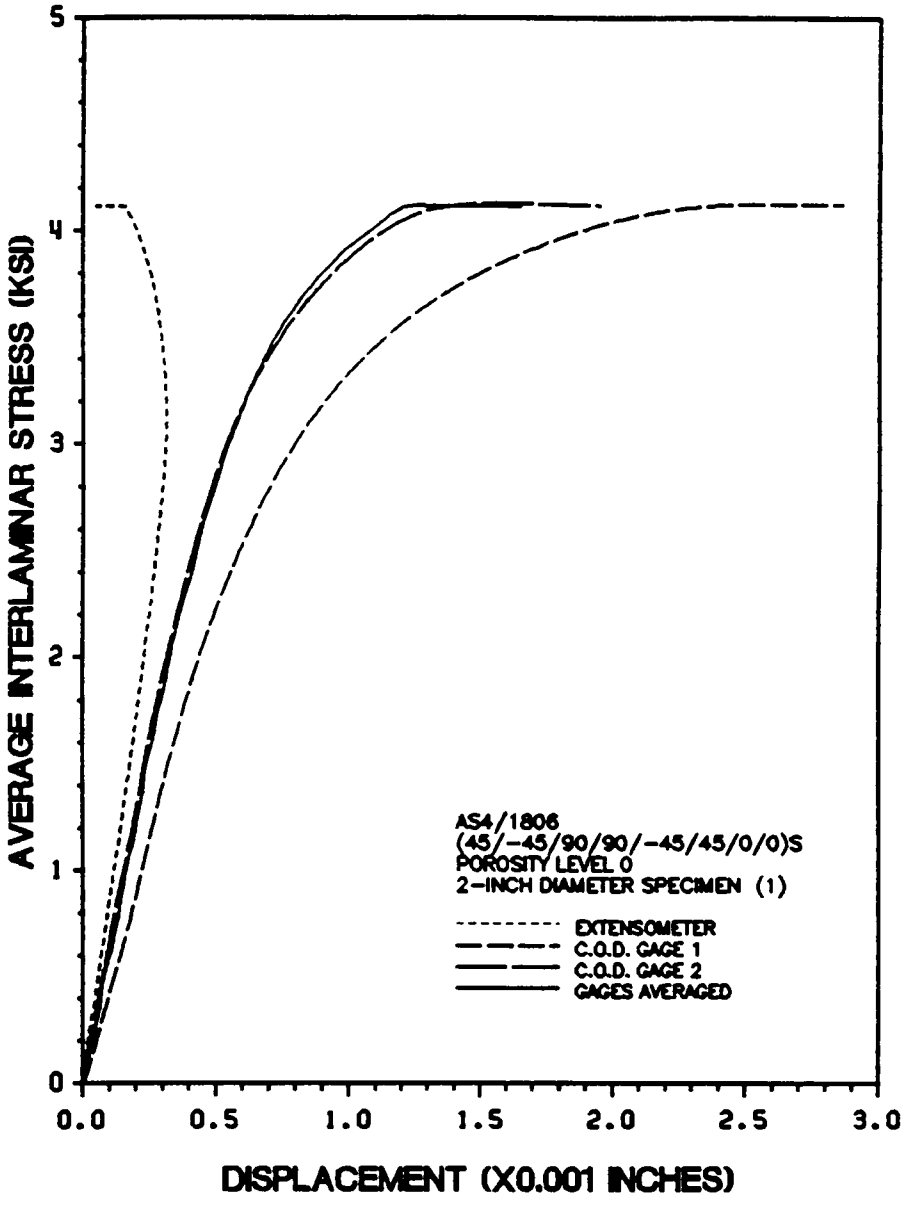

Figure 84. Flatwise Tensile Specimen Number 7-3.

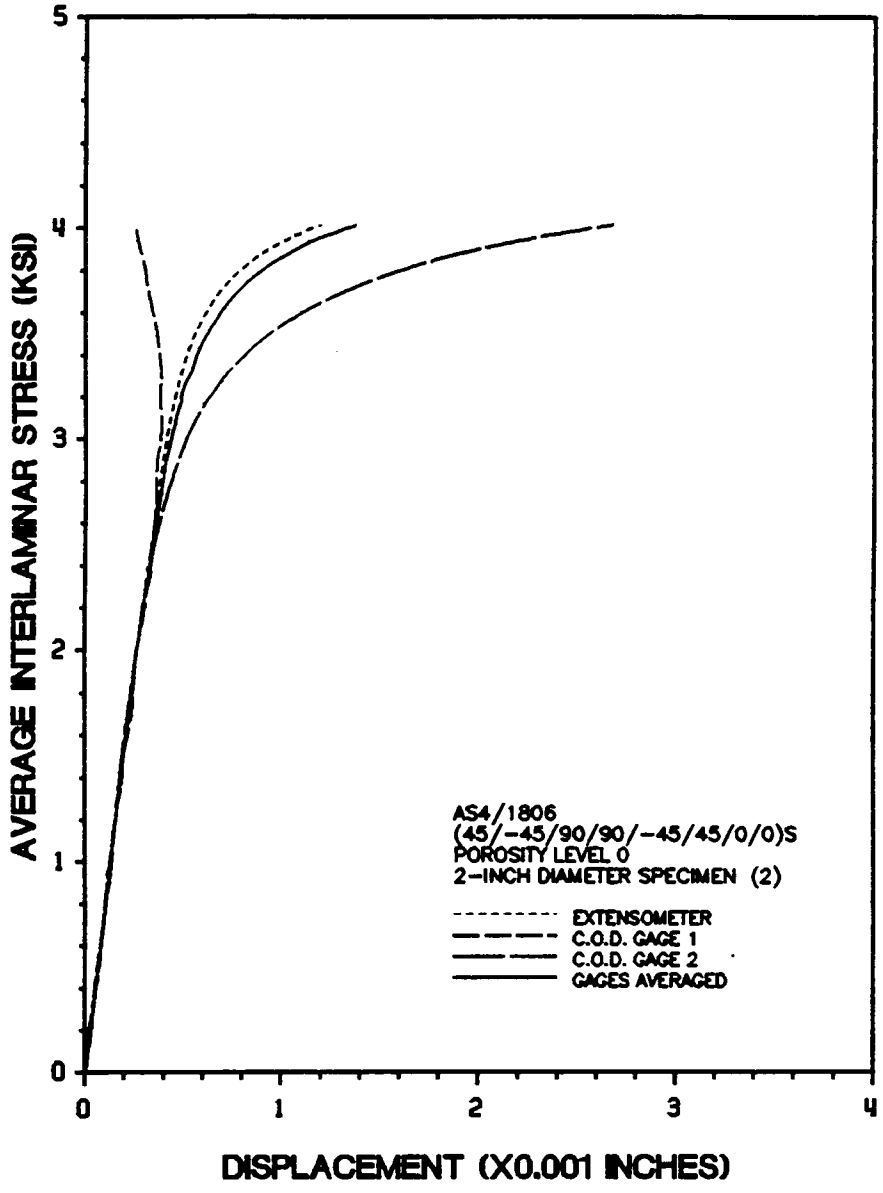

Figure 85. Flatwise Tensile Specimen Number 7-5.

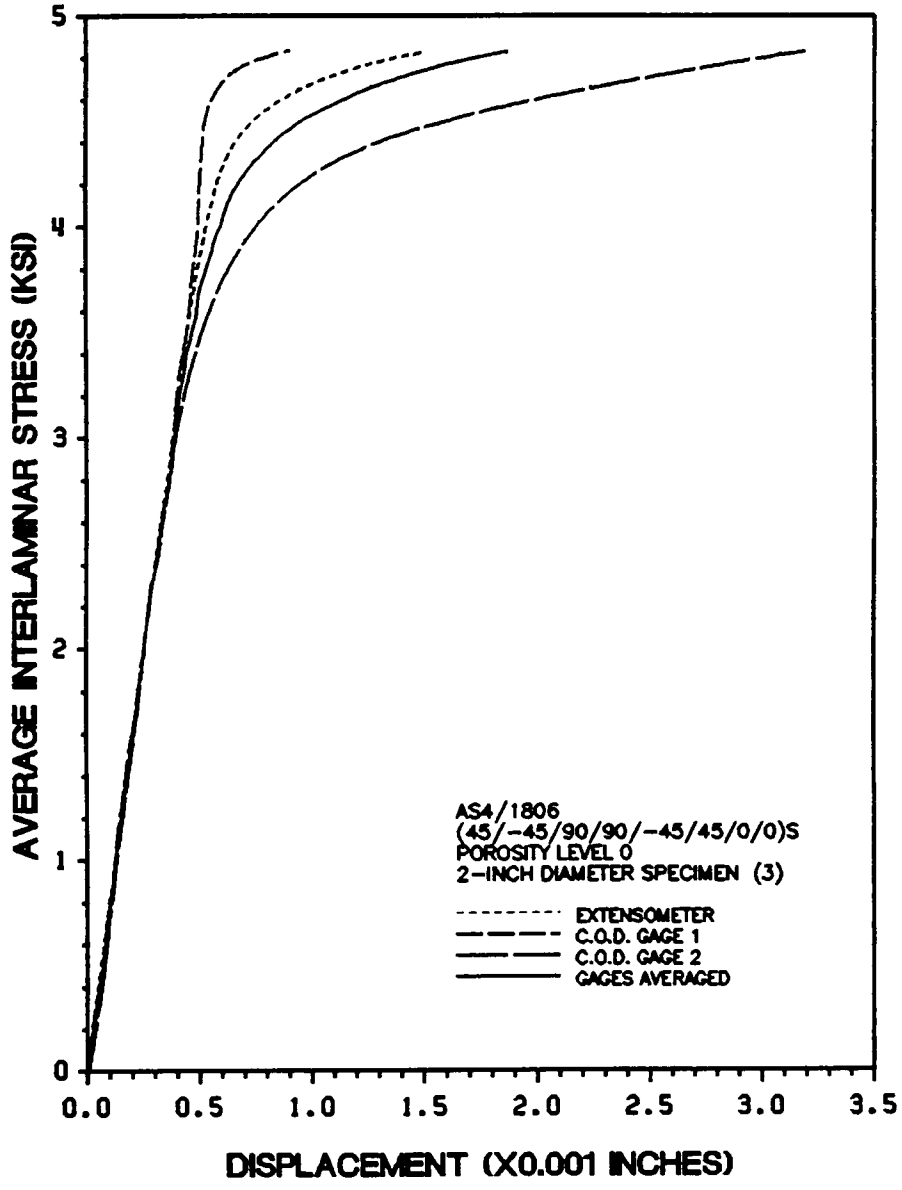

Figure 86. Flatwise Tensile Specimen Number 7-7.

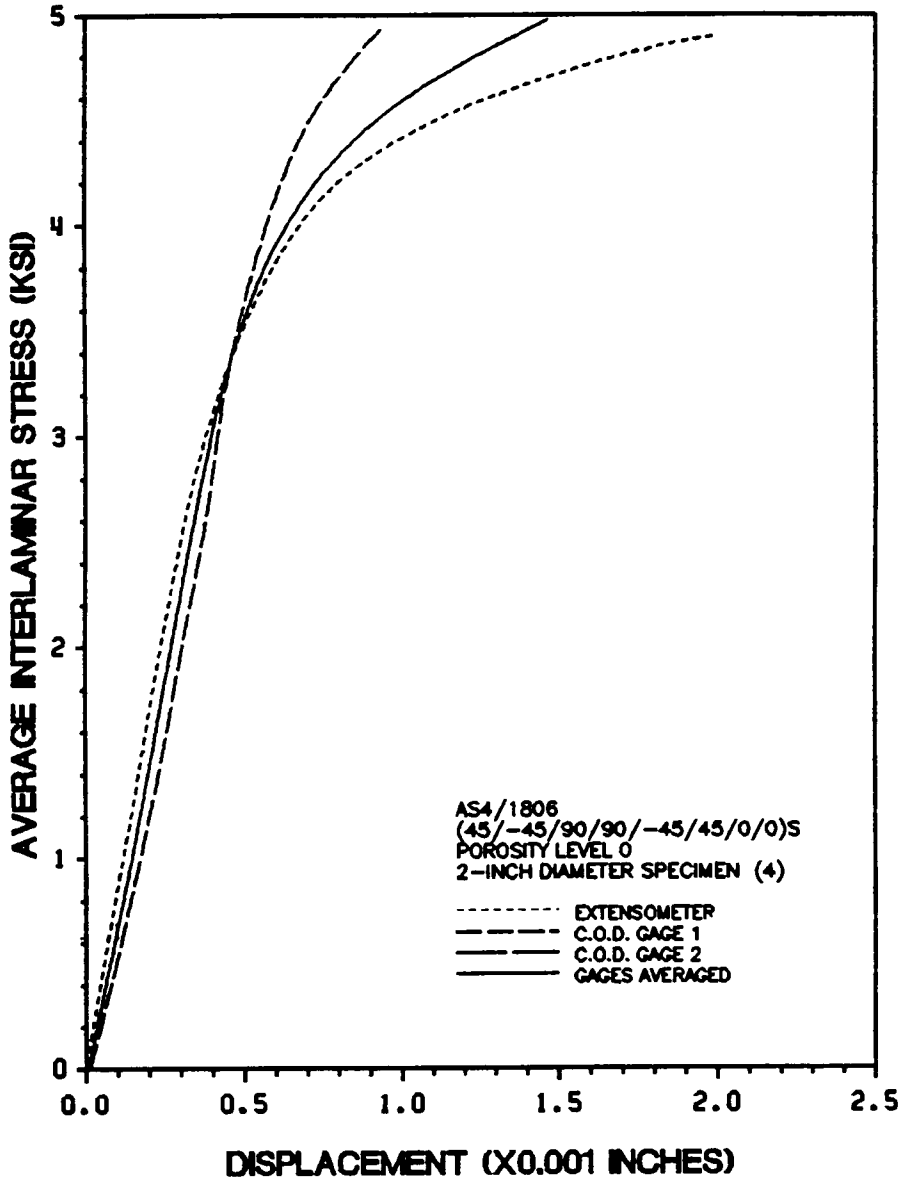

Figure 87. Flatwise Tensile Specimen Number 8-3.

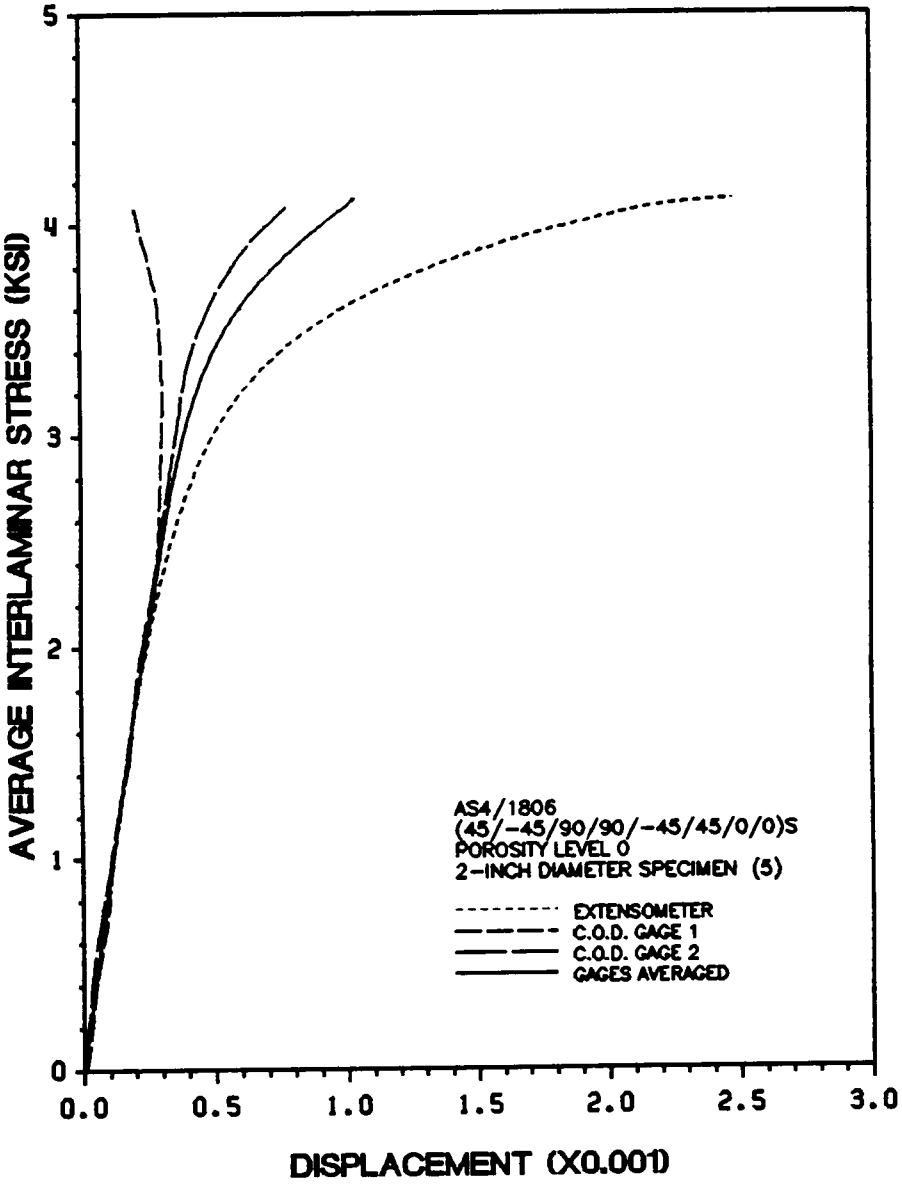

Figure 88. Flatwise Tensile Specimen Number 8-5.

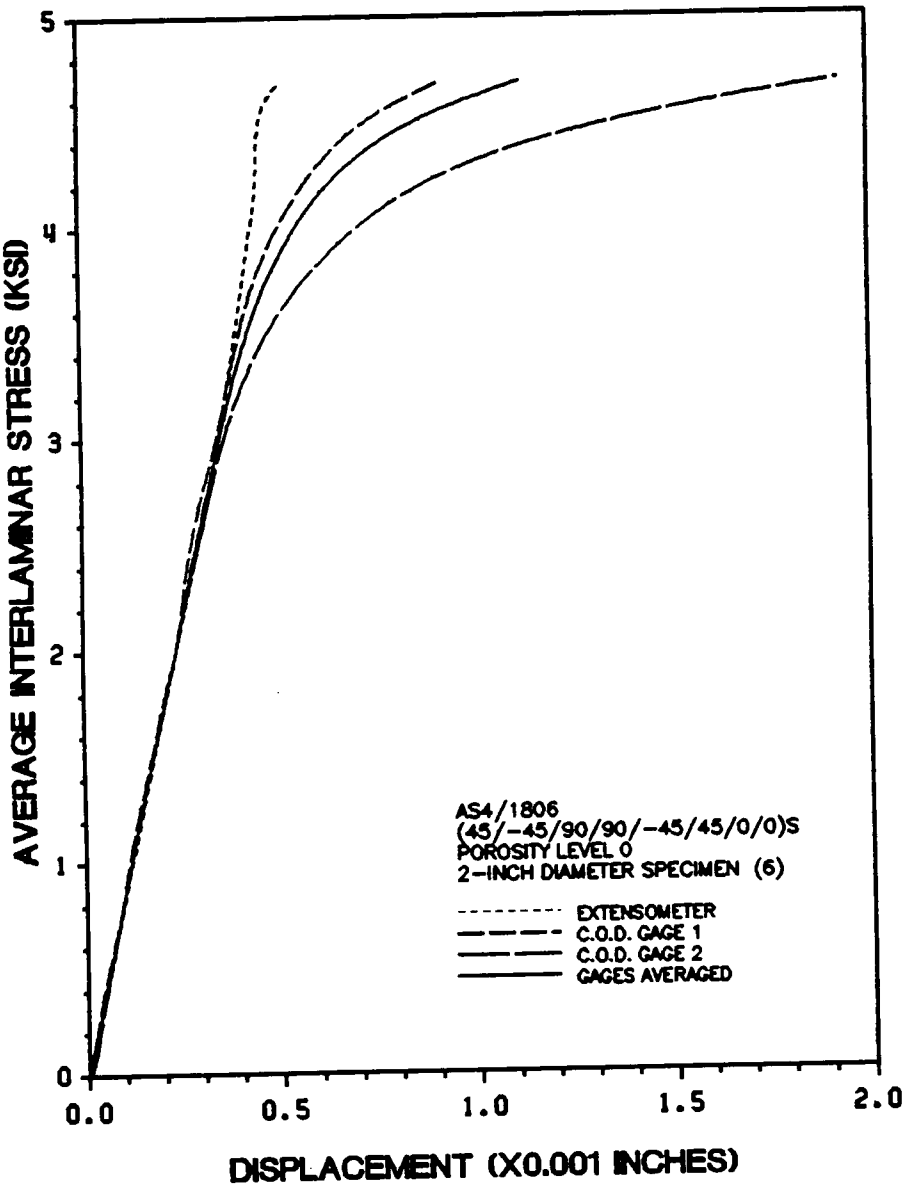

Figure 89. Flatwise Tensile Specimen Number 8-7.

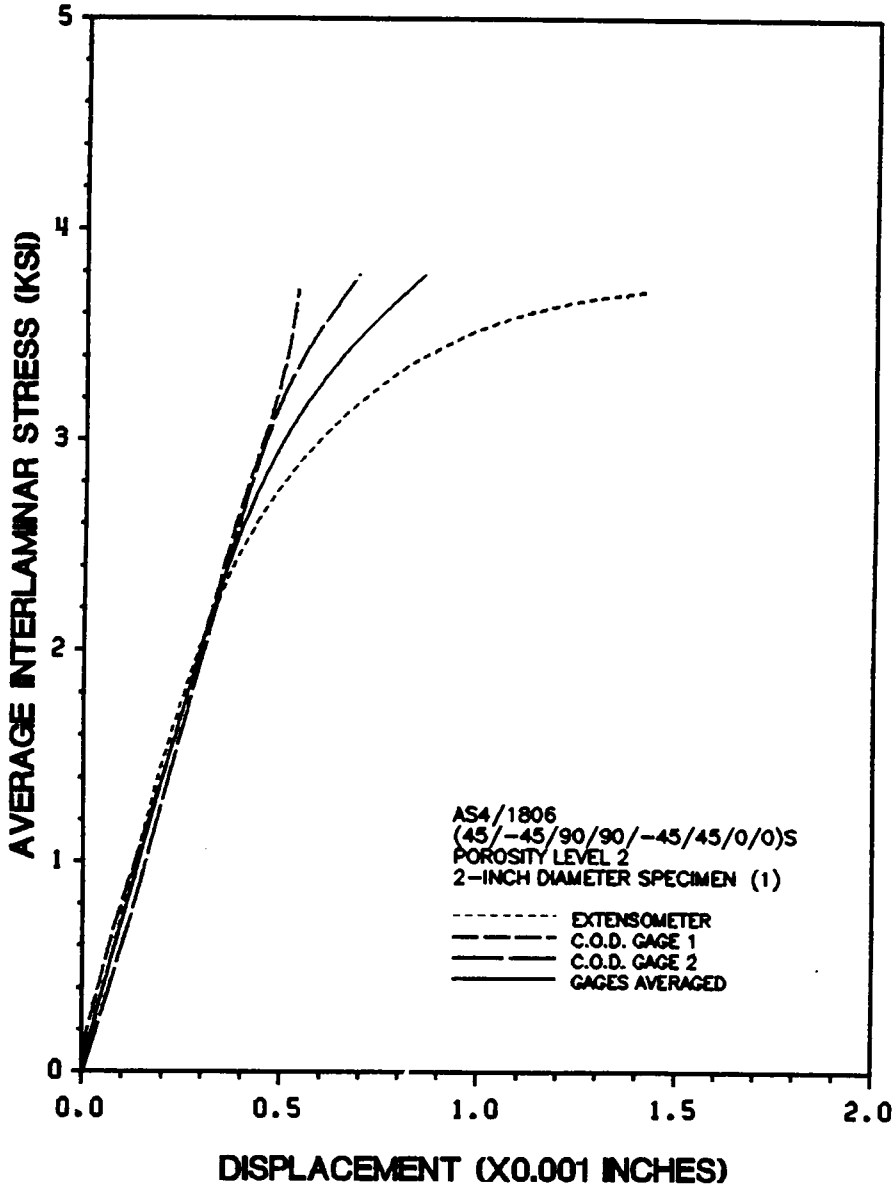

Figure 90. Flatwise Tensile Specimen Number 3-3.

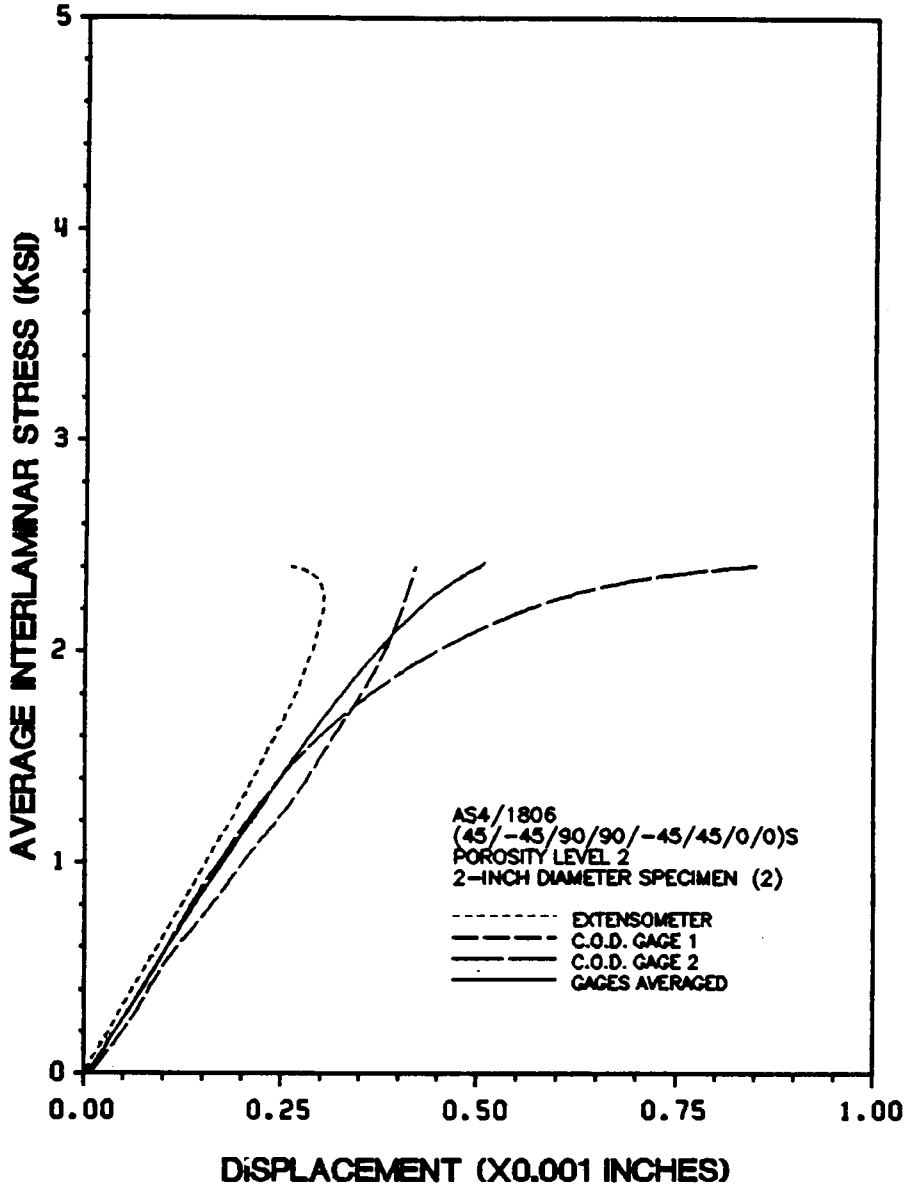

Figure 91. Flatwise Tensile Specimen Number 3-5.

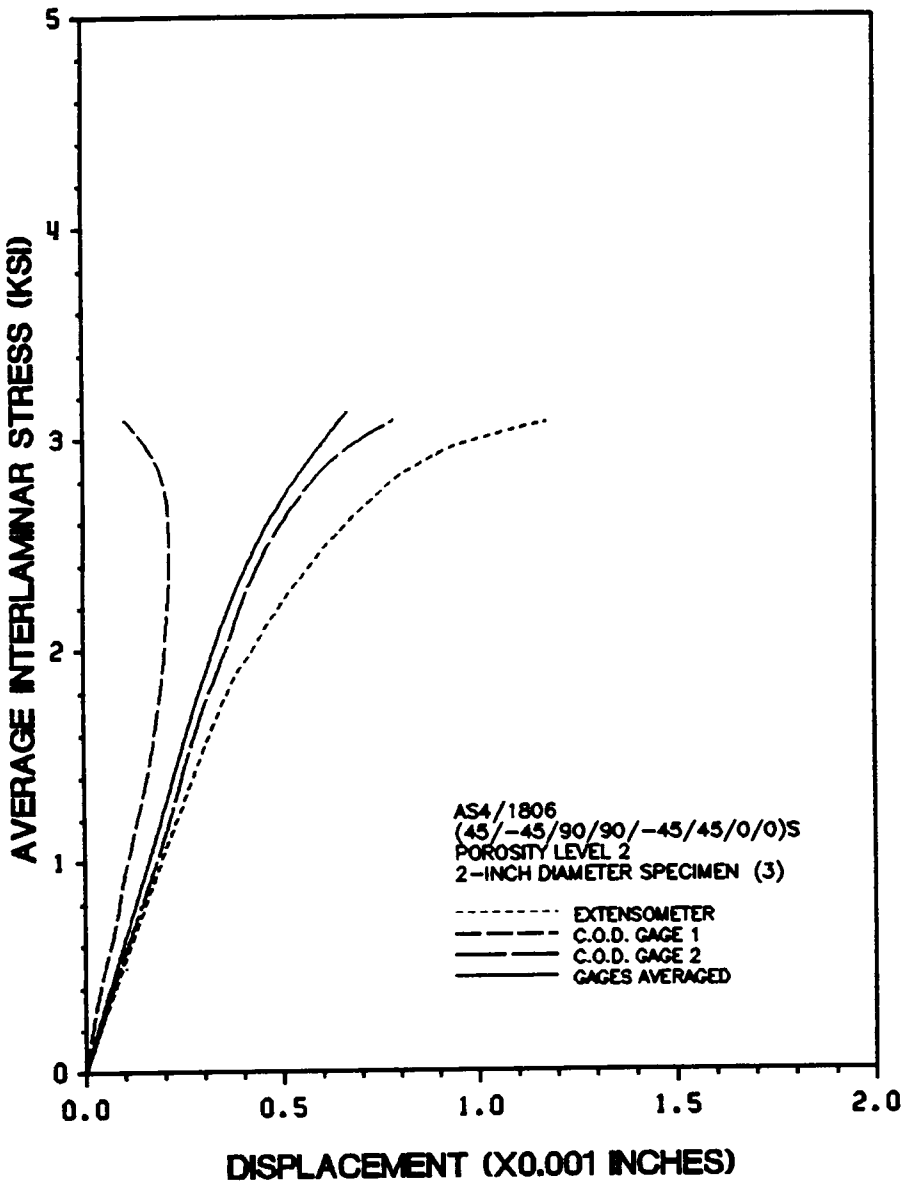

Figure 92. Flatwise Tensile Specimen Number 3-7.

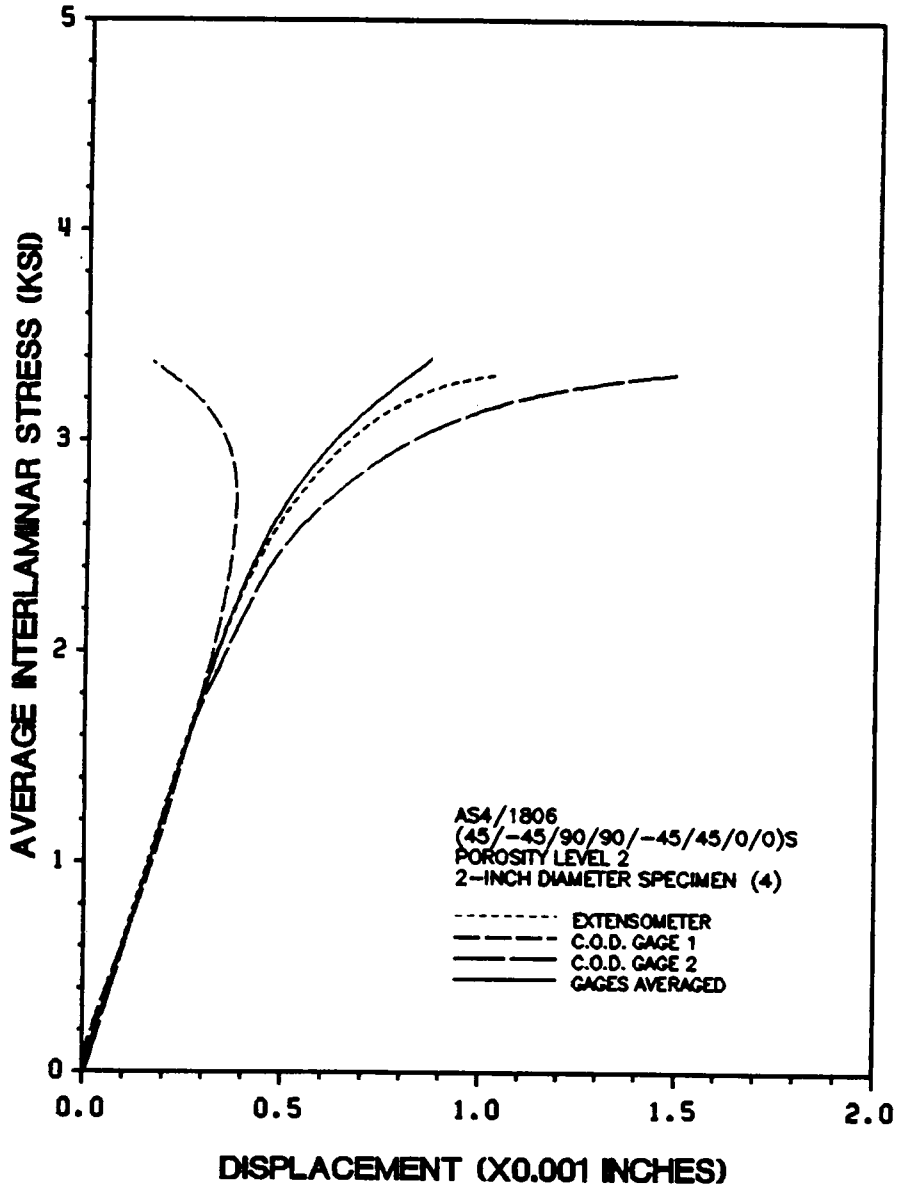

Figure 93. Flatwise Tensile Specimen Number 16-3.

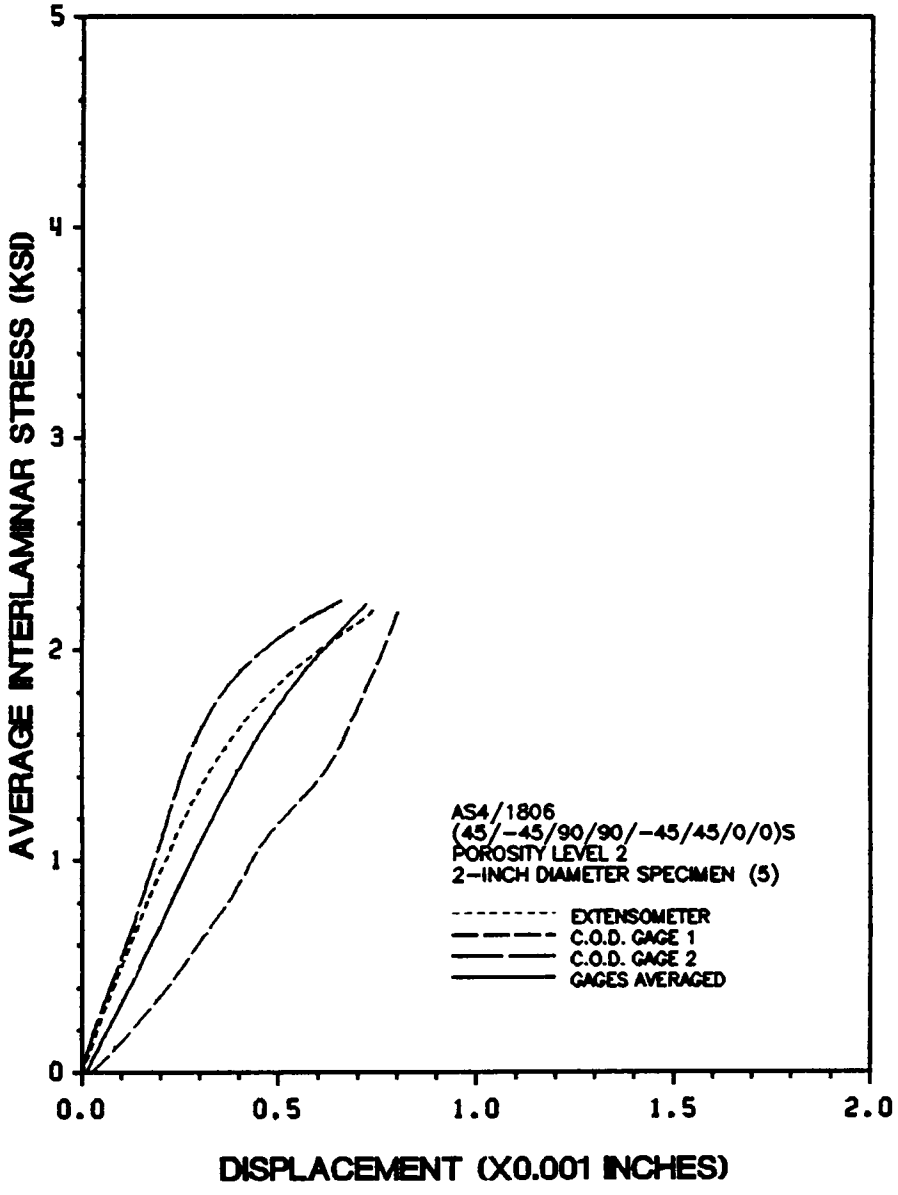

Figure 94. Flatwise Tensile Specimen Number 16-5.

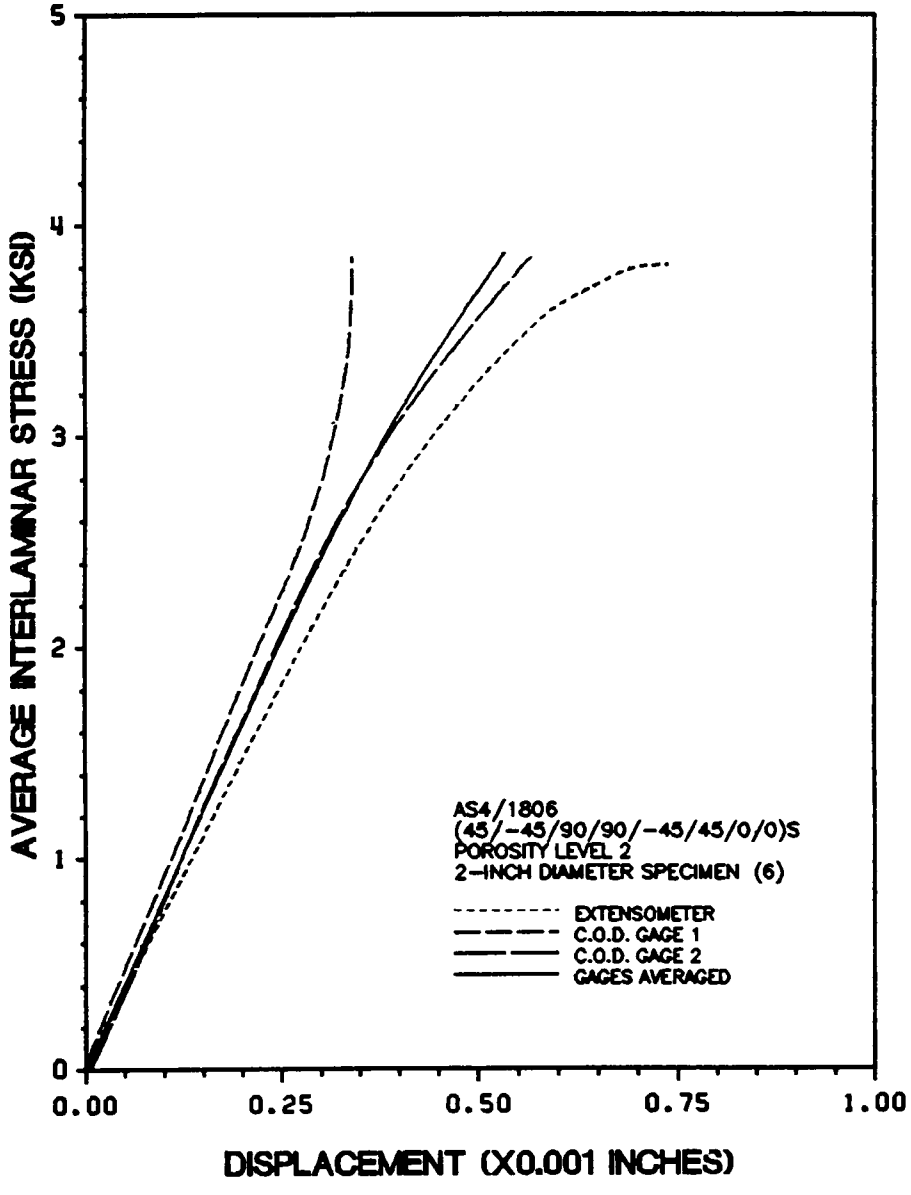

Figure 95. Flatwise Tensile Specimen Number 16-7.

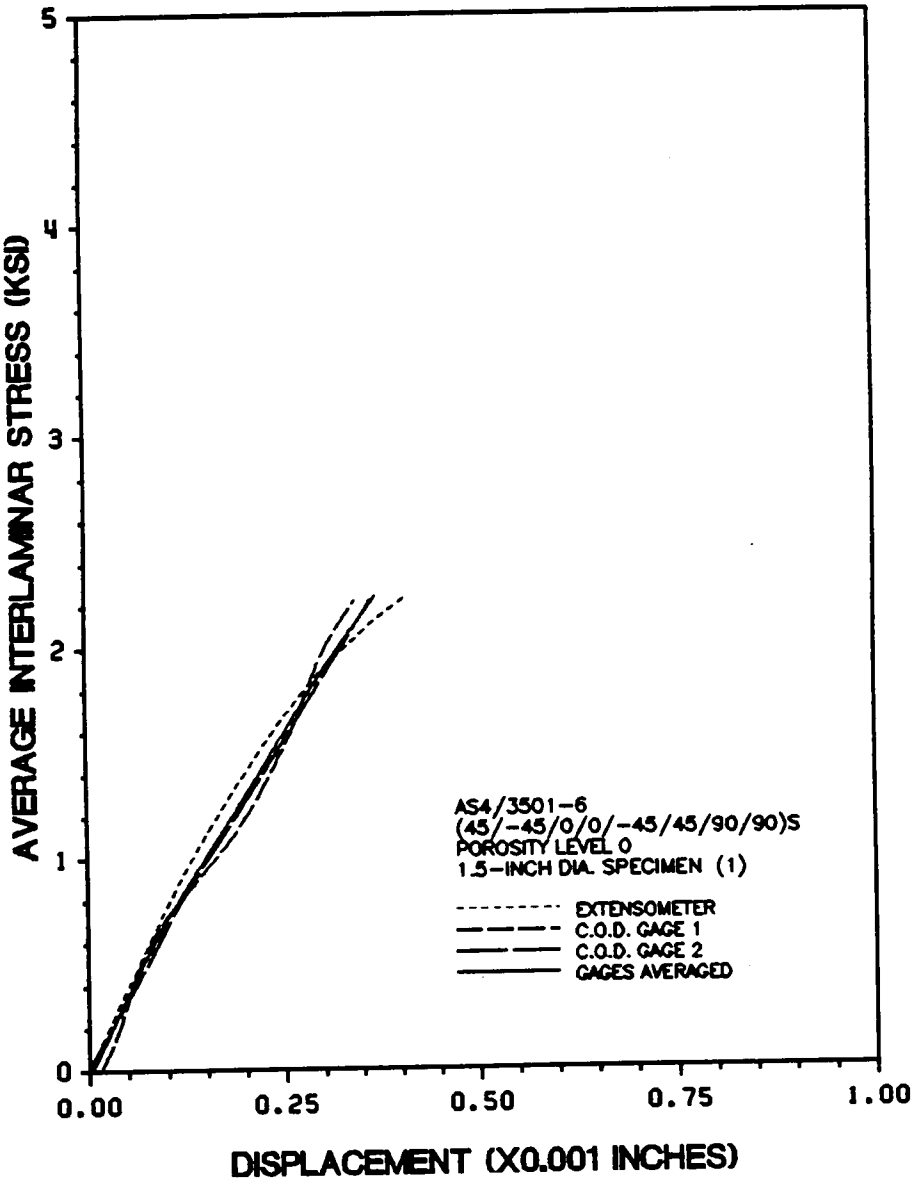

Figure 96. Flatwise Tensile Specimen Number 1-5.

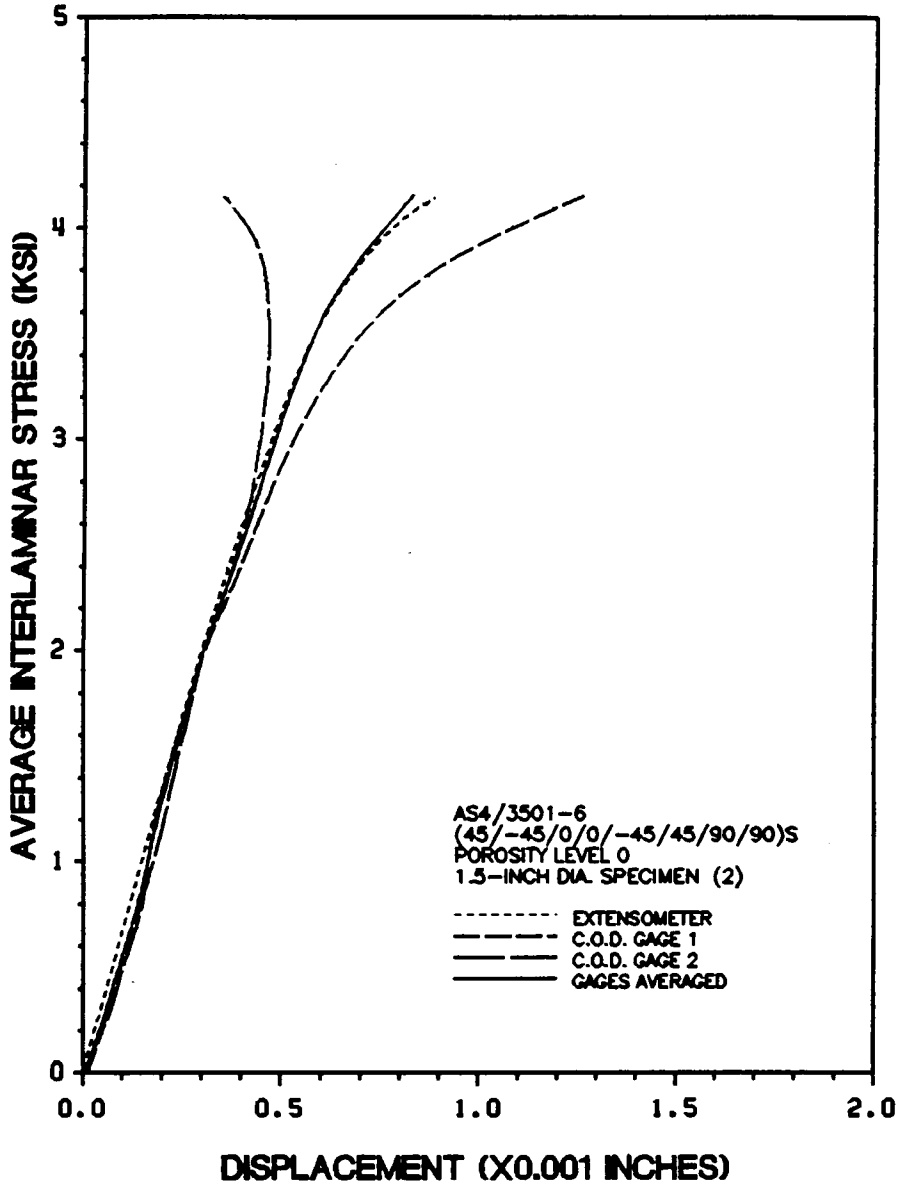

Figure 97. Flatwise Tensile Specimen Number 1-9.

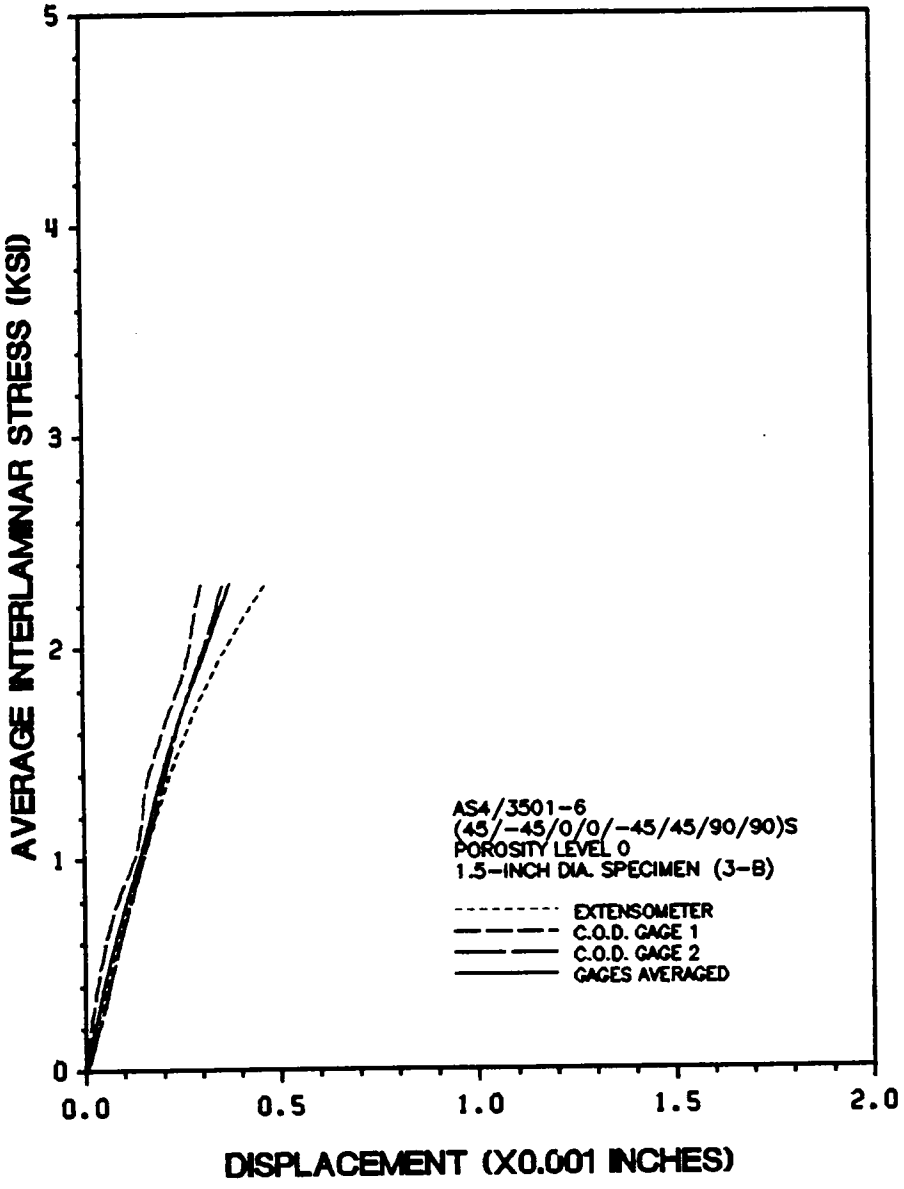

Figure 98. Flatwise Tensile Specimen Number 5-5.

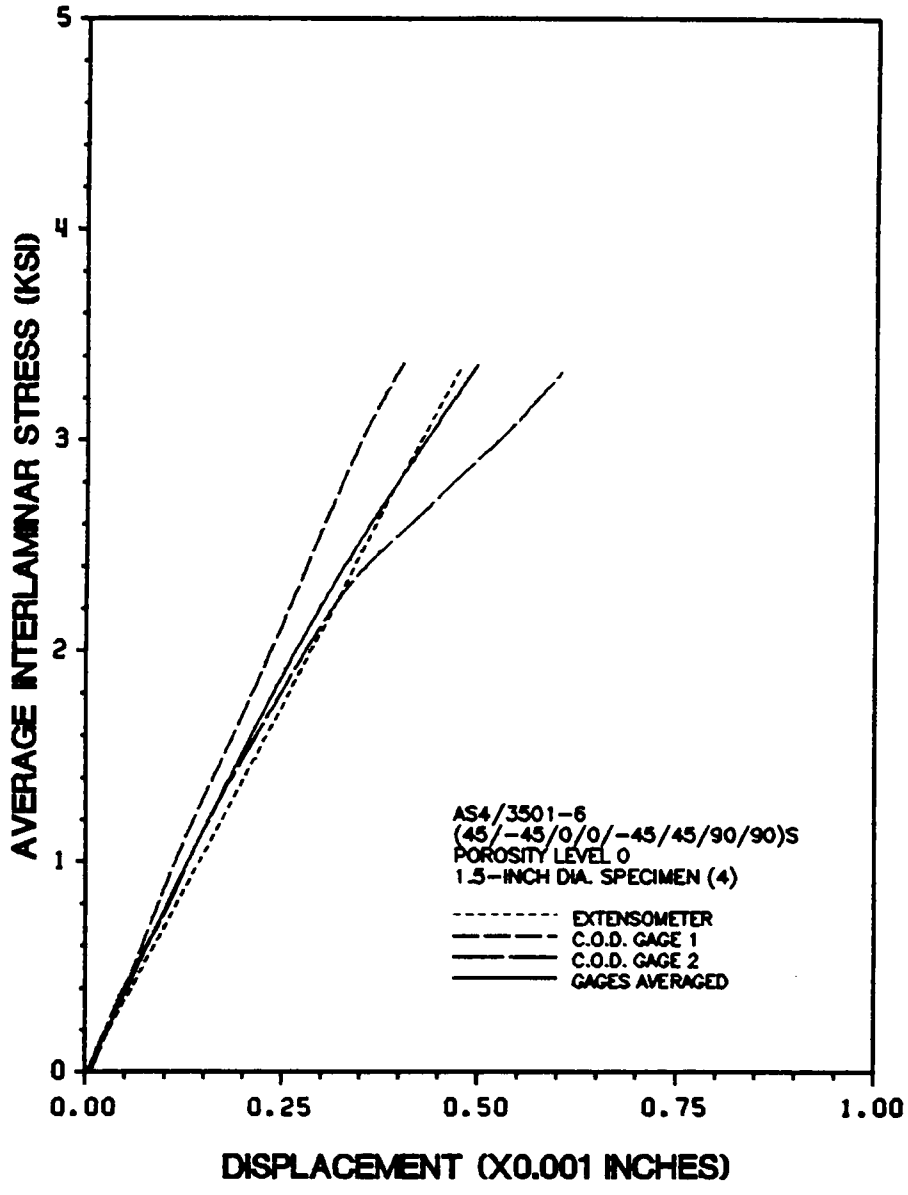

Figure 99. Flatwise Tensile Specimen Number 5-9.

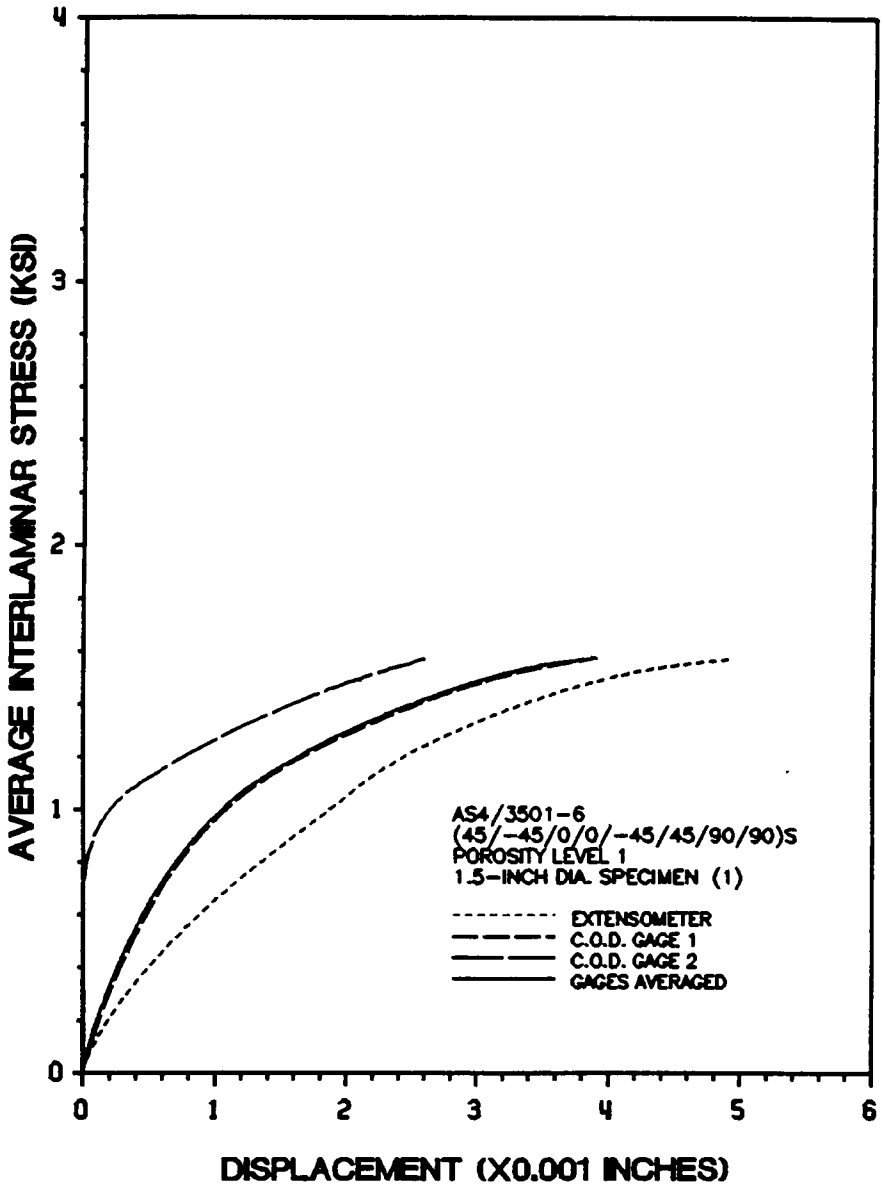

Figure 100. Flatwise Tensile Specimen Number 10-5.

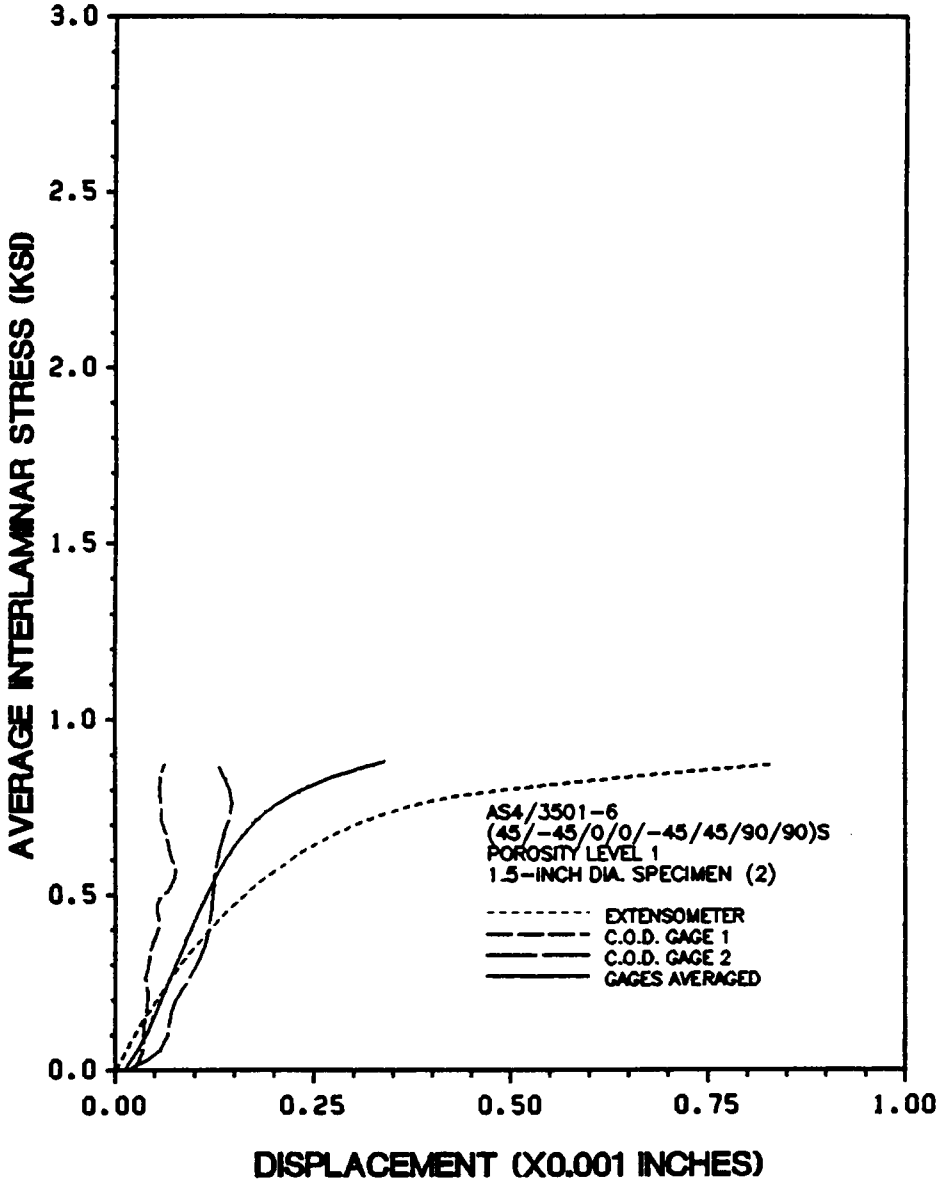

Figure 101. Flatwise Tensile Specimen Number 10-9.

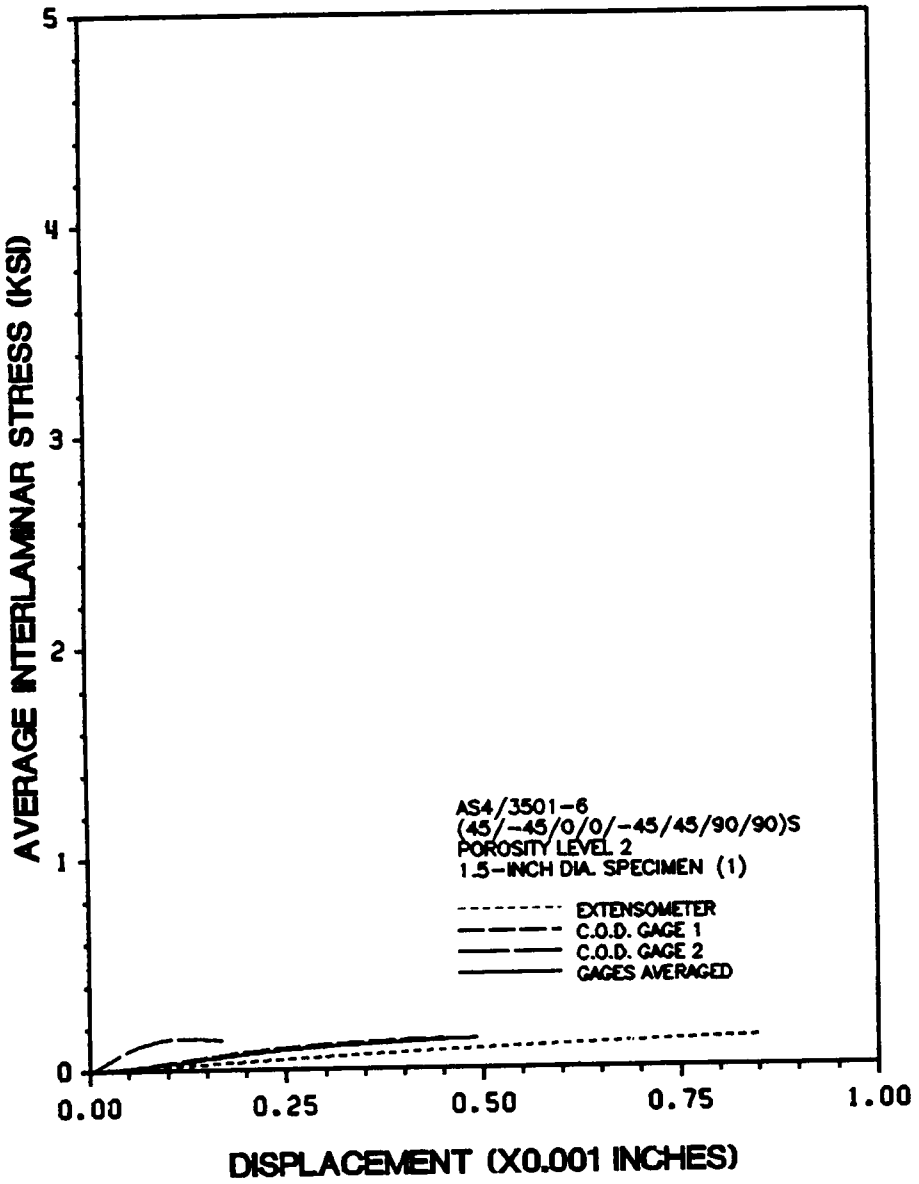

Figure 102. Flatwise Tensile Specimen Number 12-5.

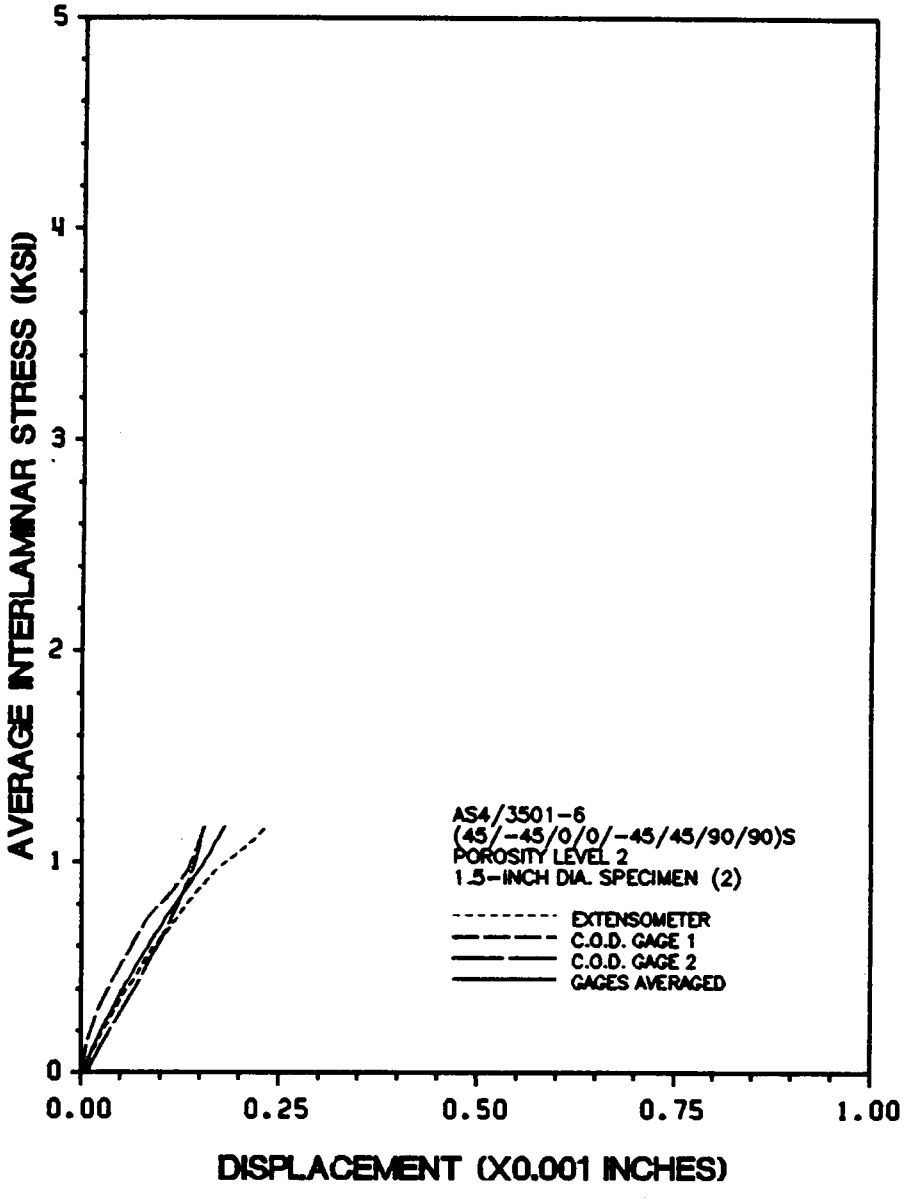

Figure 103. Flatwise Tensile Specimen Number 12-9.

GRIPPING FAILURE

Figure 104. Flatwise Tensile Specimen Number 13-5.

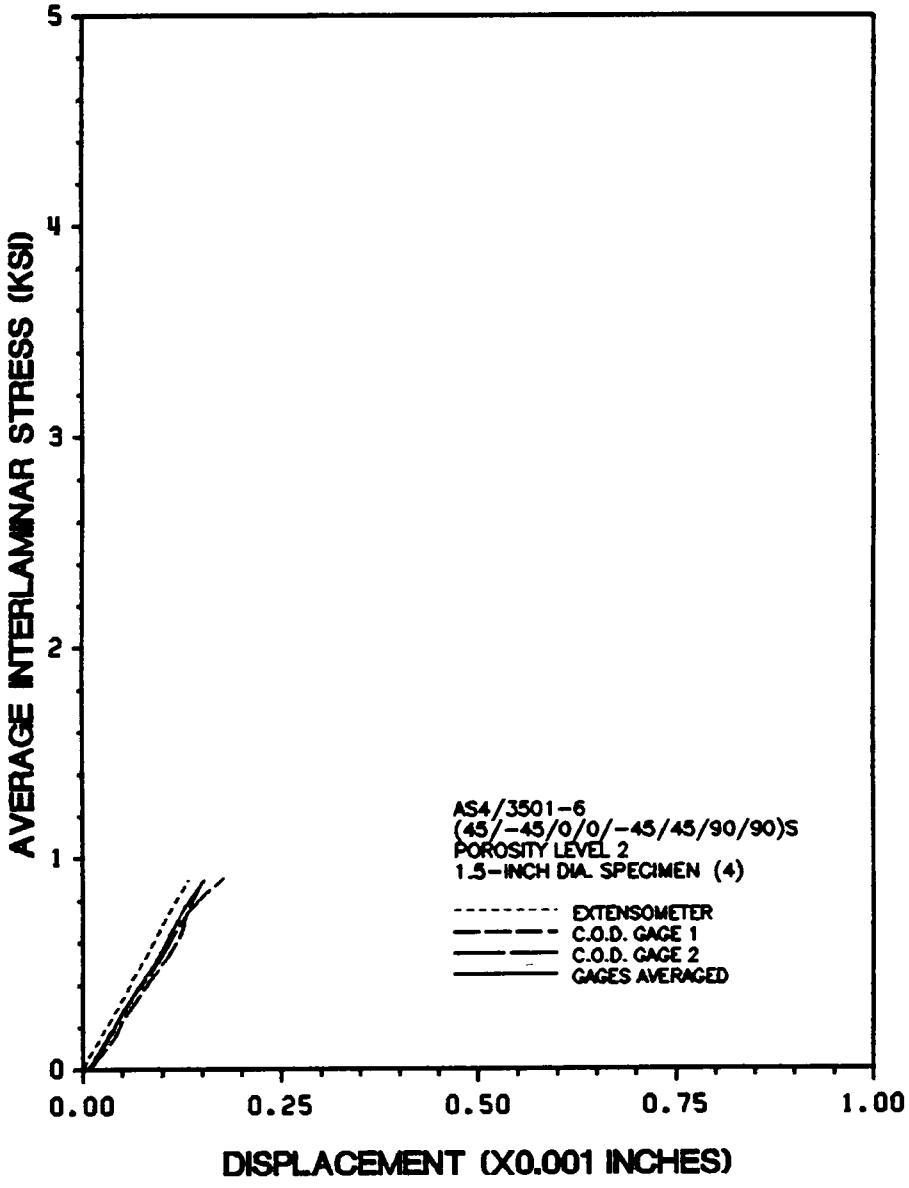

Figure 105. Flatwise Tensile Specimen Number 13-9.

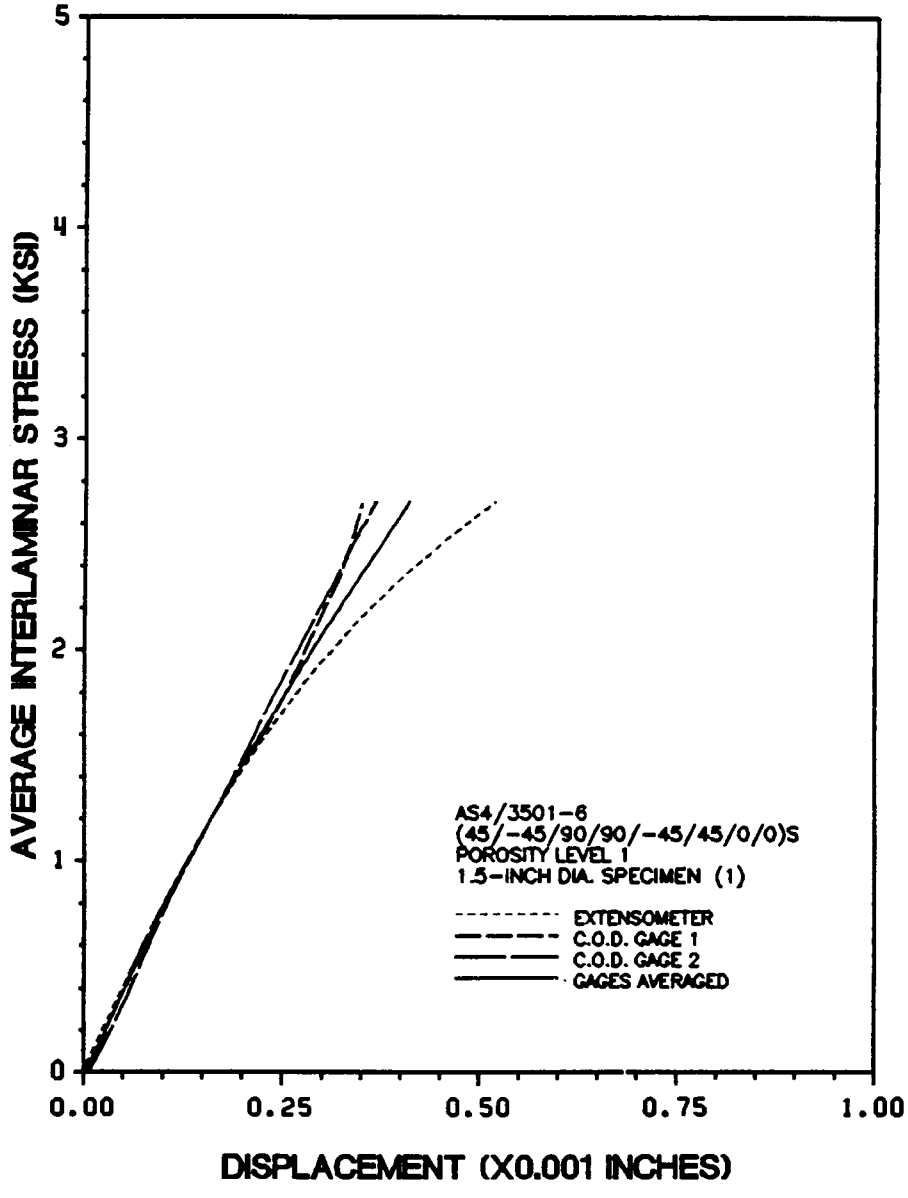

Figure 106. Flatwise Tensile Specimen Number 9-5.

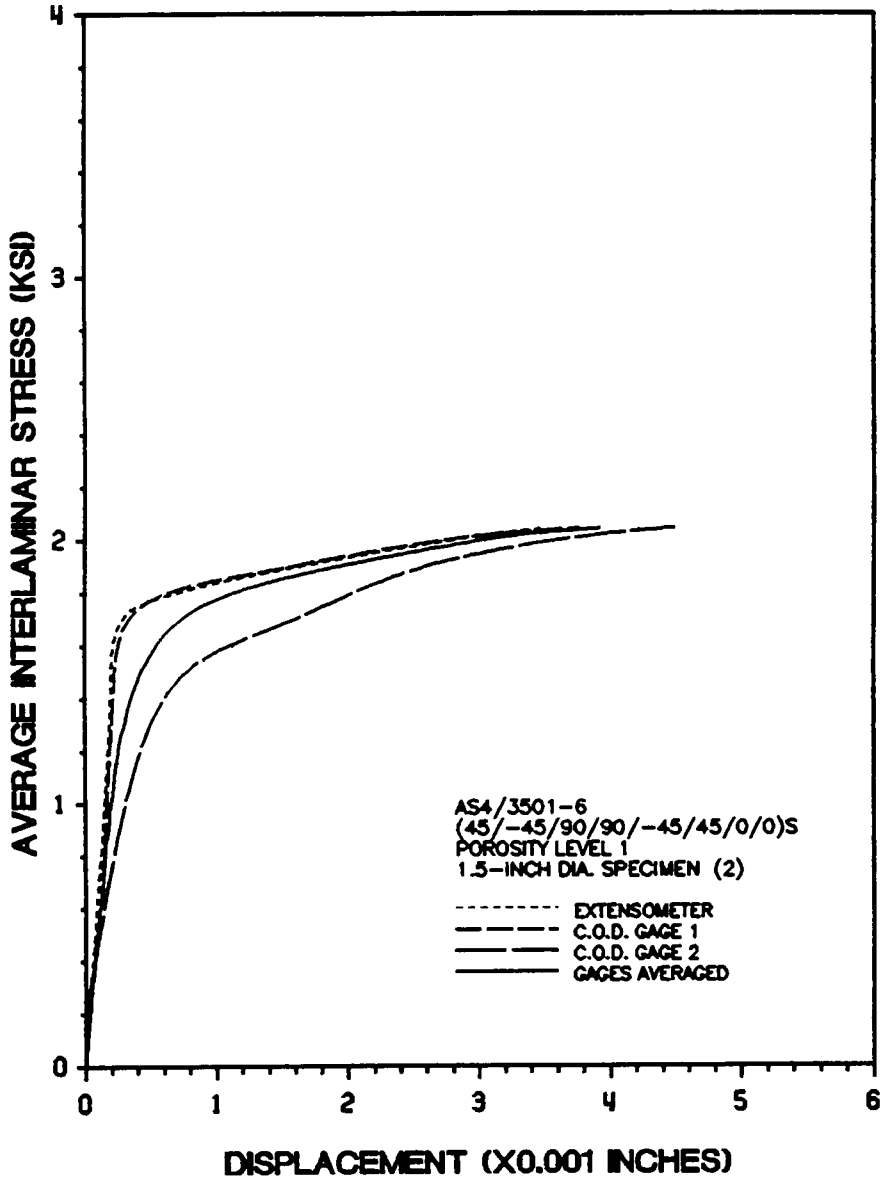

Figure 107. Flatwise Tensile Specimen Number 9-9.

Appendix B. Out-Of-Plane Tensile Data - Average Group Plots

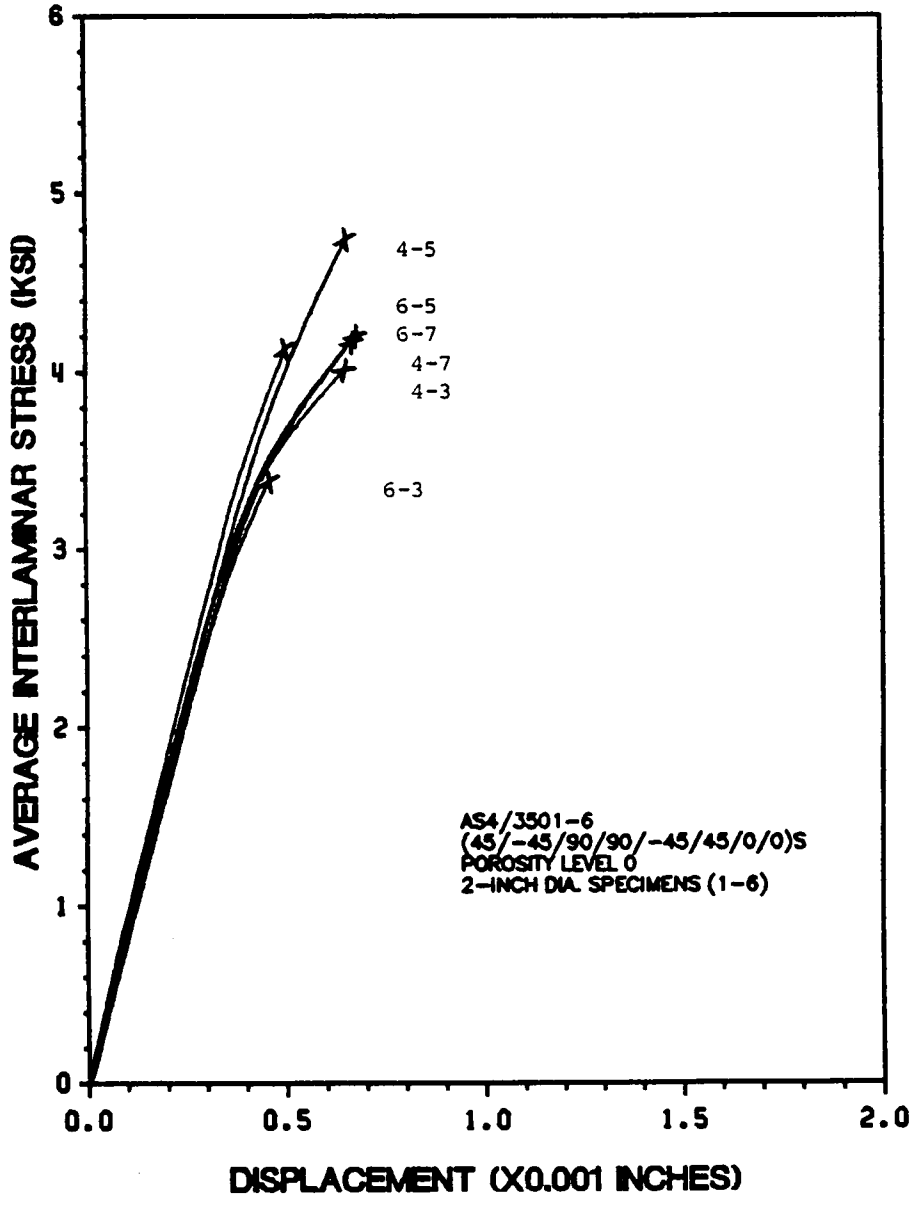

Figure 108. 2.0-Inch Diameter, AS4/3501-6 Defect Level 0 Specimens.

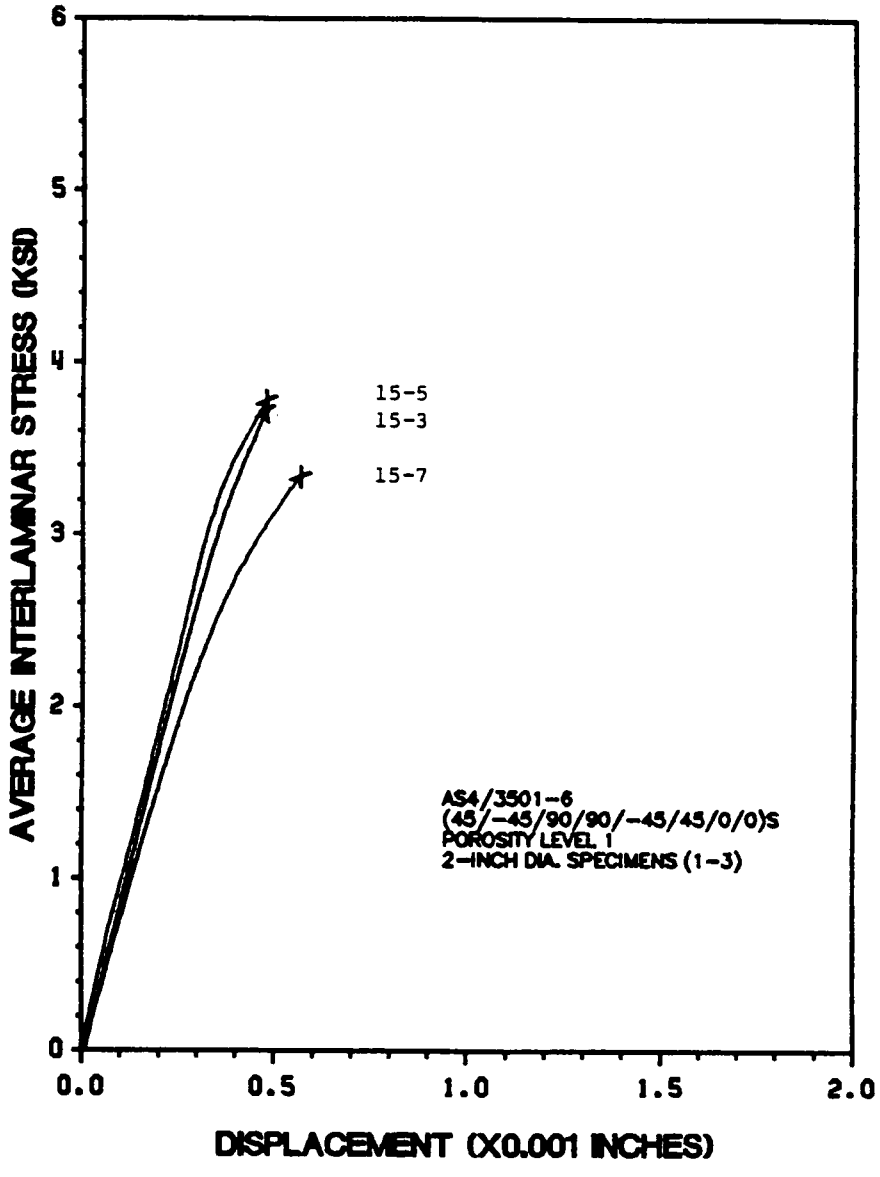

Figure 109. 2.0-Inch Diameter, AS4/3501-6 Defect Level 1 Specimens.

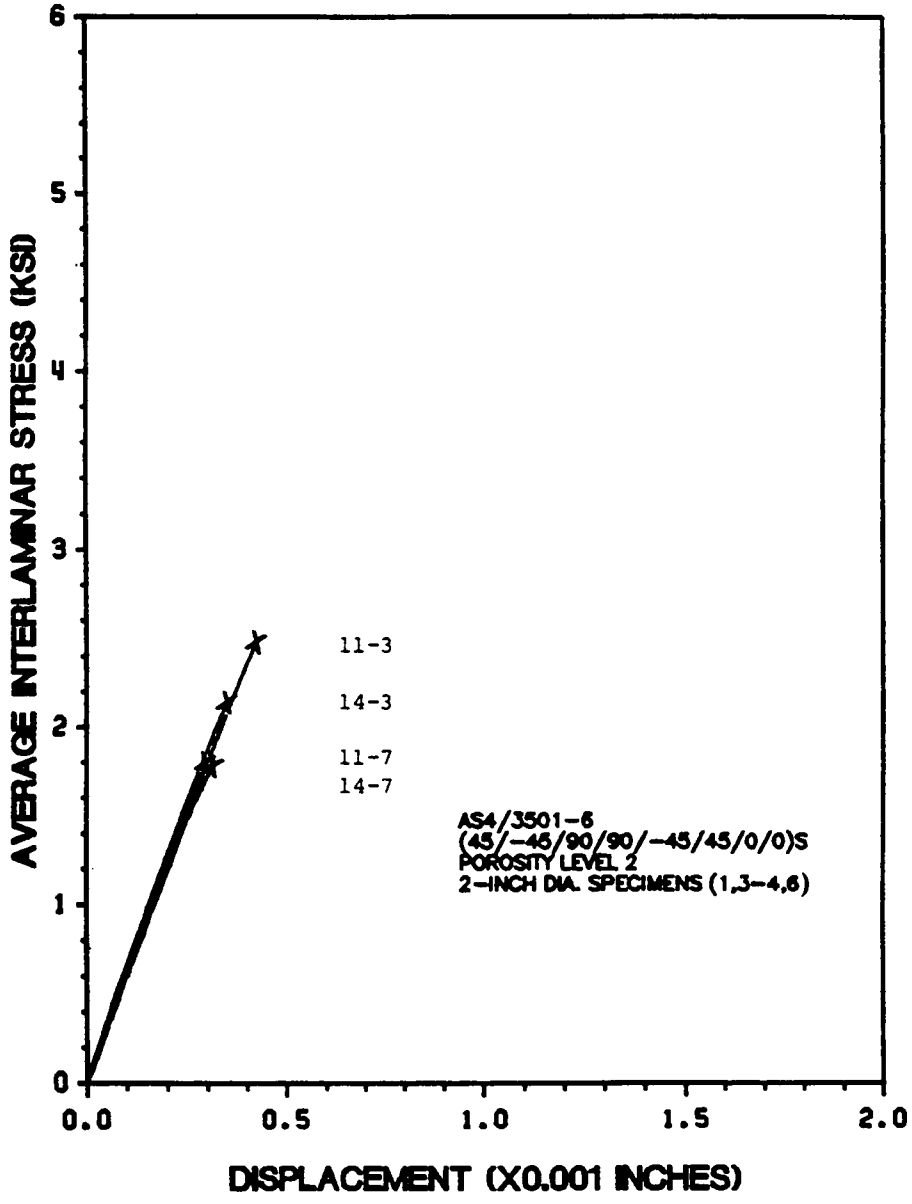

Figure 110. 2.0-Inch Diameter, AS4/3501-6 Defect Level 2 Specimens.

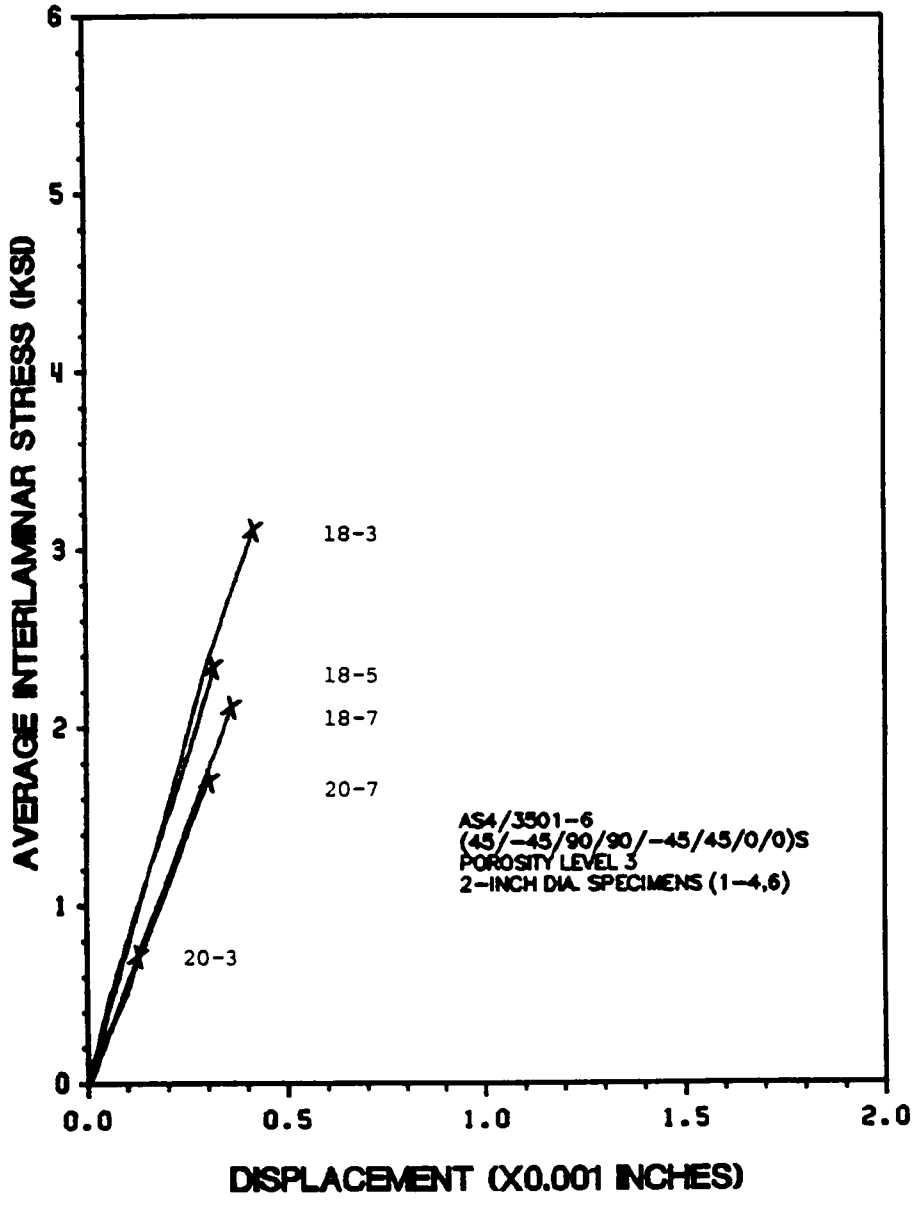

Figure 111. 2.0-Inch Diameter, AS4/3501-6 Defect Level 3 Specimens.

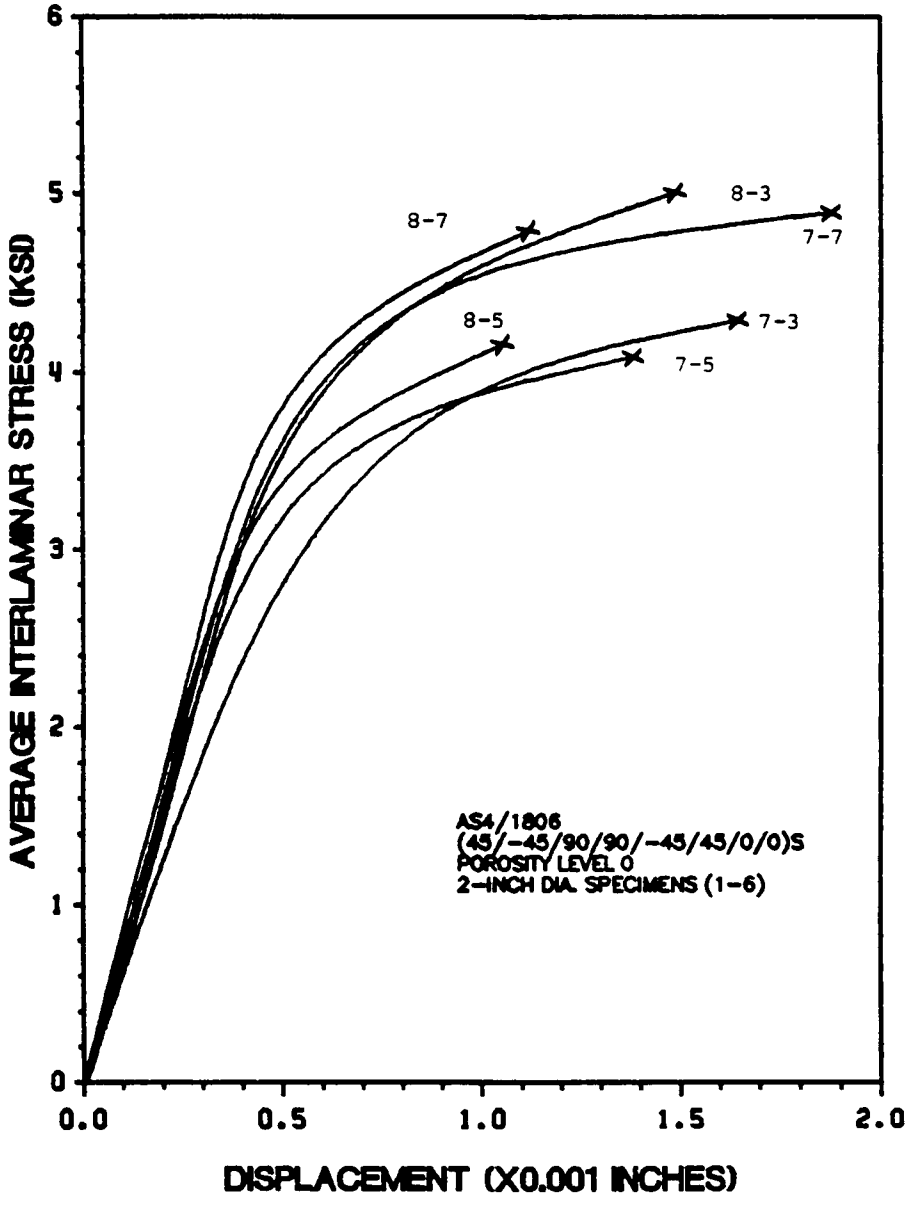

Figure 112. 2.0-Inch Diameter, AS4/1806 Defect Level 0 Specimens.

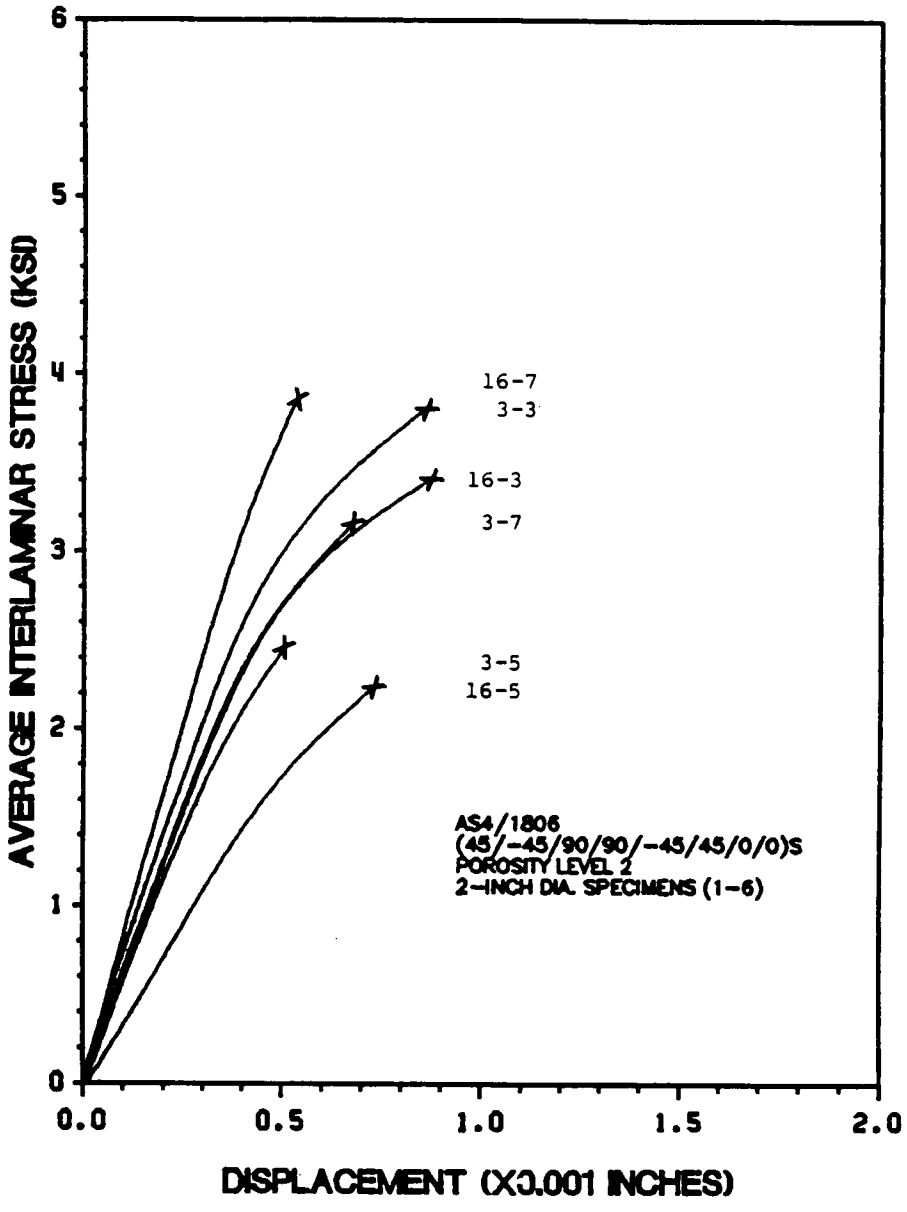

Figure 113. 2.0-Inch Diameter, AS4/1806 Defect Level 2 Specimens.

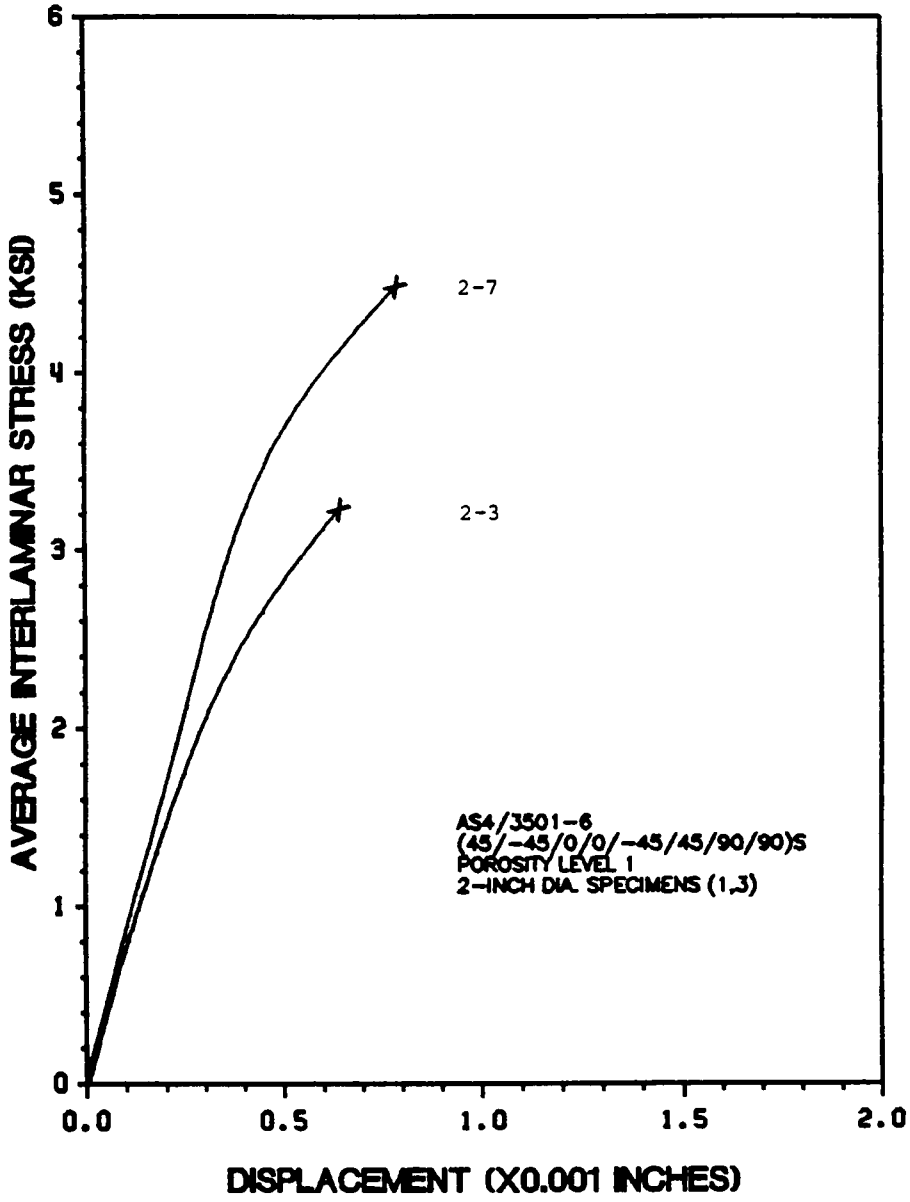

Figure 114. 2.0-Inch Diameter, AS4/3501-6 Defect Level 1 Specimens.

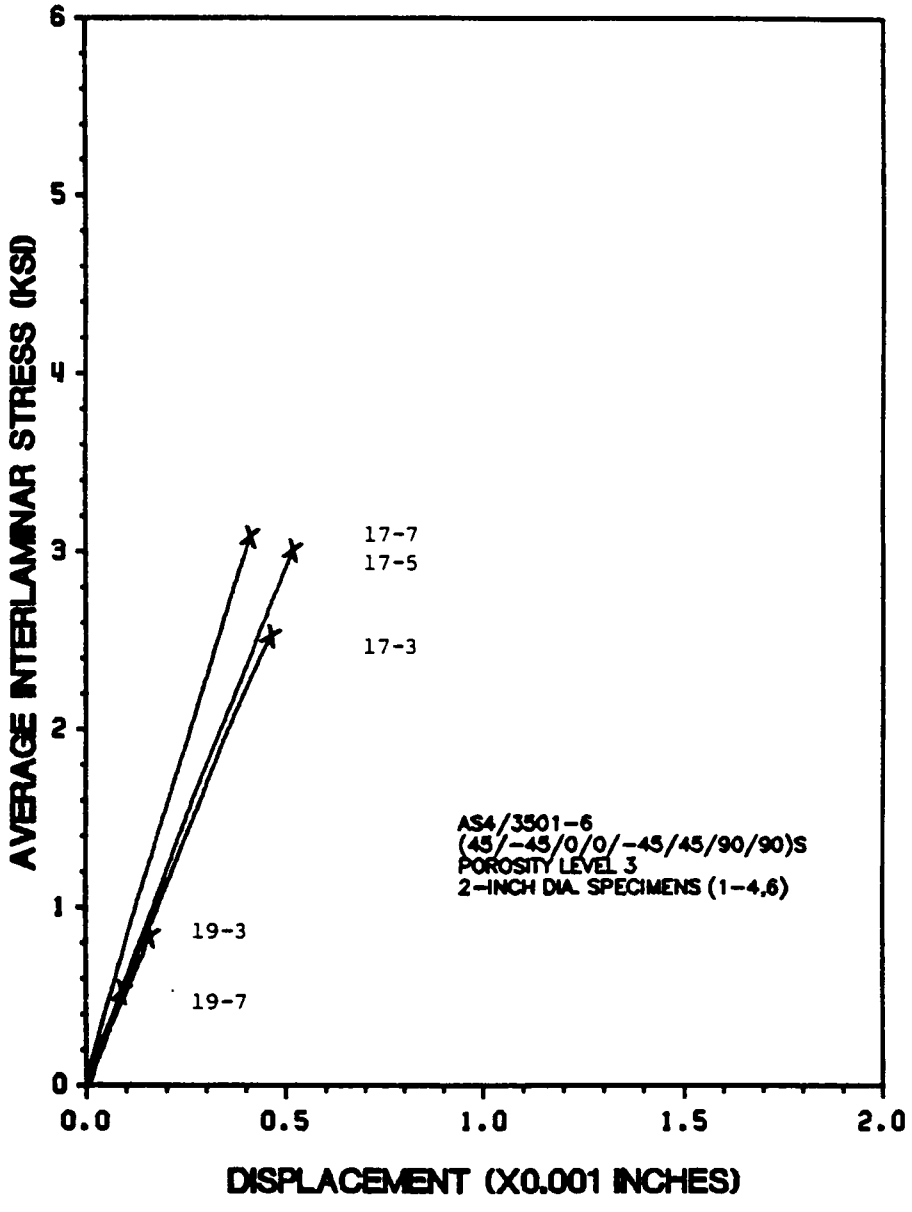

Figure 115. 2.0-Inch Diameter, AS4/3501-6 Defect Level 3 Specimens.

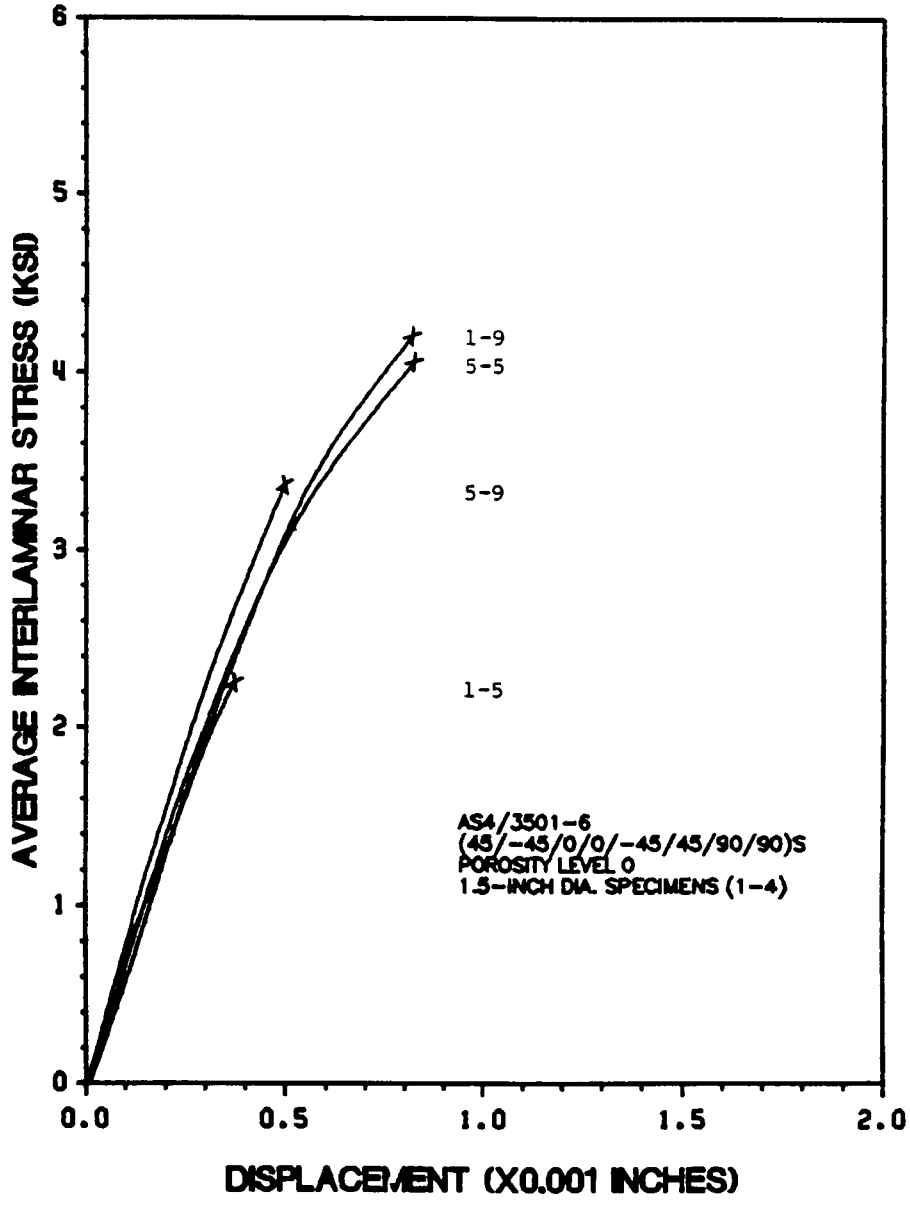

Figure 116. 1.5-Inch Diameter, AS4/3501-6 Defect Level 0 Specimens.

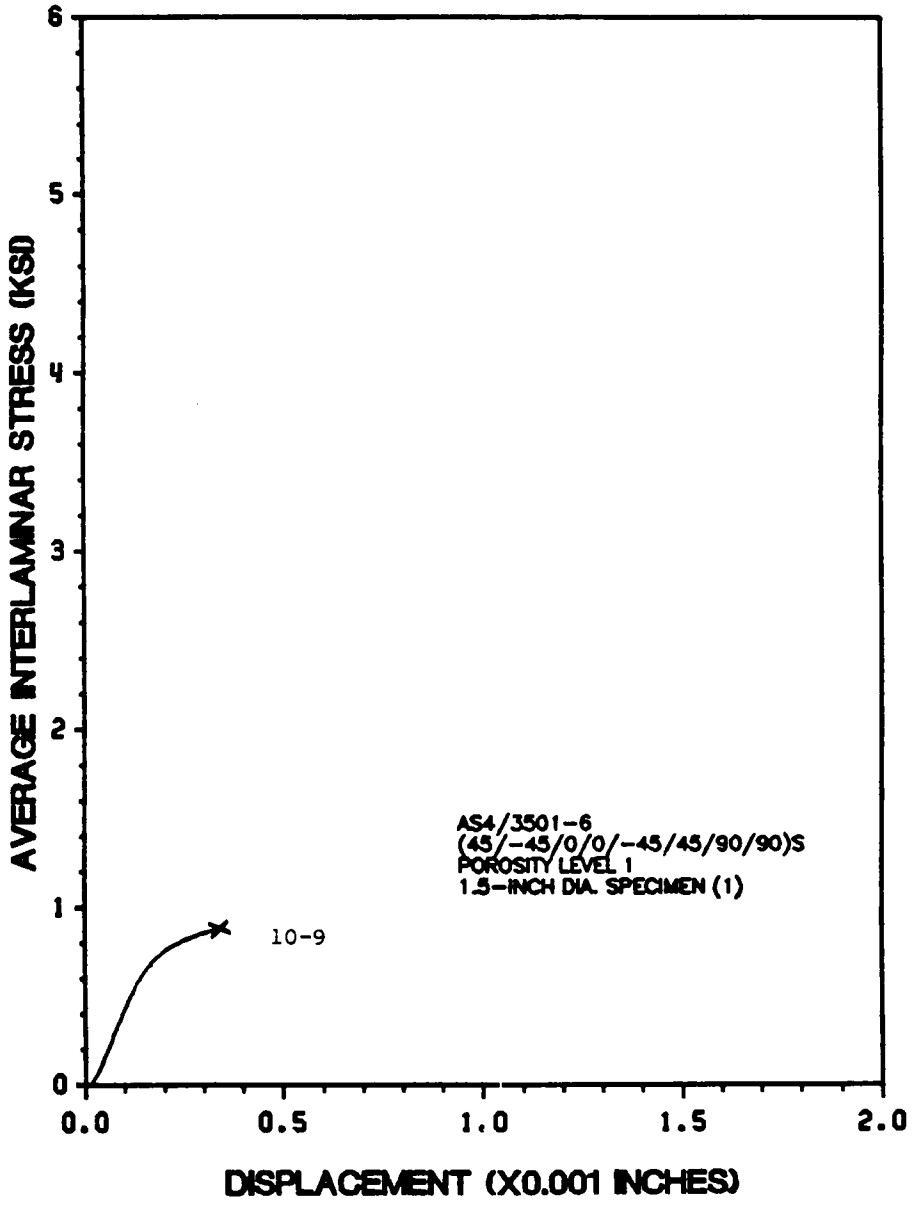

Figure 117. 1.5-Inch Diameter, AS4/3501-6 Defect Level 1 Specimens.

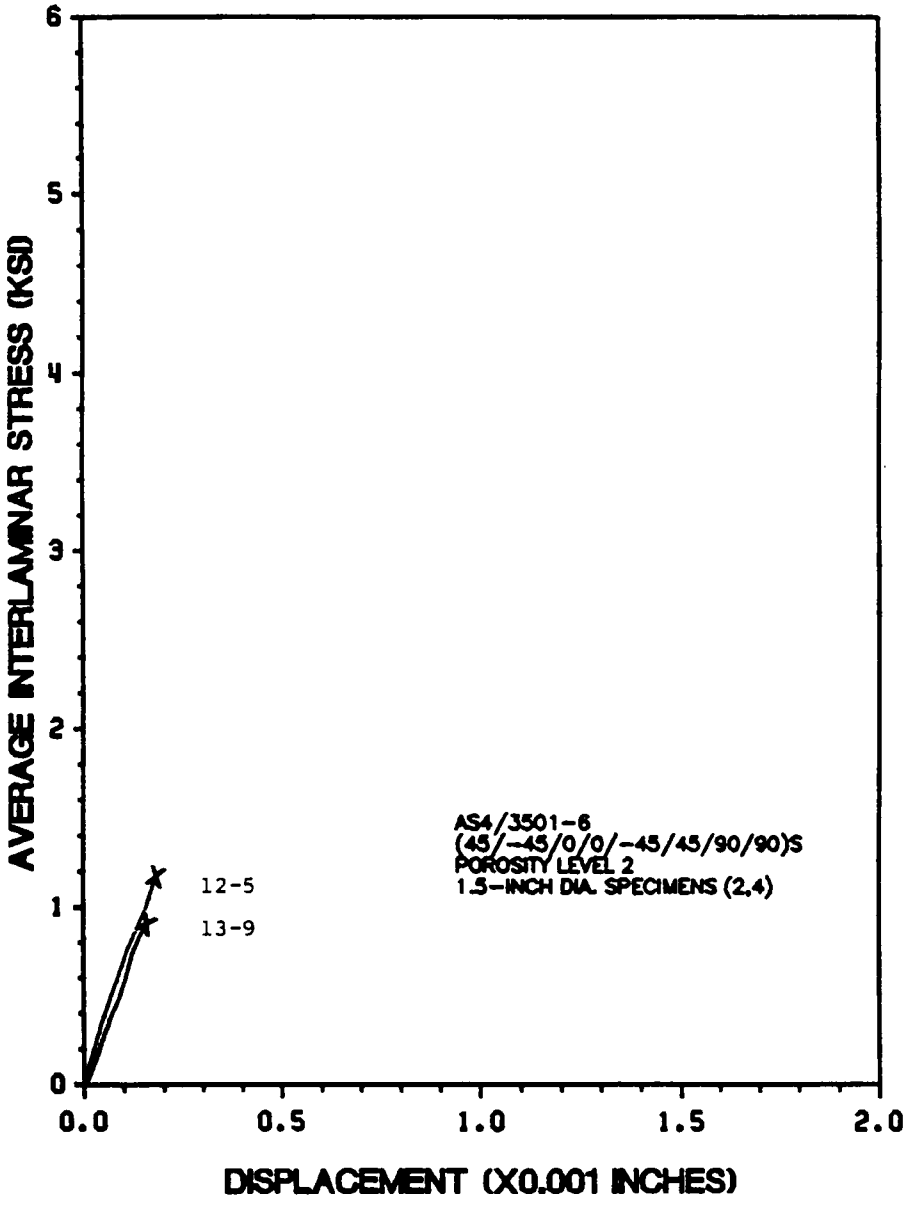

Figure 118. 1.5-Inch Diameter, AS4/3501-6 Defect Level 2 Specimens.

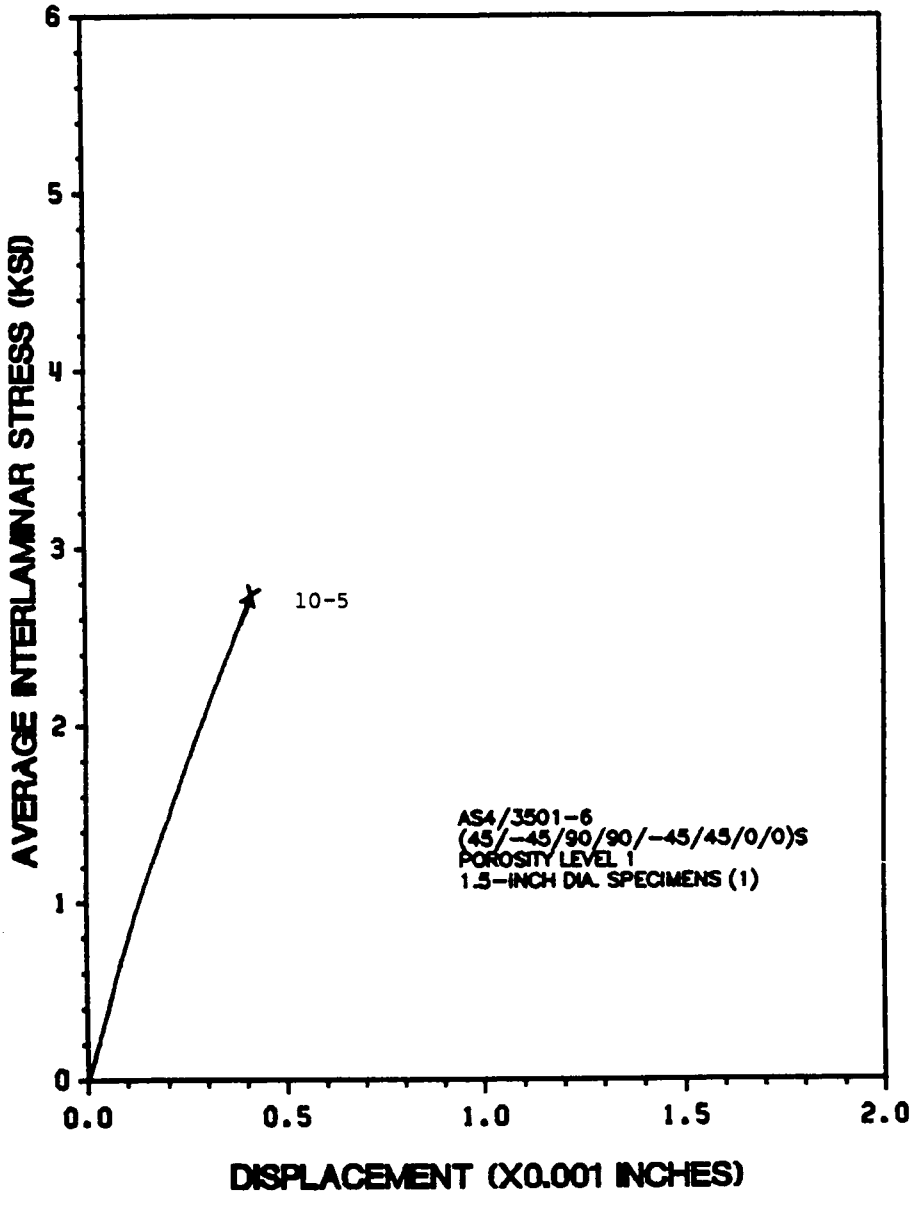

Figure 119. 1.5-Inch Diameter, AS4/3501-6 Defect Level 1 Specimens.

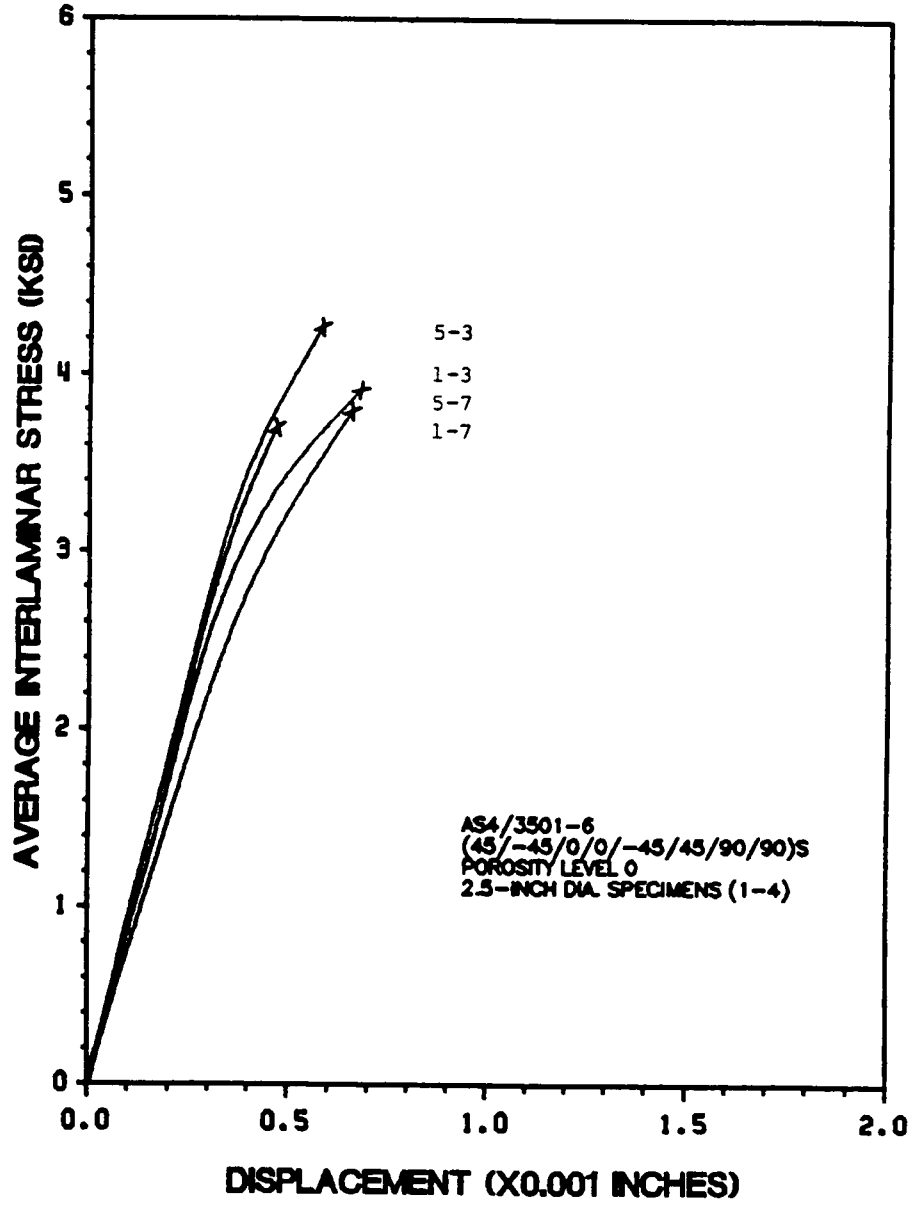

Figure 120. 2.5-Inch Diameter, AS4/3501-6 Defect Level 0 Specimens.

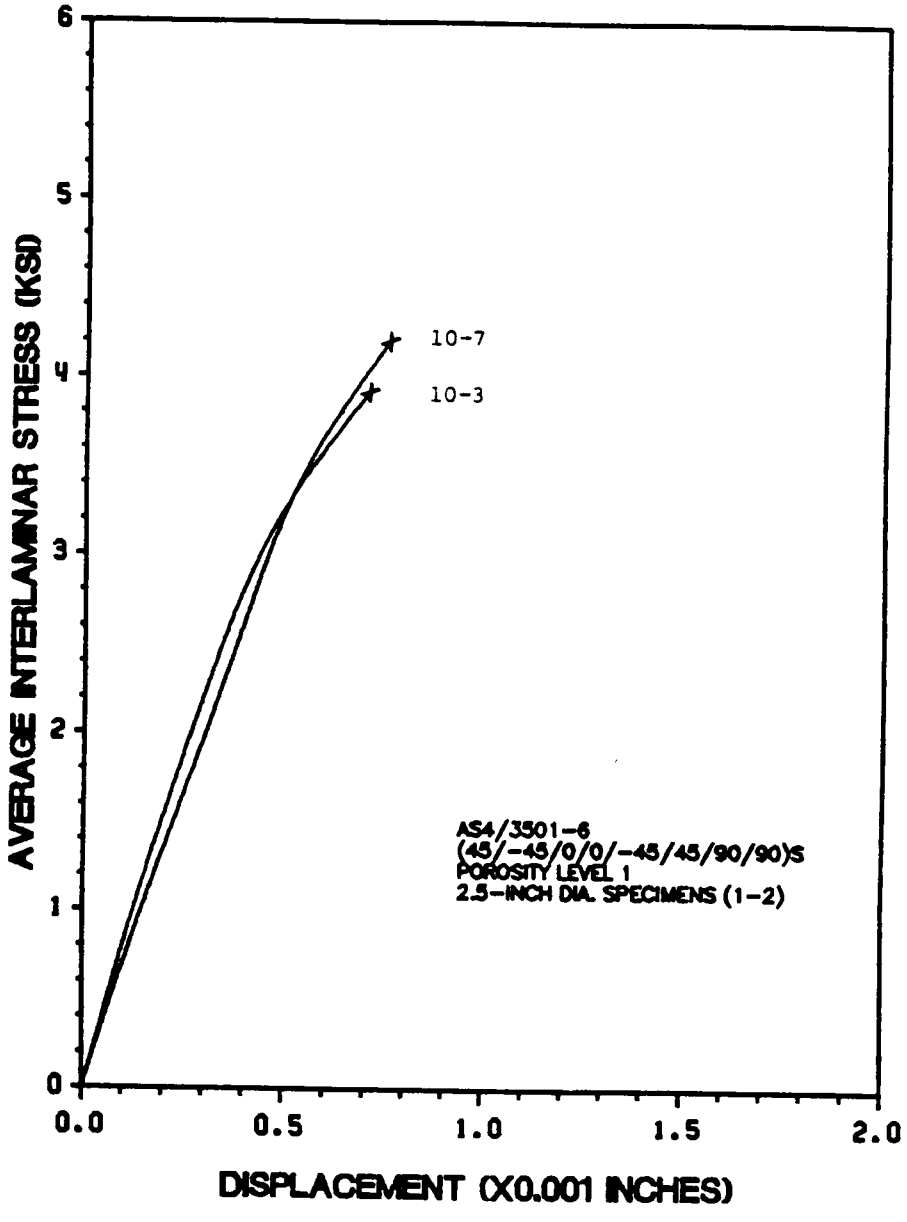

Figure 121. 2.5-Inch Diameter, AS4/3501-6 Defect Level 1 Specimens.

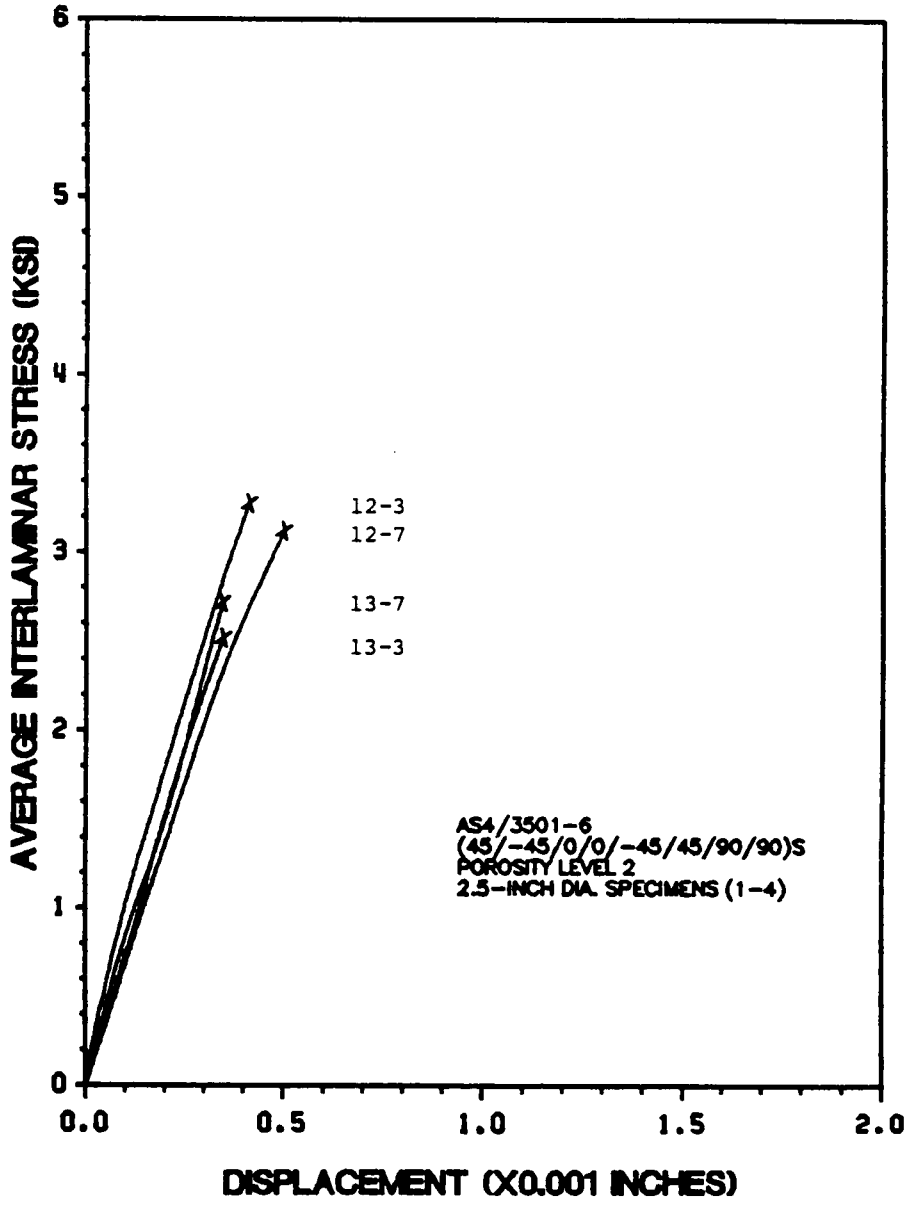

Figure 122. 2.5-Inch Diameter, AS4/3501-6 Defect Level 2 Specimens.

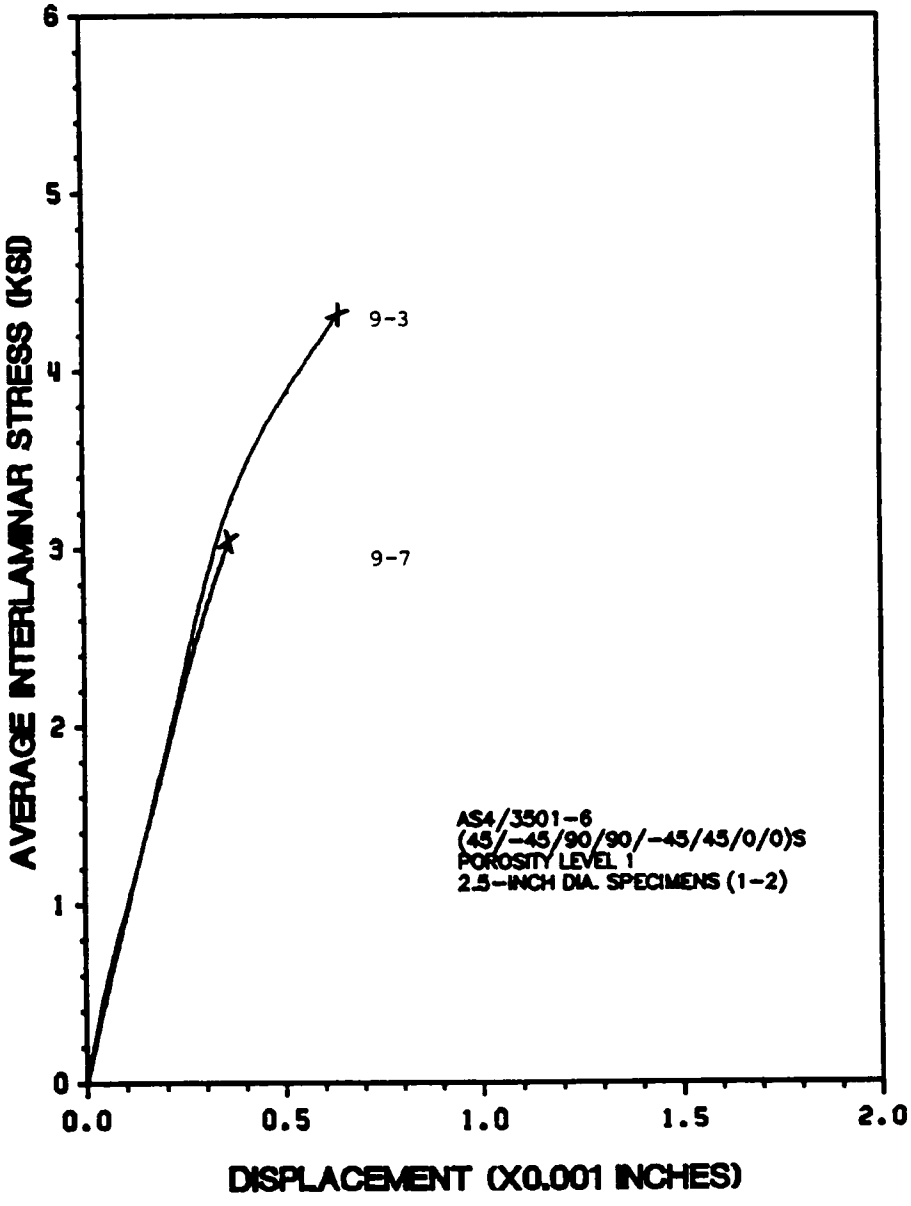

Figure 123. 2.5-Inch Diameter, AS4/3501-6 Defect Level 1 Specimens.

Appendix C. Adhesive Test Data

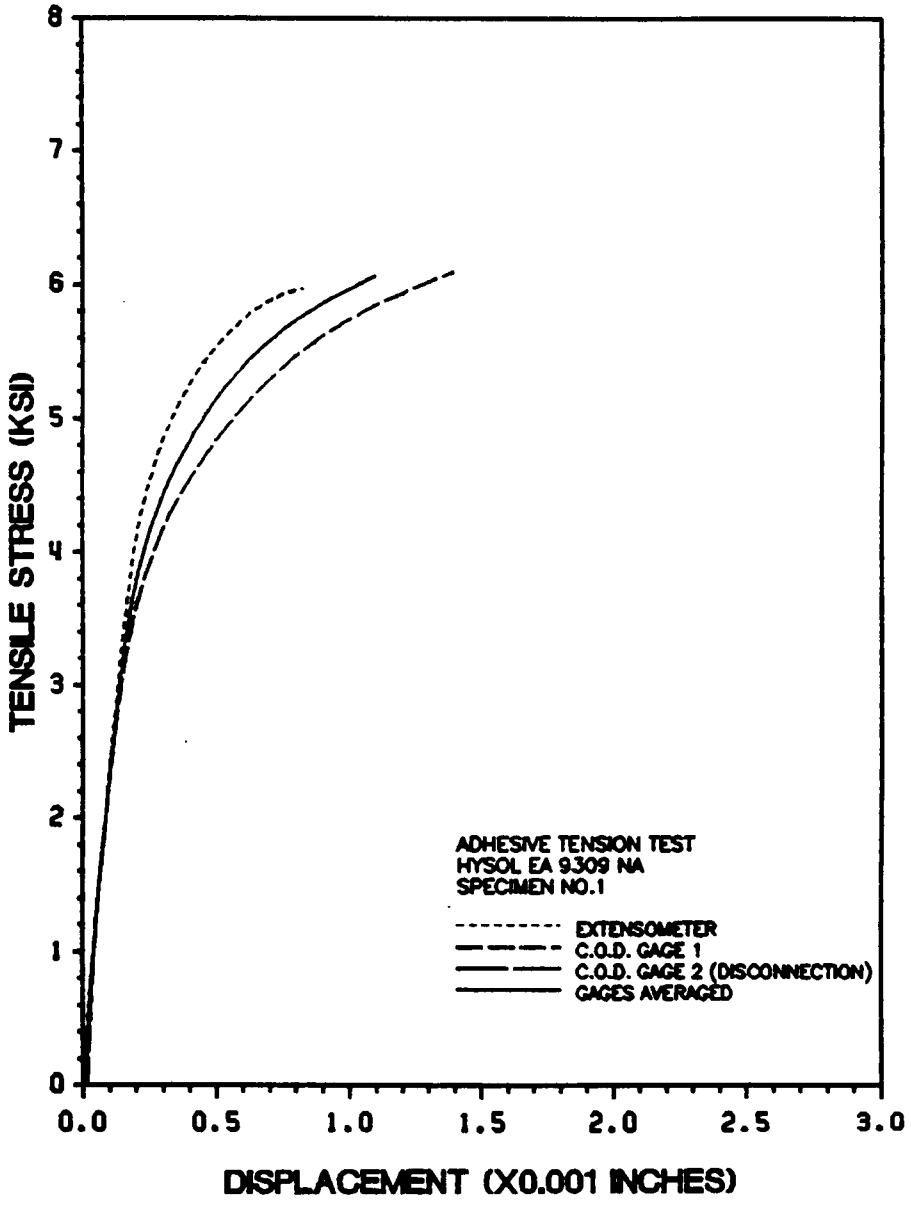

Figure 124. Adhesive Tensile Test (1), HYSOL EA 9309 NA.

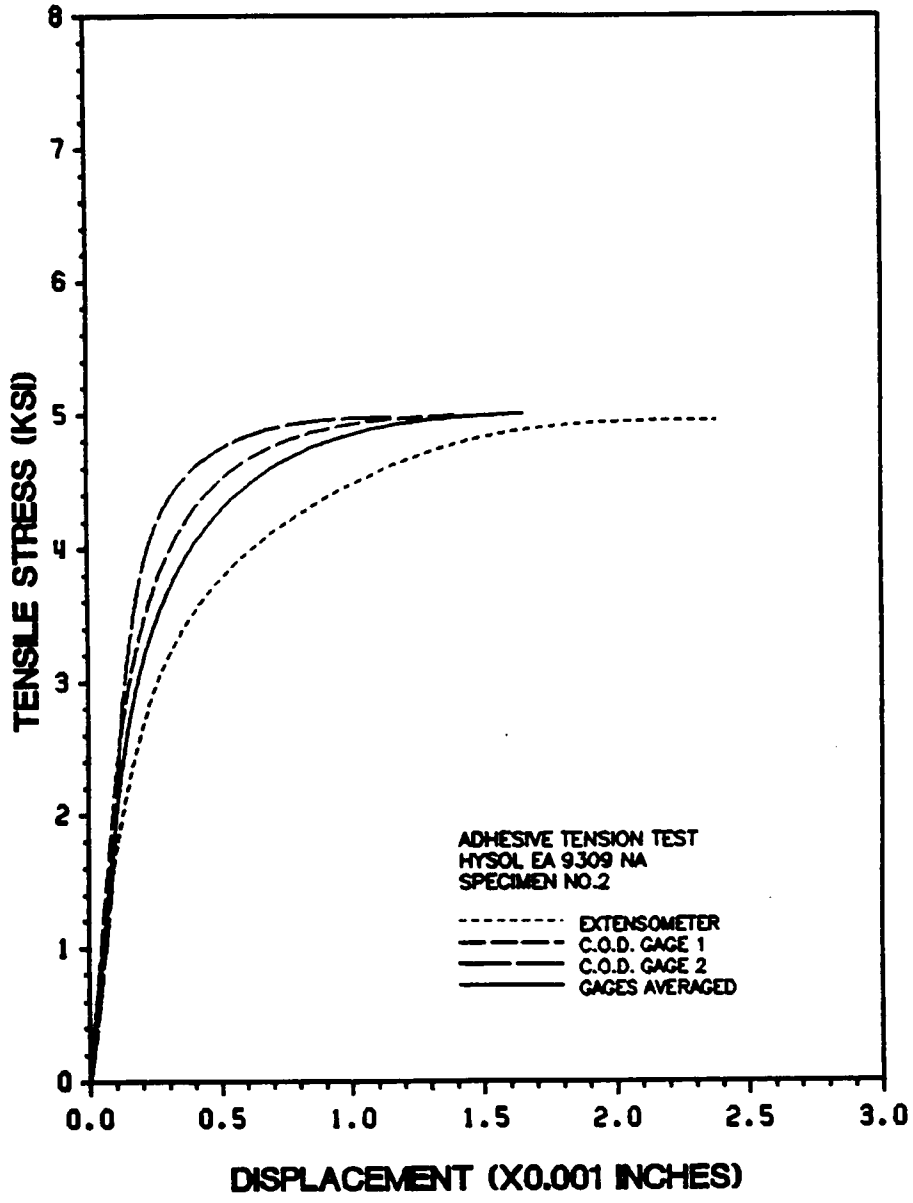

Figure 125. Adhesive Tensile Test (2), HYSOL EA 9309 NA.

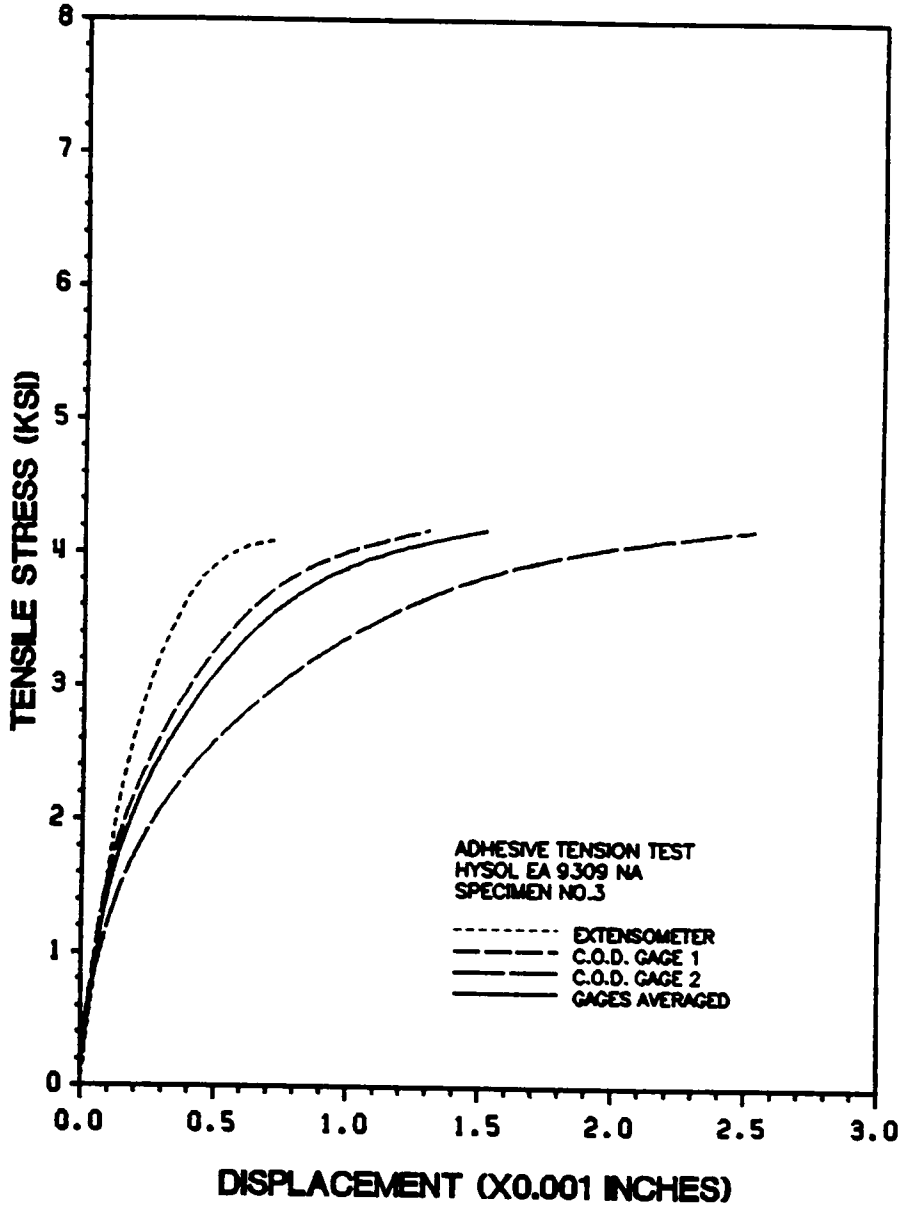

Figure 126. Adhesive Tensile Test (3), HYSOL EA 9309 NA.

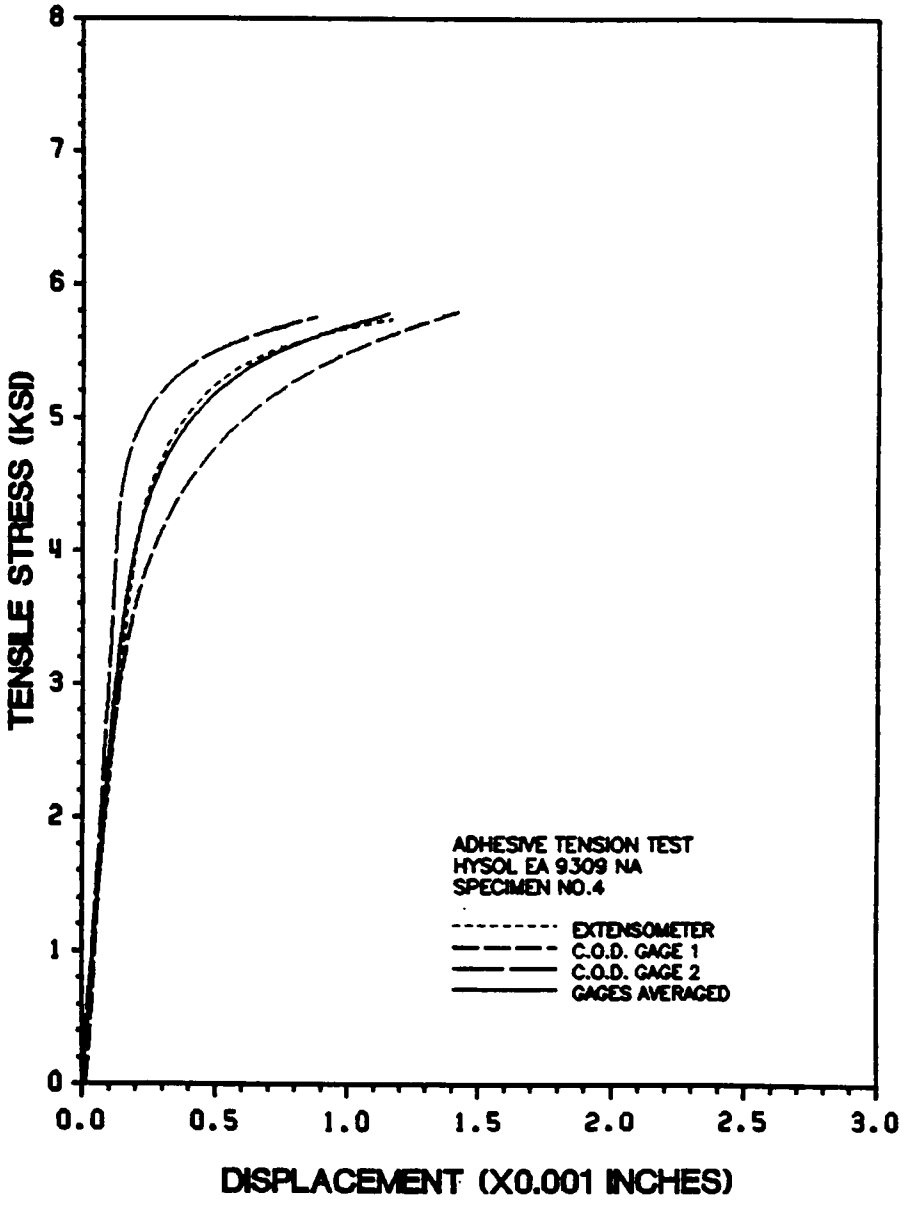

Figure 127. Adhesive Tensile Test (4), HYSOL EA 9309 NA.

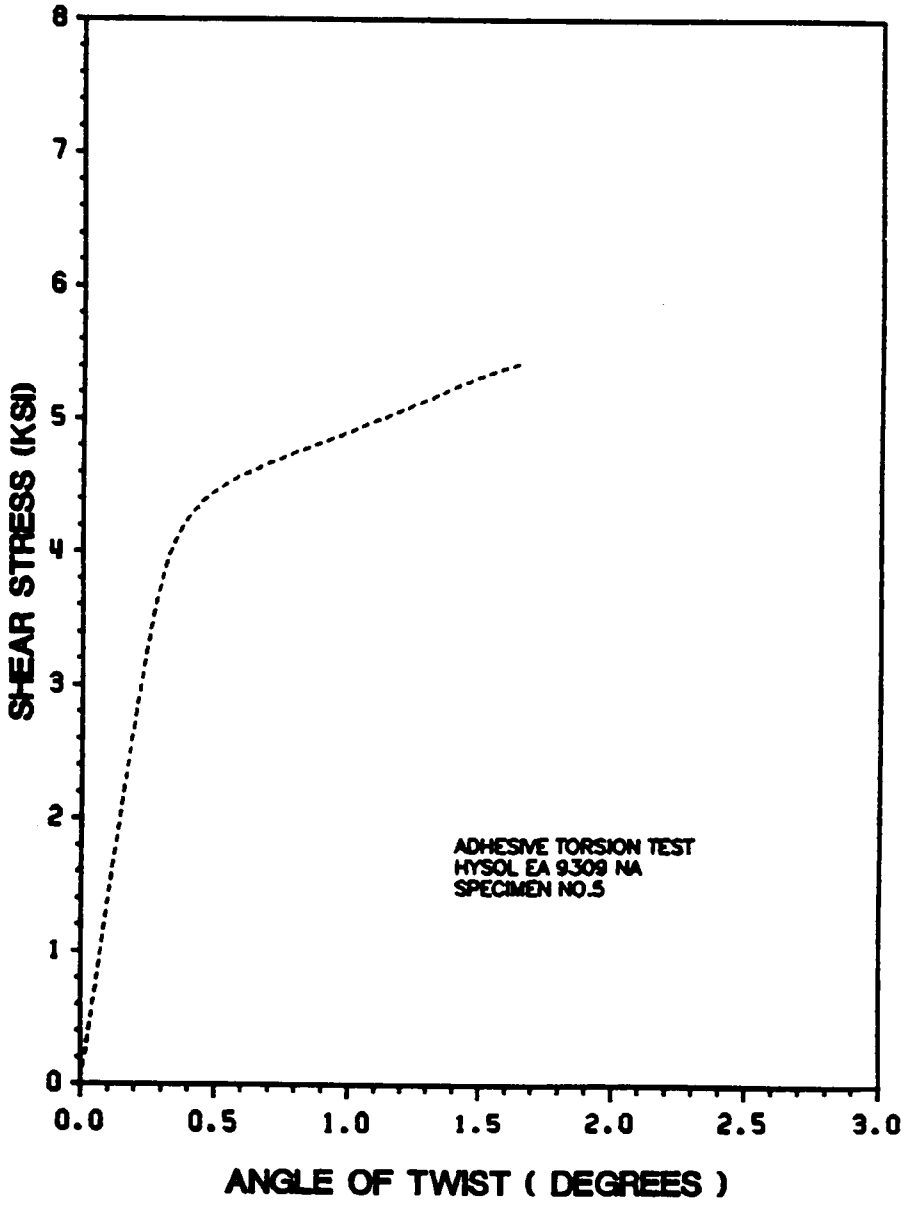

Figure 128. Adhesive Torsion Test (1), HYSOL EA 9309 NA.

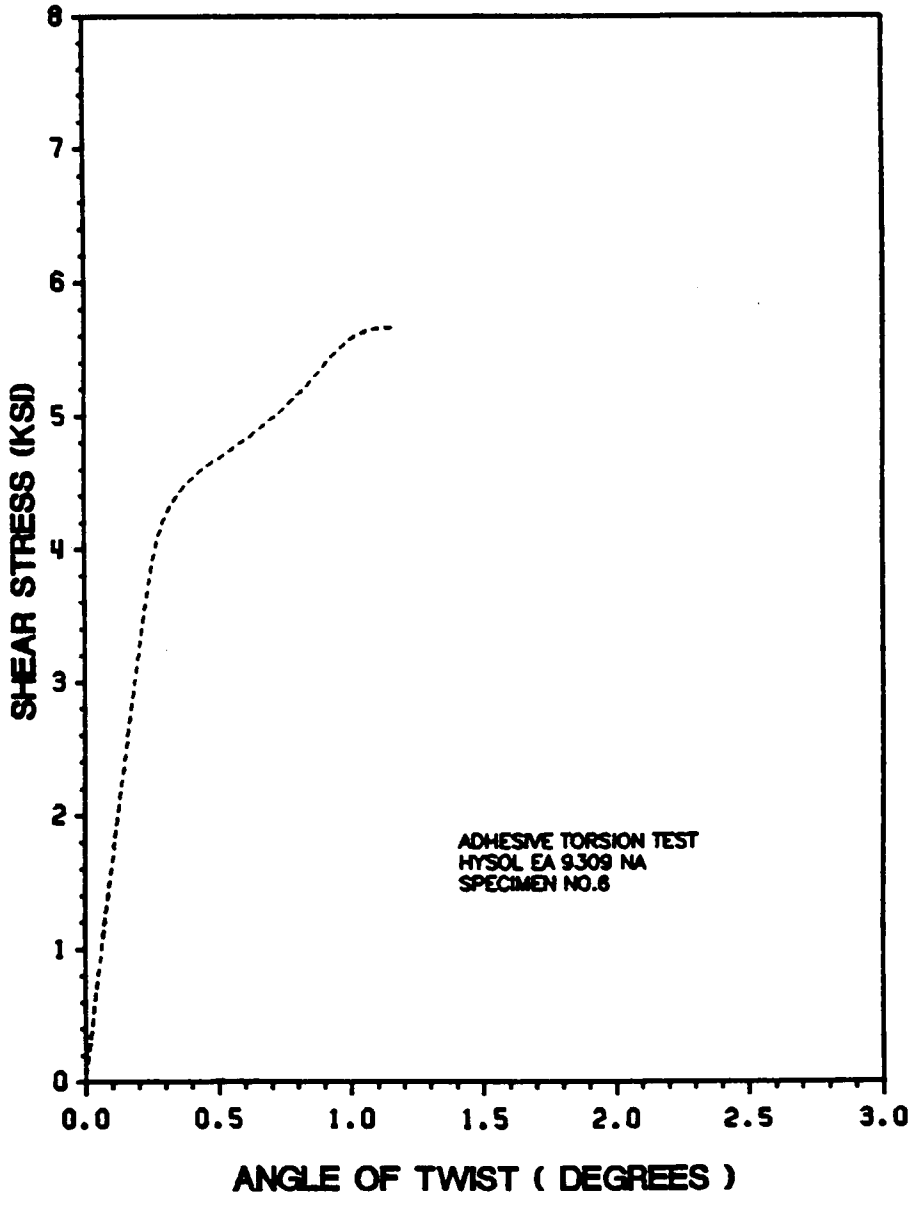

Figure 129. Adhesive Torsion Test (2), HYSOL EA 9309 NA.

Appendix D. Optical Analysis - Photomicrographs

Figure 130. Photomicrograph of AS4/1806 Specimen 7-3.

Figure 131. Photomicrograph of AS4/1806 Specimen 8-3.

Figure 132. Photomicrograph of AS4/1806 Specimen 3-7.

Figure 133. Photomicrograph of AS4/1806 Specimen 16-7.

Figure 134. Photomicrograph of AS4/3501-6 Specimen 5-3.

Figure 135. Photomicrograph of AS4/3501-6 Specimen 1-3.

Figure 136. Photomicrograph of AS4/3501-6 Specimen 10-3.

Figure 137. Photomicrograph of AS4/3501-6 Specimen 12-3.

Figure 138. Photomicrograph of AS4/3501-6 Specimen 13-7.

Figure 139. Photomicrograph of AS4/3501-6 Specimen 17-5.

Figure 140. Photomicrograph of AS4/3501-6 Specimen 19-3.

Figure 141. Photomicrograph of AS4/3501-6 Specimen 4-7.

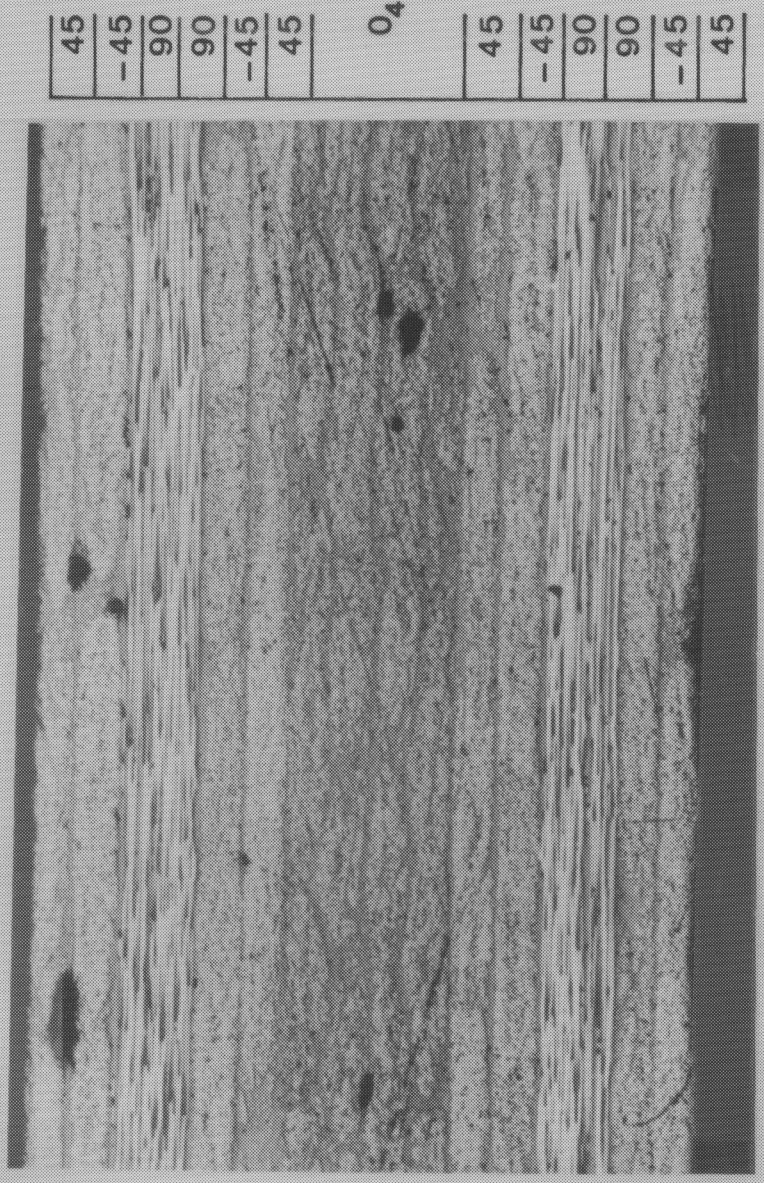

Figure 142. Photomicrograph of AS4/3501-6 Specimen 6-3.

Figure 142. Photomicrograph of AS4/3501-6 Specimen 6-3.

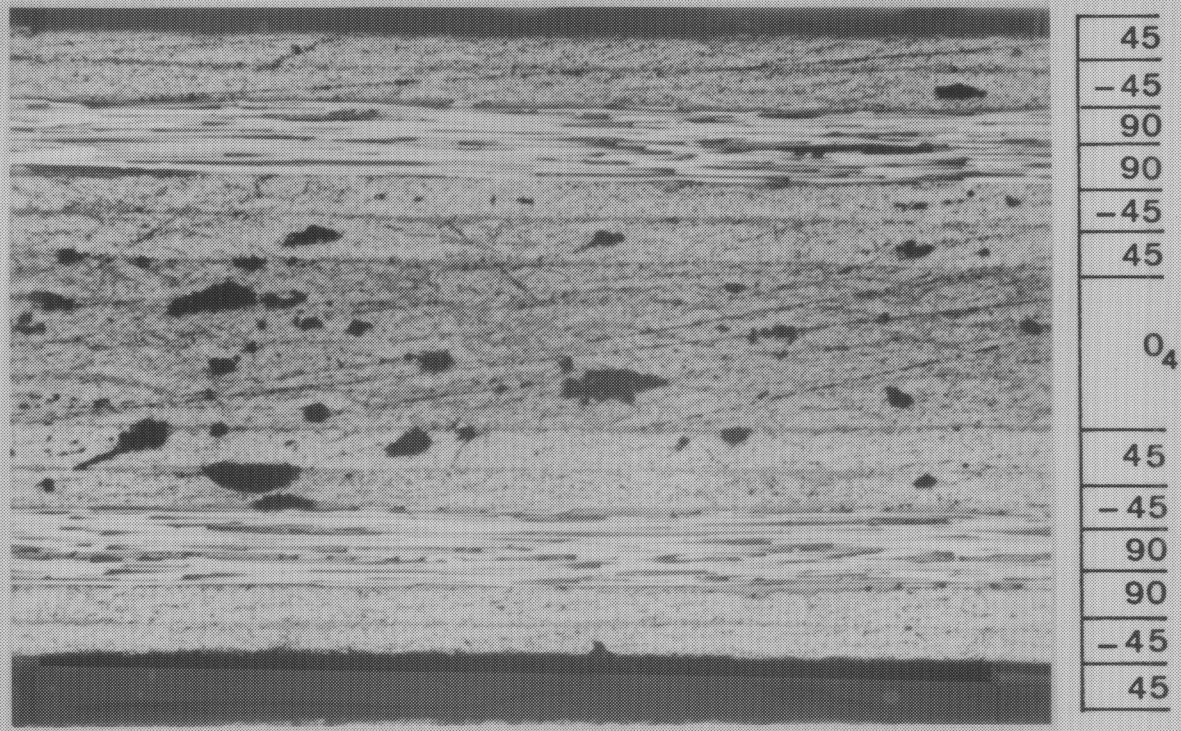

Figure 143. Photomicrograph of AS4/3501-6 Specimen 15-7.

Figure 144. Photomicrograph of AS4/3501-6 Specimen 11-3.

Figure 145. Photomicrograph of AS4/3501-6 Specimen 14-5.

Figure 146. Photomicrograph of AS4/3501-6 Specimen 18-7.

Figure 147. Photomicrograph of AS4/3501-6 Specimen 20-3(A).

Figure 148. Photomicrograph of AS4/3501-6 Specimen 20-3(B).

The vita has been removed from the scanned document